

Modulation of solid-liquid interaction for removal of dissolved
and suspended contaminants from water

By

Bishwash Shrestha

© 2022

Submitted to the graduate degree program in Mechanical Engineering and the Graduate
Faculty of the University of Kansas in partial fulfillment of the requirements for the
degree of Doctor of Philosophy

Prof. Paulette Spencer

Prof. Sara Wilson

Prof. Xinmai Yang

Prof. Reza Barati

Prof. Xianglin Li

Chair: Prof. Gibum Kwon

Date defended: 05/06/2022

The dissertation committee for Bishwash Shrestha certifies that this is the approved version of the following dissertation:

Modulation of solid-liquid interaction for removal of dissolved and suspended contaminants from water

Chair: Prof. Gibum Kwon

Date Approved: 05/06/2022

Abstract

Due to increasing concern over the shortage of freshwater, there is a dire need to remediate unconventional water sources such as agricultural, industrial, or municipal wastewater beyond what is obtainable from the hydrologic water cycle. With the advances in surface science, wastewater remediation technologies, including membrane-based and adsorption-based technologies, have been preferred due to their resilience and effectiveness. This dissertation aims to improve the existing membrane-based and adsorption-based technologies by modulating the solid-liquid interaction parameters like photocatalysis, wettability, and electrostatic force of attraction.

The first part of the dissertation discusses the fabrication of superhydrophilic and oleophobic coating, which can be utilized to separate and desalinate an oil and saline water mixture, and photocatalytically degrade the organic substances. The photocatalytic surface is coated on a commercial membrane with an ultraviolet (UV) light-curable adhesive. A mixture of photocatalytic nitrogen-doped titania (N-TiO₂) and perfluoro silane-grafted silica (F-SiO₂) nanoparticles is coated successively. The membrane resulted in a chemically heterogeneous surface with intercalating high and low surface energy regions (i.e., N-TiO₂ and F-SiO₂, respectively) that were securely bound to the commercial membrane surface. The coated membrane was then utilized for continuous separation and desalination of an oil-saline water mixture and for simultaneous photocatalytic degradation of the organic substances adsorbed on the membrane surface upon visible light irradiation.

In the second part, a photocatalytic mesh that can selectively permeate water while repelling oil was fabricated by coating a mixture of nitrogen-doped TiO₂ (N-TiO₂) and perfluoro silane-grafted SiO₂ (F-SiO₂) nanoparticles on a stainless-steel mesh. Utilizing the photocatalytic mesh, the time-

dependent evolution of the water-rich permeate flux as a result of photocatalytic degradation of the oil was studied under the visible light illumination is studied. A mathematical model was then developed that can relate the photocatalytic degradation of the organic substances deposited on a mesh surface to the evolution of the permeate flux. This model was established by integrating the Langmuir–Hinshelwood kinetics for photocatalysis and the Cassie–Baxter wettability analysis on a chemically heterogeneous mesh surface into a permeate flux relation. Consequently, the time-dependent water-rich permeate flux values are compared with those predicted by using the model. It is found that the model can predict the evolution of the water-rich permeate flux with a goodness of fit of 0.92.

In the following part, a robust in-air oleophobic hydrophilic coating for a filter was fabricated utilizing poly(ethylene glycol)diacrylate (PEGDA) and 1H,1H,2H,2H-heptadecafluorodecyl acrylate (F-acrylate). Methacryloxypropyl trimethoxysilane (MEMO) was utilized as an adhesion promoter to enhance the adhesion of the coating to the filter. The filter demonstrates robust oil repellency preventing oil adhesion and oil fouling. Utilizing the filter, gravity-driven and continuous separations of surfactant-stabilized oil-water emulsions are demonstrated. Finally, we demonstrate that the filter can be reused multiple times upon rinsing for further oil-water separations.

The fourth part of the dissertation focuses on the remediation of dissolved contaminants like PFAS. For this, electric field-aided adsorption has been explored. An inexpensive graphite adsorbent is fabricated by using a simple press, resulting in a mesoporous structure with a BET surface area of $132.9 \pm 10.0 \text{ m}^2 \text{ g}^{-1}$. Electric field-aided adsorption and desorption experiments are conducted by using a custom-made cell consisting of two graphite electrodes placed in parallel in a polydimethylsiloxane container. Unlike the conventional sorption process, a graphite electrode

exhibits a higher adsorption capacity for PFAS with a short fluoroalkyl chain (perfluoropentanoic acid, PFPA) in comparison to that with a long fluoroalkyl chain (perfluorooctanoic acid, PFOA). Upon alternating the voltage to a negative value, the retained PFPA or PFOA is released into the surrounding water. Finally, we engineered a device module mounted to a gravity-assisted apparatus to demonstrate electrosorption of PFAS and collection of high purity water.

In the last part, we demonstrate electrosorption of PFAS with varied fluoroalkyl chains by utilizing MXene-PEDOT:PSS adsorbent. Intercalation of PEDOT:PSS to the MXene help enhance the capacitive property of MXene, increasing the electrosorption of PFAS. Using the adsorbent, we demonstrate electrosorption of PFAS with varied fluoroalkyl chain lengths from water upon applying a voltage of $V = 1.0 \text{ V}$. Also, the adsorbent can desorb the PFAS from its surface when applying a voltage of $V = -1.0 \text{ V}$, which regenerates the adsorbent for further operations. Finally, a pseudo-second-order kinetic model that describes the reversible electrosorption of PFAS from MXene-PEDOT:PSS adsorbent is proposed.

Acknowledgments

I would like to express my special acknowledgment and gratitude to my advisor Prof. Dr. Gibum Kwon, for his patience, motivation, and continual support throughout my pursuit of the doctoral degree. His wisdom, guidance, and supervision throughout this pursuit have helped me grow as a researcher. I am greatly indebted for his encouragement, instruction, and immense intellectual contribution.

I would also like to thank the members of my doctoral committee: Prof. Dr. Paulette Spencer, Prof. Dr. Sara Wilson, Prof. Dr. Xinmai Yang, Prof. Dr. Reza Barati, and Prof. Dr. Xianlin Li for agreeing to be committee members regardless of their hectic schedule. I am sincerely thankful for their insightful review, comments, and encouragement. My sincere gratitude also goes to the Mechanical Engineering Department of the University of Kansas for providing me the platform and support in my pursuit of the degree. I am also grateful to the National Science Foundation, Bureau of Reclamation, and KU Office of Research for financially supporting my projects. I am also thankful to my friends, colleagues, and mentees for their support and motivation in making the journey enjoyable.

Lastly, I must express my profound appreciation and gratitude to my parents and brothers for their unwavering motivation, support, and dedication throughout my years of study. Thank you for being there for me in every moment and throughout. This achievement would not have been possible without them.

Thank you.

Bishwash Shrestha

Research Publications

This dissertation is prepared mainly based on my first-authored journal articles (P1-P4) and a research project listed below:

P1: *Shrestha, B., Ezazi, M., & Kwon, G. (2021). Engineered nanoparticles with decoupled photocatalysis and wettability for membrane-based desalination and separation of oil-saline water mixtures. Nanomaterials, 11(6), 1397.*

In this work, we engineered a visible light-responsive photocatalytic coating with superhydrophilic and oleophobic wettability both in air and underwater by utilizing nitrogen-doped titania (N-TiO₂) and perfluoro silane-grafted silica (F-SiO₂) nanoparticles. The coated membrane could be utilized for continuous separation and desalination of an oil–saline water mixture and for simultaneous photocatalytic degradation of the organic substances adsorbed on the membrane surface and flux recovery upon visible light irradiation.

P2: *Shrestha, B., Ezazi, M., Rad, S. V., & Kwon, G. (2021). Predicting kinetics of water-rich permeate flux through photocatalytic mesh under visible light illumination. Scientific reports, 11(1), 1-9.*

In this work, we conducted an experimental analysis on the effect of wettability and photocatalysis on the permeate flux through a photocatalytic material-coated stainless steel mesh and developed a mathematical relation between them under visible light illumination. The mathematical model was then utilized to predict the water-rich permeate flux through the photocatalytic mesh during

visible light illumination. The accuracy of the predicted flux values was then validated by comparing them with the experimentally acquired results.

P3: Shrestha, B., Ezazi, M., & Kwon, G. (2021). Delamination-Free In-Air and Underwater Oil-Repellent Filters for Oil-Water Separation: Gravity-Driven and Cross-Flow Operations. *Energies*, 14(21), 7429.

In this work, we report on a superhydrophilic and in-air oleophobic filter by grafting a composite mixture of poly(ethylene glycol)diacrylate (PEGDA) and 1H,1H,2H,2H-heptadecafluorodecyl acrylate (F-acrylate) via silane chemistry. This enables the resulting coating (F-PEGDA) to firmly attach to the filter surface. The filter exhibits ultralow oil adhesion forces, both in air and underwater, which results in resistance to oil fouling during oil-water separation. Utilizing this filter, separation of surfactant-stabilized oil-in-water and water-in-oil emulsions is demonstrated.

P4: Shrestha, B., Ezazi, M., Ajayan, S., & Kwon, G. (2021). Reversible adsorption and desorption of PFAS on inexpensive graphite adsorbents via alternating electric field. *RSC Advances*, 11(55), 34652-34659.

In this work, we demonstrate an inexpensive graphite adsorbent that enables reversible adsorption and desorption of PFAS with both short and long fluoroalkyl chain lengths (perfluoropentanoic acid (PFPA) and PFOA) in water upon alternating the voltage. The PFAS readily adsorbs to the graphite adsorbent upon application of a positive voltage within ≈ 10 s. We demonstrate that the adsorbed PFAS can be released into water with a high desorption efficiency of $\approx 96\%$ and $\approx 94\%$ for PFPA and PFOA, respectively, upon alternating voltage to a negative value. We also establish

a quantitative relation to describe the kinetics of electrosorption for PFAS on a graphite adsorbent surface by utilizing a pseudo second-order kinetic model.

Table of Contents

Abstract.....	iii
Acknowledgments	vi
Research Publications.....	vii
List of Figures.....	xiii
List of Tables	xix
Chapter 1. Introduction	1
1.1. Current water crisis: Shortage of freshwater due to contamination	1
1.2. Contaminants in water: suspended or dissolved	2
1.3. Wastewater remediation technologies.....	2
1.4. Membrane-based wastewater remediation technologies.....	3
1.4.1. Various membrane technologies.....	4
1.4.2. Membrane fouling.....	5
1.4.3. Mitigation of fouling.....	5
1.4.4. Photocatalytic membrane with modulated wettability: Need for decoupling of wettability and photocatalysis.....	10
1.5. Adsorption-based wastewater remediation technologies	11
1.5.1. Adsorption and regeneration of adsorbent	11
1.5.2. Electric field aided adsorption	12
1.5.3. Reversible electrosorption of dissolved contaminants (PFAS)	15
1.6. Scope of the dissertation	15
1.7. References	17
Chapter 2: Engineered Nanoparticles with Decoupled Photocatalysis and Wettability for Membrane-based Desalination and Separation of Oil-Saline Water Mixtures	28
2.1. Introduction.....	28
2.2. Experimental procedure.....	30
2.2.1. Chemicals.....	30
2.2.2. Synthesis of N-TiO ₂ nanoparticles.....	31
2.2.3. Synthesis of F-SiO ₂ nanoparticles.....	31
2.2.4. Photocatalytic membrane fabrication.....	31
2.2.5. Preparation of oil-in-water emulsion dissolved with salt.....	32
2.2.6. N-TiO ₂ and F-SiO ₂ size measurements.....	32
2.2.7. N-TiO ₂ crystal structure analyses.	32
2.2.8. N-TiO ₂ and F-SiO ₂ absorbance measurements.....	33
2.2.9. N-TiO ₂ photocatalytic performance measurements.....	33
2.2.10. Membrane surface analysis.....	33
2.2.11. Visible light intensity measurement.....	33
2.2.12. Salt and oil concentration measurements.....	34

2.2.13. Engineering a continuous separation and desalination apparatus.....	34
2.3. Results and discussion	35
2.3.1. Synthesis of N-TiO ₂ and characterization of its photocatalysis upon visible light irradiation.....	35
2.3.2. Fabrication and characterization of N-TiO ₂ /F-SiO ₂ coated membrane.....	38
2.3.3. Continuous separation and desalination of an oil-saline water mixture and simultaneous photocatalytic degradation of organic foulants upon visible light irradiation.....	45
2.3.4. Robustness of the membrane	48
2.4. Conclusions.....	52
2.5. References.....	53
Chapter 3: Predicting kinetics of water-rich permeate flux through photocatalytic mesh under visible light illumination.....	57
3.1. Introduction.....	57
3.2. Experimental procedure.....	60
3.2.1. Synthesis of N-TiO ₂ and F-SiO ₂ nanoparticles.....	60
3.2.2. Fabrication of photocatalytic mesh with selective wettability for water over oil.....	61
3.2.3. Surfactant-stabilized oil-in-water emulsion.....	61
3.2.4. Determining the nominal pore size of the mesh.....	61
3.2.5. Contact angle measurement.....	62
3.2.6. Visible light intensity measurement.....	62
3.2.7. Root mean square (RMS) roughness measurements.....	62
3.3. Results and discussion	62
3.3.1. Photocatalytic mesh fabrication and under-oil water wettability.....	62
3.3.2. Time-dependent change of mesh surface wettability submerged in oil.....	65
3.3.3. Evolution of the water-rich permeate flux	68
3.3.4. Mathematical representation of the permeate flux kinetics	72
3.3.5. Extraction of r_m , R_c , $f_{c(T)}$, and $f_{c(F)}$	73
3.3.6. Prediction of the flux	79
3.4. Conclusions.....	79
3.5. References.....	81
Chapter 4: Delamination-Free In-Air and Underwater Oil-Repellent Filters for Oil-Water Separation: Gravity-Driven and Cross-Flow Operations.....	86
4.1. Introduction.....	86
4.2. Experimental procedure.....	89
4.2.1. Grafting MEMO on the filter surface.....	89
4.2.2. Coating F-PEGDA on filter.....	90
4.2.3. Measuring pore size of filters.....	90
4.2.4. Determining the nominal pore size of the mesh.....	90
4.2.5. Contact angle measurement.....	91
4.2.6. Zeta potential measurements.....	91
4.2.7. Synthesis of oil-water emulsions.....	91
4.2.8. Dispersed phase size measurements:	92
4.2.9. Filter surface topology characterization.....	92
4.2.10. Underwater adhesion force measurements	92
4.2.11. Thermogravimetric analyses (TGA).....	92
4.2.12. Continuous separation apparatus.....	92

4.3. Results and discussion	93
4.3.1. Fabrication of a hydrophilic and in-air oleophobic filter.....	93
4.3.2. Pore size measurement.....	95
4.3.3. Wettability, surface energy, underwater oil adhesion force, and breakthrough pressure measurement	96
4.3.4. Coating robustness measurement.....	104
4.3.5. Gravity assisted oil-water separation	105
4.3.6. Continuous oil-water separation	108
4.4. Conclusions.....	110
4.5. References.....	112
Chapter 5: Reversible adsorption and desorption of PFAS on inexpensive graphite adsorbents via alternating electric field.....	116
5.1. Introduction.....	116
5.2. Experimental procedure.....	119
5.2.1. Materials.	119
5.2.2. Fabrication of graphite adsorbents.....	119
5.2.3. Characterization of graphite adsorbents.....	119
5.2.4. Reversible adsorption and desorption of PFAS.....	120
5.2.5. Fabrication of a device module for electrosorption of PFAS and gravity-assisted collection of high purity water.....	121
5.2.6. PFAS concentration measurements.	122
5.3. Results and discussion	122
5.3.1. Characterization of surface morphology, surface area, and pore size distribution of graphite adsorbents	122
5.3.2. Electrochemical analysis.....	124
5.3.3. Reversible adsorption and desorption of PFAS upon alternating electric field.....	126
5.3.4. Kinetics of the reversible electrosorption for PFAS	130
5.3.5. Electrosorption of PFAS and gravity-assisted collection of high purity water.....	132
5.4. Conclusions.....	135
5.5. References.....	136
Chapter 6: Electrosorption-driven remediation of PFAS-contaminated water with Engineered MXene/PEDOT:PSS Adsorbents.....	141
6.1. Introduction.....	141
6.2. Experimental procedure.....	144
6.2.1. Synthesis of MXene.....	144
6.2.2. Preparation of MXene-PEDOT:PSS adsorbent.	144
6.2.3. Characterization of surface morphology, chemistry, and interlayer spacing of MXene-PEDOT:PSS.....	145
6.2.4. Characterization of electrochemical properties of MXene-PEDOT:PSS.	145
6.2.5. Adsorption and desorption tests.....	146
6.3. Results and discussion	146
6.3.1. Characterization of surface and its morphology	146
6.3.2. Electrochemical characterization	149
6.3.3. Adsorption and desorption of PFAS	151
6.3.4. Kinetics of adsorption and desorption	154
6.4. Conclusions.....	156

6.5. References.....	157
Chapter 7: Dissertation Summary and Future Outlook	161
7.1. Dissertation Summary.....	161
7.2. Future Outlook.....	163
7.2.1. Photocatalytic and selective wettable membrane for wastewater remediation.....	163
7.2.2. Electric field aided sorption for wastewater remediation	164
7.3. References.....	165
Paper P1	167
Paper P2	182
Paper P3	192
Paper P4	205
Paper P1 Copyright Permission	214
Paper P2 Copyright Permission	215
Paper P3 Copyright Permission	216
Paper P4 Copyright Permission	217

List of Figures

Figure 1.1. Classification of membrane-based technologies.	4
Figure 1.2. A schematic illustrating a contact of a liquid droplet on a smooth surface.	8
Figure 1.3. Classification of a surface based on the contact angles for liquid. (a) Superomniphilic ($\theta_{\text{water}} \approx 0^\circ$ and $\theta_{\text{oil}} \approx 0^\circ$). (b) Omniphilic (θ_{water} and $\theta_{\text{oil}} < 90^\circ$). (c) Omniphobic ($90^\circ < \theta_{\text{water}}$ and $\theta_{\text{oil}} < 150^\circ$). (d) Superomniphobic (θ_{water}^* and $\theta_{\text{oil}}^* > 150^\circ$).	9
Figure 1.4. A schematic of electrosorption process.	13
Figure 2.1. (a) Schematic illustrating the synthesis of N-TiO ₂ nanoparticles by utilizing titanium butoxide (TBOT) and triethylamine (TEA) as TiO ₂ precursor and nitrogen dopant, respectively. (b) A number size distribution of N-TiO ₂ nanoparticles obtained by utilizing the DLS method.	35
Figure 2.2. (a) The XPS spectrum of N-TiO ₂ exhibiting characteristic peaks of N 1s, Ti 2p, and O 1s. The spectrum of a neat TiO ₂ is also shown for comparison. Inset shows the core level spectrum of characteristic N 1s. (b) XRD pattern of N-TiO ₂ synthesized by using a molar ratio of TEA and TBOT as 2.0. The XRD pattern of a neat TiO ₂ is also shown. (c) Ultraviolet-visible (UV-Vis) absorption spectra of N-TiO ₂ synthesized by varied molar ratios of TEA to TBOT (e.g., 0.5, 1.0, 2.0, and 3.0). Neat TiO ₂ and SiO ₂ absorption spectra are also shown for comparison.	36
Figure 2.3. (a) UV-Vis absorption spectra of water dissolved with N-TiO ₂ and Solvent Blue dye as a function of visible light irradiation time. Inset: A photograph showing the water dissolved with Solvent Blue dye after visible light irradiation for 2 h, 4 h, 8 h, and 10 h. The as-prepared water dissolved with Solvent Blue dye (concentration = 0.5 wt%) is also shown. (b) UV-Vis absorption spectra of water solutions dissolved with Solvent Blue 38 dye (concentration = 0.5 wt%) and N-TiO ₂ (concentration = 0.5 wt%) after 2h of visible light irradiation with varied intensity. The UV-Vis absorption spectra of water solution dissolved with Solvent Blue 38 dye (concentration = 0.5 wt%) and N-TiO ₂ (concentration = 0.5 wt%) after 10h in dark is also provided.	37
Figure 2.4. (a) Schematic illustrating the synthesis of F-SiO ₂ nanoparticles by utilizing tetraethyl orthosilicate (TEOS) as SiO ₂ precursor and 1H,1H,2H,2H-perfluorodecyl trichlorosilane (i.e., perfluoro silane). (b) A number size distribution of F-SiO ₂ nanoparticles obtained by utilizing the DLS method.	38
Figure 2.5. Schematic illustrating the fabrication of photocatalytic membrane with hydrophilic and oleophobic wettability. A commercial filter is coated with an ultraviolet (UV) light-curable adhesive followed by sprayed with a mixture of N-TiO ₂ and F-SiO ₂ nanoparticles. The membrane was placed under UV light for curing.	39
Figure 2.6. (a) A photograph showing a commercial filter coated with N-TiO ₂ /F-SiO ₂ (60 wt%). Inset: Scanning electron microscopy (SEM) image of the membrane surface showing a hierarchical roughness with a re-entrant texture. (b) The measured in-air advancing and receding apparent contact angles for saline water (1.0 wt% NaCl in DI water) and oil (n-hexadecane) on the membrane surface coated with N-TiO ₂ /F-SiO ₂ with varied compositions.	40
Figure 2.7. (a) The measured advancing and receding apparent contact angles, as well as adhesion force for an oil droplet (n-hexadecane) on the membrane surface coated with N-TiO ₂ /F-SiO ₂ with varied compositions submerged in saline water. (b) The normalized flux (J_n) of the permeate through the membranes coated with N-TiO ₂ /F-SiO ₂ with varied compositions. The data for the	

as-purchased commercial filter and that for the one coated only with cured adhesive is also provided for comparison.	41
Figure 2.8. A plot of the measured breakthrough pressure for saline water (1.0 wt% NaCl in DI water) of the membranes coated with N-TiO ₂ /F-SiO ₂ with varied compositions.	42
Figure 2.9. (a) The calibration curve established by calculating the electrical conductivity of water as a function of salt (NaCl) concentrations. Inset shows zoomed-in electrical conductivity data in the NaCl concentration range of 0.00-0.20 wt%. (b) The salt rejection (ζ) data of the membranes coated with N-TiO ₂ /F-SiO ₂ with varied compositions. The data of the as-purchased commercial membrane and that coated only with cured adhesive are also provided for comparison.	43
Figure 2.10. The mass loss of the membranes coated with N-TiO ₂ /F-SiO ₂ with varied compositions after 180 minutes of desalination of saline water at a flow rate of 1.5 L min ⁻¹ . For comparison, the results obtained by utilizing the membranes without cured adhesive are also shown.	44
Figure 2.11. Schematic illustrating the cross-flow apparatus that enables continuous separation and desalination of an oil-saline water mixture and simultaneous photocatalytic degradation of organic foulants adsorbed onto the membrane surface upon visible light irradiation.	45
Figure 2.12. (a) The normalized flux (J_n) of the water-rich permeate through the membranes coated with N-TiO ₂ /F-SiO ₂ with varied compositions that are subjected to sodium dodecyl sulfate (SDS)-stabilized n-hexadecane-in-water emulsion (10:90 vol:vol, n-hexadecane:water) dissolved with salt (1.0 wt% NaCl with respect to water mass). (b) The normalized flux (J_n) of the water-rich permeate through the membranes being irradiated by visible light ($I \approx 198$ mW cm ⁻²).	46
Figure 2.13. The TGA data of the water-rich permeates after the separation of SDS-stabilized oil-in-water emulsion dissolved with NaCl (1.0 wt% with respect to water mass) through the membranes coated N-TiO ₂ /F-SiO ₂ with varied compositions.	48
Figure 2.14. (a) The apparent contact angles for oil (n-hexadecane) droplet on the membranes in air and under saline water before and after visible light irradiation for 120 minutes. The data of the as-prepared membranes are also shown for comparison. (b) The FT-IR spectra of a membrane surface coated with N-TiO ₂ /F-SiO ₂ (60 wt%) after 120 minutes of visible light irradiation with an intensity of 198 mW cm ⁻² . For comparison, the FT-IR spectra of the as-prepared membrane surface is shown.	49
Figure 2.15. (a) The FT-IR spectra of the cured adhesive after 180 minutes of visible light-driven photocatalysis by N-TiO ₂ ($I \approx 198$ mW cm ⁻²). For comparison, the FT-IR spectra of the as-prepared adhesive is also shown. (b) The salt rejection (ζ) of the membranes coated with N-TiO ₂ /F-SiO ₂ with varied compositions after exposure to 60 minutes of visible light irradiation.	50
Figure 3.1. (a) Scanning electron microscopy (SEM) image of stainless steel (SS) 316 Twill Dutch weave mesh coated with N-TiO ₂ /F-SiO ₂ (50 wt%). The inset shows a higher magnification SEM image of the mesh surface. (b) The measured mass of the mesh coated with N-TiO ₂ /F-SiO ₂ with and without the cured adhesive after the standard Tape Peel off test.	63
Figure 3.2. (a) The measured in air advancing and receding apparent contact angles for water and oil (n-hexadecane) on the mesh surfaces coated with varied compositions of N-TiO ₂ /F-SiO ₂ . (b) The measured advancing and receding apparent contact angles of oil (n-hexadecane) on the mesh submerged in water.	64

- Figure 3.3.** (a) The measured apparent contact angles for water on the mesh surfaces coated with N-TiO₂/F-SiO₂ mixture with various N-TiO₂ concentrations (50 wt%, 75 wt%, and 100 wt%) that are submerged in an oil (n-hexadecane) bath as a function of submerging time. The inset images illustrate schematics of the time-dependent evolution of the water contact angles on a mesh surface submerged in oil. (b) The measured apparent contact angles for water on the mesh surfaces coated with N-TiO₂/F-SiO₂ mixture with various N-TiO₂ concentrations (50 wt%, 75 wt%, and 100 wt%) while being illuminated by visible light (Intensity (I) = 198 mW cm⁻²). Note that all meshes were precontaminated by oil for 600 minutes. 66
- Figure 3.4.** (a-b) The measured apparent contact angles of water on mesh surface submerged in oil while being illuminated by visible light with intensity of $I = 30$ mW cm⁻² (a) and $I = 100$ mW cm⁻² (b). Note that all meshes were contaminated by oil for 600 mins. 67
- Figure 3.5.** Photograph of the apparatus that enables continuous cross-flow separation of an oil-water mixture and in situ photocatalysis. (water is dyed blue and oil is dyed red). 70
- Figure 3.6.** (a) The measured flux values (J) of the water-rich permeate through the mesh coated with various N-TiO₂ concentrations (50 wt%, 75 wt%, and 100 wt%) of N-TiO₂/F-SiO₂ mixture during separation of SDS-stabilized n-hexadecane-in-water emulsion (1:9 n-hexadecane:water volumetric ratio). The inset shows zoomed-in flux values in the time interval of 60-90 minutes. (b) The measured water-rich permeate flux values (J) while being illuminated by visible light ($I \approx 198$ mW cm⁻²). Inset shows a photograph of the cross-flow setup during the test. 71
- Figure 3.7.** TGA data of the water-rich permeates after the separation of SDS-stabilized n-hexadecane-in-water emulsion by utilizing the mesh coated with various compositions of N-TiO₂/F-SiO₂. 71
- Figure 3.8.** Plots of the cosine values of the measured apparent water contact angle ($\theta_{w,o}^*$) on an N-TiO₂ surface and an F-SiO₂ surface submerged in oil (n-hexadecane) as a function of submerging time. The values of k_a and k_d for oil on N-TiO₂ and F-SiO₂ surfaces were determined by fitting equation (5). Inset: Zoomed-in plot of the $\cos\theta_{w,o}^*$ data. 76
- Figure 3.9.** (a) A plot of the cosine values of the measured apparent water contact angle ($\theta_{w,o}^*$) on an N-TiO₂ surface submerged in oil as a function of visible light illumination ($I = 198$ mW cm⁻²) time. The k_p value for N-TiO₂ was determined by fitting Equation 3.5. (b) Plot of the cosine values of the measured apparent water contact angle ($\theta_{w,o}^*$) on N-TiO₂ surface submerged in oil as a function of visible light illumination ($I = 30$ and 100 mW cm⁻²) time. 77
- Figure 3.10.** The measured and the predicted values of water-rich permeate flux (J) by using Equation 3.4 through the meshes coated with varied compositions of N-TiO₂/F-SiO₂ under visible light illumination ($I = 198$ mW cm⁻²). 79
- Figure 4.1.** Schematic demonstrating the grafting of the filter surface with MEMO and the subsequent coating with F-PEGDA. (b) FT-IR survey spectra of F-PEGDA prepared with varied compositions of F-acrylate. 93
- Figure 4.2.** SEM image showing the morphology of the filter after coating with F-PEGDA (20 wt.%). Inset shows the elemental EDS spectrum and the elemental mappings for fluorine, carbon and oxygen. 94
- Figure 4.3.** (a) The measured viscosity values of F-PEGDA solutions as a function of F-acrylate compositions. (b) The thickness of F-PEGDA coating as a function of F-acrylate compositions. (c) The nominal pore size of the resulting filters after F-PEGDA coating. 96

Figure 4.4. The measured apparent advancing and receding contact angles of water and oil (n-hexadecane) on F-PEGDA-coated filter surface with varied compositions of F-acrylate. A filter with a 6.0 μm inherent nominal pore size was used.	97
Figure 4.5. The measured ToW values for a sessile water droplet on the F-PEGDA surfaces with varying F-acrylate compositions.....	99
Figure 4.6. Advancing and receding apparent contact angles for water and oil (n-hexadecane) on F-PEGDA surface with varied compositions of F-acrylate for the filter with 2.0 μm of inherent nominal pore size.	100
Figure 4.7. The measured adhesion force of a sessile oil (n-hexadecane) droplet on the filter surfaces coated with F-PEGDA with various F-acrylate concentrations. (b) The breakthrough pressure of oil on prewetted and dry filters coated with F-PEGDA (20 wt.%). The data obtained from a filter coated with neat PEGDA are also provided for comparison. (c) The measured apparent contact angles of an oil on the F-PEGDA (20 wt.%), which was prepared with MEMO before and after being submerged in water for 1 h. For comparison, the data for F-PEGDA (20 wt.%) prepared without MEMO are also shown.	101
Figure 4.8. The breakthrough pressure of oil on prewetted and dry filters coated with F-PEGDA (20 wt.%). The data obtained from a filter coated with neat PEGDA are also provided for comparison.	102
Figure 4.9. The measured apparent contact angles of an oil on the F-PEGDA (20 wt.%), which was prepared with MEMO before and after being submerged in water for 1 h. For comparison, the data for F-PEGDA (20 wt.%) prepared without MEMO are also shown.	103
Figure 4.10. (a-b) SEM images and the EDS data (elemental mapping) showing a filter surface coated with F-PEGDA without MEMO before (a) and after submersion in water for 1 hour (b).	104
Figure 4.11. (a) SDS-stabilized oil-in-water emulsion and (b) dispersed water droplets in Tween 80-stabilized water-in-oil emulsion. The insets show the optical microscopy images of dispersed phases.	105
Figure 4.12. (a-b) Time-dependent flux measurements during the separation of oil-water mixtures under gravity by (a) prewetted and (b) dry filters coated with F-PEGDA (20 wt.%) and neat PEGDA. The inset shows images of the oil-water separation experiments with oil-in-water emulsions by utilizing a filter coated with F-PEGDA (20 wt.%).	106
Figure 4.13. The TGA plots of the permeate and retentates after the separation of both oil-in-water and water-in-oil emulsions using a filter coated with F-PEGDA (20 wt.%). The TGA data for pure water and oil are also shown for comparison.	107
Figure 4.14. (a) Time-dependent flux measurements during the continuous separation of oil-water mixtures using prewetted filters with various inherent nominal pore sizes, which were coated with F-PEGDA (20 wt.%). The inset demonstrates the separation experiment using a cross-flow apparatus. (b) Time-dependent flux measurements during the continuous separation of oil-in-water emulsion with cleaning steps in between.	108
Figure 4.15. TGA analysis of the permeates and pure water for cross-flow apparatus-based separation.	109
Figure 4.16. Measured flux values for the water-rich permeates as a function of time.	110
Figure 5.1. Scanning electron microscopy (SEM) image of a graphite adsorbent.	122
Figure 5.2. (a) Brunauer Emmett and Teller (BET) plot obtained by utilizing N_2 adsorption-desorption isotherms at -196.15°C . Inset shows isotherms in the relative pressure (P/P_0) range	

of 0.55-0.85. (b) Pore size distribution (PSD) data of a graphite adsorbent. Inset shows the PSD data of the pore diameter range of 2.0-10.0 nm.	123
Figure 5.3. (a)-(b). Cyclic voltammetry measurements of graphite adsorbent (electrode) for PFPA (a) and PFOA (b) solutions with varying concentrations at a scan rate of 10 mV s ⁻¹ . The temperature was maintained at 25.0 °C ± 1.4 °C during the measurements.....	124
Figure 5.4. Photographs of the custom-made cell for electrosorption of PFAS.	125
Figure 5.5. (a) The measured adsorption capacity for PFPA and PFOA aqueous solutions ($C_o = 0.01$ M for both solutions) at varied applied voltages, (b) The measured adsorption capacity values for PFHxA, PFHtA, PFNA, and PFDA aqueous solutions at varied voltages. Note that the concentration (C_o) for each solution was 0.01 M. The adsorption capacity values are lower for PFAS with a longer fluoroalkyl chain.	126
Figure 5.6. (a) and (b). The calibration curves established by calculating the electrical conductivity of DI water dissolved with PFPA (a) and PFOA (b) as a function of concentrations.	127
Figure 5.7. The measured adsorption capacity for PFPA and PFOA aqueous solutions ($C_o = 0.01$ M for both solutions) at varied concentrations ($V = \pm 1.2$ V).	128
Figure 5.8. The measured concentration of PFPA and PFOA aqueous solutions upon reversible adsorption and desorption ($C_o = 30$ ppm for both solutions) on graphite electrode by alternating the applied voltage between +1.2 V and -1.2 V. Note that the voltage alternated every 10 s.	129
Figure 5.9. The measured adsorption and desorption efficiency as a function of cycles.	130
Figure 5.10. (a) and (b) The measured concentrations for PFPA and PFOA aqueous solutions upon applying voltage of $V = +1.2$ V (a) or $V = -1.2$ V (b). The fitted values of concentration utilizing pseudo-second order kinetic model for adsorption (Equation 5.4) and desorption (Equation 5.5) are also provided.	131
Figure 5.11. (a) The measured concentrations for PFPA and PFOA aqueous solutions upon applying voltage of $V = +0.6$ V or $V = +0.8$ V. The fitted values of concentration utilizing pseudo-second order kinetic model for adsorption (Equation 5.4) are also provided. The rate constants for adsorption (k_1) are determined as $k_1 = 0.3424$ s ⁻¹ ($V = +0.6$ V) and $k_1 = 0.5521$ s ⁻¹ ($V = +0.8$ V) for PFPA. For PFOA, we found $k_1 = 0.6723$ s ⁻¹ ($V = +0.6$ V) and $k_1 = 1.012$ s ⁻¹ ($V = +0.8$ V). (b) The measured concentrations for PFPA and PFOA aqueous solutions upon applying voltage of $V = -0.6$ V or $V = -0.8$ V. The fitted values of concentration utilizing pseudo-second order kinetic model for desorption (Equation 5.5) are also provided. The rate constants for desorption (k_2) are determined as $k_2 = 0.5553$ s ⁻¹ ($V = -0.6$ V) and $k_2 = 0.9591$ s ⁻¹ ($V = -0.8$ V) for PFPA. For PFOA, we found $k_2 = 0.417$ s ⁻¹ ($V = -0.6$ V) and $k_2 = 1.19$ s ⁻¹ ($V = -0.8$ V).	132
Figure 5.12. The measured adsorption rate (R_a) values of the module for PFPA and PFOA aqueous solutions ($C_o = 0.01$ M) as a function of the spacer width. It is observed that a spacer width of 0.2 cm exhibits the highest R_a values for both PFPA and PFOA.	133
Figure 5.13. Photographs showing a device module utilized for gravity-assisted electro-sorption for PFOA from water.	133
Figure 5.14. (a) The measured concentrations of PFOA in the permeate after introducing 10 mL of feed PFOA solutions with varying concentrations ($C_o = 30$ ppm, 20 ppm, and 10 ppm) to the device module. (b) The measured concentrations of PFOA after desorption for solutions with varying initial concentrations ($C_o = 30$ ppm, 20 ppm, and 10 ppm) utilizing the device module.	134
Figure 5.15. (a) The measured concentrations of PFPA in the permeate after introducing 10 mL of feed PFPA solutions with varied concentrations ($C_o = 30$ ppm, 20 ppm, and 10 ppm) to the device module. (b) The measured concentrations of PFPA after desorption for solutions with	

varied initial concentrations ($C_0 = 30$ ppm, 20 ppm, and 10 ppm) utilizing the device module.	135
Figure 6.1. Schematic demonstrating the preparation of the MXene:PEDOT:PSS electrode for the electrosorption process.....	147
Figure 6.2. Schematic demonstrating the preparation of the MXene:PEDOT:PSS electrode for the electrosorption process.....	147
Figure 6.3. Cross-section morphology of the MXene intercalate with PEDOT:PSS. Inset shows the cross sectional view of the MXene-PEDOT:PSS without acid etching.....	147
Figure 6.4. (a) Cyclic voltammetry (CV) curves of MXene-PEDOT:PSS electrodes with varied compositions. (b) CV curves for MXene-PEDOT:PSS (5 wt%) electrodes with and without H_2SO_4 treatment.....	149
Figure 6.5. Capacitance of MXene-PEDOT:PSS (5%) at varied scan rate.	150
Figure 6.6. Gravimetric charge-discharge (GCD) curves of Mxene-PEDOT:PSS electrodes with varied compositions.	151
Figure 6.7. Schematic illustrating the working principle of the custom-made cell utilized for capacitive electrosorption and removal of PFAS.....	152
Figure 6.8. (a) Adsorption capacity for various PFAS with different concentrations at a given voltage of $V = 1.0$ V. (b) Adsorption capacity for various PFAS at different voltages when the concentration is 0.01 M.....	153
Figure 6.9. Adsorption (a) and desorption (b) rates for PFBA and PFOA at different voltages.	154
Figure 6.10. (a-b) Time-dependent plots demonstrating the change in the concentration of the PFAS solutions upon applying a voltage of (a) $V = +1.0$ V during the adsorption, and (b) $V = -$ 1.0 V during the desorption. The fitted values of concentration by pseudo-second order kinetic model are also provided.	155

List of Tables

Table 1.1. List of various wastewater remediation technologies.	3
Table 1.2. List of non-equilibrium-based pressure-driven membrane technologies.	4
Table 2.1. The values of the flux of the water-rich permeate through the membranes coated with N-TiO ₂ /F-SiO ₂ with varied compositions that are subjected to sodium dodecyl sulfate (SDS)-stabilized n-hexadecane-in-water emulsion (10:90 vol: vol, n-hexadecane: water) dissolved with salt (1.0 wt% NaCl with respect to water mass).	51
Table 2.2. The values of the flux of the water-rich permeate through the membranes coated with N-TiO ₂ /F-SiO ₂ with varied compositions after 60 minutes of irradiation of visible light ($I \approx 198 \text{ mW cm}^{-2}$).	51
Table 3.1. The measured r_m values of the mesh coated with N-TiO ₂ /F-SiO ₂ with varied compositions.	74
Table 3.2. The measured R_c values of the mesh coated with varied compositions of N-TiO ₂ /F-SiO ₂	75
Table 3.3. The computed values of the $f_{c(T)}$ and $f_{c(F)}$, as well as the measured values of $\theta_{w,o}^*$ for the mesh coated with N-TiO ₂ /F-SiO ₂ with varied compositions at the onset of visible light illumination ($t = 90 \text{ mins}$).	76
Table 4.1. The pore size of as-purchased filters and those coated with F-PEGDA with various F-acrylate compositions.	95
Table 4.2. The measured initial contact angles for a sessile water droplet (5 μl) on F-PEGDA surfaces with varying F-Acrylate compositions.	98
Table 4.3. The calculated solid surface energy values of F-PEGDA surfaces.	99
Table 4.4. The measured weight values of F-PEGDA (20 wt%) coated filters and calculated water uptake.	102
Table 5.1. Specific capacitance values calculated for PFPA and PFOA at varied concentrations.	125
Table 5.2. The adsorption capacity (α) values of our graphite electrode for PFPA, PFH _x A, PFHtA, PFOA, PFNA, and PFDA upon application of voltage ($V = + 1.2 \text{ V}$). Note that all solutions are at the same concentrations ($C_o = 0.01 \text{ M}$). For comparison, the adsorption capacity values measured without application of voltage (i.e., conventional sorption) are also shown.	127
Table 5.3. Langmuir isotherm parameters for PFPA and PFOA adsorption.	128
Table 6.1. Capacitance value for MXene-PEDOT:PSS electrodes with and without acid treatment.	150

Chapter 1. Introduction

1.1. Current water crisis: Shortage of freshwater due to contamination

Water is perhaps the essential element for the sustenance of life. While almost three fourth of the earth's area is covered by water, only 2.8% of the freshwater is available for human life.^{1, 2} Approximately 70% of the freshwater is concentrated in a few regions, which results in the fact that most of the population does not have the appropriate access.³ Also, due to rapid urbanization and industrial growth, the quality of available freshwater has deteriorated.⁴⁻⁶ It is reported that one in every three people has already been affected by such water contamination, and it is expected to become worse over the coming decades. Consequently, there is a creation of high water-stress regions around the world.^{7, 8}

One of the primary contributing factors to water contamination and high water stress is wastewater generated from various industrial and agricultural sectors.⁹⁻¹³ For example, in the oil refinery industry, every one barrel of crude oil processing¹⁴ generates approximately 10 barrels of wastewater (i.e., produced water).¹⁵ In California, the cumulative flow of tailwater from many farms has historically posed significant water contamination as it is discharged to surface waters such as wetlands, streams, and rivers.^{16, 17} These wastewaters contain organic and/or inorganic contaminants get mixed with water bodies (e.g., surface water and groundwater).¹⁸⁻²⁰ These contaminants^{21, 22} can accumulate in the human body through direct exposure or the food chain in the ecosystem.²³⁻²⁵ This often results in adverse effects on human health and causes chronic diseases.^{26, 27} Therefore, there is a dire need for developing technologies to remove contaminants from water and generate freshwater.

1.2. Contaminants in water: suspended or dissolved

The contaminants often found in wastewater are mostly organic compounds such as pesticides, fluorocarbons (e.g., per- and polyfluoroalkyl substances (PFAS)), aliphatic hydrocarbons (e.g., oils), polynuclear aromatic hydrocarbons (e.g., organic solvents), and plasticizers. The wastewater also contains inorganic particulates and metal ions.²³⁻²⁵ While we can classify these contaminants into organic or inorganic based on their chemical structure and components,²⁸ most wastewater remediation technologies cannot differentiate the types of contaminants.²⁹⁻³² Instead, their working principles often rely on the contaminants' solubility in water which can lead to a contaminant-specific technology. Based on the solubility in water, we classify the water-containing contaminants as suspended or dissolved.³³⁻³⁵

Suspended contaminants are substances and materials that have low solubility with water or waterborne particles that exceed 2 μm in size.³³ Most suspended contaminants in wastewater comprise organic materials such as oils, organic solvents, plasticizers, and biological organisms.³³⁻³⁵ They can cause several adverse health effects on the human body. For example, bacteria and algae (biological organisms) can cause gastrointestinal issues, which could result in chronic health effects or even death.^{23-25, 36, 37} In contrast, dissolved contaminants have high solubility with water, such as salts, pesticides, metal ions, and PFAS.³³⁻³⁵ Particularly, PFAS is an emerging contaminant that has been reported that they can cause carcinogenic diseases.^{23-25, 38, 39}

1.3. Wastewater remediation technologies

Due to its adverse effects on the community and ecosystem, various wastewater remediation technologies have been developed (see **Table 1.1**).^{40, 41} Flotation is a separation process based on the density difference.^{42, 43} For example, small oil droplets can be removed from water by increasing the buoyancy of oil. In the coagulation process, a chemical (coagulant) is added to

wastewater to induce the aggregation of contaminants.^{14, 44} Sedimentation utilizes gravity to allow the suspended contaminants to settle at the bottom of the water.^{45, 46} Distillation is one of the most prevailing techniques which utilizes the difference in boiling points of the components.^{47, 48} Membrane-based filtration utilizes a porous media (e.g., membrane) to remove contaminants based on the size exclusion.^{49, 50} Adsorption utilizes physical or chemical interaction between the adsorbent and contaminants to remove them.^{51, 52} Biodegradation is a process in which biological organisms degrade the dissolved or suspended contaminants in wastewater.^{53, 54}

Table 1.1. List of various wastewater remediation technologies.

Method	Working Principle	Reference
Floation	A process designed to remove suspended contaminants from wastewater based on the density difference.	42, 43
Coagulation	A chemical process that can induce coagulation of suspended contaminants, which is typically followed by removal with charged materials.	14, 44
Sedimentation	A gravity-driven process that allows the suspended particles to be settled at the bottom of the water.	45, 46
Distillation	A thermal process for separating suspended or dissolved contaminants by using selective boiling and condensation.	47, 48
Membranes	A process for removing contaminants by a porous membrane based on sized exclusion.	49, 50
Adsorption	A process based on the physical or chemical interaction between the adsorbent and contaminants.	51, 52
Biodegradation	A degradation process for contaminants by biological organisms.	53, 54

1.4. Membrane-based wastewater remediation technologies

Membrane-based technologies are an effective solution for removing suspended or dissolved contaminants from wastewater based on size exclusion.^{55, 56 57} They are clean, environmentally friendly, and scalable due to their simplicity and modularity.⁵⁸ Further, they are unaffected by temperature and do not cause secondary contamination because no additional chemicals are used during the operation.⁵⁹⁻⁶¹

1.4.1. Various membrane technologies

The membrane-based technologies are categorized by the driving force which enables water to permeate through while preventing the permeation of the contaminants.⁶² They can be either equilibrium or non-equilibrium-based processes.⁶³ Further, they can be grouped into pressure-driven or non-pressure-driven processes (**Figure 1.1**).

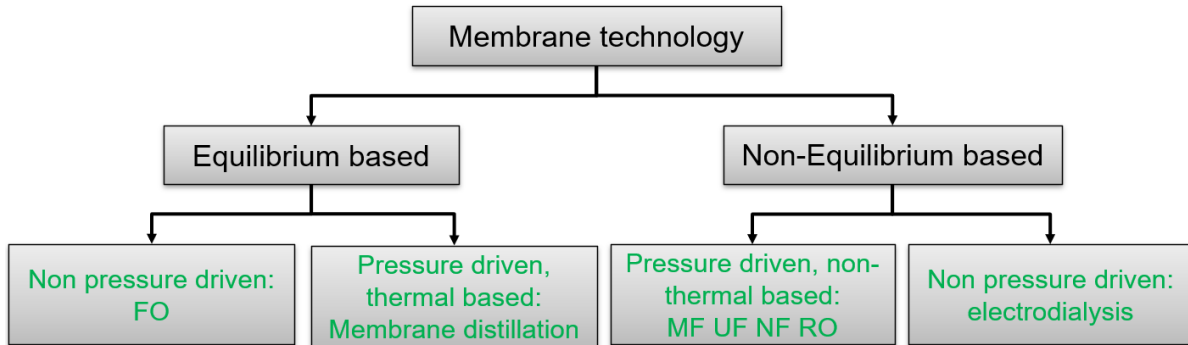


Figure 1.1. Classification of membrane-based technologies.

Non-equilibrium-based pressure-driven processes are the most prevailing membrane technologies in wastewater treatment.⁶⁴ They can be further divided into four types based on the porosity of the membrane such as microfiltration (MF), ultrafiltration (UF), nanofiltration (NF), and reverse osmosis (RO).^{58, 65} (**Table 1.2**).

Table 1.2. List of non-equilibrium-based pressure-driven membrane technologies.

Types	Molecular Weight Cut Off (kDa)	Retained diameter (µm)	Pressure (Bar)	Reference
MF	100 – 500	10 ⁻¹ – 10	1 – 3	66, 67
UF	200 – 150	10 ⁻² – 1	2 – 5	68, 69
NF	2 – 20	10 ⁻³ – 10 ⁻²	5 – 15	70, 71
RO	0.2 – 2	10 ⁻⁴ – 10 ⁻³	15 – 75	72, 73

1.4.2. Membrane fouling

A primary challenge of membranes is fouling by suspended oils or solid particles over time.^{74, 75} This results in a decline in their separation performance. For example, an RO membrane should be operated under a remarkably low (< 0.1 ppm) oil content in the feed to minimize the possibility of membrane fouling.⁷⁶ Thus, it has been considered challenging to use RO membranes to remediate oily wastewater in a single step.⁷⁴ Instead, several pretreatment processes are involved to remove any suspended or dissolved contaminants.⁷⁷ Also, membrane fouling results in a lower life expectancy of the membranes and an increase in the materials costs.⁷⁸ Furthermore, periodic membrane cleaning increases the operational cost as well as downtime.⁷⁶⁻⁷⁸

Membrane fouling can take place inside or outer surfaces.⁷⁹ Lower-pressure processes such as UF and MF suffer from internal fouling, whereas higher-pressure processes such as NF and RO undergo surface fouling.^{80 81} There are various types of foulants, including particulate, organic, inorganic, and biological microorganisms (biofouling).^{75, 82} Particulate fouling occurs when colloids (e.g., greases, oils, surfactants, clay, silt, crystals, silica sediments) adsorb to the membrane surface.⁸³ This often results in pore-blocking and cake layer formation. Fouling by organic or inorganic materials such as proteins, humic substances, nucleic acids, lipids, and salts accumulate on the membrane surface, which results in a decline of permeability.⁸⁴ Biofouling takes place when microorganisms adhere and accumulate on the membrane surface, which is followed by biofilm development.^{74, 84}

1.4.3. Mitigation of fouling

Mitigation of membrane fouling is critical to achieving successful membrane-based filtration processes.^{75, 85} Conventionally, membrane fouling was treated by a variety of cleaning methods, including physical or chemical methods.^{62, 86 87} Physical methods include sponge ball cleaning,⁸⁸

alternative flushings,⁸⁹ backwashings,⁹⁰ and air flushing⁹¹. These methods can remove the foulants from the membrane surface by non-reactive forces. In contrast, chemical methods involve reagents that can react with the foulants to reduce the foulant affinity to the membrane surface.^{92, 93} As a result, the foulants can be readily removed from the membrane surface.

More recently, preventive measures have been developed to reduce downtime during the cleaning process and to increase the life expectancy of the membranes.^{94, 95} Modulation and functionalization of the membrane surface's properties to make it become less susceptible to fouling is attractive.⁹⁴ For example, an electrically charged membrane surface can be less fouled due to the electrostatic repulsion of the foulants.⁹⁶ A membrane surface with smoother topography has a lower propensity to experience fouling as the surface does not allow for the deposition or adhesion of the foulants into the roughness.⁹⁷ Also, a sacrificial layer that can suppress the accumulation and adsorption of the foulants to the surface is introduced to membranes.⁹⁸ Furthermore, membranes possessing tailored wettability to water and foulants (e.g., oils) have exhibited that they can be fouling-resistant.⁹⁹⁻¹⁰² Lastly, membranes that can degrade the organic deposits under light irradiation and clean the surface (i.e., photocatalytic membrane) have developed. Here we briefly introduce membranes with tailored wettability and photocatalytic capability.

1.4.3.1. Photocatalytic membranes

Photocatalysis can be a promising preventive technique against membrane fouling.^{101, 102} Upon irradiation of ultraviolet (UV) or visible light, a membrane coated with a photo-responsive catalytic material can degrade any organic deposits on its surface through the redox reactions.^{103, 104} Such photocatalytic membranes are attractive because they can be triggered remotely and typically operated under ambient conditions (i.e., room temperature and 1 atm).^{101, 102}

Photocatalytic degradation of the surface adsorbed foulants has demonstrated that it can effectively restore the membrane's inherent filtration performance.^{105, 106} Titanium dioxide (TiO₂) is perhaps the most popular photocatalytic material for this purpose.¹⁰³ It can effectively degrade the organic pollutants under UV light irradiation.¹⁰⁷⁻¹⁰⁹ The resulting TiO₂ surface becomes superhydrophilic (i.e., water contact angle = 0°).^{110, 111} Madaeni et al.,¹¹² demonstrated that TiO₂ coated RO membrane can clean the surface under UV light irradiation and show recovery of the flux. Xu et al.,¹¹³ demonstrated that nitrogen (N)-doped TiO₂ coated UF membrane can degrade the organic deposits under visible light illumination. Kim et al.,¹¹⁴ prepared a hybrid thin-film-composite (TFC) membrane by self-assembly of the TiO₂ particles with the carboxylic (-COOH) functional group of aromatic polyamide thin-film layer. The membrane possesses a dramatic photobactericidal effect on *E. coli* under UV light illumination. By means of an ion-assisted deposition method, TiO₂ was directly applied to a porous Teflon sheet (PTS) by Yamashita et al.¹¹⁵ UV light irradiation of the PTS can lead to photocatalytic degradation of organic pollutants.

1.4.3.2. Membranes with modulated solid-liquid wettability

Fundamental of wetting: When a liquid droplet is placed on a surface, it can either spread or get repelled by the surface, determining the wettability.^{99, 116, 117} Such a surface wettability can be characterized by the contact angle between the liquid and solid surface. The contact angle for a liquid droplet on a smooth surface is given by Young's relation¹¹⁸:

$$\text{(Equation 1.1) } \cos \theta = \frac{\gamma_{SV} - \gamma_{SL}}{\gamma_{LV}}$$

where θ is Young's contact angle and γ_{SV} , γ_{LV} , γ_{SL} refer to the solid surface energy, liquid surface tension, and the solid-liquid interfacial tension, respectively. It can be inferred that a liquid droplet can exhibit a contact angle depending on an interplay between the interfacial energies (i.e., solid-

vapor (solid surface energy), liquid-vapor (liquid surface tension), and solid-liquid (interfacial tension)) (**Figure 1.2**).¹¹⁷ Note that the effect of gravity is neglected given that a liquid droplet is small enough.^{117, 119, 120}

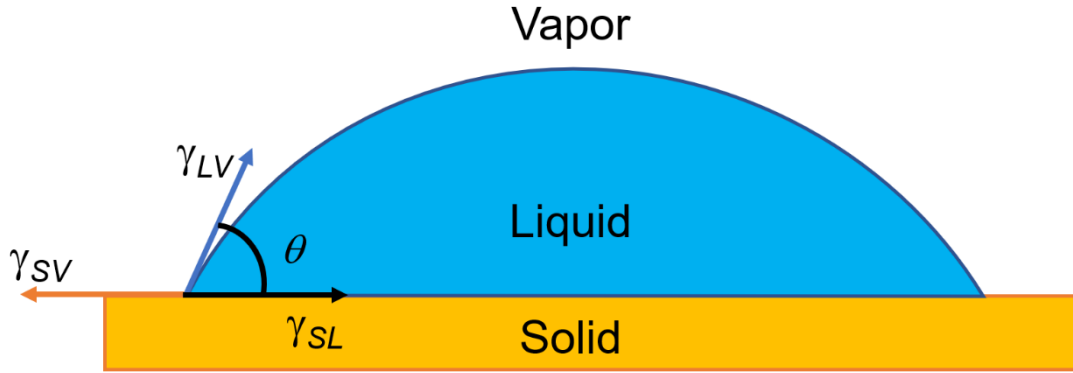


Figure 1.2. A schematic illustrating a contact of a liquid droplet on a smooth surface.

A key premise of Young's relation is that a liquid droplet must reside on an ideally smooth surface as well as the contact angle in the thermodynamic equilibrium. Thus, it is almost impossible to experimentally measure Young's contact angle.¹¹⁸ Consequently, contact angles measured on a rough surface (i.e., apparent contact angles, θ^*) are measured and reported in the literature.^{117, 121, 122} Apparent contact angles can be classified into two types, namely,¹²³ the advancing contact angle (θ_{adv}^*) and the receding contact angle (θ_{rec}^*). The advancing contact angle is typically the maximum contact angle, while the receding contact angle is the minimum contact angle on a given surface.^{99, 117} The difference between these two contact angles is called the contact angle hysteresis ($\Delta\theta = \theta_{adv} - \theta_{rec}$).¹²⁴

Based on the contact angles for water, surfaces can be grouped into four categories^{99, 116, 117, 119, 120}: superhydrophilic (SHL) when $\theta_{water} < 10^\circ$, hydrophilic (HL) when $\theta_{water} < 90^\circ$, hydrophobic (HP) when $90^\circ < \theta_{water} < 150^\circ$, and superhydrophobic (SHP) when $\theta_{water}^* > 150^\circ$. Similarly, surfaces can be grouped into superoleophilic (SOL), oleophilic (OL), oleophobic (OP),

and superoleophobic (SOP) when a surface shows oil contact angle (θ_{oil}) of $< 10^\circ$, $\theta_{oil} < 90^\circ$, $90^\circ < \theta_{oil} < 150^\circ$, and $\theta_{oil}^* > 150^\circ$. Note that a surface with hydrophilic and oleophilic wettability is called omniphilic. If a surface is both hydrophobic and oleophobic, it is called omniphobic. Similarly, if a surface is both superhydrophobic and superoleophobic, it is called superomniphobic (Figure 1.3).

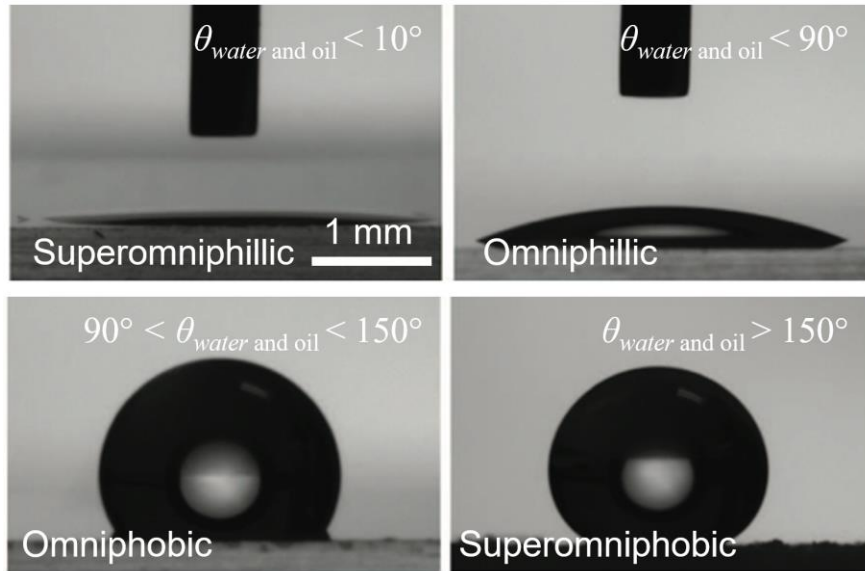


Figure 1.3. Classification of a surface based on the contact angles for liquid. (a) Superomniphillic ($\theta_{water} \approx 0^\circ$ and $\theta_{oil} \approx 0^\circ$). (b) Omniphillic (θ_{water} and $\theta_{oil} < 90^\circ$). (c) Omniphobic ($90^\circ < \theta_{water}$ and $\theta_{oil} < 150^\circ$). (d) Superomniphobic (θ_{water}^* and $\theta_{oil}^* > 150^\circ$).

Typically, a surface that is oleophobic is hydrophobic; this is because the water surface tension ($\gamma_{water} = 72.1 \text{ mN/m}$) is significantly higher than that of oils ($\gamma_{oil} = 20\text{-}30 \text{ mN/m}$).^{99, 116} Therefore, developing a hydrophilic yet oleophobic surface needs to employ special interactions between the surface and the contacting liquid.^{99, 116, 119 99, 116, 125, 126}

Membranes with modulated solid-liquid wettability: Modulating the surface wettability is attractive in practical applications, including self-cleaning^{127, 128}, microfluidics^{129, 130}, and liquids separation^{131, 132}. Kaner et al.¹³³ created a UF membrane by blending zwitterionic copolymer and polyvinylidene fluoride (PVDF). The membrane demonstrated the segregation of zwitterionic

copolymer on the surface upon contact with water which resulted in an increase in hydrophilic wettability (i.e., water contact angle $< 90^\circ$) and fouling resistance against a mixture of oil and surfactants. Xie et al.¹³⁴ fabricated a self-cleaning composite membrane that exhibited superhydrophilic and underwater superoleophobic wettability (i.e., oil contact angle $> 150^\circ$ on a surface submerged in water). The membrane was able to retain a film of water within the hierarchical structure, which significantly reduced the contact area between the oil droplets and the membrane's surface. Consequently, the membrane showed very high underwater oil contact angles and was able to readily remove both high- and low-density oils. Cheng et al.¹³⁵ integrated cross-linked hydrophilic oligomers into a polyacrylonitrile membrane that increased its wettability and resulted in a lower adhesive force on oil droplets.

1.4.4. Photocatalytic membrane with modulated wettability: Need for decoupling of wettability and photocatalysis

Membranes with modulated wettability can be further extended by incorporating photocatalytic nanoparticles¹⁰⁷⁻¹⁰⁹. Such membranes can progressively eliminate the inherent shortcomings of conventional membranes, such as membrane fouling¹⁰⁷. Zhao et al.,¹³⁶ reported polyacrylonitrile (PAN) membrane coated with a fluorinated agent and photocatalytic zinc oxide (ZnO). The membrane exhibited remediation of wastewater upon ultraviolet (UV) light irradiation and resistance to fouling. Luster et al.,¹³⁷ fabricated an N-doped TiO₂-coated alumina membrane and demonstrated photocatalytic degradation of carbamazepine as a model pollutant under simulated solar irradiation. Coelho et al.,¹³⁸ coated a filter paper with zirconia (ZrO₂)-doped cerium (Cr) to prepare a photocatalytic membrane. The membrane demonstrated the degradation of humic acid (model foulant) and flux recovery of the permeate upon visible light illumination. Despite a large volume of literature on photocatalytic membranes with modulated wettability, there is very limited research on the effect of photocatalysis on the coating materials (e.g., perfluorinated silanes) that

are incorporated to engender the desirable wettability. This is because a photocatalytic chemical reaction is non-selective. Therefore, there is a need for decoupling the photocatalysis and wettability of the membrane. To achieve this, one needs to consider the following criteria^{139, 140}. First, the membrane's wettability must remain unchanged by a photocatalytic reaction. Similarly, its physical and chemical integrity must not be affected by a photocatalytic reaction, particularly if the membrane is organic. Lastly, the coating (e.g., photocatalytic nanoparticles) needs to remain undetached when a high hydraulic shear force is exerted. In this dissertation, we will discuss how we can prepare a membrane with decoupled photocatalysis and wettability (see Chapters 2 and 3).

1.5. Adsorption-based wastewater remediation technologies

Adsorption-based technologies utilize an adsorbent that can be directly exposed to wastewater and remove suspended or dissolved contaminants without causing secondary contamination.¹⁴¹ The contaminants adhere to the adsorbent surface over time. When the concentrations of the contaminant on the adsorbent surface and that in the water become constant, thermodynamic equilibrium is reached.^{51, 142} The relation between the equilibrium amounts of contaminants adsorbed and in the water at a given temperature is an adsorption isotherm.¹⁴³ Langmuir isotherm¹⁴⁴ and Freundlich isotherm¹⁴⁵ are typically employed in literature to describe the adsorption efficiency of contaminants.¹⁴³

1.5.1. Adsorption and regeneration of adsorbent

Based on the interaction forces, adsorption can be either physical or chemical adsorption.¹⁴⁶ Physical adsorption process can take place all over the adsorbent surfaces (i.e., not location-specific). For example, electrostatic interaction¹⁴⁷ allows an adsorbent to attract and retain contaminants from the water. Various parameters, including adsorbent surface area, temperature, pressure, and nature of contaminants, affect this physical adsorption process.¹⁴⁷ Adsorption caused

by chemical forces¹⁴⁸ is highly location-specific. It usually takes place at the reaction centers on the adsorbent surface. An example of chemical adsorption is the chemical bond formation between the contaminants and the adsorbent surface.

Any adsorbents have limited adsorption capacity.⁹⁷⁻¹⁴⁹ When adsorbents with low-cost (e.g., powdered activated carbon (PAC) and biochar) reach their adsorption capacity, they are simply disposed of or incinerated.¹⁵⁰⁻¹⁵² However, this can be problematic because it can cause secondary contamination and increase the material cost.¹⁵³ Another method to deal with the saturated adsorbents is regeneration to restore their inherent adsorption capacity.¹⁵⁴⁻¹⁵⁵ Effective regeneration of the saturated adsorbent makes the adsorption-based wastewater remediation technologies not only economical but also environmentally friendlier.^{156, 157} Given that most adsorbents manufactured with costs¹⁵⁸, their recyclability is an important factor in view of the economic efficiency of the entire adsorption process.^{159, 160} Regeneration of adsorbents can also be an important step to recover the adsorbed contaminants.¹⁶¹ Particularly, this is desirable when the contaminants are valuable products (noble metal ions) or need to be sampled (PFAS).^{162, 163}

1.5.2. Electric field aided adsorption

Electric field aided adsorption (i.e., electrosorption) is a process that produces clean water from dissolved contaminants like metal ions, salts, and PFAS.¹⁶⁴ In this process, ions, and counterions are electrostatically attracted to oppositely charged electrodes and adsorb on the surface to form regions of excess charge known as electrical double layers (EDL) (**Figure 1.4**)¹⁶⁵. As a result, the concentration of the charged species in the solution depletes, leaving behind a deionized (DI) water stream.¹⁶⁶ The theoretical efficiency of the electrosorption process is reported to surpass most of the remediation technologies at contaminants concentrations below 10 g L⁻¹.¹⁶⁷ Also, due to the creation of EDL on the adsorbent, the adsorbent's adsorption capacity and kinetics are relatively

higher compare to that of physical or chemical adsorption.¹⁶⁸ Further, the electrosorption process has more flexibility than membrane-based separations due to the vast array of ion-selective electrodes and electrode coatings.³

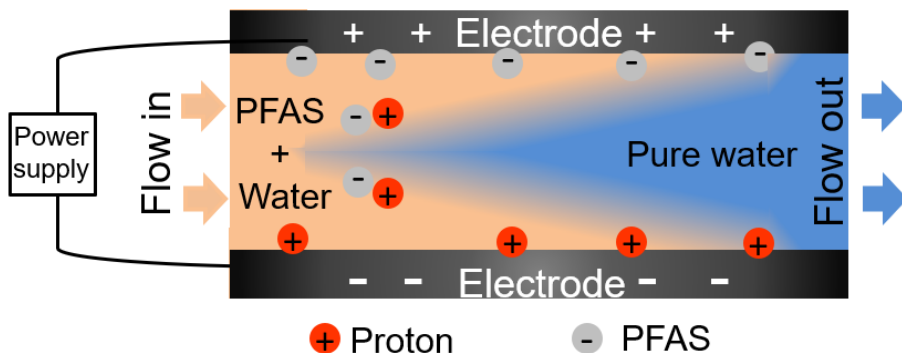


Figure 1.4. A schematic of electrosorption process.

1.5.2.1. Working principles

Electrosorption is an electrochemical technique employing high-surface-area, conductive materials that adsorb ions from contaminated water.¹⁶⁹ In this system, two electrodes are submerged in an electrolyte (e.g., contaminated water). Upon application of an electric field in between the electrodes, cations migrate towards the negatively charged cathode and anions towards the anode due to coulombic forces, and electric charge is built up at the surface of the electrode.¹⁶⁶ At the surface of the electrode, the charges form an EDL. Capacitive deionization (CDI)^{170, 171} utilizes an electrosorption process to remove dissolved ions from water. A model for the interface between an electrode and an electrolyte has been established based on the Gouy-Chapman-Stern (GCS) theory.^{172 173} Based on the GCS model, an EDL is composed of the Stern layer¹⁷⁴ (i.e., a fixed capacity region at the electrode surface created due to the finite size of adsorbed ions) and a diffuse layer with a mixture of ions and counterions.^{175, 176} The GCS model is usually used to describe systems in which the EDL is small compared to the size of the pores.

The diffuse layer does not have a precise width; instead, ion concentrations progressively decay with increasing distance from the surface.¹⁷⁵ The Debye length (λ_D) is a characteristic distance for the counterion concentration and potential to decay by a factor of e (≈ 2.7). Empirically, one can consider the diffuse layer to have ended after 2- or 3-times the Debye length.¹⁷⁵ At equilibrium, the ion distribution profiles can be described in first approximation by the Boltzmann distribution, which is the basis of the Poisson–Boltzmann equation.¹⁷⁵

1.5.2.2. Adsorbents for electrosorption

An effective electrosorption process requires the adsorbent to fulfill the following design criteria. First, it should possess a large specific surface area that serves as an adsorption site. Also, it should exhibit durability against chemically and thermally aggressive environments.¹⁷⁷⁻¹⁸⁰ Furthermore, it should demonstrate high capacitance and electrical conductivity. Commonly, carbon-based materials are the best choice for electrode material.¹⁸¹

Activated carbon: Activated carbon has a high surface area to volume ratio with hierarchical pore geometries. Also, it shows fast charge transfer and ion diffusion kinetics which is ideal for the electrosorption process.¹⁶⁸

Carbon aerogels: Carbon aerogels have a monolithic mesoporous structure (as opposed to the particulate structure of activated carbon) which contributes to fast ion diffusion kinetics. Ions can easily diffuse through the mesoporous structure while retaining high adsorption capacity. It also has a high specific surface area, low thermal expansion coefficient, and is highly chemically resistant, ideal for electrosorption.¹⁸²

Graphene: Recently, graphene has emerged as a promising candidate for electrosorption as it has large specific surface areas and high conductivity.¹⁸³ It demonstrates that its physicochemical properties can be readily modulated by chemical reactions.

Mesoporous carbon: Similar to graphene, mesoporous carbon possesses a high surface area which has been considered an emerging material for electrosorption.¹⁸⁴

MXene: MXene, a new class of two-dimensional metal carbide, carbonitride, and nitride (i.e., MXene), has emerged as a competitive adsorbent for the electrosorption process due to its high capacitance and electrical conductivity.¹⁸⁵ The layered structure of MXene allows the dissolved ions to be readily inserted and adsorbed to the surface (i.e., ion intercalation).¹⁸⁶

1.5.3. Reversible electrosorption of dissolved contaminants (PFAS)

Considering that electrosorption employs the electrostatic and coulombic force of attraction between an electrode and ionized species, it can effectively remove dissolved contaminants such as PFAS. Li et al.¹⁷⁷ utilized electrochemical assistance to enhance PFOA and PFOS adsorption by a multiwalled carbon nanotube. Nu et al.¹⁸⁰ utilized an electrode made of carbon nanotube and graphene mixture for PFAS removal. Similarly, Wang et al.¹⁷⁸ utilized carbon nanotube in continuous flow mode electrode to remove PFAS from water. Compared to conventional adsorbents that primarily rely on hydrophobic interaction with PFAS, the electrosorption process can be effective for removing short-chain PFAS.^{180, 187} Another important feature of electrosorption for PFAS is the on-demand desorption process which can be initiated by reversing the voltage. This enables not only the regeneration of adsorbents but the collection of concentrated PFAS solutions for further analyses.

1.6. Scope of the dissertation

Overall, this dissertation comprises four journal articles published during my Ph.D. (P1, P2, P3, and P4) and one project. The overarching objective of this dissertation is to develop novel technologies for removing the dissolved and/or suspended contaminants from wastewater by modulating solid-liquid interaction. In Ch. 2 and Ch. 3, we developed a visible light-responsive

photocatalytic surface with hydrophilic and oleophobic wettability for the separation of oil-in-water emulsions. We investigated the relationship between the photocatalytic degradation of the organic deposits on the membrane surface and the permeability. In Ch. 4, we developed a robust in-air oleophobic and hydrophilic membrane that can separate surfactant-stabilized oil-water mixtures. Finally, in Ch. 5 and Ch. 6, we developed the electrosorption process for the remediation of PFAS-contaminated water. A graphite (Ch. 5) and MXene (Ch. 6) were utilized as electrode adsorbents.

1.7. References

1. Desa, U., World population prospects 2019: Highlights. *New York (US): United Nations Department for Economic and Social Affairs* **2019**, 11 (1), 125.
2. Covich, A., Water in crisis: a guide to the world's fresh water resources. *Water and Ecosystems* **1993**, 40, 55.
3. Suresh, A.; Hill, G. T.; Hoenig, E.; Liu, C., Electrochemically mediated deionization: a review. *Molecular Systems Design & Engineering* **2021**, 6 (1), 25-51.
4. Tchobanoglous, G.; Burton, F. L.; Stensel, H. D., Wastewater engineering. *Management* **1991**, 7 (1), 4.
5. Droste, R. L.; Gehr, R. L., *Theory and practice of water and wastewater treatment*. John Wiley & Sons: 2018.
6. De Zuane, J., Drinking water quality standards and controls. **1990**.
7. Pavon, C., Water Scarce Countries, Present and Future. *World data lab. Lindengasse. Vienna, Austria* **2020**.
8. Water, U., World Water Day-Factsheet. *United Nations: New York, NY, USA* **2019**.
9. Ranade, V. V.; Bhandari, V. M., *Industrial wastewater treatment, recycling and reuse*. Butterworth-Heinemann: 2014.
10. Jain, S. K.; Singh, V. P., Water crisis. *Journal of comparative social welfare* **2010**, 26 (2-3), 215-237.
11. Barlow, M., *Blue covenant: The global water crisis and the coming battle for the right to water*. McClelland & Stewart: 2009.
12. Srinivasan, V.; Lambin, E. F.; Gorelick, S. M.; Thompson, B. H.; Rozelle, S., The nature and causes of the global water crisis: Syndromes from a meta - analysis of coupled human - water studies. *Water Resources Research* **2012**, 48 (10).
13. Condon, M., Rural America's Drinking Water Crisis. *Human Rights Magazine* **2019**, 44 (2), 12.
14. Bratby, J., *Coagulation and flocculation in water and wastewater treatment*. IWA publishing: 2016.
15. Jafarinejad, S., A comprehensive study on the application of reverse osmosis (RO) technology for the petroleum industry wastewater treatment. *Journal of Water and Environmental Nanotechnology* **2017**, 2 (4), 243-264.
16. Valley, S., Groundwater availability of the Central Valley aquifer, California. *US Geological Survey professional paper* **2009**.
17. Goebel, T. H.; Hosseini, S. M.; Cappa, F.; Hauksson, E.; Ampuero, J.-P.; Aminzadeh, F.; Saleeby, J. B., Wastewater disposal and earthquake swarm activity at the southern end of the Central Valley, California. *Geophysical Research Letters* **2016**, 43 (3), 1092-1099.
18. Friedler, E.; Butler, D.; Alfiya, Y., Wastewater composition. *Source separation and decentralization for wastewater management* **2013**, 241-257.
19. Henze, M.; Comeau, Y., Wastewater characterization. *Biological wastewater treatment: Principles modelling and design* **2008**, 33-52.
20. Lenka, S. P.; Kah, M.; Padhye, L. P., A review of the occurrence, transformation, and removal of poly-and perfluoroalkyl substances (PFAS) in wastewater treatment plants. *Water research* **2021**, 199, 117187.

21. Rajkumar, B.; Sharma, G.; Paul, A., Isolation and characterization of heavy metal resistant bacteria from Barak River contaminated with pulp paper mill effluent, South Assam. *Bulletin of environmental contamination and toxicology* **2012**, *89* (2), 263-268.
22. Gaur, V. K.; Sharma, P.; Sirohi, R.; Awasthi, M. K.; Dussap, C.-G.; Pandey, A., Assessing the impact of industrial waste on environment and mitigation strategies: A comprehensive review. *Journal of Hazardous Materials* **2020**, *398*, 123019.
23. Agrawal, K.; Bhatt, A.; Bhardwaj, N.; Kumar, B.; Verma, P., Integrated approach for the treatment of industrial effluent by physico-chemical and microbiological process for sustainable environment. In *Combined application of physico-chemical & microbiological processes for industrial effluent treatment plant*, Springer: 2020; pp 119-143.
24. Pelch, K. E.; Reade, A.; Wolffe, T. A.; Kwiatkowski, C. F., PFAS health effects database: Protocol for a systematic evidence map. *Environment international* **2019**, *130*, 104851.
25. DeWitt, J. C., *Toxicological effects of perfluoroalkyl and polyfluoroalkyl substances*. Springer: 2015.
26. Cao, Y.; Ng, C., Absorption, distribution, and toxicity of per-and polyfluoroalkyl substances (PFAS) in the brain: a review. *Environmental Science: Processes & Impacts* **2021**.
27. Sunderland, E. M.; Hu, X. C.; Dassuncao, C.; Tokranov, A. K.; Wagner, C. C.; Allen, J. G., A review of the pathways of human exposure to poly-and perfluoroalkyl substances (PFASs) and present understanding of health effects. *Journal of exposure science & environmental epidemiology* **2019**, *29* (2), 131-147.
28. Sonune, A.; Ghate, R., Developments in wastewater treatment methods. *Desalination* **2004**, *167*, 55-63.
29. Tarpeh, W. A.; Chen, X., Making wastewater obsolete: Selective separations to enable circular water treatment. *Environmental Science and Ecotechnology* **2021**, *5*, 100078.
30. Miotto Menino, N.; da Silveira Salla, J.; do Nascimento, M. S.; Dallago, R. M.; Peralta, R. A.; Moreira, R. F., High-performance hydrophobic magnetic hydrotalcite for selective treatment of oily wastewater. *Environmental Technology* **2021**, 1-12.
31. Vu, C. T.; Wu, T., Recent progress in adsorptive removal of per-and poly-fluoroalkyl substances (PFAS) from water/wastewater. *Critical Reviews in Environmental Science and Technology* **2020**, 1-40.
32. Liu, X.; Ge, L.; Li, W.; Wang, X.; Li, F., Layered double hydroxide functionalized textile for effective oil/water separation and selective oil adsorption. *ACS applied materials & interfaces* **2015**, *7* (1), 791-800.
33. Wang, X.; Jin, P.; Zhao, H.; Meng, L., Classification of contaminants and treatability evaluation of domestic wastewater. *Frontiers of Environmental Science & Engineering in China* **2007**, *1* (1), 57-62.
34. Guibal, E.; Van Vooren, M.; Dempsey, B. A.; Roussy, J., A review of the use of chitosan for the removal of particulate and dissolved contaminants. *Separation science and technology* **2006**, *41* (11), 2487-2514.
35. Ellis, T. G., Chemistry of wastewater. *Encyclopedia of life support system (EOLSS)* **2004**, *2*, 1-10.
36. Winder, C.; Balouet, J.-C., The toxicity of commercial jet oils. *Environmental research* **2002**, *89* (2), 146-164.
37. Gutierrez, M.; Etxebarria, J.; De Las Fuentes, L., Evaluation of wastewater toxicity: comparative study between Microtox® and activated sludge oxygen uptake inhibition. *Water Research* **2002**, *36* (4), 919-924.

38. Stohs, S. J.; Bagchi, D., Oxidative mechanisms in the toxicity of metal ions. *Free radical biology and medicine* **1995**, *18* (2), 321-336.
39. Gaballah, S.; Swank, A.; Sobus, J. R.; Howey, X. M.; Schmid, J.; Catron, T.; McCord, J.; Hines, E.; Strynar, M.; Tal, T., Evaluation of developmental toxicity, developmental neurotoxicity, and tissue dose in zebrafish exposed to GenX and other PFAS. *Environmental health perspectives* **2020**, *128* (4), 047005.
40. Patterson, J. W., *Industrial wastewater treatment technology*. **1985**.
41. Liu, D. H.; Lipták, B. G., *Wastewater treatment*. CRC Press: 2020.
42. Rubio, J.; Souza, M.; Smith, R., Overview of flotation as a wastewater treatment technique. *Minerals engineering* **2002**, *15* (3), 139-155.
43. Pouet, M.-F.; Grasmick, A., Urban wastewater treatment by electrocoagulation and flotation. *Water science and technology* **1995**, *31* (3-4), 275-283.
44. Song, Z.; Williams, C.; Edyvean, R., Treatment of tannery wastewater by chemical coagulation. *Desalination* **2004**, *164* (3), 249-259.
45. Song, Z.; Williams, C.; Edyvean, R., Sedimentation of tannery wastewater. *Water Research* **2000**, *34* (7), 2171-2176.
46. Carlsson, B., An introduction to sedimentation theory in wastewater treatment. *Systems and Control Group, Uppsala University* **1998**.
47. Gryta, M.; Tomaszewska, M.; Karakulski, K., Wastewater treatment by membrane distillation. *Desalination* **2006**, *198* (1-3), 67-73.
48. Zhou, Y.; Shi, C.; Dong, G., Analysis of a mechanical vapor recompression wastewater distillation system. *Desalination* **2014**, *353*, 91-97.
49. Tanudjaja, H. J.; Hejase, C. A.; Tarabara, V. V.; Fane, A. G.; Chew, J. W., Membrane-based separation for oily wastewater: A practical perspective. *Water research* **2019**, *156*, 347-365.
50. Konvensional, B. T., A review of oilfield wastewater treatment using membrane filtration over conventional technology. *Malays. J. Anal. Sci* **2017**, *21*, 643-658.
51. Cooney, D. O., *Adsorption design for wastewater treatment*. CRC press: 1998.
52. De Gisi, S.; Lofrano, G.; Grassi, M.; Notarnicola, M., Characteristics and adsorption capacities of low-cost sorbents for wastewater treatment: a review. *Sustainable Materials and Technologies* **2016**, *9*, 10-40.
53. Liu, Z.-h.; Kanjo, Y.; Mizutani, S., Removal mechanisms for endocrine disrupting compounds (EDCs) in wastewater treatment—physical means, biodegradation, and chemical advanced oxidation: a review. *Science of the total environment* **2009**, *407* (2), 731-748.
54. Bernhard, M.; Müller, J.; Knepper, T. P., Biodegradation of persistent polar pollutants in wastewater: Comparison of an optimised lab-scale membrane bioreactor and activated sludge treatment. *Water research* **2006**, *40* (18), 3419-3428.
55. Baker, R. W., Overview of membrane science and technology. *Membrane technology and applications* **2004**, *3*, 1-14.
56. Scott, K.; Hughes, R.; Hughes, R., *Industrial membrane separation technology*. Springer Science & Business Media: 1996.
57. Ravanchi, M. T.; Kaghazchi, T.; Kargari, A., Application of membrane separation processes in petrochemical industry: a review. *Desalination* **2009**, *235* (1-3), 199-244.
58. Singh, R.; Hankins, N., *Emerging membrane technology for sustainable water treatment*. Elsevier: 2016.

59. Raza, W.; Lee, J.; Raza, N.; Luo, Y.; Kim, K.-H.; Yang, J., Removal of phenolic compounds from industrial waste water based on membrane-based technologies. *Journal of industrial and engineering chemistry* **2019**, *71*, 1-18.
60. Kamali, M.; Suhas, D.; Costa, M. E.; Capela, I.; Aminabhavi, T. M., Sustainability considerations in membrane-based technologies for industrial effluents treatment. *Chemical Engineering Journal* **2019**, *368*, 474-494.
61. Nascimento, T. A.; Fdz-Polanco, F.; Peña, M., Membrane-based technologies for the up-concentration of municipal wastewater: a review of pretreatment intensification. *Separation & Purification Reviews* **2020**, *49* (1), 1-19.
62. Obotey Ezugbe, E.; Rathilal, S., Membrane technologies in wastewater treatment: a review. *Membranes* **2020**, *10* (5), 89.
63. Jhaveri, J. H.; Murthy, Z., A comprehensive review on anti-fouling nanocomposite membranes for pressure driven membrane separation processes. *Desalination* **2016**, *379*, 137-154.
64. Chollom, M. N. Treatment and reuse of reactive dye effluent from textile industry using membrane technology. 2014.
65. Muro, C.; Riera, F.; del Carmen Díaz, M., Membrane separation process in wastewater treatment of food industry. In *Food industrial processes—methods and equipment*, InTech, Rijeka Rijeka, Croatia: 2012; pp 253-280.
66. Wakeman, R.; Williams, C., Additional techniques to improve microfiltration. *Separation and Purification Technology* **2002**, *26* (1), 3-18.
67. Saboyainsta, L. V.; Maubois, J.-L., Current developments of microfiltration technology in the dairy industry. *Le Lait* **2000**, *80* (6), 541-553.
68. Michaels, A. S.; Nelsen, L.; Porter, M. C., Ultrafiltration. In *Membrane processes in industry and biomedicine*, Springer: 1971; pp 197-232.
69. Ferry, J. D., Ultrafilter Membranes and Ultrafiltration. *Chemical reviews* **1936**, *18* (3), 373-455.
70. Mohammad, A. W.; Teow, Y.; Ang, W.; Chung, Y.; Oatley-Radcliffe, D.; Hilal, N., Nanofiltration membranes review: Recent advances and future prospects. *Desalination* **2015**, *356*, 226-254.
71. Bowen, W. R.; Mukhtar, H., Characterisation and prediction of separation performance of nanofiltration membranes. *Journal of membrane science* **1996**, *112* (2), 263-274.
72. Greenlee, L. F.; Lawler, D. F.; Freeman, B. D.; Marrot, B.; Moulin, P., Reverse osmosis desalination: water sources, technology, and today's challenges. *Water research* **2009**, *43* (9), 2317-2348.
73. Malaeb, L.; Ayoub, G. M., Reverse osmosis technology for water treatment: State of the art review. *Desalination* **2011**, *267* (1), 1-8.
74. Bartels, C. R.; Wilf, M.; Andes, K.; Iong, J., Design considerations for wastewater treatment by reverse osmosis. *Water science and technology* **2005**, *51* (6-7), 473-482.
75. Guo, W.; Ngo, H.-H.; Li, J., A mini-review on membrane fouling. *Bioresource technology* **2012**, *122*, 27-34.
76. Lee, S.; Lueptow, R. M., Reverse osmosis filtration for space mission wastewater: membrane properties and operating conditions. *Journal of Membrane Science* **2001**, *182* (1-2), 77-90.
77. Anis, S. F.; Hashaikeh, R.; Hilal, N., Reverse osmosis pretreatment technologies and future trends: A comprehensive review. *Desalination* **2019**, *452*, 159-195.

78. Prihasto, N.; Liu, Q.-F.; Kim, S.-H., Pre-treatment strategies for seawater desalination by reverse osmosis system. *Desalination* **2009**, *249* (1), 308-316.
79. Güell, C.; Davis, R. H., Membrane fouling during microfiltration of protein mixtures. *Journal of Membrane Science* **1996**, *119* (2), 269-284.
80. Shang, R.; Vuong, F.; Hu, J.; Li, S.; Kemperman, A. J.; Nijmeijer, K.; Cornelissen, E. R.; Heijman, S. G.; Rietveld, L. C., Hydraulically irreversible fouling on ceramic MF/UF membranes: Comparison of fouling indices, foulant composition and irreversible pore narrowing. *Separation and Purification Technology* **2015**, *147*, 303-310.
81. Tang, C. Y.; Chong, T.; Fane, A. G., Colloidal interactions and fouling of NF and RO membranes: a review. *Advances in colloid and interface science* **2011**, *164* (1-2), 126-143.
82. Shi, X.; Tal, G.; Hankins, N. P.; Gitis, V., Fouling and cleaning of ultrafiltration membranes: A review. *Journal of Water Process Engineering* **2014**, *1*, 121-138.
83. Henry, C.; Minier, J.-P.; Lefèvre, G., Towards a description of particulate fouling: From single particle deposition to clogging. *Advances in colloid and interface science* **2012**, *185*, 34-76.
84. Amy, G., Fundamental understanding of organic matter fouling of membranes. *Desalination* **2008**, *231* (1-3), 44-51.
85. Tummons, E.; Han, Q.; Tanudjaja, H. J.; Hejase, C. A.; Chew, J. W.; Tarabara, V. V., Membrane fouling by emulsified oil: A review. *Separation and Purification Technology* **2020**, *248*, 116919.
86. Gao, Y.; Qin, J.; Wang, Z.; Østerhus, S. W., Backpulsing technology applied in MF and UF processes for membrane fouling mitigation: A review. *Journal of Membrane Science* **2019**, *587*, 117136.
87. Hube, S.; Eskafi, M.; Hrafnkelsdóttir, K. F.; Bjarnadóttir, B.; Bjarnadóttir, M. Á.; Axelsdóttir, S.; Wu, B., Direct membrane filtration for wastewater treatment and resource recovery: A review. *Science of the Total Environment* **2020**, *710*, 136375.
88. Issa, M.; Geissen, S.-U.; Vogelpohl, A., Reduction of energy demand for UF cross-flow membranes in MBR by sponge ball cleaning. *Membrane and Water Treatment* **2021**, *12* (2), 65-73.
89. AlSawaftah, N.; Abuwatfa, W.; Darwish, N.; Hussein, G., A comprehensive review on membrane fouling: Mathematical modelling, prediction, diagnosis, and mitigation. *Water* **2021**, *13* (9), 1327.
90. Cui, Z.; Wang, J.; Zhang, H.; Ngo, H. H.; Jia, H.; Guo, W.; Gao, F.; Yang, G.; Kang, D., Investigation of backwashing effectiveness in membrane bioreactor (MBR) based on different membrane fouling stages. *Bioresour. Technol.* **2018**, *269*, 355-362.
91. Gruskevica, K.; Mezule, L., Cleaning methods for ceramic ultrafiltration membranes affected by organic fouling. *Membranes* **2021**, *11* (2), 131.
92. Huang, J.; Luo, J.; Chen, X.; Feng, S.; Wan, Y., How do chemical cleaning agents act on polyamide nanofiltration membrane and fouling layer? *Industrial & Engineering Chemistry Research* **2020**, *59* (40), 17653-17670.
93. Li, K.; Li, S.; Huang, T.; Dong, C.; Li, J.; Zhao, B.; Zhang, S., Chemical cleaning of ultrafiltration membrane fouled by humic substances: comparison between hydrogen peroxide and sodium hypochlorite. *International journal of environmental research and public health* **2019**, *16* (14), 2568.
94. Yalcinkaya, F.; Boyraz, E.; Maryska, J.; Kucerova, K., A review on membrane technology and chemical surface modification for the oily wastewater treatment. *Materials* **2020**, *13* (2), 493.

95. Qiu, W.-Z.; Yang, H.-C.; Xu, Z.-K., Dopamine-assisted co-deposition: an emerging and promising strategy for surface modification. *Advances in Colloid and Interface Science* **2018**, *256*, 111-125.
96. Chourifa, H.; Bouloussa, H.; Migonney, V.; Falentin-Daudré, C., Review of titanium surface modification techniques and coatings for antibacterial applications. *Acta biomaterialia* **2019**, *83*, 37-54.
97. Amani, H.; Arzaghi, H.; Bayandori, M.; Dezfuli, A. S.; Pazoki - Toroudi, H.; Shafiee, A.; Moradi, L., Controlling cell behavior through the design of biomaterial surfaces: a focus on surface modification techniques. *Advanced materials interfaces* **2019**, *6* (13), 1900572.
98. Liu, C.; Guo, Y.; Zhang, J.; Tian, B.; Lin, O.; Liu, Y.; Zhang, C., Tailor-made high-performance reverse osmosis membranes by surface fixation of hydrophilic macromolecules for wastewater treatment. *RSC advances* **2019**, *9* (31), 17766-17777.
99. Kwon, G.; Post, E. R.; Kota, A. K.; Li, C.; Speer, D. L.; Guenther, A. J.; Reams, J. T.; Lamison, K. R.; Mabry, J. M.; Tuteja, A., Continuous Liquid-Liquid Extraction and in-Situ Membrane Separation of Miscible Liquid Mixtures. *Langmuir* **2021**, *37* (46), 13595-13601.
100. Huang, S.; Ras, R. H.; Tian, X., Antifouling membranes for oily wastewater treatment: Interplay between wetting and membrane fouling. *Current opinion in colloid & interface science* **2018**, *36*, 90-109.
101. Nasir, A. M.; Awang, N.; Jaafar, J.; Ismail, A. F.; Othman, M. H. D.; Rahman, M. A.; Aziz, F.; Yajid, M. A. M., Recent progress on fabrication and application of electrospun nanofibrous photocatalytic membranes for wastewater treatment: A review. *Journal of Water Process Engineering* **2021**, *40*, 101878.
102. Riaz, S.; Park, S.-J., An overview of TiO₂-based photocatalytic membrane reactors for water and wastewater treatments. *Journal of industrial and engineering chemistry* **2020**, *84*, 23-41.
103. Al-Mamun, M.; Kader, S.; Islam, M.; Khan, M., Photocatalytic activity improvement and application of UV-TiO₂ photocatalysis in textile wastewater treatment: A review. *Journal of Environmental Chemical Engineering* **2019**, *7* (5), 103248.
104. Najafidoust, A.; Allahyari, S.; Rahemi, N.; Tasbihi, M., Uniform coating of TiO₂ nanoparticles using biotemplates for photocatalytic wastewater treatment. *Ceramics International* **2020**, *46* (4), 4707-4719.
105. Shrestha, B.; Ezazi, M.; Kwon, G., Engineered nanoparticles with decoupled photocatalysis and wettability for membrane-based desalination and separation of oil-saline water mixtures. *Nanomaterials* **2021**, *11* (6), 1397.
106. Choi, H.; Stathatos, E.; Dionysiou, D. D., Photocatalytic TiO₂ films and membranes for the development of efficient wastewater treatment and reuse systems. *Desalination* **2007**, *202* (1-3), 199-206.
107. Qing, W.; Liu, F.; Yao, H.; Sun, S.; Chen, C.; Zhang, W., Functional catalytic membrane development: A review of catalyst coating techniques. *Advances in Colloid and Interface Science* **2020**, 102207.
108. Li, Q.; Zhao, T.; Li, M.; Li, W.; Yang, B.; Qin, D.; Lv, K.; Wang, X.; Wu, L.; Wu, X., One-step construction of Pickering emulsion via commercial TiO₂ nanoparticles for photocatalytic dye degradation. *Appl. Catal., B* **2019**, *249*, 1-8.
109. Li, X.; Wu, X.; Liu, S.; Li, Y.; Fan, J.; Lv, K., Effects of fluorine on photocatalysis. *Chinese Journal of Catalysis* **2020**, *41* (10), 1451-1467.

110. Qahtan, T. F.; Gondal, M. A.; Dastageer, M. A.; Kwon, G.; Ezazi, M.; Al-Kuban, M. Z., Thermally Sensitized Membranes for Crude Oil–Water Remediation under Visible Light. *ACS Appl. Mater. Interfaces* **2020**, *12* (43), 48572-48579.
111. Lv, Y.; Zhang, C.; He, A.; Yang, S. J.; Wu, G. P.; Darling, S. B.; Xu, Z. K., Photocatalytic Nanofiltration Membranes with Self - Cleaning Property for Wastewater Treatment. *Adv. Funct. Mater.* **2017**, *27* (27), 1700251.
112. Madaeni, S.; Ghaemi, N., Characterization of self-cleaning RO membranes coated with TiO₂ particles under UV irradiation. *Journal of Membrane Science* **2007**, *303* (1-2), 221-233.
113. Xu, C.; Killmeyer, R.; Gray, M. L.; Khan, S. U., Photocatalytic effect of carbon-modified n-TiO₂ nanoparticles under visible light illumination. *Applied Catalysis B: Environmental* **2006**, *64* (3-4), 312-317.
114. Kim, S. H.; Kwak, S.-Y.; Sohn, B.-H.; Park, T. H., Design of TiO₂ nanoparticle self-assembled aromatic polyamide thin-film-composite (TFC) membrane as an approach to solve biofouling problem. *Journal of Membrane Science* **2003**, *211* (1), 157-165.
115. Yamashita, H.; Harada, M.; Misaka, J.; Takeuchi, M.; Ichihashi, Y.; Goto, F.; Ishida, M.; Sasaki, T.; Anpo, M., Application of ion beam techniques for preparation of metal ion-implanted TiO₂ thin film photocatalyst available under visible light irradiation: metal ion-implantation and ionized cluster beam method. *Journal of synchrotron radiation* **2001**, *8* (2), 569-571.
116. Kota, A. K.; Kwon, G.; Choi, W.; Mabry, J. M.; Tuteja, A., Hygro-responsive membranes for effective oil–water separation. *Nature communications* **2012**, *3* (1), 1-8.
117. Tuteja, A.; Choi, W.; Ma, M.; Mabry, J. M.; Mazzella, S. A.; Rutledge, G. C.; McKinley, G. H.; Cohen, R. E., Designing superoleophobic surfaces. *Science* **2007**, *318* (5856), 1618-1622.
118. Young, T., Philos. Trans. R. Soc., London. **1805**.
119. Choi, W.; Tuteja, A.; Mabry, J. M.; Cohen, R. E.; McKinley, G. H., A modified Cassie–Baxter relationship to explain contact angle hysteresis and anisotropy on non-wetting textured surfaces. *Journal of colloid and interface science* **2009**, *339* (1), 208-216.
120. Tuteja, A.; Choi, W.; Mabry, J. M.; McKinley, G. H.; Cohen, R. E., Robust omniphobic surfaces. *Proceedings of the National Academy of Sciences* **2008**, *105* (47), 18200-18205.
121. Cassie, A.; Baxter, S., Trans. Faraday Soc. **1944**.
122. Wenzel, R. N., Resistance of solid surfaces to wetting by water. *Industrial & Engineering Chemistry* **1936**, *28* (8), 988-994.
123. Hoffman, R. L., A study of the advancing interface. I. Interface shape in liquid–gas systems. *Journal of colloid and interface science* **1975**, *50* (2), 228-241.
124. Gao, L.; McCarthy, T. J., Contact angle hysteresis explained. *Langmuir* **2006**, *22* (14), 6234-6237.
125. Wang, Y.; Gong, X., Special oleophobic and hydrophilic surfaces: approaches, mechanisms, and applications. *Journal of Materials Chemistry A* **2017**, *5* (8), 3759-3773.
126. Ikhsan, S. N. W.; Yusof, N.; Aziz, F.; Ismail, A. F.; Jaafar, J.; Salleh, W. N. W.; Misdan, N., Superwetting materials for hydrophilic-oleophobic membrane in oily wastewater treatment. *Journal of Environmental Management* **2021**, *290*, 112565.
127. Eseev, M.; Goshev, A.; Kapustin, S.; Tsykareva, Y., Creation of Superhydrophobic Coatings Based on MWCNTs Xerogel. *Nanomaterials* **2019**, *9* (11), 1584.
128. Dong, S.; Wang, Z.; An, L.; Li, Y.; Wang, B.; Ji, H.; Wang, H., Facile Fabrication of a Superhydrophobic Surface with Robust Micro-/Nanoscale Hierarchical Structures on Titanium Substrate. *Nanomaterials* **2020**, *10* (8), 1509.

129. Li, J.; Qin, Q. H.; Shah, A.; Ras, R. H.; Tian, X.; Jokinen, V., Oil droplet self-transportation on oleophobic surfaces. *Sci. Adv.* **2016**, *2* (6), e1600148.
130. Geng, H.; Bai, H.; Fan, Y.; Wang, S.; Ba, T.; Yu, C.; Cao, M.; Jiang, L., Unidirectional water delivery on a superhydrophilic surface with two-dimensional asymmetrical wettability barriers. *Materials Horizons* **2018**, *5* (2), 303-308.
131. Lv, J.; Gong, Z.; He, Z.; Yang, J.; Chen, Y.; Tang, C.; Liu, Y.; Fan, M.; Lau, W.-M., 3D printing of a mechanically durable superhydrophobic porous membrane for oil–water separation. *J. Mater. Chem. A* **2017**, *5* (24), 12435-12444.
132. Sun, S.; Zhu, L.; Liu, X.; Wu, L.; Dai, K.; Liu, C.; Shen, C.; Guo, X.; Zheng, G.; Guo, Z., Superhydrophobic shish-kebab membrane with self-cleaning and oil/water separation properties. *ACS Sustainable Chem. Eng.* **2018**, *6* (8), 9866-9875.
133. Kaner, P.; Dudchenko, A. V.; Mauter, M. S.; Asatekin, A., Zwitterionic copolymer additive architecture affects membrane performance: fouling resistance and surface rearrangement in saline solutions. *Journal of Materials Chemistry A* **2019**, *7* (9), 4829-4846.
134. Xie, A.; Cui, J.; Yang, J.; Chen, Y.; Dai, J.; Lang, J.; Li, C.; Yan, Y., Photo-Fenton self-cleaning membranes with robust flux recovery for an efficient oil/water emulsion separation. *Journal of Materials Chemistry A* **2019**, *7* (14), 8491-8502.
135. Cheng, X.; Sun, Z.; Yang, X.; Li, Z.; Zhang, Y.; Wang, P.; Liang, H.; Ma, J.; Shao, L., Construction of superhydrophilic hierarchical polyacrylonitrile nanofiber membranes by in situ asymmetry engineering for unprecedentedly ultrafast oil–water emulsion separation. *Journal of Materials Chemistry A* **2020**.
136. Zhao, J.; Zhu, W.; Wang, X.; Liu, L.; Yu, J.; Ding, B., Environmentally benign modification of breathable nanofibrous membranes exhibiting superior waterproof and photocatalytic self-cleaning properties. *Nanoscale Horizons* **2019**, *4* (4), 867-873.
137. Luster, E.; Avisar, D.; Horovitz, I.; Lozzi, L.; Baker, M. A.; Grilli, R.; Mamane, H., N-doped TiO₂-coated ceramic membrane for carbamazepine degradation in different water qualities. *Nanomaterials* **2017**, *7* (8), 206.
138. Bortot Coelho, F. E.; Gionco, C.; Paganini, M. C.; Calza, P.; Magnacca, G., Control of Membrane Fouling in Organics Filtration Using Ce-Doped Zirconia and Visible Light. *Nanomaterials* **2019**, *9* (4), 534.
139. Wang, D.; Liu, Y.; Liu, X.; Zhou, F.; Liu, W.; Xue, Q., Towards a tunable and switchable water adhesion on a TiO₂ nanotube film with patterned wettability. *Chemical Communications* **2009**, (45), 7018-7020.
140. Horovitz, I.; Gitis, V.; Avisar, D.; Mamane, H., Ceramic-based photocatalytic membrane reactors for water treatment—where to next? *Reviews in Chemical Engineering* **2020**, *36* (5), 593-622.
141. Wang, J.; Zhuang, S., Removal of cesium ions from aqueous solutions using various separation technologies. *Reviews in Environmental Science and Bio/Technology* **2019**, *18* (2), 231-269.
142. Joos, P., *Dynamic surface phenomena*. VSP: 1999.
143. Foo, K. Y.; Hameed, B. H., Insights into the modeling of adsorption isotherm systems. *Chemical engineering journal* **2010**, *156* (1), 2-10.
144. Langmuir, I., The adsorption of gases on plane surfaces of glass, mica and platinum. *Journal of the American Chemical society* **1918**, *40* (9), 1361-1403.
145. Adamson, A. W.; Gast, A. P., *Physical chemistry of surfaces*. Interscience publishers New York: 1967; Vol. 15.

146. Salis, A.; Meloni, D.; Ligas, S.; Casula, M. F.; Monduzzi, M.; Solinas, V.; Dumitriu, E., Physical and chemical adsorption of *Mucor javanicus* lipase on SBA-15 mesoporous silica. Synthesis, structural characterization, and activity performance. *Langmuir* **2005**, *21* (12), 5511-5516.
147. Bruch, L. W.; Cole, M. W.; Zaremba, E., *Physical adsorption: forces and phenomena*. Courier Dover Publications: 2007.
148. Webb, P. A., Introduction to chemical adsorption analytical techniques and their applications to catalysis. *Micromeritics Instrument Corp. Technical Publications* **2003**, 1-12.
149. Razmi, F. A.; Ngadi, N.; Wong, S.; Inuwa, I. M.; Opotu, L. A., Kinetics, thermodynamics, isotherm and regeneration analysis of chitosan modified pandan adsorbent. *Journal of cleaner production* **2019**, *231*, 98-109.
150. Mondal, M. K.; Garg, R., A comprehensive review on removal of arsenic using activated carbon prepared from easily available waste materials. *Environmental Science and Pollution Research* **2017**, *24* (15), 13295-13306.
151. Thompson, K. A.; Shimabuku, K. K.; Kearns, J. P.; Knappe, D. R.; Summers, R. S.; Cook, S. M., Environmental comparison of biochar and activated carbon for tertiary wastewater treatment. *Environmental science & technology* **2016**, *50* (20), 11253-11262.
152. Patra, J.; Panda, S.; Dhal, N., Biochar as a low-cost adsorbent for heavy metal removal: A review. *Int. J. Res. Biosci* **2017**, *6* (1), 1-7.
153. Salvador, F.; Martin-Sanchez, N.; Sanchez-Hernandez, R.; Sanchez-Montero, M. J.; Izquierdo, C., Regeneration of carbonaceous adsorbents. Part I: thermal regeneration. *Microporous and Mesoporous Materials* **2015**, *202*, 259-276.
154. Dai, Y.; Zhang, N.; Xing, C.; Cui, Q.; Sun, Q., The adsorption, regeneration and engineering applications of biochar for removal organic pollutants: a review. *Chemosphere* **2019**, *223*, 12-27.
155. Kulkarni, S.; Kaware, J., Regeneration and recovery in adsorption-a review. *International Journal of Innovative Science, Engineering & Technology* **2014**, *1* (8), 61-64.
156. Pan, M.; Shan, C.; Zhang, X.; Zhang, Y.; Zhu, C.; Gao, G.; Pan, B., Environmentally friendly in situ regeneration of graphene aerogel as a model conductive adsorbent. *Environmental science & technology* **2018**, *52* (2), 739-746.
157. Meng, J.; Ren, M.; Wang, S.; Gao, J.; Shan, X.; Hu, J., A smart adsorbent with ability of environmentally friendly regeneration for p-nitrophenol removal in aqueous solution. *Journal of Inorganic and Organometallic Polymers and Materials* **2021**, *31* (6), 2381-2392.
158. Mohan, D.; Singh, K. P.; Singh, G.; Kumar, K., Removal of dyes from wastewater using flyash, a low-cost adsorbent. *Industrial & engineering chemistry research* **2002**, *41* (15), 3688-3695.
159. Patel, H., Review on solvent desorption study from exhausted adsorbent. *Journal of Saudi Chemical Society* **2021**, *25* (8), 101302.
160. Daud, Z.; Rosli, M. A.; Abdul Latiff, A. A.; Ridzuan, M. B.; Awang, H.; Abdul Halim, A. In *Micro-peat as a potential low-cost adsorbent material for COD and NH₃-N removal*, Defect and Diffusion Forum, Trans Tech Publ: 2018; pp 297-301.
161. Maruyama, T.; Terashima, Y.; Takeda, S.; Okazaki, F.; Goto, M., Selective adsorption and recovery of precious metal ions using protein-rich biomass as efficient adsorbents. *Process Biochemistry* **2014**, *49* (5), 850-857.

162. Ezazi, M.; Shrestha, B.; Kwon, G., Lower Critical Solution Temperature-Driven Catch and Release of Perfluoroalkyl Substances from Water: Remediation and Sampling. *ACS Applied Polymer Materials* **2021**, 3 (8), 4139-4146.
163. Becanova, J.; Saleeba, Z. S.; Stone, A.; Robuck, A. R.; Hurt, R. H.; Lohmann, R., A graphene-based hydrogel monolith with tailored surface chemistry for PFAS passive sampling. *Environmental Science: Nano* **2021**, 8 (10), 2894-2907.
164. Lissaneddine, A.; Pons, M.-N.; Aziz, F.; Ouazzani, N.; Mandi, L.; Mousset, E., A critical review on the electrosorption of organic compounds in aqueous effluent—Influencing factors and engineering considerations. *Environmental Research* **2022**, 204, 112128.
165. Han, Y.; Quan, X.; Chen, S.; Zhao, H.; Cui, C.; Zhao, Y., Electrochemically enhanced adsorption of phenol on activated carbon fibers in basic aqueous solution. *Journal of colloid and interface science* **2006**, 299 (2), 766-771.
166. Li, H.; Gao, Y.; Pan, L.; Zhang, Y.; Chen, Y.; Sun, Z., Electrosorptive desalination by carbon nanotubes and nanofibres electrodes and ion-exchange membranes. *Water research* **2008**, 42 (20), 4923-4928.
167. Choi, J.; Dorji, P.; Shon, H. K.; Hong, S., Applications of capacitive deionization: Desalination, softening, selective removal, and energy efficiency. *Desalination* **2019**, 449, 118-130.
168. Hou, C.-H.; Huang, C.-Y., A comparative study of electrosorption selectivity of ions by activated carbon electrodes in capacitive deionization. *Desalination* **2013**, 314, 124-129.
169. Soffer, A.; Folman, M., The electrical double layer of high surface porous carbon electrode. *Journal of Electroanalytical Chemistry and Interfacial Electrochemistry* **1972**, 38 (1), 25-43.
170. Chen, R.; Sheehan, T.; Ng, J. L.; Brucks, M.; Su, X., Capacitive deionization and electrosorption for heavy metal removal. *Environmental Science: Water Research & Technology* **2020**, 6 (2), 258-282.
171. Welgemoed, T.; Schutte, C. F., Capacitive deionization technology™: an alternative desalination solution. *Desalination* **2005**, 183 (1-3), 327-340.
172. Oren, Y., Capacitive deionization (CDI) for desalination and water treatment—past, present and future (a review). *Desalination* **2008**, 228 (1-3), 10-29.
173. Gouy, M., Sur la constitution de la charge électrique à la surface d'un électrolyte. *J. Phys. Theor. Appl.* **1910**, 9 (1), 457-468.
174. Stern, O., Zur theorie der elektrolytischen doppelschicht. *Zeitschrift für Elektrochemie und angewandte physikalische Chemie* **1924**, 30 (21 - 22), 508-516.
175. Porada, S.; Zhao, R.; Van Der Wal, A.; Presser, V.; Biesheuvel, P., Review on the science and technology of water desalination by capacitive deionization. *Progress in materials science* **2013**, 58 (8), 1388-1442.
176. Suss, M.; Porada, S.; Sun, X.; Biesheuvel, P.; Yoon, J.; Presser, V., Water desalination via capacitive deionization: what is it and what can we expect from it? *Energy & Environmental Science* **2015**, 8 (8), 2296-2319.
177. Li, X.; Chen, S.; Quan, X.; Zhang, Y., Enhanced adsorption of PFOA and PFOS on multiwalled carbon nanotubes under electrochemical assistance. *Environmental science & technology* **2011**, 45 (19), 8498-8505.
178. Wang, S.; Li, X.; Zhang, Y.; Quan, X.; Chen, S.; Yu, H.; Zhao, H., Electrochemically enhanced adsorption of PFOA and PFOS on multiwalled carbon nanotubes in continuous flow mode. *Chinese science bulletin* **2014**, 59 (23), 2890-2897.

179. Kim, K.; Baldaguez Medina, P.; Elbert, J.; Kayiwa, E.; Cusick, R. D.; Men, Y.; Su, X., Molecular Tuning of Redox - Copolymers for Selective Electrochemical Remediation. *Advanced Functional Materials* **2020**, 2004635.
180. Niu, Z.; Wang, Y.; Lin, H.; Jin, F.; Li, Y.; Niu, J., Electrochemically enhanced removal of perfluorinated compounds (PFCs) from aqueous solution by CNTs-graphene composite electrode. *Chemical Engineering Journal* **2017**, 328, 228-235.
181. Baroud, T. N.; Giannelis, E. P., High salt capacity and high removal rate capacitive deionization enabled by hierarchical porous carbons. *Carbon* **2018**, 139, 614-625.
182. Pekala, R.; Farmer, J.; Alviso, C.; Tran, T.; Mayer, S.; Miller, J.; Dunn, B., Carbon aerogels for electrochemical applications. *Journal of non-crystalline solids* **1998**, 225, 74-80.
183. Li, H.; Lu, T.; Pan, L.; Zhang, Y.; Sun, Z., Electrosorption behavior of graphene in NaCl solutions. *Journal of Materials Chemistry* **2009**, 19 (37), 6773-6779.
184. Gao, T.; Li, H.; Zhou, F.; Gao, M.; Liang, S.; Luo, M., Mesoporous carbon derived from ZIF-8 for high efficient electrosorption. *Desalination* **2019**, 451, 133-138.
185. Zhang, J.; Seyedin, S.; Qin, S.; Wang, Z.; Moradi, S.; Yang, F.; Lynch, P. A.; Yang, W.; Liu, J.; Wang, X., Highly conductive Ti₃C₂T_x MXene hybrid fibers for flexible and elastic fiber - shaped supercapacitors. *Small* **2019**, 15 (8), 1804732.
186. Bao, W.; Tang, X.; Guo, X.; Choi, S.; Wang, C.; Gogotsi, Y.; Wang, G., Porous cryo-dried MXene for efficient capacitive deionization. *Joule* **2018**, 2 (4), 778-787.
187. Saeidi, N.; Kopinke, F.-D.; Georgi, A., Controlling adsorption of perfluoroalkyl acids on activated carbon felt by means of electrical potentials. *Chemical Engineering Journal* **2021**, 416, 129070.

Chapter 2: Engineered Nanoparticles with Decoupled Photocatalysis and Wettability for Membrane-based Desalination and Separation of Oil-Saline Water Mixtures

This chapter is adapted from **Paper P1**.

Abstract: Membrane-based separation technologies are the cornerstone of remediating unconventional water sources, including brackish and industrial or municipal wastewater, as they are relatively energy-efficient and versatile. However, membrane fouling by dissolved and suspended substances in the feed stream remains a primary challenge that currently prevents these membranes from being used in real practices. Thus, we directly address this challenge by applying a superhydrophilic, and oleophobic coating to a commercial membrane surface, which can be utilized to separate and desalinate an oil and saline water mixture, and photocatalytically degrade the organic substances. We fabricated the photocatalytic membrane by coating a commercial membrane with an ultraviolet (UV) light-curable adhesive. Then, we sprayed it with a mixture of photocatalytic nitrogen-doped titania (N-TiO₂) and perfluoro silane-grafted silica (F-SiO₂) nanoparticles. The membrane was placed under UV light, which resulted in a chemically heterogeneous surface with intercalating high and low surface energy regions (i.e., N-TiO₂ and F-SiO₂, respectively) that were securely bound to the commercial membrane surface. We demonstrated that the coated membrane could be utilized for continuous separation and desalination of an oil-saline water mixture and for simultaneous photocatalytic degradation of the organic substances adsorbed on the membrane surface upon visible light irradiation.

2.1. Introduction

Modulating the surface wettability plays a vital role in a solid-liquid system and has found increasing interest in practical applications, including self-cleaning^{1,2}, microfluidics^{3,4}, and liquids separation^{5,6}. Based on the contact angle (θ) for high (e.g., water) and low (oil) surface tension liquids, a surface can be grouped into four wettability; omniphobic ($\theta_{\text{water}} > 90^\circ$ and $\theta_{\text{oil}} > 90^\circ$), hydrophobic and oleophilic ($\theta_{\text{water}} > 90^\circ$ and $\theta_{\text{oil}} < 90^\circ$), hydrophilic and oleophobic ($\theta_{\text{water}} < 90^\circ$ and $\theta_{\text{oil}} > 90^\circ$), and omniphilic ($\theta_{\text{water}} < 90^\circ$ and $\theta_{\text{oil}} < 90^\circ$)^{7, 8}. We⁹⁻¹¹ and others¹²⁻¹⁴ have demonstrated that a low surface energy coating in conjunction with surface texture can result in a non-wetting Cassie-Baxter state with air trapped between the contacting liquid and the solid surface.

Organofluorine is perhaps the most prevailing material to lower the overall surface free energy and render the surface repellent to liquids¹⁰. It has been extensively employed to fabricate not only

a surface with omniphobic^{15, 16} or superomniphobic wettability (i.e., $\theta_{\text{water}}^* > 150^\circ$ and $\theta_{\text{oil}}^* > 150^\circ$)^{9, 17, 18} but that with a selective (i.e., hydrophobic and oleophilic or hydrophilic and oleophobic) wettability¹⁹⁻²². For example, Mertens et al.¹⁹ utilized a combination of photolithography and oxygen plasma treatment to fabricate a nanocrystalline diamond surface with hydrophobic and hydrophilic arrays. Howarter et al.²⁰ grafted a perfluorinated polyethylene glycol on a silicon surface which can exhibit hydrophilic and oleophobic wettability.

The utility of surfaces with selective wettability can be further extended by incorporating them with photocatalytic nanoparticles that can degrade organic substances upon light irradiation²³⁻²⁵. Such a photocatalytic surface with selective wettability has demonstrated a potential for a wide range of practical applications, including anti-fouling^{26, 27}, self-cleaning^{28, 29}, and bactericidal coating³⁰. Recent studies³¹⁻³⁴ have revealed that membranes with selective wettability can further benefit by incorporating photocatalytic nanoparticles that can radically transform physical filtration into chemically reactive processes. Thus, it can progressively eliminate the inherent shortcomings of conventional membrane-based filtration, such as pollutant degradation and membrane fouling²³. Zhao et al.³⁵ reported a polyacrylonitrile membrane coated with a fluorinated agent and photocatalytic ZnO. The membrane exhibited remediation of wastewater upon ultraviolet (UV) light irradiation and resistance to fouling. Luster et al.³⁶ fabricated an N-doped TiO₂-coated alumina membrane and demonstrated the photocatalytic degradation of carbamazepine (CBZ) as a model pollutant under simulated solar irradiation. Further, Coelho et al.²⁶ coated a filter paper with zirconia-doped cerium to prepare a photocatalytic membrane. The membrane demonstrated flux recovery by photocatalytic degradation of humic acid as foulant. Before these photocatalytic membranes with desired wettability can be utilized for practical applications, they need to fulfill the following three conditions^{37, 38}. First, the membrane's

wettability must remain unchanged by a photocatalytic reaction. Similarly, its physical and chemical integrity must not be affected by a photocatalytic reaction, particularly if the membrane is organic. Lastly, the coating (e.g., photocatalytic nanoparticles) needs to remain undetached when a high hydraulic shear force is exerted.

In this work, we engineered a visible light-responsive photocatalytic coating with superhydrophilic and oleophobic wettability both in air and underwater by utilizing nitrogen-doped titania (N-TiO₂) and perfluoro silane-grafted silica (F-SiO₂) nanoparticles. The coating was sprayed onto a commercial membrane surface with UV-curable adhesive. Subsequent irradiation of UV light resulted in a chemically heterogeneous surface with intercalating high surface energy (N-TiO₂) and low surface energy (F-SiO₂) regions that are securely bound to the surface. Both the wettability and the integrity of the membrane remained unaffected throughout the photocatalytic degradation process of the organic substances when exposed to visible light irradiation. This can be attributed to the robust chemistry of the cured adhesive that protected the perfluoro silane molecules grafted to the SiO₂ nanoparticles as well as the underlying membrane from the reactive radical species generated when it was exposed to visible light irradiation. Thus, the coated membrane can be utilized for continuous separation and desalination of an oil-saline water mixture and simultaneous photocatalytic degradation of the organic substances adsorbed on the membrane surface upon visible light irradiation.

2.2. Experimental procedure

2.2.1. Chemicals.

Titanium butoxide (TBOT), tetraethyl orthosilicate (TEOS), triethylamine (TEA), Sodium dodecyl sulfate (SDS), and Sodium chloride (NaCl) were purchased from Millipore Sigma. 1H,1H,2H,2H-perfluorodecyl trichlorosilane (perfluoro silane) was purchased from Alfa Aesar. Ethanol, acetone,

isopropyl alcohol, hydrochloric acid (HCl), nitric acid (HNO₃), and n-hexadecane were purchased from Fisher Scientific. Norland ultraviolet (UV) light-curable optical adhesive (NOA 61) was purchased from Norland Products Inc. Commercial TRISEP ACM5 membrane was purchased from Sterlitech.

2.2.2. Synthesis of N-TiO₂ nanoparticles.

Titanium butoxide (TBOT, 5.0 g) was added dropwise to isopropyl alcohol (79 g), followed by the addition of deionized (DI) water (910 g). Nitric acid (HNO₃, 0.01 M) was added to the solution to adjust the pH = 2. Subsequently, triethylamine was added dropwise to the solution. Please note that the molar ratios of TEA to TBOT were 0.5, 1.0, 2.0, and 3.0. The solution was stirred for 12 h at 30 °C. The precipitates were collected by centrifugation and thoroughly rinsed with DI water and ethanol. Upon vacuum drying for 10 hours, the deep-yellow nitrogen-doped titanium dioxide (N-TiO₂) nanoparticles were obtained.

2.2.3. Synthesis of F-SiO₂ nanoparticles.

Tetraethyl orthosilicate (TEOS, 1.0 g) was added dropwise to a solution of hydrochloric acid (HCl, 0.01 M) in DI water (100 g), followed by the addition of 1H,1H,2H,2H-perfluorodecyl trichlorosilane (1.0 g). The solution was stirred for 60 minutes at 60 °C, and the precipitates were collected by centrifugation. Following a thorough rinsing with DI water and ethanol and after 10 h of vacuum drying, the perfluoro silane-grafted silica (F-SiO₂) nanoparticles were obtained.

2.2.4. Photocatalytic membrane fabrication.

A commercial membrane surface was spin-coated with a Norland ultraviolet (UV) light-curable optical adhesive (NOA 61) (1.0 wt% in acetone). Please note that the commercial membrane (i.e., Sterlitech TRISEP ACM5) consists of three layers, a thin polyamide layer with a molecular weight cut-off equal to 100 Da, and a porous polysulfone layer, and a non-woven polyester as the support.

Suspension of N-TiO₂ and F-SiO₂ nanoparticles mixture (i.e., N-TiO₂/F-SiO₂) in DI water (10 wt%) was then sprayed (iWata spray gun) onto the adhesive-coated membrane for one minute. The spraying distance and nitrogen gas pressure were maintained at 15 cm and 200 kPa, respectively. Please note that the concentration of N-TiO₂ nanoparticles in the N-TiO₂/F-SiO₂ mixture was 0, 20 wt%, 40 wt%, 60 wt%, 80 wt%, and 100 wt%. Subsequently, the membrane surface was irradiated by a long-wavelength UV light (100 W, $\lambda = 365$ nm, Analytikjena) for 5 minutes to cure the adhesive. The membrane was thoroughly rinsed with DI water and ethanol.

2.2.5. Preparation of oil-in-water emulsion dissolved with salt.

An oil-in-water emulsion containing salt was prepared by vigorous mixing of n-hexadecane and DI water (10:90 vol%:vol% n-hexadecane: water) dissolved with salt (NaCl, 1.0 wt% with respect to water mass). Sodium dodecyl sulfate (SDS, 0.015 wt%) was added to stabilize the emulsion.

2.2.6. N-TiO₂ and F-SiO₂ size measurements.

The average size of N-TiO₂ and F-SiO₂ nanoparticles was measured by utilizing dynamic light scattering (DLS) (ZetaPALS zeta potential analyzer, Brookhaven Instruments) equipped with a BI-9000AT digital autocorrelator. Suspensions of N-TiO₂ (0.01 wt%) and F-SiO₂ (0.01 wt%) were prepared in DI water, followed by ultrasonication.

2.2.7. N-TiO₂ crystal structure analyses.

The crystal structure of N-TiO₂ was studied by powder X-ray Diffraction (XRD) (PANalytical Model X'Pert PRO diffractometer) with Cu K α radiation ($k = 1.54$ Å) by scanning at a rate of 2° (2θ) min⁻¹. X-ray Photoelectron Spectroscopy (XPS) was utilized to study the nitrogen doping of N-TiO₂. XPS was conducted by a Phi Versaprobe II utilizing monochromatic source Mg Ka.

2.2.8. N-TiO₂ and F-SiO₂ absorbance measurements.

Ultraviolet-Visible (UV-Vis) spectrophotometry was utilized to analyze the nanoparticles' absorbance spectrum. UV-Vis spectrophotometry was conducted by utilizing a Thermo Evolution 600 at a scan rate of 240 nm min⁻¹ and a data interval of 2 nm.

2.2.9. N-TiO₂ photocatalytic performance measurements.

The photocatalysis performance of N-TiO₂ nanoparticles was analyzed by conducting the dye degradation test. UV-Vis spectrophotometry was utilized to study the dye degradation performance. N-TiO₂ nanoparticles (0.5 wt%) were dispersed in DI water dissolved with Solvent Blue 38 dye (0.5 wt%). 20 mL of the dispersion was poured into a glass beaker equipped with a magnetic stirrer. The visible light (13.1 W, Sugarcube ultraLED) guide was submerged into the beaker to irradiate the dispersion. A small quantity (2 mL) of the dispersion was taken every 1 h. It was centrifuged and filtered by filter paper, followed by UV-Vis spectrophotometry. UV-Vis spectrophotometry was conducted at a scan rate of 240 nm min⁻¹ and a data interval of 2 nm.

2.2.10. Membrane surface analysis.

Scanning Electron Microscopy (SEM, FEI Versa 3D DualBeam) was utilized to study the surface porosity and texture of the N-TiO₂/F-SiO₂ coated membrane. An accelerating voltage of 10 kV was utilized. All surfaces were sputter-coated with a gold layer (\approx 4-5 nm) to prevent the charging effect.

2.2.11. Visible light intensity measurement.

A photometer (Fisherbrand Traceable DualDisplay Lightmeter) was utilized to measure the intensity of the incident visible light on the membrane surface. The photometer was placed underneath the top cover of the cross-flow cell and irradiated by the visible light source from the

same distance (≈ 5 cm) at which the membrane was irradiated during the separation and desalination.

2.2.12. Salt and oil concentration measurements.

We determined the salt concentration in the water-rich permeate by calculating the electrical conductivity of the permeate and compared the value with the calibration curve. Two probes (1 cm² each) of a multimeter (Gardner Bender GDT-3190) at a distance of 2 cm were submerged in the permeate (20 mL). The multimeter measures the electrical resistance (R), which is converted to electrical resistivity. Subsequently, the inverse of electrical resistivity yields the electrical conductivity (κ). We determined the oil concentration by utilizing thermogravimetric analyses (TGA, PerkinElmer PYRIS 1). Approximately 10 mg of the water-rich permeate was heated from room temperature (≈ 22 °C) to 110 °C at a rate of 5 °C min⁻¹, followed by maintaining at 110 °C for 50 minutes.

2.2.13. Engineering a continuous separation and desalination apparatus.

We engineered a continuous separation and desalination apparatus consisting of a cross-flow cell (CF042A, Sterlitech), a feed storage tank, a pump (2SF22SEEL, WEG industries), a differential pressure gauge (OMEGA DPG409-500DWU), a visible light source, and a permeate tank. The membrane with an effective surface area of ≈ 42 cm² was sandwiched in between two transparent acrylic counterparts of the cross-flow cell. The membrane surface was irradiated by visible light with varying intensities.

2.3. Results and discussion

2.3.1. Synthesis of N-TiO₂ and characterization of its photocatalysis upon visible light irradiation.

To fabricate a visible-light-responsive photocatalytic coating with selective wettability (i.e., hydrophilic and oleophobic), we utilized a mixture of nitrogen-doped titanium dioxide (N-TiO₂) and perfluoro silane-grafted silica (F-SiO₂) nanoparticles. N-TiO₂ can degrade organic substances when it is exposed to visible light irradiation³⁹ and exhibit hydrophilic wettability⁴⁰, while F-SiO₂ can lower the overall surface free energy (γ_{sv})⁴¹. We hypothesized that an optimal balance of N-TiO₂ and F-SiO₂ can result in hydrophilic and oleophobic wettability.

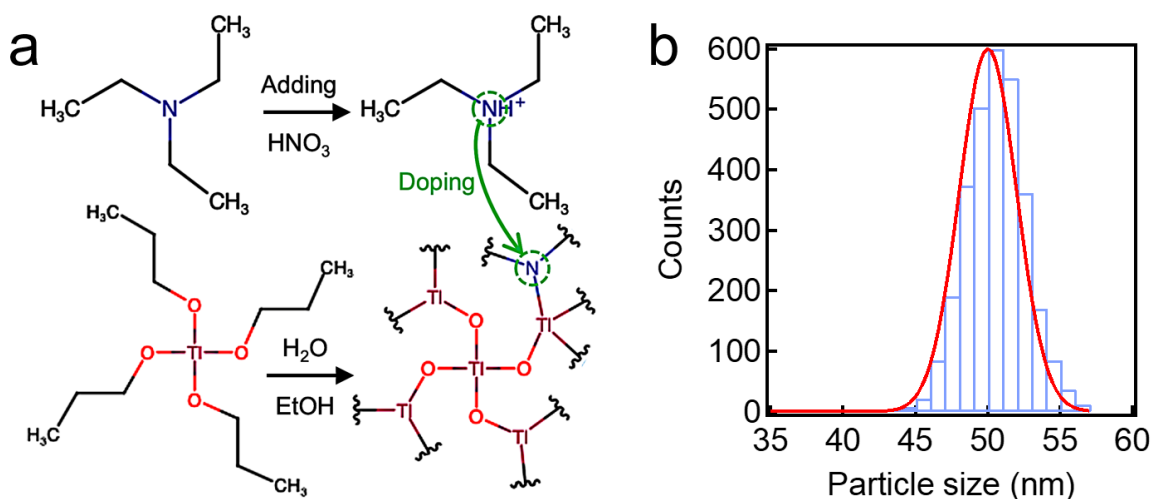


Figure 2.1. (a) Schematic illustrating the synthesis of N-TiO₂ nanoparticles by utilizing titanium butoxide (TBOT) and triethylamine (TEA) as TiO₂ precursor and nitrogen dopant, respectively. (b) A number size distribution of N-TiO₂ nanoparticles obtained by utilizing the DLS method.

To verify this hypothesis, we first synthesized N-TiO₂ nanoparticles by utilizing the sol-gel method⁴² (further described in the **Experimental procedure**). Triethylamine (TEA) and titanium butoxide (TBOT) were used as a nitrogen dopant and a TiO₂ precursor (**Figure 2.1a**). Hydrolysis of TBOT (concentration = 0.5 wt%) in an acidic solution (pH \approx 2.0) that was dissolved with TEA (concentration = 0.3 wt%) resulted in N-TiO₂ nanoparticles with an average diameter of 50 nm \pm

1 nm (**Figure 2.1b**). During this reaction, TEA introduces nitrogen (e.g., elemental nitrogen or complex nitrogen species such as NO, NO₂, and NH) into the TiO₂ lattice⁴³. X-ray photoelectron spectroscopy (XPS) spectra demonstrate a peak at a binding energy of ≈ 399.2 eV, which indicates the presence of anionic nitrogen from the O-Ti-N bond⁴², while a neat TiO₂ lacks such a peak (**Figure 2.2a**).

X-ray diffraction (XRD) patterns were utilized to determine the crystal structure of N-TiO₂ nanoparticles (**Figure 2.2b**). The characteristic peaks at $2\theta = 25.27^\circ, 37.94^\circ, 48.16^\circ, 54.07^\circ, 55.12^\circ, 62.73^\circ, 69.06^\circ, 70.65^\circ,$ and 75.33° correspond to the anatase phase with lattice planes (101), (103), (200), (105), (211), (204), (116), (220), and (107), respectively. Nitrogen doping resulted in a slight decrease in the intensity of these peaks (i.e., broadening). This can be attributed to the alteration in the crystallite size. Note that doping with nitrogen did not cause any phase transformation.

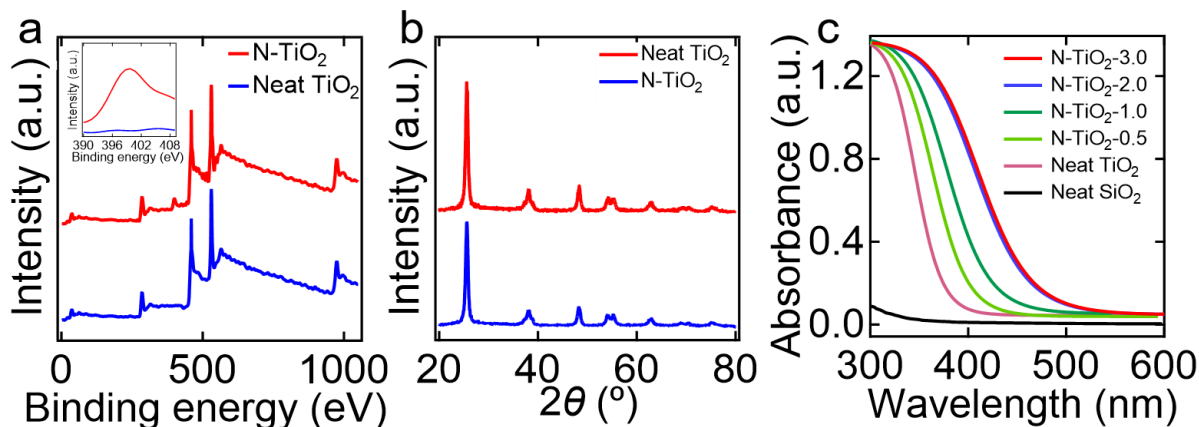


Figure 2.2. (a) The XPS spectrum of N-TiO₂ exhibiting characteristic peaks of N 1s, Ti 2p, and O 1s. The spectrum of a neat TiO₂ is also shown for comparison. Inset shows the core level spectrum of characteristic N 1s. (b) XRD pattern of N-TiO₂ synthesized by using a molar ratio of TEA and TBOT as 2.0. The XRD pattern of a neat TiO₂ is also shown. (c) Ultraviolet-visible (UV-Vis) absorption spectra of N-TiO₂ synthesized by varied molar ratios of TEA to TBOT (e.g., 0.5, 1.0, 2.0, and 3.0). Neat TiO₂ and SiO₂ absorption spectra are also shown for comparison.

Doping with nitrogen can narrow the bandgap energy of the TiO₂, which may extend the absorption spectra further toward the visible light region (i.e., $390 \text{ nm} < \lambda < 750 \text{ nm}$)⁴⁴. The ultraviolet-visible

(UV-Vis) spectrophotometry data verified that N-TiO₂ absorbs a broad range of the visible light spectrum, whereas neat TiO₂ and SiO₂ showed negligible absorption (**Figure 1c**). Furthermore, the results showed that the N-TiO₂ fabricated with a higher molar ratio of TEA to TBOT (i.e., higher dopant concentration) tended to exhibit stronger absorbance in the range of wavelengths from 390 nm to 750 nm. However, once the molar ratio exceeds 2.0, this will have a negligible effect on the absorbance of the resulting N-TiO₂. Thus, we utilized a molar ratio of TEA to TBOT of 2.0 (hereafter denoted as N-TiO₂) in this study.

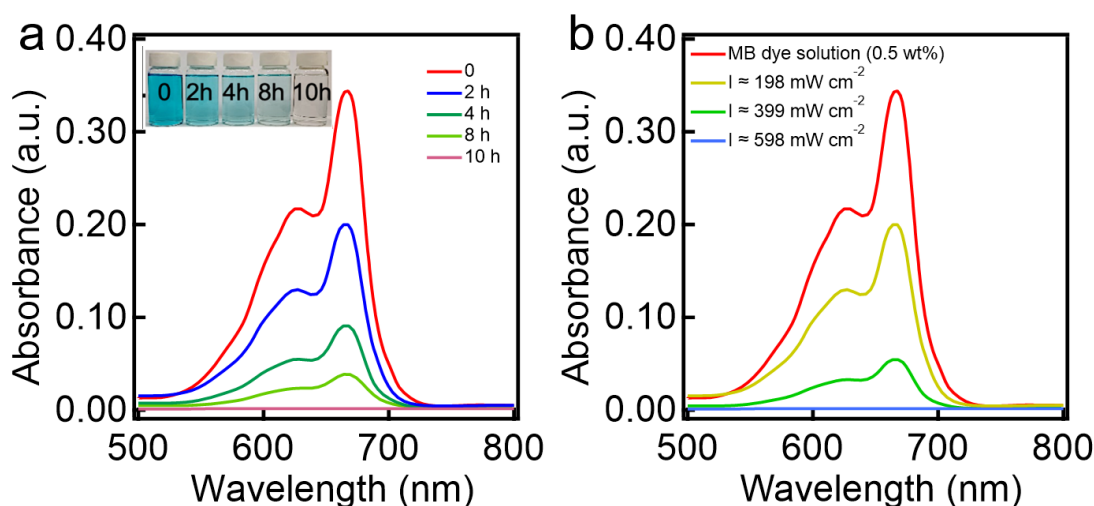


Figure 2.3. (a) UV-Vis absorption spectra of water dissolved with N-TiO₂ and Solvent Blue dye as a function of visible light irradiation time. Inset: A photograph showing the water dissolved with Solvent Blue dye after visible light irradiation for 2 h, 4 h, 8 h, and 10 h. The as-prepared water dissolved with Solvent Blue dye (concentration = 0.5 wt%) is also shown. (b) UV-Vis absorption spectra of water solutions dissolved with Solvent Blue 38 dye (concentration = 0.5 wt%) and N-TiO₂ (concentration = 0.5 wt%) after 2h of visible light irradiation with varied intensity. The UV-Vis absorption spectra of water solution dissolved with Solvent Blue 38 dye (concentration = 0.5 wt%) and N-TiO₂ (concentration = 0.5 wt%) after 10h in dark is also provided.

Given that the resulting N-TiO₂ exhibits a photocatalytic anatase crystalline phase, we demonstrated that it could degrade organic substances upon visible light irradiation. **Figure 2.3a** presents the time-dependent degeneration of the absorbance for water dissolved with organic dye (Solvent Blue 38, concentration = 0.5 wt%) and N-TiO₂ (concentration = 0.5 wt%). The light intensity (I) was maintained at $I \approx 198 \text{ mW cm}^{-2}$ (See **Experimental procedure**). The water

solution became nearly colorless after 10 hours of irradiation, indicating that almost all of the dye molecules were degraded. Please note that the dye molecules degraded more rapidly when placed under higher intensity light (**Figure 2.3b**).

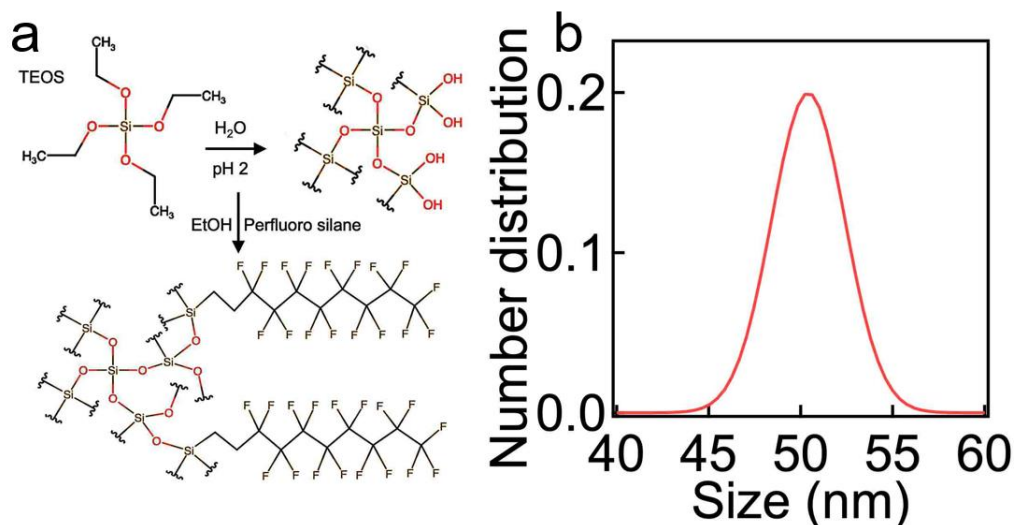


Figure 2.4. (a) Schematic illustrating the synthesis of F-SiO₂ nanoparticles by utilizing tetraethyl orthosilicate (TEOS) as SiO₂ precursor and 1H,1H,2H,2H-perfluorodecyl trichlorosilane (i.e., perfluoro silane). (b) A number size distribution of F-SiO₂ nanoparticles obtained by utilizing the DLS method.

Figure 2.4a demonstrates the synthesis of silica nanoparticles with low surface energy (F-SiO₂) by hydrolysis of tetraethyl orthosilicate (TEOS) followed by grafting of 1H,1H,2H,2H-perfluorodecyl trichlorosilane (i.e., perfluoro silane) (See also **Experimental procedure**). We determined the size distributions of F-SiO₂ nanoparticles by utilizing the DLS method. The DLS data revealed that the average size of F-SiO₂ nanoparticles is 50 nm ± 2 nm (**Figure 2.4b**). It is worth noting that the average size of F-SiO₂ nanoparticles is very close to that of N-TiO₂ nanoparticles (See **Figure 2.1b**). This is critical to ensure that the N-TiO₂/F-SiO₂ mixture forms a homogeneous and uniform coating on the membrane surface.

2.3.2. Fabrication and characterization of N-TiO₂/F-SiO₂ coated membrane.

Figure 2.5 shows a schematic illustrating the overall process of membrane fabrication. By utilizing N-TiO₂ and F-SiO₂ nanoparticles, we created a photocatalytic membrane with hydrophilic and

oleophobic wettability both in air and saline water. A commercial filter (TRISEP ACM5) was utilized as a membrane on which our visible light-responsive photocatalytic coating with selective wettability was applied. Please note that the TRISEP ACM5 was chosen because of its applicability to a wide range of separation processes⁴⁵. First, we spin-coated the membrane surface with a thiol-ene-based UV-curable adhesive. Immediately following this step, a solution of N-TiO₂ and F-SiO₂ (i.e., N-TiO₂/F-SiO₂) (concentration = 10 wt%, **Experimental procedure**) was sprayed for one minute. Then, the membrane was irradiated with UV light ($\lambda = 365$ nm, Intensity ≈ 78 mW cm⁻²) for five minutes at room temperature (≈ 22 °C) to cure the adhesive. Please note that we varied the concentrations of N-TiO₂/F-SiO₂ (e.g., 0, 20 wt%, 40 wt%, 60 wt%, 80 wt%, and 100 wt%).

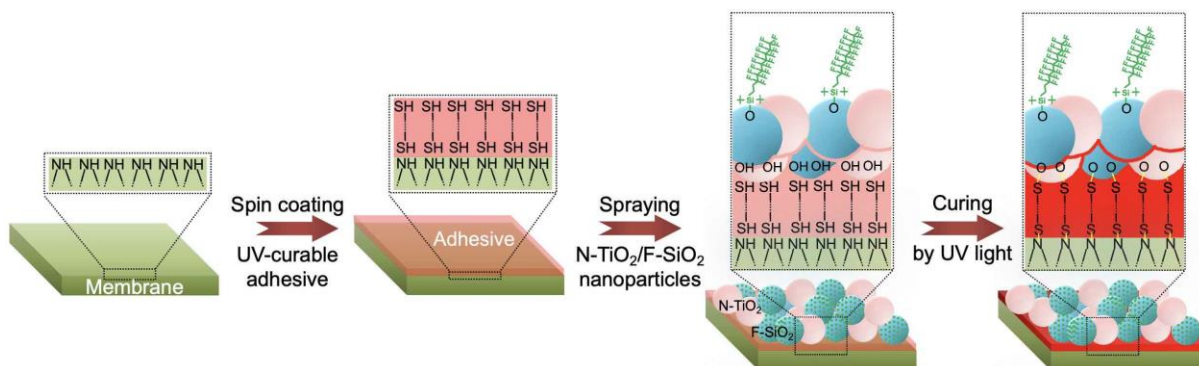


Figure 2.5. Schematic illustrating the fabrication of photocatalytic membrane with hydrophilic and oleophobic wettability. A commercial filter is coated with an ultraviolet (UV) light-curable adhesive followed by sprayed with a mixture of N-TiO₂ and F-SiO₂ nanoparticles. The membrane was placed under UV light for curing.

The resulting membrane's surface is covered with N-TiO₂/F-SiO₂ coating possessing a hierarchical roughness with a re-entrant texture (**Figure 2.6a** and the inset image). We measured the advancing (θ^*_{adv}) and receding (θ^*_{rec}) contact angles for saline water (1.0 wt% NaCl in DI water, $\gamma_{lv} = 72.1$ mN m⁻¹) and oil (n-hexadecane, $\gamma_{lv} = 27.5$ mN m⁻¹) in air (**Figure 2.6b**). The results indicated that a membrane coated with N-TiO₂/F-SiO₂ with a lower N-TiO₂ concentration exhibited higher

contact angles for both saline water and oil. We found that when the N-TiO₂ concentration reached 60 wt%, the contact angle for saline water became zero (i.e., $\theta^*_{\text{saline water, adv (in-air)}} = 0^\circ$ and $\theta^*_{\text{saline water, rec (in-air)}} = 0^\circ$) while that for oil remained constant ($\theta^*_{\text{oil, adv (in-air)}} = 95^\circ \pm 4^\circ$, $\theta^*_{\text{oil, rec (in-air)}} = 61^\circ \pm 3^\circ$). Further increases in the N-TiO₂ concentrations resulted in sharp decreases in contact angles for oil.

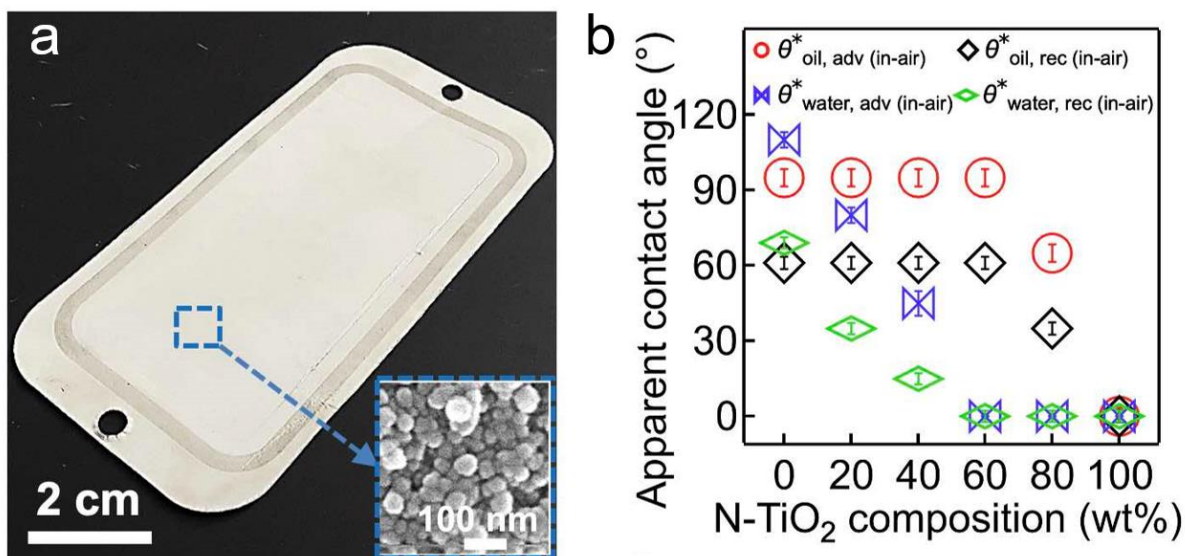


Figure 2.6. (a) A photograph showing a commercial filter coated with N-TiO₂/F-SiO₂ (60 wt%). Inset: Scanning electron microscopy (SEM) image of the membrane surface showing a hierarchical roughness with a re-entrant texture. (b) The measured in-air advancing and receding apparent contact angles for saline water (1.0 wt% NaCl in DI water) and oil (n-hexadecane) on the membrane surface coated with N-TiO₂/F-SiO₂ with varied compositions.

Given that membrane operations in real-world applications often result in continuous immersion in liquids (e.g., water), we also measured the contact angles for oil on the membrane surface submerged in saline water (**Figure 2.7a**). The results indicated that a membrane with a lower in-air water contact angle is likely to have a higher oil contact angle when submerged in saline water. For example, a membrane coated with N-TiO₂/F-SiO₂ of 60 wt% N-TiO₂ (i.e., N-TiO₂/F-SiO₂ (60 wt%)) exhibited $\theta^*_{\text{oil, adv (under saline water)}} = 175^\circ \pm 3^\circ$ and $\theta^*_{\text{oil, rec (under saline water)}} = 171^\circ \pm 2^\circ$, while the one coated with N-TiO₂/F-SiO₂ (20 wt%) exhibited $\theta^*_{\text{oil, adv (under saline water)}} = 169^\circ \pm 2^\circ$ and $\theta^*_{\text{oil, rec}}$

(under saline water) = $161^\circ \pm 3^\circ$. The results can be further corroborated by analyzing the adhesion force of an oil droplet (n-hexadecane) placed on the membrane surface that was submerged in saline water⁴⁶ (**Figure 2.7a**). The adhesion force was 1.1 ± 0.3 mN on a membrane coated with N-TiO₂/F-SiO₂ (60 wt%) and 1.7 ± 0.4 mN on a membrane coated with N-TiO₂/F-SiO₂ (20 wt%).

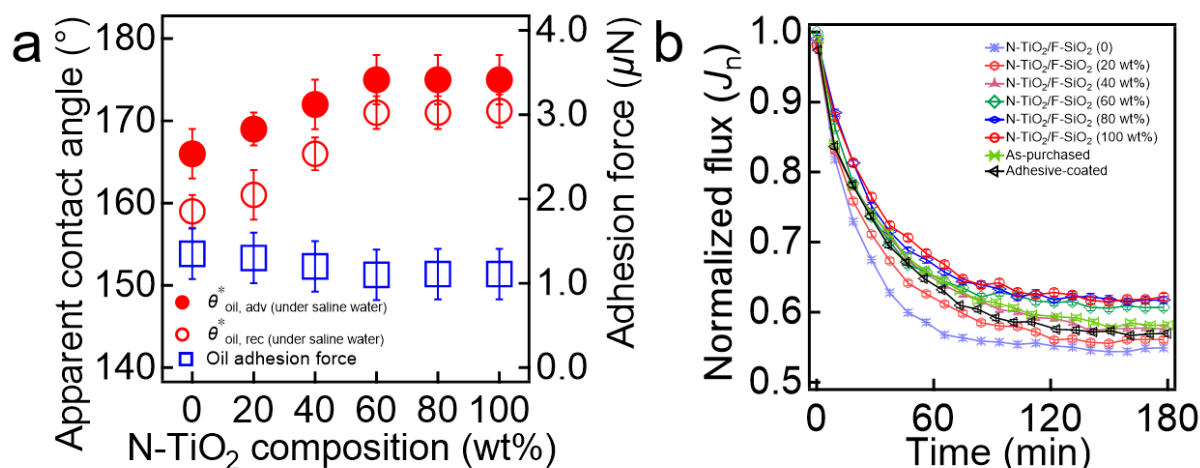


Figure 2.7. (a) The measured advancing and receding apparent contact angles, as well as adhesion force for an oil droplet (n-hexadecane) on the membrane surface coated with N-TiO₂/F-SiO₂ with varied compositions submerged in saline water. (b) The normalized flux (J_n) of the permeate through the membranes coated with N-TiO₂/F-SiO₂ with varied compositions. The data for the as-purchased commercial filter and that for the one coated only with cured adhesive is also provided for comparison.

The membrane's wettability for saline water can affect the flux because it determines the breakthrough pressure (i.e., the maximum pressure difference across the membrane that is required for a liquid to permeate through it)⁴⁷. We measured the flux of saline water (1.0 wt% NaCl in DI water) through the membranes coated with various concentrations of N-TiO₂/F-SiO₂. A total of 100 L of saline water was continuously fed for 180 minutes through the membrane, which was attached to a crossflow cell. We measured the volume of the permeate every 10 minutes. It must be noted that the transmembrane pressure (TMP, i.e., the pressure exerted across the membrane) was maintained at $\Delta p \approx 760$ kPa \pm 9 kPa. **Figure 2.7b** shows the normalized flux (J_n) of the

permeate, which is defined as J_t/J_0 , where $J_t = \Delta m/A\rho\Delta t\Delta p$. Here Δm represents the change in the permeate mass during a particular time interval (i.e., $\Delta t = 10$ minutes). A is the membrane's projected area ($A \approx 42 \text{ cm}^2$) and ρ is the density of the permeate ($\rho = 1000 \text{ kg m}^{-3}$). J_0 symbolizes the flux over the TMP value obtained during the first three minutes of submersion. While J_n gradually decreased and reached a constant value ($J_n \approx 0.59 \pm 0.04$) after approximately $t = 150$ minutes for all membranes, one coated with N-TiO₂/F-SiO₂ with a higher concentration of N-TiO₂ showed less of a decrease in the J_n value at $t = 150$ minutes. For example, a membrane coated with

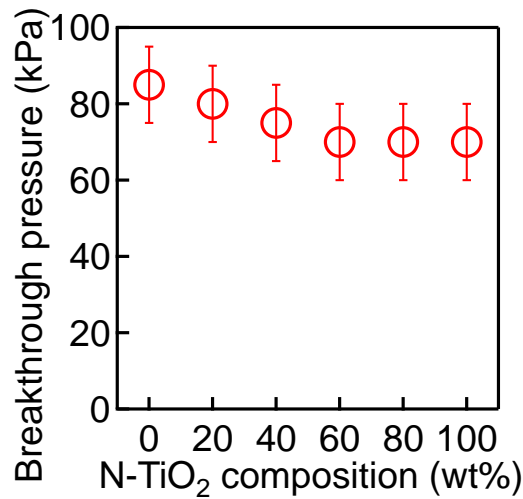


Figure 2.8. A plot of the measured breakthrough pressure for saline water (1.0 wt% NaCl in DI water) of the membranes coated with N-TiO₂/F-SiO₂ with varied compositions.

N-TiO₂/F-SiO₂ (60 wt%) yielded a J_n value of 0.61, whereas one coated with N-TiO₂/F-SiO₂ (20 wt%) showed a value of 0.56 at $t = 150$ minutes. This finding can be attributed to the difference in breakthrough pressure of saline water⁴⁷ (**Figure 2.8**). Please note that the as-purchased filter and the one coated only with the cured adhesive exhibited $J_n = 0.59$ and $J_n = 0.58$, respectively, at $t = 150$ minutes (**Figure 2.7b**). This clearly indicates that neither the cured adhesive nor the N-TiO₂/F-SiO₂ coating affects the membrane's flux.

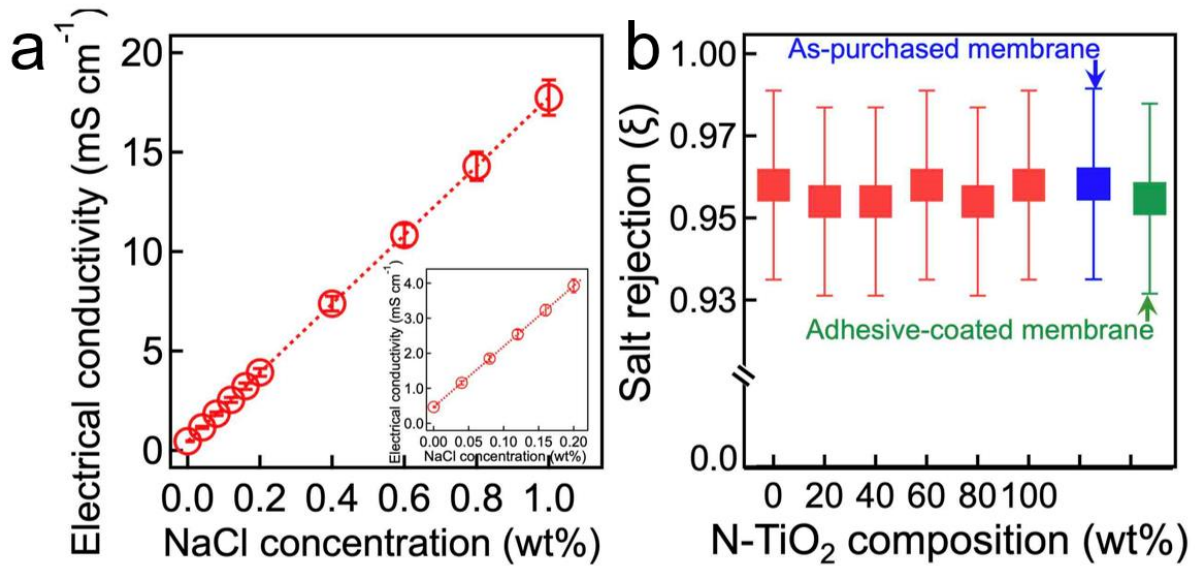


Figure 2.9. (a) The calibration curve established by calculating the electrical conductivity of water as a function of salt (NaCl) concentrations. Inset shows zoomed-in electrical conductivity data in the NaCl concentration range of 0.00-0.20 wt%. (b) The salt rejection (ξ) data of the membranes coated with N-TiO₂/F-SiO₂ with varied compositions. The data of the as-purchased commercial membrane and that coated only with cured adhesive are also provided for comparison.

We then measured the salt rejection (ξ) of the membranes coated with various concentrations of N-TiO₂/F-SiO₂. **Figure 2.9a** presents the calibration curve of the electrical conductivity of DI water as a function of NaCl concentrations. Here, we define the salt rejection as $\xi = 1 - \sigma_f/\sigma_o$, where σ_o and σ_f are the concentrations of salt in the feed of saline water (i.e., 1.0 wt%) and those in the permeate obtained in $t = 180$ minutes, respectively. By comparing the ξ values for the membranes coated with various compositions of N-TiO₂/F-SiO₂ with those of the as-purchased commercial membrane or those coated only with cured adhesive, we found that the N-TiO₂/F-SiO₂ had a negligible effect on salt rejection (**Figure 2.9b**).

High shear force by the feed stream exerted on the membranes often causes the delamination of the coating from the membrane surface. We evaluated the adhesion of N-TiO₂/F-SiO₂ to the commercial membrane surface by measuring the mass of the membranes after 180 minutes of continuous desalination of saline water (1.0 wt% NaCl in DI water) at a flow rate of 1.5 L min⁻¹ and compared the values with that of the as-prepared membranes. Here we utilized a high-precision balance (Mettler Toledo XS105 DU, precision = 0.010 ± 0.002 mg). The results show that the mass of the as-prepared membranes and those of the membranes after the test remained nearly unchanged (i.e., the mass loss < 0.1%, **Figure 2.10**). Here we define the mass loss (m_L) as $m_L = (1 - m_f/m_o) \times 100$, where m_o and m_f are the initial mass of the N-TiO₂/F-SiO₂ mixture coated to the membrane and that after subjecting the membrane to saline water, desalination for 180 minutes, respectively. This can be attributed to the cured adhesive, which can hold N-TiO₂ and F-SiO₂ nanoparticles together and securely bind them to the membrane surface by forming an interlocking structure between the nanoparticles and the membrane. In contrast, the membranes prepared without cured adhesive exhibited $\approx 89 \pm 2\%$ mass loss.

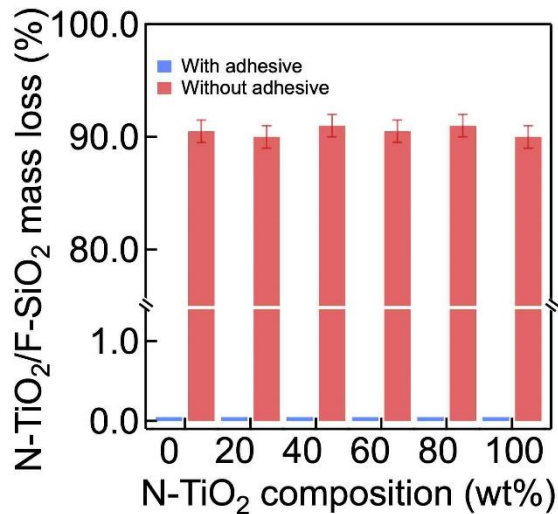


Figure 2.10. The mass loss of the membranes coated with N-TiO₂/F-SiO₂ with varied compositions after 180 minutes of desalination of saline water at a flow rate of 1.5 L min⁻¹. For comparison, the results obtained by utilizing the membranes without cured adhesive are also shown.

2.3.3. Continuous separation and desalination of an oil-saline water mixture and simultaneous photocatalytic degradation of organic foulants upon visible light irradiation.

The photocatalytic capability of our coating, in conjunction with its hydrophilic and oleophobic wettability both in air and under saline water, enables the membrane to separate and desalinate an oil-saline water mixture while simultaneously degrading the organic foulants adsorbed onto the membrane surface during exposure to visible light irradiation^{48, 49}. To demonstrate this, we mounted the membrane to an apparatus and irradiated it with visible light (**Figure 2.11**). The feed oil-saline water mixture was continuously fed to the cell while the water-rich permeate continuously passed through the membrane and collected in a permeate tank. Here we utilized an n-hexadecane-in-water emulsion (10:90 vol:vol, n-hexadecane:water) dissolved with salt (1.0 wt% NaCl with respect to water mass) that was stabilized by sodium dodecyl sulfate (SDS) (See **Experimental procedure**). We tested membranes coated with various concentrations of N-TiO₂/SiO₂. Of note, all membranes were prewetted by soaking them in saline water (1.0 wt% NaCl) for 150 minutes to obtain a constant flux over TMP (J_{prewet}) before being subjected to the feed emulsion.

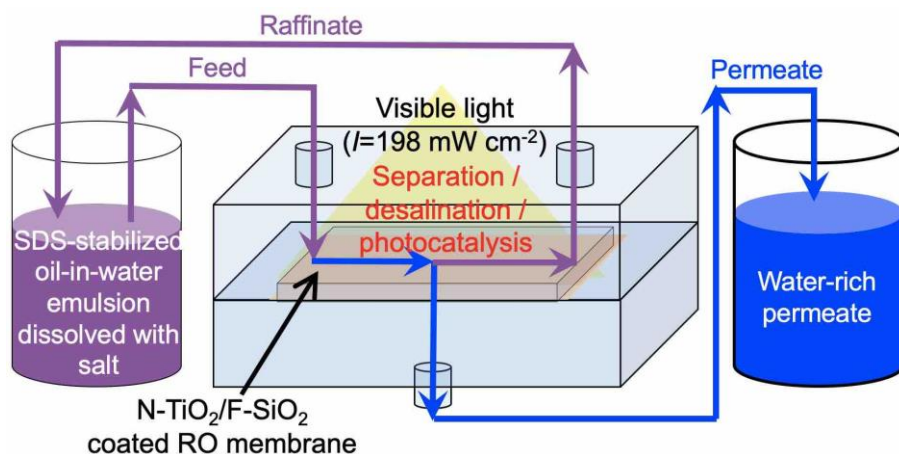


Figure 2.11. Schematic illustrating the cross-flow apparatus that enables continuous separation and desalination of an oil-saline water mixture and simultaneous photocatalytic degradation of organic foulants adsorbed onto the membrane surface upon visible light irradiation.

When the feed emulsion was introduced, the flux of the water-rich permeate began to rapidly decrease due to membrane fouling by oil (**Figure 2.12a** and **Table 2.1**). This is a consequence of oil adsorption to the membrane surface which can hamper the permeation of water and cause a rapid decline in the flux. Note that J_n is defined as J_t/J_{prewet} . According to our findings, an N-TiO₂/F-SiO₂-coated membrane with a higher N-TiO₂ composition exhibited a steeper decrease in flux. For example, when a membrane was coated with N-TiO₂/F-SiO₂ (80 wt%), $J_n \approx 0.17$ ($J_t \approx 0.0135 \text{ Lm}^{-2}\text{h}^{-1}\text{kPa}^{-1}$); however, when it was coated with N-TiO₂/F-SiO₂ (20 wt%), $J_n \approx 0.30$ ($J_t \approx 0.0163 \text{ Lm}^{-2}\text{h}^{-1}\text{kPa}^{-1}$) at $t = 180$ minutes. This can be primarily attributed to the fact that N-TiO₂ is more vulnerable to oil adsorption⁵⁰ while F-SiO₂ can repel it⁵¹. Note that such a rapid flux decline of membranes after the introduction of an oil-water mixture has been reported^{52, 53}.

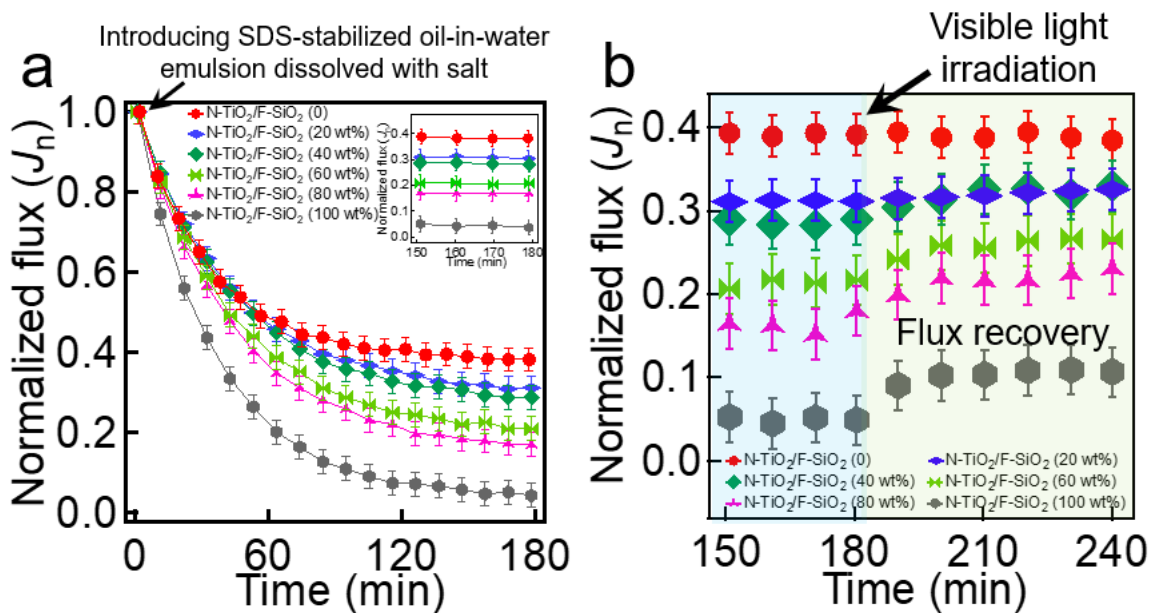


Figure 2.12. (a) The normalized flux (J_n) of the water-rich permeate through the membranes coated with N-TiO₂/F-SiO₂ with varied compositions that are subjected to sodium dodecyl sulfate (SDS)-stabilized n-hexadecane-in-water emulsion (10:90 vol:vol, n-hexadecane:water) dissolved with salt (1.0 wt% NaCl with respect to water mass). (b) The normalized flux (J_n) of the water-rich permeate through the membranes being irradiated by visible light ($I \approx 198 \text{ mW cm}^{-2}$).

When the water-rich permeate flux reached a constant value at $t = 180$ minutes, we began to irradiate the membrane surface with visible light ($I \approx 198 \text{ mW cm}^{-2}$) to induce photocatalytic degradation of the surface adsorbed oil. This is a result of electron-hole (e^-h^+) pairs generated upon light irradiation with an energy greater than the bandgap energy of a photocatalyst (e.g., N-TiO₂)⁵⁴. The electrons and holes can react with the ambient molecules (e.g., oxygen or water) and generate reactive radicals such as hydroxyl, which can remove organic contaminants such as oil by chemical oxidation (or reduction)³¹. The membrane was then continuously subjected to a fresh feed emulsion. We observed that a membrane coated with N-TiO₂/F-SiO₂ with a higher concentration of N-TiO₂ caused a more significant increase in the J_n value, which is a direct result of the photocatalysis-driven recovery of the clean membrane surface that exhibits a lower breakthrough pressure for saline water (**Figure 2.12b** and **Table 2.2**). For example, a membrane coated with N-TiO₂/F-SiO₂ (80 wt%) showed $J_n \approx 0.24$ ($J_t \approx 0.0190 \text{ Lm}^{-2}\text{h}^{-1}\text{kPa}^{-1}$) while that coated with N-TiO₂/F-SiO₂ (20 wt%) exhibited $J_n \approx 0.31$ ($J_t \approx 0.0174 \text{ Lm}^{-2}\text{h}^{-1}\text{kPa}^{-1}$) after 60 minutes of irradiation.

While an in situ photocatalysis-driven recoveries of the clean membrane surface is presented in this work, a majority of previous studies have demonstrated it ex-situ. For example, Zhang et al.³³ synthesized an electrospun membrane-anchored with photocatalytic β -FeOOH nanorods. The membrane demonstrated that it could photocatalytically degrade the surface adsorbed organic matter and recover its flux upon a visible light after 40 minutes. Peyravi et al.⁵⁵ incorporated photocatalytic TiO₂/zeolite into a composite membrane and demonstrated $\approx 83.6\%$ flux recovery under UV irradiation. Liu et al.³⁴ fabricated a membrane utilizing TiO₂/carbon nitride nanosheets and showed membrane surface cleaning with a flux recovery ratio of $>95\%$. Also, Kovács et al.⁵⁶ demonstrated that a TiO₂-coated ultrafiltration membrane could almost completely recover its

original flux after 1 hour of UV irradiation. Further, Xie et al.⁵⁷ fabricated a photocatalytic membrane using β -FeOOH, which demonstrated >98% of flux recovery within 10 minutes under visible light.

2.3.4. Robustness of the membrane

2.3.4.1. Determining the oil concentration in the water-rich permeate

Although our membranes are fouled by oil during the separation of the oil-saline water mixture, we showed that the oil concentration in the water-rich permeate remained very low. We determined the oil concentration by utilizing thermogravimetric analyses (TGA, PerkinElmer PYRIS 1). Approximately 10 mg of the water-rich permeate was heated from room temperature ($\approx 22\text{ }^\circ\text{C}$) to $110\text{ }^\circ\text{C}$ at a rate of $5\text{ }^\circ\text{C min}^{-1}$, followed by maintaining at $110\text{ }^\circ\text{C}$ for 50 minutes. Given that the boiling points of water and oil (n-hexadecane) are $100\text{ }^\circ\text{C}$ and $\approx 287\text{ }^\circ\text{C}$, respectively, the sample remaining after TGA can be assumed as pure oil. **Figure 2.13** shows the TGA data of the water-rich permeate through the membranes coated with N-TiO₂/F-SiO₂ with varied compositions. The

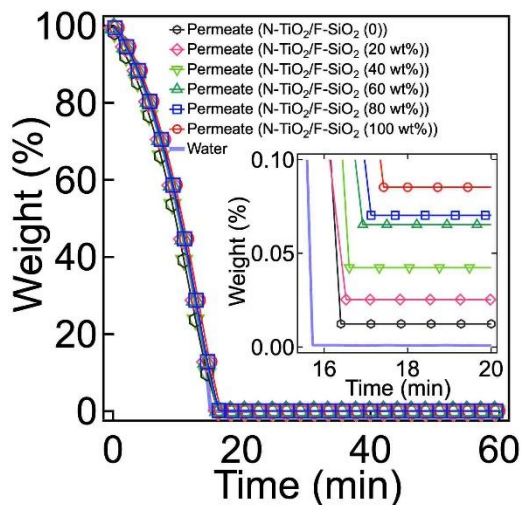


Figure 2.13. The TGA data of the water-rich permeates after the separation of SDS-stabilized oil-in-water emulsion dissolved with NaCl (1.0 wt% with respect to water mass) through the membranes coated N-TiO₂/F-SiO₂ with varied compositions.

results indicate that the concentrations of oil in the water-rich permeates are very low (i.e., < 0.1 wt%). This can be attributed to the membranes' extremely low permeability.

2.3.4.2. Effect of photocatalytic degradation reaction on the F-SiO₂.

We also measured the contact angles for oil and saline water after 60 minutes of visible light irradiation and found that they remained unchanged (**Figure 2.14a**). We attribute this to the fact that the membrane's surface chemistry remained unchanged. **Figure 2.14b** presents the FT-IR spectra of a membrane's surface coated with N-TiO₂/F-SiO₂ (60 wt%) after 120 minutes of visible light irradiation ($I \approx 198 \text{ mW cm}^{-2}$). By comparing it with that of the as-prepared membrane, we can verify that the surface chemistry remains unaffected. Particularly, the absorption peaks in the range of $\approx 1100 \text{ cm}^{-1}$ to $\approx 1400 \text{ cm}^{-1}$ which correspond to C-F in perfluoro silane, remained nearly unchanged.

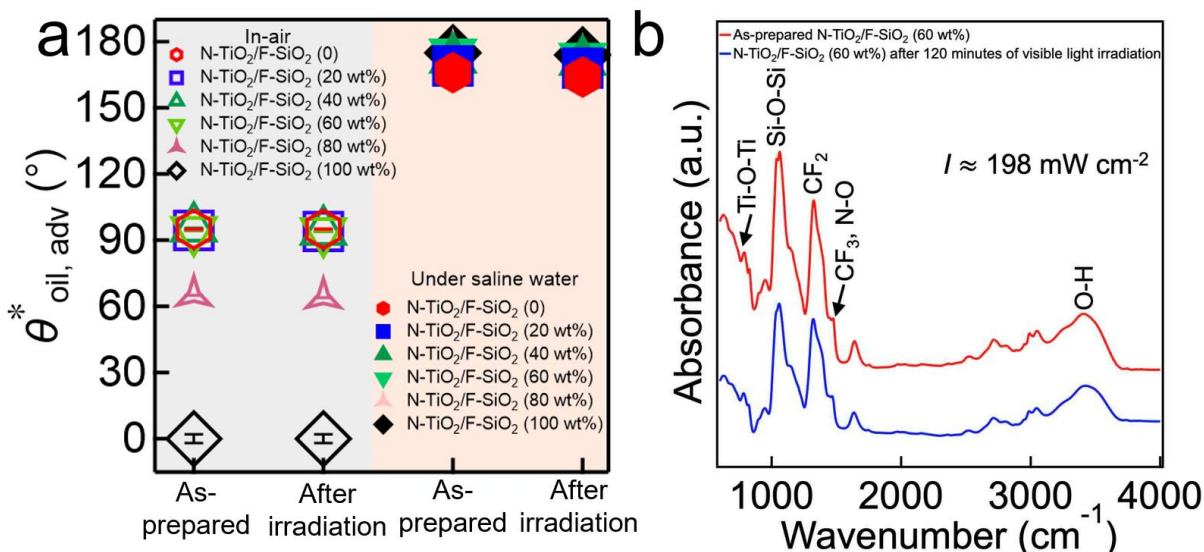


Figure 2.14. (a) The apparent contact angles for oil (n-hexadecane) droplet on the membranes in air and under saline water before and after visible light irradiation for 120 minutes. The data of the as-prepared membranes are also shown for comparison. (b) The FT-IR spectra of a membrane surface coated with N-TiO₂/F-SiO₂ (60 wt%) after 120 minutes of visible light irradiation with an intensity of 198 mW cm^{-2} . For comparison, the FT-IR spectra of the as-prepared membrane surface is shown.

2.3.4.3. The cured adhesive layer and salt rejection after visible-light-driven photocatalysis

We verified that the cured adhesive (Norland Optical Adhesive 61) remains unaffected after visible-light-driven photocatalysis on the membrane surface. We conducted FT-IR measurements by utilizing PerkinElmer Spectrum 400 FT-IR Spectrometer in attenuated total reflectance (ATR) mode. The FT-IR spectra were recorded at a resolution of 4 cm^{-1} for 16 scans. A sample was prepared by mixing adhesive and N-TiO₂ with a 1:1 weight ratio in acetone (solute concentration = 1.0 wt%), followed by casting the mixture on a polytetrafluoroethylene (PTFE) substrate. Then, the film was cured by UV light ($\lambda = 365\text{ nm}$, $I \approx 78\text{ mW cm}^{-2}$) for 5 minutes at room temperature ($\approx 22\text{ }^\circ\text{C}$). Finally, the film was detached from the substrate and ground for FT-IR measurements. The survey spectra of the adhesive after 180 minutes of visible light irradiation ($I \approx 198\text{ mW cm}^{-2}$) are shown in **Figure 2.15a**. Note that the spectra of neat N-TiO₂ were set as the background. By comparing the survey spectra with that of the as-prepared adhesive, we found that the absorption peaks underwent negligible alterations after visible-light-driven photocatalysis.

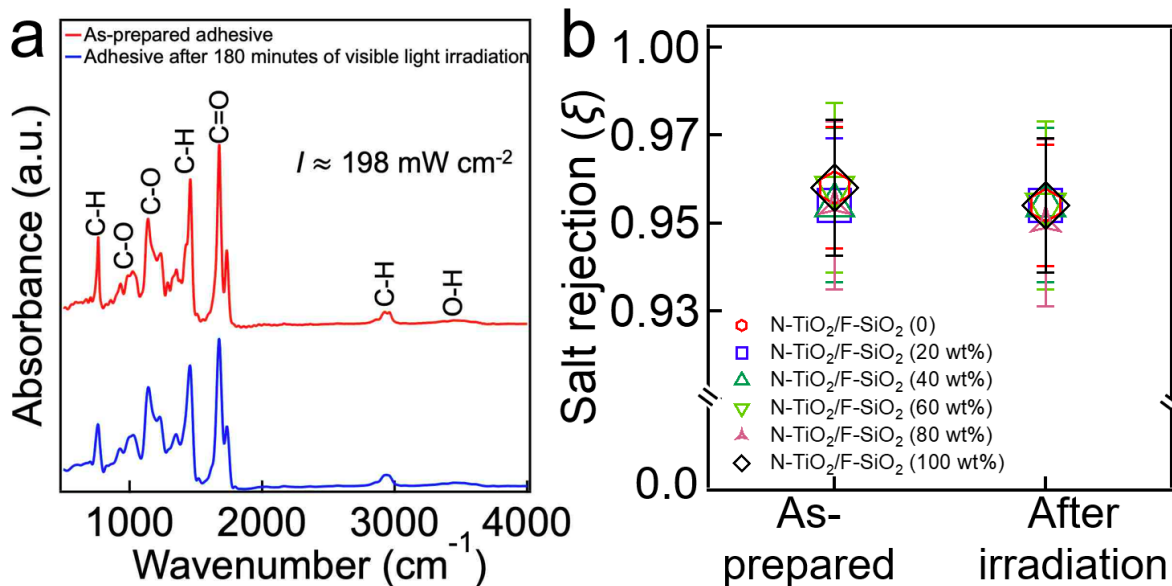


Figure 2.15. (a) The FT-IR spectra of the cured adhesive after 180 minutes of visible light-driven photocatalysis by N-TiO₂ ($I \approx 198\text{ mW cm}^{-2}$). For comparison, the FT-IR spectra of the as-prepared adhesive is also shown. (b) The salt rejection (ξ) of the membranes coated with N-TiO₂/F-SiO₂ with varied compositions after exposure to 60 minutes of visible light irradiation.

Table 2.1. The values of the flux of the water-rich permeate through the membranes coated with N-TiO₂/F-SiO₂ with varied compositions that are subjected to sodium dodecyl sulfate (SDS)-stabilized n-hexadecane-in-water emulsion (10:90 vol: vol, n-hexadecane: water) dissolved with salt (1.0 wt% NaCl with respect to water mass).

N-TiO₂/F-SiO₂ compositions	Flux at t = 0 (J₀, Lm⁻²h⁻¹kPa⁻¹)	Flux at t = 180 minutes (J_t, Lm⁻²h⁻¹kPa⁻¹)
N-TiO ₂ /F-SiO ₂ (0)	0.0467	0.0177
N-TiO ₂ /F-SiO ₂ (20 wt%)	0.0547	0.0163
N-TiO ₂ /F-SiO ₂ (40 wt%)	0.0627	0.0174
N-TiO ₂ /F-SiO ₂ (60 wt%)	0.0786	0.0157
N-TiO ₂ /F-SiO ₂ (80 wt%)	0.0826	0.0135
N-TiO ₂ /F-SiO ₂ (100 wt%)	0.0826	0.0033

Table 2.2. The values of the flux of the water-rich permeate through the membranes coated with N-TiO₂/F-SiO₂ with varied compositions after 60 minutes of irradiation of visible light ($I \approx 198$ mW cm⁻²)

N-TiO₂/F-SiO₂ compositions	Flux at t = 180 minutes (before irradiation, Lm⁻²h⁻¹kPa⁻¹)	Flux at t = 240 minutes (after 60 minutes irradiation, Lm⁻²h⁻¹kPa⁻¹)
N-TiO ₂ /F-SiO ₂ (0)	0.0177	0.0177
N-TiO ₂ /F-SiO ₂ (20 wt%)	0.0163	0.0174
N-TiO ₂ /F-SiO ₂ (40 wt%)	0.0174	0.0200
N-TiO ₂ /F-SiO ₂ (60 wt%)	0.0157	0.0212
N-TiO ₂ /F-SiO ₂ (80 wt%)	0.0135	0.0190
N-TiO ₂ /F-SiO ₂ (100 wt%)	0.0033	0.0090

The salt rejection (ζ) of the membranes coated with various concentrations of N-TiO₂/F-SiO₂ was measured after 60 minutes of visible light irradiation. The salt rejection remained almost constant (**Figure 2.15b**). We attribute this to the cured adhesive layer, which protected the commercial

membrane's active layer (e.g., polyamide) from a reactive radical species that was generated from exposure to visible light irradiation.

2.4. Conclusions

In summary, we have developed a photocatalytic coating with hydrophilic and oleophobic wettability by intercalating a mixture of visible light-responsive N-TiO₂ and low surface energy F-SiO₂ nanoparticles. We tested the feasibility of our coating in membranes by spraying it on a commercial membrane surface with UV-curable adhesive. Subsequent irradiation of UV light resulted in a chemically heterogeneous surface with intercalating high surface energy (N-TiO₂) and low surface energy (F-SiO₂) regions that are securely bound to the surface. Our membrane can recover the flux upon visible light irradiation. We attributed this to the photocatalytic degradation of the surface adsorbed oil when placed under visible light irradiation. Such photocatalytic degradation did not compromise the wettability or integrity of the membrane due to the robust chemistry of the adhesive. We engineered an apparatus that enabled the continuous separation and desalination of a surfactant-stabilized oil-in-water emulsion that was dissolved with salt and the photocatalytic degradation of organic substances that were adsorbed on the coated membrane surface when it was exposed to visible light irradiation. It was found that the coated membrane was able to recover its permeate flux *in situ* when placed under visible light irradiation. We envision that our membrane will have a wide range of practical applications, including wastewater treatment, fuel purification, and desalinating brackish water.

2.5. References

1. Eseev, M.; Goshev, A.; Kapustin, S.; Tsykareva, Y., Creation of Superhydrophobic Coatings Based on MWCNTs Xerogel. *Nanomaterials* **2019**, *9* (11), 1584.
2. Dong, S.; Wang, Z.; An, L.; Li, Y.; Wang, B.; Ji, H.; Wang, H., Facile Fabrication of a Superhydrophobic Surface with Robust Micro-/Nanoscale Hierarchical Structures on Titanium Substrate. *Nanomaterials* **2020**, *10* (8), 1509.
3. Li, J.; Qin, Q. H.; Shah, A.; Ras, R. H.; Tian, X.; Jokinen, V., Oil droplet self-transportation on oleophobic surfaces. *Sci. Adv.* **2016**, *2* (6), e1600148.
4. Geng, H.; Bai, H.; Fan, Y.; Wang, S.; Ba, T.; Yu, C.; Cao, M.; Jiang, L., Unidirectional water delivery on a superhydrophilic surface with two-dimensional asymmetrical wettability barriers. *Materials Horizons* **2018**, *5* (2), 303-308.
5. Lv, J.; Gong, Z.; He, Z.; Yang, J.; Chen, Y.; Tang, C.; Liu, Y.; Fan, M.; Lau, W.-M., 3D printing of a mechanically durable superhydrophobic porous membrane for oil–water separation. *J. Mater. Chem. A* **2017**, *5* (24), 12435-12444.
6. Sun, S.; Zhu, L.; Liu, X.; Wu, L.; Dai, K.; Liu, C.; Shen, C.; Guo, X.; Zheng, G.; Guo, Z., Superhydrophobic shish-kebab membrane with self-cleaning and oil/water separation properties. *ACS Sustainable Chem. Eng.* **2018**, *6* (8), 9866-9875.
7. Kwon, G.; Post, E.; Tuteja, A., Membranes with selective wettability for the separation of oil-water mixtures. *MRS Communications* **2015**, *5* (3), 475-494.
8. Law, K. Y.; Zhao, H., *Surface Wetting: Characterization, Contact Angle, and Fundamentals*. Springer International Publishing: 2015.
9. Ezazi, M.; Shrestha, B.; Klein, N.; Lee, D. H.; Seo, S.; Kwon, G., Self-healable superomniphobic surfaces for corrosion protection. *ACS Appl. Mater. Interfaces* **2019**, *11* (33), 30240-30246.
10. Kota, A. K.; Kwon, G.; Tuteja, A., The design and applications of superomniphobic surfaces. *NPG Asia Mater.* **2014**, *6* (7), e109.
11. Vahabi, H.; Wang, W.; Popat, K. C.; Kwon, G.; Holland, T. B.; Kota, A. K., Metallic superhydrophobic surfaces via thermal sensitization. *Appl. Phys. Lett.* **2017**, *110* (25), 251602.
12. Brown, P. S.; Bhushan, B., Mechanically durable, superomniphobic coatings prepared by layer-by-layer technique for self-cleaning and anti-smudge. *J. Colloid Interface Sci.* **2015**, *456*, 210-218.
13. Moiz, A.; Padhye, R.; Wang, X., Durable superomniphobic surface on cotton fabrics via coating of silicone rubber and fluoropolymers. *Coatings* **2018**, *8* (3), 104.
14. Zhang, H.; Ji, X.; Liu, L.; Ren, J.; Tao, F.; Qiao, C., Versatile, mechanochemically robust, sprayed superomniphobic coating enabling low surface tension and high viscous organic liquid bouncing. *Chem. Eng. J.* **2020**, *402*, 126160.
15. Vilcnik, A.; Jerman, I.; Šurca Vuk, A.; Kozelj, M.; Orel, B.; Tomsic, B.; Simoncic, B.; Kovac, J., Structural properties and antibacterial effects of hydrophobic and oleophobic sol–gel coatings for cotton fabrics. *Langmuir* **2009**, *25* (10), 5869-5880.
16. Hayn, R. A.; Owens, J. R.; Boyer, S. A.; McDonald, R. S.; Lee, H. J., Preparation of highly hydrophobic and oleophobic textile surfaces using microwave-promoted silane coupling. *Journal of Materials Science* **2011**, *46* (8), 2503-2509.
17. Wang, W.; Salazar, J.; Vahabi, H.; Joshi - Imre, A.; Voit, W. E.; Kota, A. K., Metamorphic superomniphobic surfaces. *Adv. Mater.* **2017**, *29* (27), 1700295.

18. Yun, G.-T.; Jung, W.-B.; Oh, M. S.; Jang, G. M.; Baek, J.; Kim, N. I.; Im, S. G.; Jung, H.-T., Springtail-inspired superomniphobic surface with extreme pressure resistance. *Sci. Adv.* **2018**, *4* (8), eaat4978.
19. Mertens, M.; Mohr, M.; Bruehne, K.; Fecht, H.-J.; Łojkowski, M.; Świążkowski, W.; Łojkowski, W., Patterned hydrophobic and hydrophilic surfaces of ultra-smooth nanocrystalline diamond layers. *Appl. Surf. Sci.* **2016**, *390*, 526-530.
20. Howarter, J. A.; Youngblood, J. P., Self - Cleaning and Next Generation Anti - Fog Surfaces and Coatings. *Macromolecular rapid communications* **2008**, *29* (6), 455-466.
21. Jayaramulu, K.; Geyer, F.; Petr, M.; Zboril, R.; Vollmer, D.; Fischer, R. A., Shape controlled hierarchical porous hydrophobic/oleophilic metal - organic nanofibrous gel composites for oil adsorption. *Adv. Mater.* **2017**, *29* (12), 1605307.
22. Brown, P.; Atkinson, O.; Badyal, J., Ultrafast oleophobic–hydrophilic switching surfaces for antifogging, self-cleaning, and oil–water separation. *ACS Appl. Mater. Interfaces* **2014**, *6* (10), 7504-7511.
23. Qing, W.; Liu, F.; Yao, H.; Sun, S.; Chen, C.; Zhang, W., Functional catalytic membrane development: A review of catalyst coating techniques. *Advances in Colloid and Interface Science* **2020**, 102207.
24. Li, Q.; Zhao, T.; Li, M.; Li, W.; Yang, B.; Qin, D.; Lv, K.; Wang, X.; Wu, L.; Wu, X., One-step construction of Pickering emulsion via commercial TiO₂ nanoparticles for photocatalytic dye degradation. *Appl. Catal., B* **2019**, *249*, 1-8.
25. Li, X.; Wu, X.; Liu, S.; Li, Y.; Fan, J.; Lv, K., Effects of fluorine on photocatalysis. *Chinese Journal of Catalysis* **2020**, *41* (10), 1451-1467.
26. Bortot Coelho, F. E.; Gionco, C.; Paganini, M. C.; Calza, P.; Magnacca, G., Control of Membrane Fouling in Organics Filtration Using Ce-Doped Zirconia and Visible Light. *Nanomaterials* **2019**, *9* (4), 534.
27. Liu, T.; Wang, L.; Liu, X.; Sun, C.; Lv, Y.; Miao, R.; Wang, X., Dynamic photocatalytic membrane coated with ZnIn₂S₄ for enhanced photocatalytic performance and antifouling property. *Chem. Eng. J.* **2020**, *379*, 122379.
28. Qahtan, T. F.; Gondal, M. A.; Dastageer, M. A.; Kwon, G.; Ezazi, M.; Al-Kuban, M. Z., Thermally Sensitized Membranes for Crude Oil–Water Remediation under Visible Light. *ACS Appl. Mater. Interfaces* **2020**, *12* (43), 48572-48579.
29. Lv, Y.; Zhang, C.; He, A.; Yang, S. J.; Wu, G. P.; Darling, S. B.; Xu, Z. K., Photocatalytic Nanofiltration Membranes with Self - Cleaning Property for Wastewater Treatment. *Adv. Funct. Mater.* **2017**, *27* (27), 1700251.
30. Yu, J. C.; Ho, W.; Lin, J.; Yip, H.; Wong, P. K., Photocatalytic activity, antibacterial effect, and photoinduced hydrophilicity of TiO₂ films coated on a stainless steel substrate. *Environ. Sci. Technol.* **2003**, *37* (10), 2296-2301.
31. Ezazi, M.; Shrestha, B.; Kim, S. I.; Jeong, B.; Gorney, J.; Hutchison, K.; Lee, D. H.; Kwon, G., Selective Wettability Membrane for Continuous Oil– Water Separation and In Situ Visible Light - Driven Photocatalytic Purification of Water. *Global Challenges* **2020**, *4* (10), 2000009.
32. Song, S.; Yang, H.; Zhou, C.; Cheng, J.; Jiang, Z.; Lu, Z.; Miao, J., Underwater superoleophobic mesh based on BiVO₄ nanoparticles with sunlight-driven self-cleaning property for oil/water separation. *Chem. Eng. J.* **2017**, *320*, 342-351.
33. Zhang, L.; He, Y.; Ma, L.; Chen, J.; Fan, Y.; Zhang, S.; Shi, H.; Li, Z.; Luo, P., Hierarchically Stabilized PAN/β-FeOOH Nanofibrous Membrane for Efficient Water Purification

with Excellent Antifouling Performance and Robust Solvent Resistance. *ACS Appl. Mater. Interfaces* **2019**, *11* (37), 34487-34496.

34. Liu, Y.; Su, Y.; Guan, J.; Cao, J.; Zhang, R.; He, M.; Gao, K.; Zhou, L.; Jiang, Z., 2D Heterostructure Membranes with Sunlight - Driven Self - Cleaning Ability for Highly Efficient Oil-Water Separation. *Adv. Funct. Mater.* **2018**, *28* (13), 1706545.

35. Zhao, J.; Zhu, W.; Wang, X.; Liu, L.; Yu, J.; Ding, B., Environmentally benign modification of breathable nanofibrous membranes exhibiting superior waterproof and photocatalytic self-cleaning properties. *Nanoscale Horizons* **2019**, *4* (4), 867-873.

36. Luster, E.; Avisar, D.; Horovitz, I.; Lozzi, L.; Baker, M. A.; Grilli, R.; Mamane, H., N-doped TiO₂-coated ceramic membrane for carbamazepine degradation in different water qualities. *Nanomaterials* **2017**, *7* (8), 206.

37. Wang, D.; Liu, Y.; Liu, X.; Zhou, F.; Liu, W.; Xue, Q., Towards a tunable and switchable water adhesion on a TiO₂ nanotube film with patterned wettability. *Chemical Communications* **2009**, (45), 7018-7020.

38. Horovitz, I.; Gitis, V.; Avisar, D.; Mamane, H., Ceramic-based photocatalytic membrane reactors for water treatment—where to next? *Reviews in Chemical Engineering* **2020**, *36* (5), 593-622.

39. Di Valentin, C.; Finazzi, E.; Pacchioni, G.; Selloni, A.; Livraghi, S.; Paganini, M. C.; Giamello, E., N-doped TiO₂: Theory and experiment. *Chemical Physics* **2007**, *339* (1-3), 44-56.

40. Premkumar, J., Development of super-hydrophilicity on nitrogen-doped TiO₂ thin film surface by photoelectrochemical method under visible light. *Chemistry of Materials* **2004**, *16* (21), 3980-3981.

41. Brassard, J.-D.; Sarkar, D. K.; Perron, J., Synthesis of monodisperse fluorinated silica nanoparticles and their superhydrophobic thin films. *ACS Applied Materials & Interfaces* **2011**, *3* (9), 3583-3588.

42. Burda, C.; Lou, Y.; Chen, X.; Samia, A. C.; Stout, J.; Gole, J. L., Enhanced nitrogen doping in TiO₂ nanoparticles. *Nano Letters* **2003**, *3* (8), 1049-1051.

43. Cong, Y.; Zhang, J.; Chen, F.; Anpo, M., Synthesis and characterization of nitrogen-doped TiO₂ nanophotocatalyst with high visible light activity. *The Journal of Physical Chemistry C* **2007**, *111* (19), 6976-6982.

44. Yang, G.; Jiang, Z.; Shi, H.; Xiao, T.; Yan, Z., Preparation of highly visible-light active N-doped TiO₂ photocatalyst. *Journal of Materials Chemistry* **2010**, *20* (25), 5301-5309.

45. Zhang, Z.; Zhang, W.; Lichtfouse, E., *Membranes for Environmental Applications*. Springer International Publishing: 2020.

46. Furmidge, C., Studies at phase interfaces. I. The sliding of liquid drops on solid surfaces and a theory for spray retention. *Journal of Colloid Science* **1962**, *17* (4), 309-324.

47. Tuteja, A.; Choi, W.; Ma, M.; Mabry, J. M.; Mazzella, S. A.; Rutledge, G. C.; McKinley, G. H.; Cohen, R. E., Designing superoleophobic surfaces. *Science* **2007**, *318* (5856), 1618-1622.

48. Kwon, G.; Kota, A. K.; Li, Y.; Sohani, A.; Mabry, J. M.; Tuteja, A., On - demand separation of oil - water mixtures. *Advanced Materials* **2012**, *24* (27), 3666-3671.

49. Kwon, G.; Panchanathan, D.; Mahmoudi, S. R.; Gondal, M. A.; McKinley, G. H.; Varanasi, K. K., Visible light guided manipulation of liquid wettability on photoresponsive surfaces. *Nature Communications* **2017**, *8* (1), 1-8.

50. Vaiano, V.; Sacco, O.; Sannino, D.; Navarra, W.; Daniel, C.; Venditto, V., Influence of aggregate size on photoactivity of N-doped TiO₂ particles in aqueous suspensions under visible light irradiation. *Journal of Photochemistry and Photobiology A: Chemistry* **2017**, *336*, 191-197.

51. Hsieh, C.-T.; Chang, B.-S.; Lin, J.-Y., Improvement of water and oil repellency on wood substrates by using fluorinated silica nanocoating. *Applied Surface Science* **2011**, 257 (18), 7997-8002.
52. Mohammadi, T.; Kazemimoghadam, M.; Saadabadi, M., Modeling of membrane fouling and flux decline in reverse osmosis during separation of oil in water emulsions. *Desalination* **2003**, 157 (1-3), 369-375.
53. Mondal, S.; Wickramasinghe, S. R., Produced water treatment by nanofiltration and reverse osmosis membranes. *Journal of Membrane Science* **2008**, 322 (1), 162-170.
54. Hoffmann, M. R.; Martin, S. T.; Choi, W.; Bahnemann, D. W., Environmental applications of semiconductor photocatalysis. *Chem. Rev.* **1995**, 95 (1), 69-96.
55. Peyravi, M.; Jahanshahi, M.; Mirmousaei, S. M.; Lau, W.-J., Dynamically Coated Photocatalytic Zeolite-TiO₂ Membrane for Oil-in-Water Emulsion Separation. *Arabian Journal for Science and Engineering* **2020**, 1-9.
56. Kovács, I.; Veréb, G.; Kertész, S.; Beszédes, S.; Hodúr, C.; László, Z., Investigation of surface and filtration properties of TiO₂ coated ultrafiltration polyacrylonitrile membranes. *Water Science and Technology* **2018**, 77 (4), 931-938.
57. Xie, A.; Cui, J.; Yang, J.; Chen, Y.; Dai, J.; Lang, J.; Li, C.; Yan, Y., Photo-Fenton self-cleaning membranes with robust flux recovery for an efficient oil/water emulsion separation. *J. Mater. Chem. A* **2019**, 7 (14), 8491-8502.

Chapter 3: Predicting kinetics of water-rich permeate flux through photocatalytic mesh under visible light illumination

This chapter is adapted from **Paper P2**.

Abstract: Membrane-based separation technologies are attractive to remediating unconventional water sources, including brackish, industrial, and municipal wastewater, due to their versatility and relatively high energy efficiency. However, membrane fouling by dissolved or suspended organic substances remains a primary challenge that can result in an irreversible decline of the permeate flux. To overcome this, membranes have been incorporated with photocatalytic materials that can degrade these organic substances deposited on the surface upon light illumination. While such photocatalytic membranes have demonstrated that they can recover their inherent permeability, less information is known about the effect of photocatalysis on the kinetics of the permeate flux. In this work, a photocatalytic mesh that can selectively permeate water while repelling oil was fabricated by coating a mixture of nitrogen-doped TiO₂ (N-TiO₂) and perfluoro silane-grafted SiO₂ (F-SiO₂) nanoparticles on a stainless steel mesh. Utilizing the photocatalytic mesh, the time-dependent evolution of the water-rich permeate flux as a result of photocatalytic degradation of the oil was studied under visible light illumination. A mathematical model was developed that can relate the photocatalytic degradation of the organic substances deposited on a mesh surface to the evolution of the permeate flux. This model was established by integrating the Langmuir–Hinshelwood kinetics for photocatalysis and the Cassie–Baxter wettability analysis on a chemically heterogeneous mesh surface into a permeate flux relation. Consequently, the time-dependent water-rich permeate flux values are compared with those predicted by using the model. It is found that the model can predict the evolution of the water-rich permeate flux with a goodness of fit of 0.92.

3.1. Introduction

With growing environmental awareness and tighter regulations, there is an increase in investments in developing water remediation technologies.¹⁻⁸ Membrane-based technologies are attractive because they are relatively energy-efficient and versatile to different effluents generated in industrial processes.⁹⁻¹² One of the primary challenges of membranes is fouling by dissolved or suspended organic substances that can get adsorbed on the membrane surface or pore walls.^{13, 14} This results in a decrease in permeability and can eventually shorten the membrane's life cycle.¹⁴⁻¹⁶ Therefore, membrane-based remediation technologies often involve prefiltration to remove the suspended or dissolved substances.¹⁷ Also, membranes are periodically subjected to cleaning processes such as backwashing, forward flushing, and chemical treatment to remove the surface-

deposited contaminants.^{18, 19} While these methodologies are effective and widely employed in real applications, they can irreversibly degrade membrane's performance over time.^{20, 21}

Manipulating the membrane's wettability has been reported as an alternative to enhance its fouling resistance.²²⁻²⁵ For example, membranes with hydrophilic (i.e., water contact angle $< 90^\circ$) or superhydrophilic (i.e., water contact angle $\approx 0^\circ$) wettability can prevent adsorption of the organic substances (e.g., oil) to the surface by allowing water to form a thin film.²⁶⁻²⁸ Also, these membranes can exhibit selective permeation for water while repelling oils, which enables separation of oil-water mixtures with a high separation efficiency²⁹. In comparison, membranes possessing lower solid surface energy (γ_{sv}) can repel the organic substances without needing a water film.³⁰⁻³² We⁶ have reported fouling-resistant membranes that can separate oil-water mixtures with an insignificant decline in the permeate flux by combining hydrophilic (or superhydrophilic) wettability along with lower solid surface energy.

Membranes with selective wettability have been incorporated with photocatalytic materials (e.g., TiO_2 ,^{6, 33} N-TiO_2 ,³⁴ $\alpha\text{-Fe}_2\text{O}_3$,^{16, 35} Fe_3O_4 ,³⁶ WO_3 ,³⁷ ZnO ,³⁸ BiVO_4 ,⁷ $\alpha\text{-FeOOH}$,³⁹ MoO_3 ,⁴⁰ Co_3O_4 ,⁴¹ $\text{Gd}_2\text{ZnMnO}_6/\text{ZnO}$ ⁴²) that can degrade the organic substances deposited on the surface upon light illumination. These membranes have demonstrated that they can oxidize (or reduce) the organic substances either dissolved in a liquid (e.g., water) or adsorbed on the membrane surface when irradiated by light with an energy higher than their bandgap energy.^{43, 44} This can clean the membrane's surface and purify the permeate. Moreover, these photocatalytic membranes can recover the water-rich permeate flux upon light illumination after being fouled by organic substances. For example., Zhang et al.⁴⁵ demonstrated in situ recovery of the water-rich permeate flux utilizing a nitrogen doped TiO_2 coated membrane under visible light illumination. Guo et al.⁴⁶ fabricated a photocatalytic membrane by utilizing BiOBr/Ag nanoparticles that can degrade

organic dyes (e.g., methylene Blue, crystal Violet, acid Red 18, and acid Yellow 36) upon UV light illumination and recover the water-rich permeate flux. Liu et al.⁴⁷ fabricated a PVDF-Ni-ZnO composite membrane and demonstrated in situ photocatalysis-driven recovery of the water-rich permeate flux during the filtration of an aqueous solution dissolved with organic substances (e.g., humic acid, sodium alginate, bovine serum albumin). Recently, we^{3, 6} developed photocatalytic membranes by coating a commercial filter with a mixture of visible light-active iron-doped TiO₂ or nitrogen-doped TiO₂ and perfluorosilane-grafted SiO₂. These membranes have demonstrated in situ recovery of the water-rich permeate flux upon visible light illumination during oil-water separation.

An increase in the permeate flux upon light illumination has been attributed to the photocatalytic degradation of the organic substances deposited on the membrane surface.^{27, 48, 49} Also, such photocatalytic membranes have demonstrated that they exhibit a time-dependent evolution of the surface chemistry heterogeneity (e.g., clean and contaminated regions) upon light illumination, which can be quantitatively described by the contact angle measurements.^{6, 22, 50-52} To our knowledge, quantitative relationships of the evolution of surface chemistry heterogeneity on a membrane surface and that of permeate flux upon visible light illumination are lacking. Establishing such a relationship is critical to understanding both membrane fouling and photocatalytic cleaning mechanisms, which enables one to design a separation membrane with tailored performance.

Based on these findings, herein, we conducted an experimental analysis on the effect of wettability and photocatalysis on the permeate flux through a photocatalytic material-coated stainless steel mesh and developed a mathematical relation between them under visible light illumination. For this, we fabricated a photocatalytic mesh utilizing a stainless steel mesh coated with nitrogen-

doped TiO₂ (N-TiO₂) and perfluorosilane-grafted SiO₂ (F-SiO₂) nanoparticles mixture. A mathematical model was derived by integrating the Langmuir–Hinshelwood kinetic model of photocatalysis^{22, 30} and the Cassie–Baxter analysis of the contact angles for water on a photocatalytic surface⁵³ into a permeate flux relation.⁵⁴ The mathematical model was then utilized to predict the water-rich permeate flux through the photocatalytic mesh during visible light illumination. The accuracy of the predicted flux values was then validated by comparing them with the experimentally acquired results.

3.2. Experimental procedure

3.2.1. Synthesis of N-TiO₂ and F-SiO₂ nanoparticles.

N-TiO₂ and F-SiO₂ nanoparticles were synthesized by employing a modified sol-gel method according to the procedures in our previous work.⁶ For N-TiO₂, titanium butoxide (TBOT, 5.0 g) was added dropwise to a mixture of isopropyl alcohol (IPA) and DI water (1:9 volumetric ratio, IPA: DI water). The pH of the solution was adjusted to 2.0±0.1 by adding nitric acid (0.01 M). Subsequently, triethylamine with a molar ratio of 2.0 with respect to TBOT was added dropwise to the solution. After stirring the solution for 12 h at 30 °C, the precipitates were collected by centrifugation and thoroughly rinsed with ethanol and DI water. The product was vacuum dried to obtain N-TiO₂. For synthesizing F-SiO₂, tetraethyl orthosilicate (TEOS, 1.0 g) was mixed with a 0.01 M hydrochloric acid in DI water (100 g). 1H,1H,2H,2H-perfluorodecyl trichlorosilane (1.0 g) was then added to the mixture dropwise. The solution was magnetically stirred for 60 minutes at 60 °C, and the centrifugation was utilized to collect the resulting precipitates. The precipitates were then thoroughly rinsed with ethanol and DI water, followed by vacuum drying to obtain F-SiO₂ nanoparticles.

3.2.2. Fabrication of photocatalytic mesh with selective wettability for water over oil.

Stainless steel (SS) 316 Twill Dutch weave mesh (area = 42 cm²) was cleaned with ethanol in an ultrasonic bath for 10 minutes. The mesh was then dip-coated in a Norland ultraviolet (UV) light-curable optical adhesive (NOA 61) (1.0 wt% in acetone). Subsequently, a dispersion of N-TiO₂/F-SiO₂ mixture in DI water (solute concentration = 10 wt%) was sprayed (IWata Eclipse, Anest IWata) onto the adhesive-coated mesh for one minute. The spraying distance and nitrogen gas pressure were maintained at 15 cm and 200 kPa, respectively. The concentrations of N-TiO₂ nanoparticles in the N-TiO₂/F-SiO₂ mixture were 0, 25 wt%, 50 wt%, 75 wt%, and 100 wt%. The mesh was then illuminated by a long-wavelength UV light (100 W, $\lambda = 365$ nm, UVA Blak-Ray B100A, Analytikjena) for 5 minutes to cure the adhesive. Finally, the fabricated photocatalytic mesh was thoroughly rinsed with ethanol and DI water.

3.2.3. Surfactant-stabilized oil-in-water emulsion.

The surface texture of a mesh coated with N-TiO₂/F-SiO₂ nanoparticles was characterized by field-emission scanning electron microscopy (FESEM, FEI Versa 3D). The characterizations were performed at an accelerating voltage of 10 kV.

3.2.4. Determining the nominal pore size of the mesh.

Filter retention analysis^{3, 55} was utilized to determine the nominal pore size of the mesh. We sequentially fed monodisperse SiO₂ particles with various diameters to the mesh in the order of the lowest to the highest diameter. We calculated the proportion of the particles retained on the mesh for each diameter according to $\%R = M_R/M_T$, where M_R and M_T are the mass of SiO₂ retained on the mesh and the total mass of that introduced to the mesh, respectively. We assigned the diameter of SiO₂ as the nominal pore size of the mesh if $\%R$ exceeds 50% for that particular diameter. Note that we used SiO₂ particles with diameters of 120, 150, 200, 300, 400, 500, 600,

and 750 nm and prepared suspensions in ethanol with a concentration of 50 mg mL⁻¹. We measured the %*R* as 66, 69, and 71%, with the SiO₂ possessing a diameter of 400 nm for meshes coated with N-TiO₂/F-SiO₂ mixture with 50, 75, and 100 wt% of N-TiO₂, respectively. Therefore, 400 nm was assigned as the nominal pore size of meshes.

3.2.5. Contact angle measurement.

All contact angle measurements were conducted by utilizing a Ramehart 190-U1 goniometer. About 3 μL of liquids were used during the measurements.

3.2.6. Visible light intensity measurement.

The average size of N-TiO₂ and F-SiO₂ nanoparticles was measured by utilizing dynamic light scattering (DLS) (ZetaPALS zeta potential analyzer, Brookhaven Instruments) equipped with a BI-9000AT digital autocorrelator. Suspensions of N-TiO₂ (0.01 wt%) and F-SiO₂ (0.01 wt%) were prepared in DI water, followed by ultrasonication.

3.2.7. Root mean square (RMS) roughness measurements.

An optical profiler (Veeco Wyko NT 1100) was utilized to measure the root mean square (RMS) surface roughness of coated meshes. The scan rate was set to 50 nm s⁻¹. The scanned area was 5 μm × 5 μm.

3.3. Results and discussion

3.3.1. Photocatalytic mesh fabrication and under-oil water wettability.

A mixture of nitrogen-doped TiO₂ (N-TiO₂) and perfluorosilane-grafted SiO₂ (F-SiO₂) nanoparticles were utilized to fabricate a visible light-active photocatalytic mesh (see **Experimental procedure**). Please note that the synthesis of a mixture of N-TiO₂ and F-SiO₂ nanoparticles (i.e., N-TiO₂/F-SiO₂) was reported in previous work⁶, which demonstrated selective wettability for water over oil (i.e., hydrophilic and oleophobic wettability). Briefly, a dispersion of

N-TiO₂/F-SiO₂ in deionized (DI) water (solute concentration = 10 wt%) was sprayed onto stainless steel (SS) 316 Twill Dutch weave mesh (SS mesh) for one minute. Note that the SS mesh was pre-treated with an ultraviolet (UV)-curable adhesive. Here, we utilized dispersions with varied N-TiO₂ concentrations in the N-TiO₂/F-SiO₂ mixture (i.e., 0, 25 wt%, 50 wt%, 75 wt%, and 100 wt%). Subsequently, the SS mesh was illuminated by a long-wavelength UV light (100 W, $\lambda = 365$ nm) for 5 minutes to completely cure the adhesive. Finally, the resulting mesh was thoroughly rinsed with ethanol and DI water.

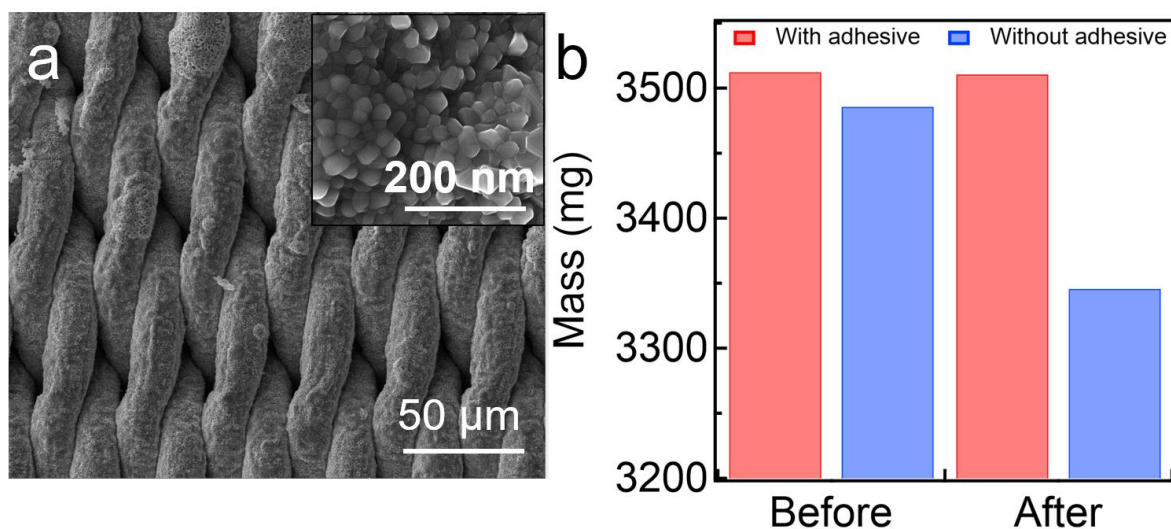


Figure 3.1. (a) Scanning electron microscopy (SEM) image of stainless steel (SS) 316 Twill Dutch weave mesh coated with N-TiO₂/F-SiO₂ (50 wt%). The inset shows a higher magnification SEM image of the mesh surface. (b) The measured mass of the mesh coated with N-TiO₂/F-SiO₂ with and without the cured adhesive after the standard Tape Peel off test.

Figure 3.1a demonstrates a scanning electron microscopy (SEM) image of a SS mesh coated with N-TiO₂/F-SiO₂ mixture that includes 50 wt% N-TiO₂ (i.e., N-TiO₂/F-SiO₂ (50 wt%)). The mesh surface was evenly coated with N-TiO₂/F-SiO₂ nanoparticles showing a hierarchical structure (i.e., surface texture with two or more length scales⁵⁶) with a root mean square (RMS) surface roughness³ of $0.75 \mu\text{m} \pm 0.03 \mu\text{m}$ (see **Experimental procedure**). Further, the nominal pore size of the mesh was measured as $0.40 \mu\text{m} \pm 0.03 \mu\text{m}$ after coating with N-TiO₂/F-SiO₂ mixture (See

Experimental procedure). Please note that the mesh exhibited mechanical robustness against external stress because the cured adhesive can securely hold nanoparticles on the mesh surface (**Figure 3.1b**). We measured the adhesion strength of N-TiO₂/F-SiO₂ nanoparticles to the mesh surface by utilizing the standard ASTM D3359 Tape Peel-off test. The mass of the mesh before and after the test was measured by utilizing a high precision scale (Mettler Toledo XS105 DU, precision = 0.01 mg). Note that the mass of the as-purchased mesh was 3349.5 mg ± 50 mg. The results show that the mass of the mesh coated with N-TiO₂/F-SiO₂ nanoparticles utilizing the ultraviolet (UV)-curable adhesive (NOA 61) remains almost unchanged. This can be attributed to the cured adhesive, which can hold the N-TiO₂/F-SiO₂ nanoparticles together and securely bind them to the mesh surface by forming an interlocking structure. In contrast, the mesh coated with N-TiO₂/F-SiO₂ nanoparticles without adhesive exhibited ≈89±2 % mass loss after the Tape Peel-off test.

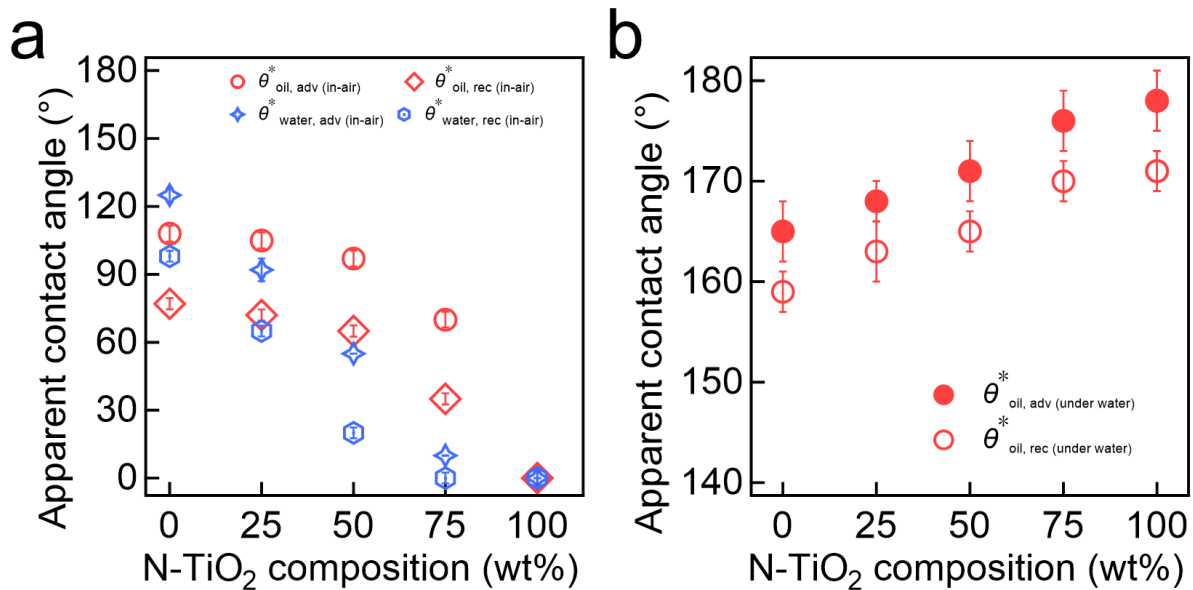


Figure 3.2. (a) The measured in air advancing and receding apparent contact angles for water and oil (n-hexadecane) on the mesh surfaces coated with varied compositions of N-TiO₂/F-SiO₂. (b) The measured advancing and receding apparent contact angles of oil (n-hexadecane) on the mesh submerged in water.

We⁶ have demonstrated that a commercial filter surface coated with N-TiO₂/F-SiO₂ mixture can exhibit varying wettability for water and oil depending on the composition of N-TiO₂ and F-SiO₂. Here, we measured in air apparent advancing (θ_{adv}^*) and receding (θ_{rec}^*) contact angles of water ($\gamma_{lv} = 72.1 \text{ mN m}^{-1}$) and oil (n-hexadecane, $\gamma_{lv} = 27.5 \text{ mN m}^{-1}$) on the mesh surfaces coated with various compositions of N-TiO₂/F-SiO₂ (**Figure 3.2a**). The results indicate that a mesh coated with N-TiO₂/F-SiO₂ with a lower N-TiO₂ concentration exhibits higher contact angles for both water and oil. When the N-TiO₂ concentration reached 50 wt%, the contact angles of water becomes lower than oil contact angles (i.e., $\theta_{water,adv}^* \text{ (in-air)} = 55^\circ \pm 2^\circ$ and $\theta_{water,rec}^* \text{ (in-air)} = 20^\circ \pm 2^\circ$ while those for oil measured as $\theta_{oil,adv}^* \text{ (in-air)} = 97^\circ \pm 2^\circ$, $\theta_{oil,rec}^* \text{ (in-air)} = 65^\circ \pm 2^\circ$). Note that a mesh coated with only N-TiO₂ (i.e., N-TiO₂/F-SiO₂ (100 wt%)) exhibits both water and oil contact angles zero. We also measured the apparent advancing and receding contact angles of oil (n-hexadecane) on the mesh submerged in water (**Figure 3.2b**). The results indicate that a mesh exhibiting a lower water contact angle in air shows a higher underwater oil contact angle. For example, a mesh coated with N-TiO₂/F-SiO₂ (50 wt%) exhibits $\theta_{oil,adv}^* \text{ (under water)} = 171^\circ \pm 5^\circ$ and $\theta_{oil,rec}^* \text{ (under water)} = 165^\circ \pm 5^\circ$ while that coated with N-TiO₂/F-SiO₂ (25 wt%) shows $\theta_{oil,adv}^* \text{ (under water)} = 168^\circ \pm 5^\circ$ and $\theta_{oil,rec}^* \text{ (under water)} = 163^\circ \pm 4^\circ$.

3.3.2. Time-dependent change of mesh surface wettability submerged in oil

When a hydrophilic (or superhydrophilic) surface is fouled by oil, it often exhibits an increase in the water contact angles.²² To study the fouling behavior, we submerged our coated mesh in an oil (n-hexadecane) bath and measured the underoil apparent contact angles for water ($\theta_{w,o}^*$) as a function of submerging time. The results show that a mesh coated with a higher concentration of N-TiO₂ shows a steeper increase in the values of $\theta_{w,o}^*$ (**Figure 3.3a**). For example, a mesh coated with N-TiO₂/F-SiO₂ (100 wt%) shows $\theta_{w,o}^* = 97^\circ \pm 3^\circ$ while those coated with N-TiO₂/F-SiO₂ (75

wt%) and N-TiO₂/F-SiO₂ (50 wt%) exhibits 88°±3° and 107°±3°, respectively, at $t = 300$ minutes. Please note that the values of $\theta_{w,o}^*$ on as-prepared meshes coated with N-TiO₂/F-SiO₂ (100 wt%) and N-TiO₂/F-SiO₂ (75 wt%) were zero while we measured $\theta_{w,o}^* = 79^\circ \pm 3^\circ$ on an as-prepared mesh coated with N-TiO₂/F-SiO₂ (50 wt%). Such a transition to underoil hydrophobicity (i.e., $\theta_{w,o}^* > 90^\circ$) can be attributed to an increase in the area fraction of the oil adsorbed region on the coated mesh surface, which lowers the solid surface energy.^{22,29} Note that the $\theta_{w,o}^*$ values became constant at 176°±2°, 171°±4°, and 178°±2° on a mesh coated with N-TiO₂/F-SiO₂ (50 wt%), N-TiO₂/F-SiO₂ (75 wt%), and N-TiO₂/F-SiO₂ (100 wt%), respectively, at $t = 1800$ minutes.

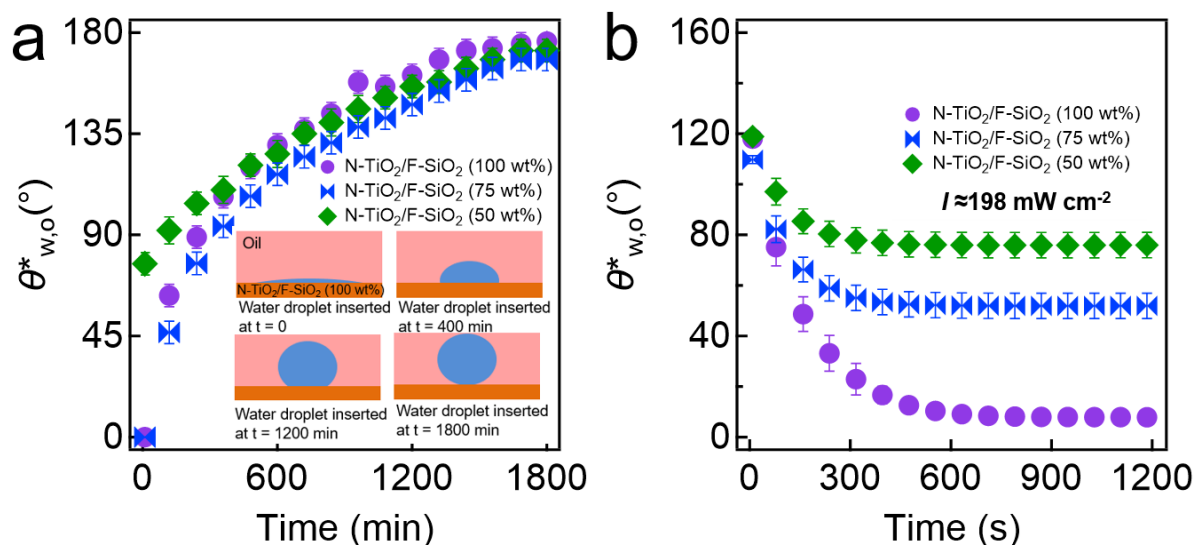


Figure 3.3. (a) The measured apparent contact angles for water on the mesh surfaces coated with N-TiO₂/F-SiO₂ mixture with various N-TiO₂ concentrations (50 wt%, 75 wt%, and 100 wt%) that are submerged in an oil (n-hexadecane) bath as a function of submerging time. The inset images illustrate schematics of the time-dependent evolution of the water contact angles on a mesh surface submerged in oil. (b) The measured apparent contact angles for water on the mesh surfaces coated with N-TiO₂/F-SiO₂ mixture with various N-TiO₂ concentrations (50 wt%, 75 wt%, and 100 wt%) while being illuminated by visible light (Intensity (I) = 198 mW cm⁻²). Note that all meshes were precontaminated by oil for 600 minutes.

When an oil-contaminated photocatalytic mesh surface is illuminated by light, it can exhibit a conversion to underoil hydrophilic (or superhydrophilic) wettability due to photocatalytic

degradation of the surface adsorbed oil molecules which can lead to an increase in the area fraction of clean (i.e., high solid surface energy) regions.^{22, 29} We conducted in situ measurements for the $\theta_{w,o}^*$ values on our mesh under visible light illumination ($I \approx 198 \text{ mW cm}^{-2}$). All meshes were pre-contaminated with oil for 600 minutes. Upon the onset of visible light illumination, the $\theta_{w,o}^*$ values started to decrease rapidly and reached constant values after $t \approx 900 \text{ s}$ (i.e., ≈ 15 minutes, see **Figure 3.3b**). Note that a mesh coated with a N-TiO₂/F-SiO₂ mixture with a higher concentration of N-TiO₂ exhibits a more rapid decrease in the $\theta_{w,o}^*$ values. For example, a mesh coated with N-TiO₂/F-SiO₂ (75%) showed $\theta_{w,o}^* = 51^\circ \pm 3^\circ$ whereas that coated with N-TiO₂/F-SiO₂ (50%) exhibited $\theta_{w,o}^* = 75^\circ \pm 3^\circ$ at $t \approx 900 \text{ s}$. Note that a mesh coated with N-TiO₂/F-SiO₂ (100%) can completely recover its inherent hydrophilic wettability.

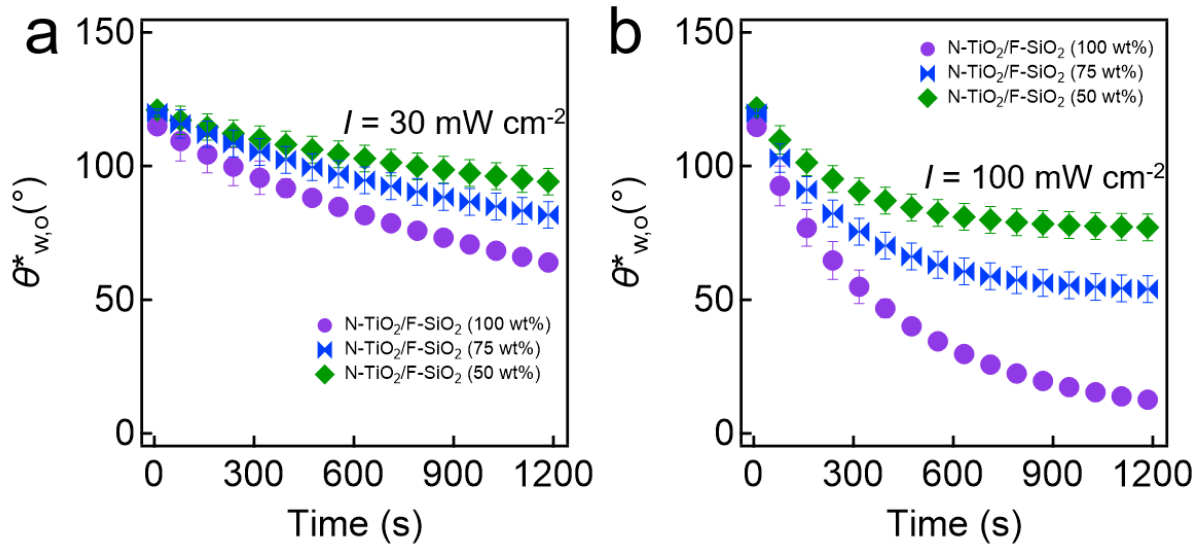


Figure 3.4. (a-b) The measured apparent contact angles of water on mesh surface submerged in oil while being illuminated by visible light with intensity of $I = 30 \text{ mW cm}^{-2}$ (a) and $I = 100 \text{ mW cm}^{-2}$ (b). Note that all meshes were contaminated by oil for 600 mins.

We also demonstrated that visible light illumination with a higher intensity could result in a more rapid change in the $\theta_{w,o}^*$ values. **Figures 3.4a and 3.4b** show the time-dependent $\theta_{w,o}^*$ values measured on the meshes coated with various compositions of N-TiO₂/F-SiO₂ submerged in oil

while illuminated by visible light intensity of $I = 100 \text{ mW cm}^{-2}$ and 30 mW cm^{-2} , respectively. Please note that we utilized the meshes contaminated by oil for 600 mins. The results show that the values of $\theta_{w,o}^*$ decrease at a higher rate on a mesh surface irradiated by higher intensity visible light. For example, a mesh coated with N-TiO₂/F-SiO₂ (75 wt%) shows a decrease in the value of $\theta_{w,o}^*$ to $62^\circ \pm 3^\circ$ in 600 s when irradiated by light with an intensity of $I = 100 \text{ mW cm}^{-2}$ whereas the $\theta_{w,o}^*$ becomes $99^\circ \pm 3^\circ$ when $I = 30 \text{ mW cm}^{-2}$.

3.3.3. Evolution of the water-rich permeate flux

The selective wettability for water over oil, along with its photocatalytic degradation capability, enables our mesh to exhibit enhanced resistance to oil fouling and photocatalytic cleaning of the surface under light illumination when subjected to an oil-water mixture.^{22, 29} A continuous cross-flow separation apparatus^{6, 57} was utilized to conduct oil-water separation and in situ photocatalysis (**Figure 3.5**). Here, a feed oil-water mixture is continuously fed by a plunger pump, and the water-rich permeate passes through the mesh and is collected in a container. An n-hexadecane-in-water emulsion (1:9 volumetric ratio, n-hexadecane: water) stabilized by a surfactant (sodium dodecyl sulfate, SDS) was utilized (See **Experimental procedure**). Note that a mesh was prewetted by SDS-dissolved water (SDS concentration = 0.015 wt% with respect to water weight) for 30 minutes (flow rate = $2.0 \text{ L s}^{-1} \pm 0.2 \text{ L s}^{-1}$) to obtain a constant flux (J_o) for the water-rich permeate before introducing a feed emulsion. The transmembrane pressure (Δp , i.e., the difference in pressure at two opposite sides of the mesh) was maintained at $\Delta p = 13.0 \text{ kPa} \pm 0.5 \text{ kPa}$ for prewetting process.

When a feed oil-in-water emulsion was introduced ($\Delta p = 13.0 \text{ kPa} \pm 0.7 \text{ kPa}$ and flow rate = $2.0 \text{ L s}^{-1} \pm 0.1 \text{ L s}^{-1}$), the flux values (J) for the water-rich permeate rapidly decreased, which can be primarily attributed to fouling of the mesh surface by oil (**Figure 3.6a**).^{3, 6, 15, 39, 58} The results show

that a mesh coated with N-TiO₂/F-SiO₂ with a higher concentration of N-TiO₂ exhibits a steeper decrease in the J values that eventually reaches lower values at $t \approx 90$ minutes. For example, a mesh coated with N-TiO₂/F-SiO₂ (50 wt%) exhibits $J \approx 261 \text{ L m}^{-2} \text{ h}^{-1}$ (LMH) while that coated with N-TiO₂/F-SiO₂ (75 wt%) shows $J \approx 253 \text{ LMH}$ at $t \approx 90$ minutes. Given that the J_0 values were $\approx 435 \text{ LMH}$ and $\approx 441 \text{ LMH}$ for a mesh coated with 50 wt% N-TiO₂ and 75 wt% N-TiO₂, respectively, they correspond to $\approx 60\%$ and $\approx 57\%$ of the respective J_0 values. Please note that the J values were measured by a relation⁵⁹, $J = \Delta m(A\rho\Delta t)^{-1}$. Here, Δm represents the change in the water-rich permeate mass for a given time interval ($\Delta t = 5$ minutes), A is the projected area of the mesh ($A = 42 \text{ cm}^2$), and ρ is the density of the permeate ($\rho \approx 0.998 \text{ g cm}^{-3}$).

When the water-rich permeate flux exhibited a constant value at $t \approx 90$ minutes (i.e., illumination time, $t_i = 0$), we started illuminating the mesh surface with visible light ($I \approx 198 \text{ mW cm}^{-2}$) while the mesh was continuously subjected to a fresh feed emulsion. **Figure 3.6b** shows that the J values start to increase upon visible light illumination. This indicates cleaning of the oil-contaminated mesh surface, which consequently results in a lower breakthrough pressure (i.e., a minimum applied pressure at which the water permeates through the mesh) for the water-rich permeate.^{3, 6} Also, a mesh coated with a higher concentration of N-TiO₂ exhibited a higher recovery rate of the permeate flux values. For example, a mesh coated with N-TiO₂/F-SiO₂ (50 wt%) showed $J \approx 291 \text{ LMH}$ after 60 minutes of visible light illumination (i.e., $t_i = 60$ minutes), whereas that coated with N-TiO₂/F-SiO₂ (75 wt%) showed $J \approx 315 \text{ LMH}$. This corresponds to 17% and 30% recovery.

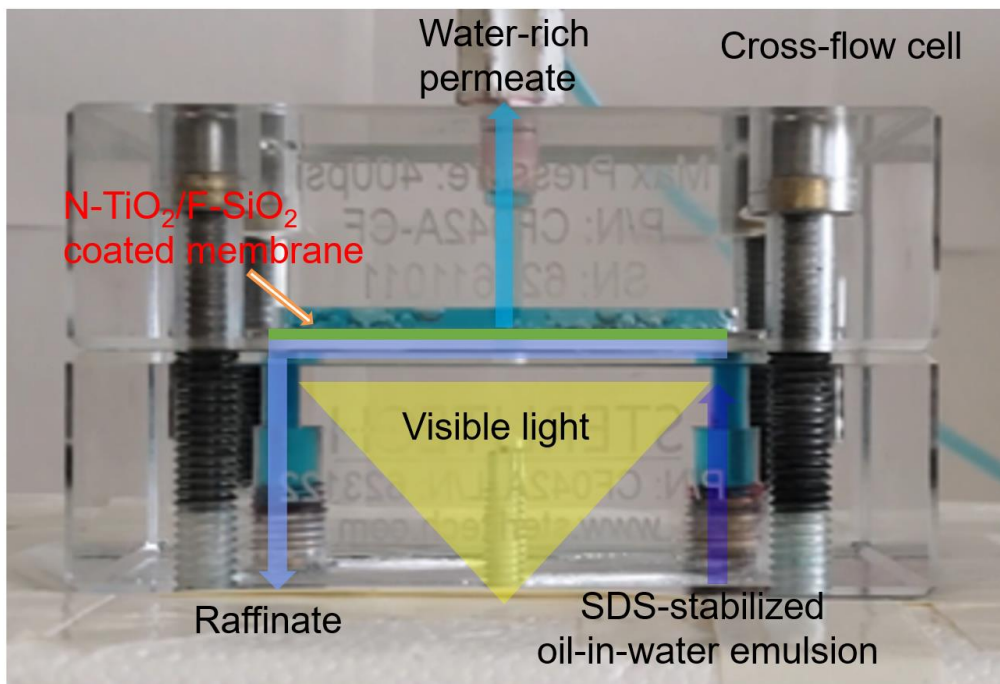


Figure 3.5. Photograph of the apparatus that enables continuous cross-flow separation of an oil-water mixture and in situ photocatalysis. (water is dyed blue and oil is dyed red).

Also, note that the oil concentration in the water-rich permeate remains very low (i.e., < 0.2 wt%) despite a decrease in water-rich permeate flux. Thermogravimetric analyses (TGA, PerkinElmer PYRIS 1) were employed to measure the concentration of oil in the water-rich permeate obtained from the separation of SDS-stabilized n-hexadecane-in-water emulsion. Approximately 10 mg of the water-rich permeate was heated from room temperature (≈ 22 °C) to 110 °C at a rate of 5 °C min^{-1} followed by maintaining the temperature (110 °C) for 50 mins, given that the boiling points of water and oil (n-hexadecane⁶⁰) are 100 °C and ≈ 287 °C, respectively, the remnant in the TGA can be assumed as pure n-hexadecane. **Figure 3.7** shows the TGA data of the water-rich permeate through the mesh coated with N-TiO₂/F-SiO₂ with varied compositions. The results indicate that the oil concentrations in the water-rich permeate are very low (i.e., < 0.2 wt%).

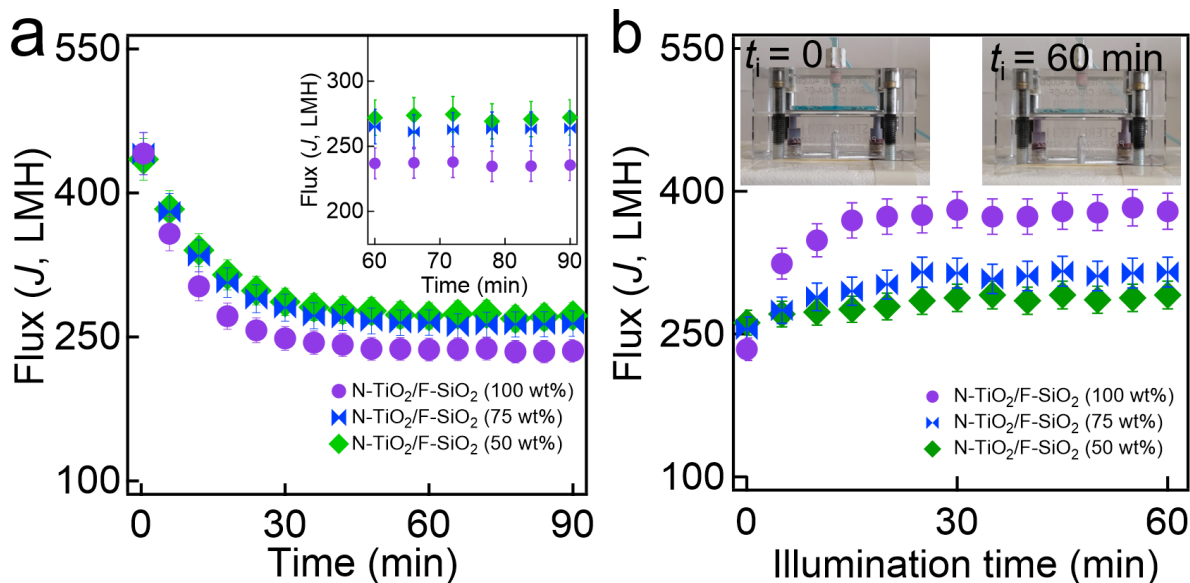


Figure 3.6. (a) The measured flux values (J) of the water-rich permeate through the mesh coated with various N-TiO₂ concentrations (50 wt%, 75 wt%, and 100 wt%) of N-TiO₂/F-SiO₂ mixture during separation of SDS-stabilized n-hexadecane-in-water emulsion (1:9 n-hexadecane:water volumetric ratio). The inset shows zoomed-in flux values in the time interval of 60-90 minutes. (b) The measured water-rich permeate flux values (J) while being illuminated by visible light ($I \approx 198 \text{ mW cm}^{-2}$). Inset shows a photograph of the cross-flow setup during the test.

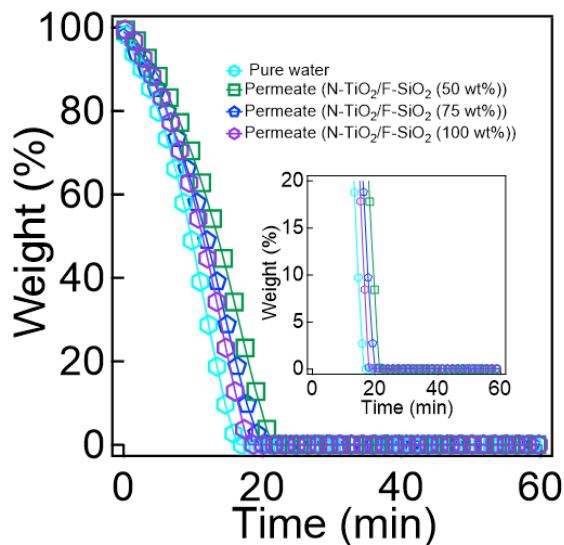


Figure 3.7. TGA data of the water-rich permeates after the separation of SDS-stabilized n-hexadecane-in-water emulsion by utilizing the mesh coated with various compositions of N-TiO₂/F-SiO₂.

3.3.4. Mathematical representation of the permeate flux kinetics

It is postulated that the extent of permeate flux recovery upon light illumination depends on various experimental parameters that include the incident light intensity (I) and the active surface area (A) of the N-TiO₂/F-SiO₂ coating, and the photocatalytic degradation rate (k_p).⁶¹ Here, we develop a mathematical model that can describe the time-dependent evolution of the water-rich permeate flux through a mesh coated with N-TiO₂/F-SiO₂ upon visible light illumination.

When a photocatalytic mesh surface is subjected to oil submerged in water while being illuminated by visible light, three chemical reactions can take place: adsorption, desorption, and photocatalytic degradation of oil molecules.^{30, 62-64} We²² recently showed that these reactions obey the first-order kinetics. Assuming that N-TiO₂ is photocatalytic⁶⁵⁻⁶⁷ while F-SiO₂ is not⁶, the following differential equation can be obtained, which describes a time-dependent photocatalysis-driven evolution of the area fraction of the mesh surface contaminated with oil ($f_c(t_i)$):

$$\text{(Equation 3.1)} \quad \frac{d}{dt} f_c(t_i) = f_T \times \frac{d}{dt} f_{c(T)}(t_i) + f_F \times \frac{d}{dt} f_{c(F)}(t_i)$$

where $f_{(T)}$ and $f_{(F)}$ are the area fraction of N-TiO₂ and F-SiO₂, respectively. The subscripts T and F symbolize N-TiO₂ and F-SiO₂, respectively. Solving Equation 3.1 by substituting $\frac{d}{dt} f_{c(T)}(t_i) = k_{a(T)} f_{nc(T)} - k_{d(T)} f_{c(T)} - k_{p(T)} f_{c(T)}$ and $\frac{d}{dt} f_{c(F)}(t_i) = k_{a(F)} f_{nc(F)} - k_{d(F)} f_{c(F)}$, where k_a , k_d , and k_p are the rate constant values for adsorption, desorption, and photocatalytic degradation of oil, respectively, on a particular phase (e.g., N-TiO₂ or F-SiO₂), and $f_{nc(T)} = 1 - f_{c(T)}$ and $f_{nc(F)} = 1 - f_{c(F)}$ (i.e., non-contaminated area fraction of each phase, $f_{nc(T)}$ or $f_{nc(F)}$) results in:

$$\text{(Equation 3.2)} \quad f_c(t_i) = \left[\frac{k_{a(T)}}{K(T)} - \left(\frac{k_{a(T)}}{K(T)} - f_{c(T)}(t_i = 0) \right) e^{-(K(T))t_i} \right] \times f_{(T)} + \left[\frac{k_{a(F)}}{K(F)} - \left(\frac{k_{a(F)}}{K(F)} - f_{c(F)}(t_i = 0) \right) e^{-(K(F))t_i} \right] \times f_{(F)}$$

where $f_{c(T)}(t_i = 0)$ and $f_{c(F)}(t_i = 0)$ are the initial area fraction of the contaminated regions for N-TiO₂ and F-SiO₂ at the start of visible light illumination, respectively, which are assumed to be zero. Here $K_{(T)}$ and $K_{(F)}$ are defined as $K_{(T)} = k_{a(T)} + k_{d(T)} + k_{p(T)}$ and $K_{(F)} = k_{a(F)} + k_{d(F)}$, respectively.

The time-dependent flux of the water-rich permeate under visible light illumination ($J(t_i)$) can be written as⁵⁴:

$$\text{(Equation 3.3)} \quad J(t_i) = \Delta P / [(r_m + R_c/A(1 - f_c(t_i)))\mu]$$

where ΔP and A are the transmembrane pressure and the total surface area of the mesh, respectively. r_m and R_c are the resistance per unit area of the mesh to the permeation of the water-rich permeate originating from the mesh itself and oil contamination, respectively. μ is the dynamic viscosity of the water-rich permeate⁶⁸ (≈ 0.953 mPa-s). By substituting $f_c(t_i)$ in Equation 3.3, we obtain the following equation:

$$\text{(Equation 3.4)} \quad J(t_i) = \Delta P / \left[\left\{ r_m + \frac{R_c}{A} \times \frac{1}{\left(1 - \left(f_{(F)} \left[\frac{k_{a(T)}}{K_{(T)}} - \left(\frac{k_{a(T)}}{K_{(T)}} - f_{c(T)}(t_i=0) \right) e^{-(K_{(T)})t_i} \right] \times f_{(T)} + \left[\frac{k_{a(F)}}{K_{(F)}} - \left(\frac{k_{a(F)}}{K_{(F)}} - f_{c(F)}(t_i=0) \right) e^{-(K_{(F)})t_i} \right] \times f_{(F)} \right) \right) \right\} \mu \right]$$

This equation describes the time-dependent evolution of the water-rich permeate flux through the mesh subjected to oil upon illumination by visible light.

3.3.5. Extraction of r_m , R_c , $f_{c(T)}$, and $f_{c(F)}$

To predict the values of water-rich permeate flux using Equation 3.4 in the main text, we need to determine the values of the resistance per unit area of the mesh to the permeation of water-rich

permeate (r_m), resistance by oil contamination (R_c), as well as the area fraction of the oil-contaminated regions for N-TiO₂ and F-SiO₂ ($f_{c(T)}$ and $f_{c(F)}$) at the time of visible light illumination.

(i) Calculating r_m values: A mesh was first subjected to DI water for 60 mins at $\Delta P = 13.0 \text{ kPa} \pm 0.7 \text{ kPa}$ by using the cross-flow apparatus. The J ($t=60\text{mins}$) values were measured. Given that the r_m is expressed by

$$\text{(Equation 3.5)} \quad r_m = \frac{\Delta P}{(J(t))\mu}$$

we obtain the r_m value by plugging in $\Delta P = 13.0 \text{ kPa}$ and J (t). Note that the R_c and $f_{c(t=60\text{mins})}$ are zero. **Table 3.1** lists the r_m values for the mesh coated with N-TiO₂/F-SiO₂ with varied compositions.

Table 3.1. The measured r_m values of the mesh coated with N-TiO₂/F-SiO₂ with varied compositions.

N-TiO ₂ /F-SiO ₂ composition	r_m (L ⁻¹ m ²)
N-TiO ₂ /F-SiO ₂ (50 wt%)	43333 ± 500
N-TiO ₂ /F-SiO ₂ (75 wt%)	38172 ± 500
N-TiO ₂ /F-SiO ₂ (100 wt%)	29917 ± 300

(ii) R_c values: A mesh was subjected to n-hexadecane-in-water emulsion (1:9 volumetric ratio, n-hexadecane: water) that was stabilized by sodium dodecyl sulfate (SDS) for 60 mins at $\Delta P = 13.0 \text{ kPa} \pm 0.7 \text{ kPa}$ using a cross-flow apparatus. By rearranging Equation 3.3, the R_c is given as

(Equation 3.6)

$$R_c = A \left(\frac{\Delta P}{(J(t))\mu} - r_m \right) \left(1 - \left(f_{(F)} \left[\frac{k_{a(T)}}{k_{a(T)}+k_{d(T)}+k_{p(T)}} - \left(\frac{k_{a(T)}}{k_{a(T)}+k_{d(T)}+k_{p(T)}} - f_{c(T)}(0) \right) e^{-(k_{a(T)}+k_{d(T)}+k_{p(T)})t} \right] \times f_{(T)} \right) + \left[\frac{k_{a(F)}}{k_{a(F)}+k_{d(F)}} - \left(\frac{k_{a(F)}}{k_{a(F)}+k_{d(F)}} - f_{c(F)}(0) \right) e^{-(k_{a(F)}+k_{d(F)})t} \right] \times f_{(F)} \right) \right)$$

We obtain the R_c values by plugging in the same variables that were used in R_c measurement (i.e., in $\Delta P = 13.0$ kPa, $A = 42$ cm², and r_m values of respective mesh). The R_c values listed in **Table 3.1** were also used. The calculated R_c values for the mesh coated with N-TiO₂/F-SiO₂ with varied compositions are in **Table 3.2**.

Table 3.2. The measured R_c values of the mesh coated with varied compositions of N-TiO₂/F-SiO₂.

N-TiO ₂ /F-SiO ₂ composition	R_c (L ⁻¹ m ⁴)
N-TiO ₂ /F-SiO ₂ (50 wt%)	16.9 ± 0.6
N-TiO ₂ /F-SiO ₂ (75 wt%)	20.4 ± 0.5
N-TiO ₂ /F-SiO ₂ (100 wt%)	23.4 ± 0.6

(iii) $f_{c(T)}(t)$ and $f_{c(F)}(t)$ values: We determined the values of $f_{c(T)}(t)$ and $f_{c(F)}(t)$ at the time of visible light illumination by plugging the values of rate constants (i.e., k_a , k_d , and k_p) and $\theta^*_{w,o}$ in Equation 3.7. **Table 3.3** lists the computed values of $f_{c(T)}$ and $f_{c(F)}$ ($t = 90$ mins, at the time of light illumination), as well as the measured values of $\theta^*_{w,o}$.

Table 3.3. The computed values of the $f_{c(T)}$ and $f_{c(F)}$, as well as the measured values of $\theta_{w,o}^*$ for the mesh coated with N-TiO₂/F-SiO₂ with varied compositions at the onset of visible light illumination ($t = 90$ mins).

N-TiO ₂ /F-SiO ₂ composition	$\theta_{w,o}^*$	$f_{c(T)}$ ($t = 90$ minutes)	$f_{c(F)}$ ($t = 90$ minutes)
N-TiO ₂ /F-SiO ₂ (50 wt%)	$89^\circ \pm 3^\circ$	0.80	0.1
N-TiO ₂ /F-SiO ₂ (75 wt%)	$46^\circ \pm 1^\circ$	0.80	0.1
N-TiO ₂ /F-SiO ₂ (100 wt%)	$63^\circ \pm 3^\circ$	0.80	-

The values of k_a and k_d can be determined by analyzing the time-dependent evolution of the $\theta_{w,o}^*$ values in the dark, whereas the k_p values can be determined under visible light illumination. In our recent work²², we demonstrated that these rate constants (k_a , k_d , and k_p) could be related to the measured $\theta_{w,o}^*$ values on a photocatalytic surface. Here, we develop a new relation by considering

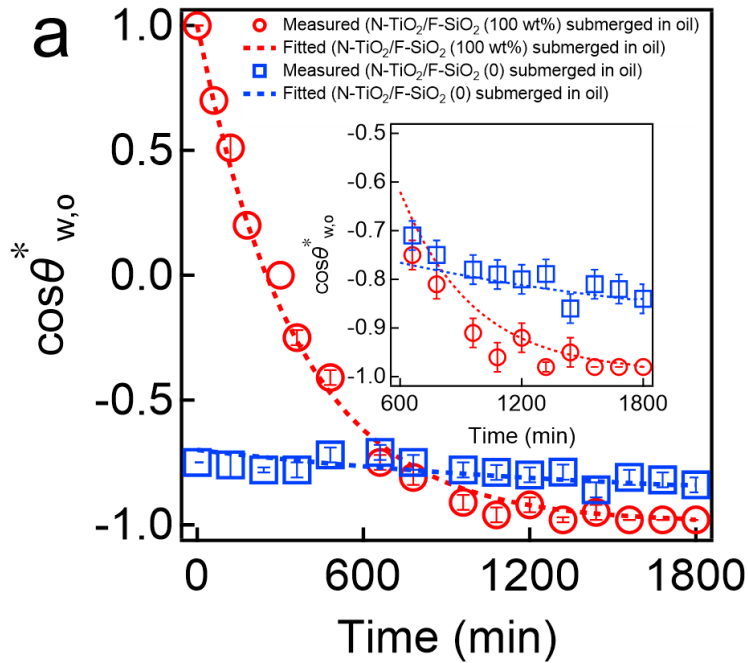


Figure 3.8. Plots of the cosine values of the measured apparent water contact angle ($\theta_{w,o}^*$) on an N-TiO₂ surface and an F-SiO₂ surface submerged in oil (n-hexadecane) as a function of submerging time. The values of k_a and k_d for oil on N-TiO₂ and F-SiO₂ surfaces were determined by fitting equation (5). Inset: Zoomed-in plot of the $\cos \theta_{w,o}^*$ data.

that our mesh surface is heterogeneous, consisting of photocatalytic N-TiO₂ and inert (i.e., non-catalytic) F-SiO₂. By integrating the Langmuir–Hinshelwood kinetics for photocatalysis^{22, 30} and the Cassie–Baxter wettability analysis⁵³ on a chemically heterogeneous mesh surface, we can obtain a relation given as:

$$\text{(Equation 3.7)} \quad \cos\theta_{w,o}^* = 1 - 2 \left(\left[\frac{k_{a(T)}}{K(T)} - \left(\frac{k_{a(T)}}{K(T)} - f_{c(T)}(t_i = 0) \right) e^{-(K(T))t_i} \right] \times f_{(T)} + \left[\frac{k_{a(F)}}{K(F)} - \left(\frac{k_{a(F)}}{K(F)} - f_{c(F)}(t_i = 0) \right) e^{-(K(F))t_i} \right] \times f_{(F)} \right)$$

The values of k_a , k_d , and k_p for a given phase (e.g., N-TiO₂ or F-SiO₂) can be obtained by fitting Equation 3.5 to the cosine values of the experimentally measured $\theta_{w,o}^*$ values. **Figure 3.8** shows a plot of the cosine values of the experimentally measured $\theta_{w,o}^*$ on N-TiO₂ and F-SiO₂ surfaces submerged in oil as a function of submerging time. Note that we utilized the $\theta_{w,o}^*$ values of N-

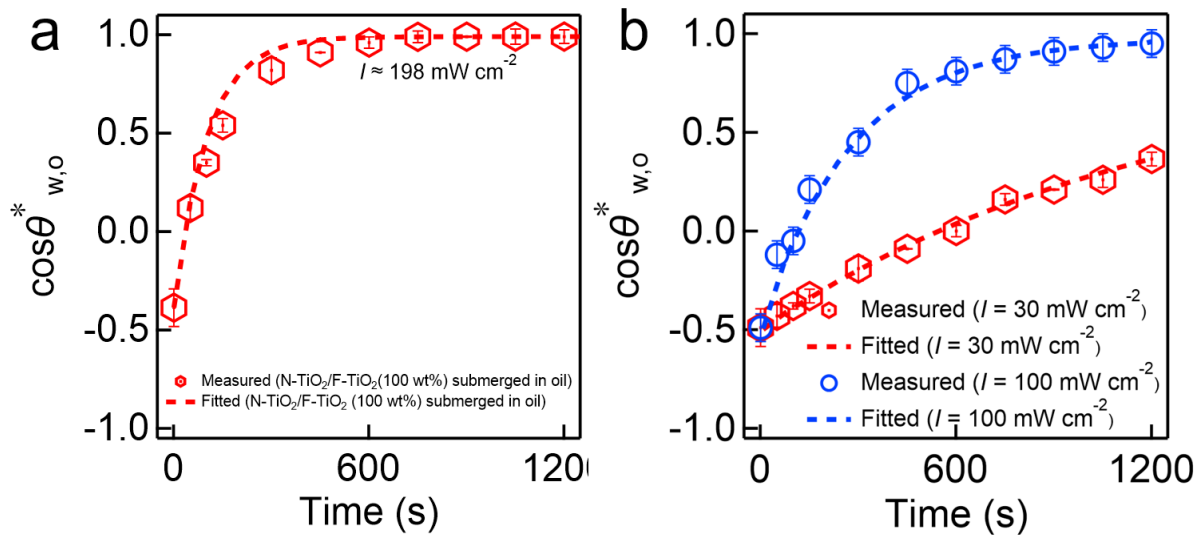


Figure 3.9. (a) A plot of the cosine values of the measured apparent water contact angle ($\theta_{w,o}^*$) on an N-TiO₂ surface submerged in oil as a function of visible light illumination ($I = 198 \text{ mW cm}^{-2}$) time. The k_p value for N-TiO₂ was determined by fitting Equation 3.5. (b) Plot of the cosine values of the measured apparent water contact angle ($\theta_{w,o}^*$) on N-TiO₂ surface submerged in oil as a function of visible light illumination ($I = 30$ and 100 mW cm^{-2}) time.

TiO₂/F-SiO₂ (100%) shown in **Figure 3.3**. We obtained the values of k_a and k_d for oil on an N-TiO₂ surface as $k_{a(T)} = 4.65 \times 10^{-5} \text{ s}^{-1}$ and $k_{d(T)} = 2.3 \times 10^{-7} \text{ s}^{-1}$, respectively, while those on an F-SiO₂ surface were $k_{a(F)} = 9.54 \times 10^{-6} \text{ s}^{-1}$ and $k_{d(F)} = 4.06 \times 10^{-7} \text{ s}^{-1}$, respectively. Please note that the k_a value for oil on an F-SiO₂ surface is an order of magnitude lower than that on an N-TiO₂ surface, which clearly indicates that F-SiO₂ is more resistant to oil adsorption.

Similarly, the k_p value can be obtained by fitting Equation 3.5 to the cosine values of the experimentally measured time-dependent $\theta_{w,o}^*$ on a surface that was submerged in oil and placed under visible light illumination (**Figure 3.9a**). Note that the $\theta_{w,o}^*$ values of N-TiO₂/F-SiO₂ (100%) shown in **Figure 3.3b** were utilized. The $k_{p(T)}$ value for N-TiO₂ is $9.8 \times 10^{-3} \text{ s}^{-1}$ which is two orders of magnitude higher than the $k_{a(T)}$ value ($k_{a(T)} = 4.65 \times 10^{-5} \text{ s}^{-1}$). Thus, it can be inferred that N-TiO₂ can rapidly clean itself upon visible light illumination despite being submerged in oil. Note that the k_p value for the F-SiO₂ surface (i.e., $k_{p(F)}$) is zero. We also determined the k_p values for the N-TiO₂ surface upon being irradiated by visible light with varying intensities ($I = 30$ and 100 mW cm^{-2}) by fitting Equation 3.5 in the main text to the cosine values of the experimentally measured $\theta_{w,o}^*$ values (**Figure 3.9b**). The k_p values were obtained as $3.5 \times 10^{-4} \text{ s}^{-1}$ and $8.9 \times 10^{-3} \text{ s}^{-1}$ for $I = 30$ and 100 mW cm^{-2} , respectively. Note that the highest intensity using our light source is $I = 198 \text{ mW cm}^{-2}$.

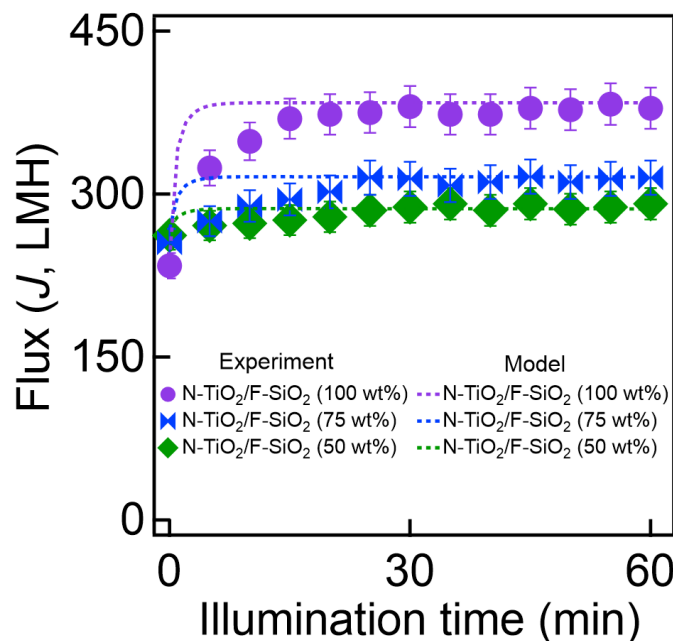


Figure 3.10. The measured and the predicted values of water-rich permeate flux (J) by using Equation 3.4 through the meshes coated with varied compositions of N-TiO₂/F-SiO₂ under visible light illumination ($I = 198 \text{ mW cm}^{-2}$).

3.3.6. Prediction of the flux

Finally, we calculated the $J(t_i)$ values for the mesh coated with varied compositions of N-TiO₂/F-SiO₂ by using the values of k_a , k_d , and k_p in Equation 3.4 and compared them with the experimentally measured values. **Figure 3.10** shows that they match reasonably well with a goodness of fit equal to 0.92.

3.4. Conclusions

In summary, a photocatalytic mesh with selective wettability for water over oil was developed by coating a mixture of N-TiO₂/F-SiO₂ onto a surface of a stainless steel mesh. The mesh was utilized to study the kinetics of the water-rich permeate flux as a result of the photocatalytic degradation of the surface-adsorbed oil under visible light illumination. A mathematical model was derived by integrating the Langmuir–Hinshelwood kinetics of photocatalysis and the Cassie–Baxter wettability analysis on a chemically heterogeneous surface into a permeate flux relation. Finally,

this model demonstrated that it could predict the evolution of the water-rich permeate flux through the photocatalytic mesh with a goodness of fit of 0.92. We envision that the outcomes of this study can find applicability in designing and optimizing photocatalytic membranes for multiphase interfacial engineering applications such as oil-water separation.

3.5. References

1. Etchepare, R.; Oliveira, H.; Azevedo, A.; Rubio, J., Separation of emulsified crude oil in saline water by dissolved air flotation with micro and nanobubbles. *Separation and Purification Technology* **2017**, *186*, 326-332.
2. Vocciante, M.; Bagatin, R.; Ferro, S., Enhancements in electrokinetic remediation technology: focus on water management and wastewater recovery. *Chemical Engineering Journal* **2017**, *309*, 708-716.
3. Ezazi, M.; Shrestha, B.; Kim, S. I.; Jeong, B.; Gorney, J.; Hutchison, K.; Lee, D. H.; Kwon, G., Selective Wettability Membrane for Continuous Oil– Water Separation and In Situ Visible Light - Driven Photocatalytic Purification of Water. *Global Challenges* **2020**, *4* (10), 2000009.
4. Jiang, C.; Liu, W.; Yang, M.; Liu, C.; He, S.; Xie, Y.; Wang, Z., Robust multifunctional superhydrophobic fabric with UV induced reversible wettability, photocatalytic self-cleaning property, and oil-water separation via thiol-ene click chemistry. *Applied Surface Science* **2019**, *463*, 34-44.
5. Kota, A. K.; Kwon, G.; Choi, W.; Mabry, J. M.; Tuteja, A., Hygro-responsive membranes for effective oil–water separation. *Nature communications* **2012**, *3* (1), 1-8.
6. Shrestha, B.; Ezazi, M.; Kwon, G., Engineered Nanoparticles with Decoupled Photocatalysis and Wettability for Membrane-Based Desalination and Separation of Oil-Saline Water Mixtures. *Nanomaterials* **2021**, *11* (6), 1397.
7. Song, S.; Yang, H.; Zhou, C.; Cheng, J.; Jiang, Z.; Lu, Z.; Miao, J., Underwater superoleophobic mesh based on BiVO₄ nanoparticles with sunlight-driven self-cleaning property for oil/water separation. *Chemical Engineering Journal* **2017**, *320*, 342-351.
8. Tetteh, E.; Rathilal, S.; Naidoo, D., Photocatalytic degradation of oily waste and phenol from a local South Africa oil refinery wastewater using response methodology. *Scientific Reports* **2020**, *10* (1), 1-12.
9. Shenvi, S. S.; Isloor, A. M.; Ismail, A., A review on RO membrane technology: Developments and challenges. *Desalination* **2015**, *368*, 10-26.
10. Luttmiah, K.; Verliefde, A.; Roest, K.; Rietveld, L. C.; Cornelissen, E., Forward osmosis for application in wastewater treatment: a review. *Water research* **2014**, *58*, 179-197.
11. Mohammad, A. W.; Teow, Y.; Ang, W.; Chung, Y.; Oatley-Radcliffe, D.; Hilal, N., Nanofiltration membranes review: Recent advances and future prospects. *Desalination* **2015**, *356*, 226-254.
12. Woo, S.; Park, H. R.; Park, J.; Yi, J.; Hwang, W., Robust and continuous oil/water separation with superhydrophobic glass microfiber membrane by vertical polymerization under harsh conditions. *Scientific Reports* **2020**, *10* (1), 1-10.
13. Tummons, E.; Han, Q.; Tanudjaja, H. J.; Hejase, C. A.; Chew, J. W.; Tarabara, V. V., Membrane fouling by emulsified oil: A review. *Separation and Purification Technology* **2020**, *248*, 116919.
14. Guo, W.; Ngo, H.-H.; Li, J., A mini-review on membrane fouling. *Bioresource technology* **2012**, *122*, 27-34.
15. Kovács, I.; Veréb, G.; Kertész, S.; Hodúr, C.; László, Z., Fouling mitigation and cleanability of TiO₂ photocatalyst-modified PVDF membranes during ultrafiltration of model oily wastewater with different salt contents. *Environmental Science and Pollution Research* **2018**, *25* (35), 34912-34921.

16. Qahtan, T. F.; Gondal, M. A.; Dastageer, M. A.; Kwon, G.; Ezazi, M.; Al-Kuban, M. Z., Thermally Sensitized Membranes for Crude Oil–Water Remediation under Visible Light. *ACS Applied Materials & Interfaces* **2020**, *12* (43), 48572-48579.
17. Ali, I.; Gupta, V., Advances in water treatment by adsorption technology. *Nature protocols* **2006**, *1* (6), 2661-2667.
18. Zhang, W.; Luo, J.; Ding, L.; Jaffrin, M. Y., A review on flux decline control strategies in pressure-driven membrane processes. *Industrial & Engineering Chemistry Research* **2015**, *54* (11), 2843-2861.
19. Chen, J. P.; Kim, S.; Ting, Y., Optimization of membrane physical and chemical cleaning by a statistically designed approach. *Journal of membrane Science* **2003**, *219* (1-2), 27-45.
20. Wang, Z.; Ma, J.; Tang, C. Y.; Kimura, K.; Wang, Q.; Han, X., Membrane cleaning in membrane bioreactors: a review. *Journal of membrane science* **2014**, *468*, 276-307.
21. Zsirai, T.; Buzatu, P.; Aerts, P.; Judd, S., Efficacy of relaxation, backflushing, chemical cleaning and clogging removal for an immersed hollow fibre membrane bioreactor. *Water research* **2012**, *46* (14), 4499-4507.
22. Panchanathan, D.; Kwon, G.; Qahtan, T. F.; Gondal, M. A.; Varanasi, K. K.; McKinley, G. H., Kinetics of photoinduced wettability switching on nanoporous titania surfaces under oil. *Advanced Materials Interfaces* **2017**, *4* (21), 1700462.
23. Liu, Y.; Su, Y.; Li, Y.; Zhao, X.; Jiang, Z., Improved antifouling property of PVDF membranes by incorporating an amphiphilic block-like copolymer for oil/water emulsion separation. *RSC Advances* **2015**, *5* (27), 21349-21359.
24. Zhang, L.; Zhong, Y.; Cha, D.; Wang, P., A self-cleaning underwater superoleophobic mesh for oil-water separation. *Scientific Reports* **2013**, *3* (1), 1-5.
25. Li, Y.; Zhang, H.; Fan, M.; Zheng, P.; Zhuang, J.; Chen, L., A robust salt-tolerant superoleophobic alginate/graphene oxide aerogel for efficient oil/water separation in marine environments. *Scientific reports* **2017**, *7* (1), 1-7.
26. Kaner, P.; Dudchenko, A. V.; Mauter, M. S.; Asatekin, A., Zwitterionic copolymer additive architecture affects membrane performance: fouling resistance and surface rearrangement in saline solutions. *Journal of Materials Chemistry A* **2019**, *7* (9), 4829-4846.
27. Xie, A.; Cui, J.; Yang, J.; Chen, Y.; Dai, J.; Lang, J.; Li, C.; Yan, Y., Photo-Fenton self-cleaning membranes with robust flux recovery for an efficient oil/water emulsion separation. *Journal of Materials Chemistry A* **2019**, *7* (14), 8491-8502.
28. Cheng, X.; Sun, Z.; Yang, X.; Li, Z.; Zhang, Y.; Wang, P.; Liang, H.; Ma, J.; Shao, L., Construction of superhydrophilic hierarchical polyacrylonitrile nanofiber membranes by in situ asymmetry engineering for unprecedentedly ultrafast oil–water emulsion separation. *J. Mater. Chem. A* **2020**.
29. Nishimoto, S.; Sawai, Y.; Kameshima, Y.; Miyake, M., Underwater superoleophobicity of TiO₂ nanotube arrays. *Chemistry Letters* **2014**, *43* (4), 518-520.
30. Foran, P. S.; Boxall, C.; Denison, K. R., Photoinduced superhydrophilicity: a kinetic study of time dependent photoinduced contact angle changes on TiO₂ surfaces. *Langmuir* **2012**, *28* (51), 17647-17655.
31. Yang, J.; Zhang, Z.; Xu, X.; Zhu, X.; Men, X.; Zhou, X., Superhydrophilic–superoleophobic coatings. *Journal of Materials Chemistry* **2012**, *22* (7), 2834-2837.
32. Zhu, X.; Tu, W.; Wee, K.-H.; Bai, R., Effective and low fouling oil/water separation by a novel hollow fiber membrane with both hydrophilic and oleophobic surface properties. *Journal of Membrane Science* **2014**, *466*, 36-44.

33. Huo, J.; Yuan, C.; Wang, Y., Nanocomposites of three-dimensionally ordered porous TiO₂ decorated with Pt and reduced graphene oxide for the visible-light photocatalytic degradation of waterborne pollutants. *ACS Applied Nano Materials* **2019**, *2* (5), 2713-2724.
34. Lee, A.; Libera, J. A.; Waldman, R. Z.; Ahmed, A.; Avila, J. R.; Elam, J. W.; Darling, S. B., Conformal nitrogen - doped TiO₂ photocatalytic coatings for sunlight - activated membranes. *Advanced Sustainable Systems* **2017**, *1* (1-2), 1600041.
35. Tan, B. Y. L.; Juay, J.; Liu, Z.; Sun, D., Flexible Hierarchical TiO₂/Fe₂O₃ Composite Membrane with High Separation Efficiency for Surfactant - Stabilized Oil - Water Emulsions. *Chemistry - An Asian Journal* **2016**, *11* (4), 561-567.
36. Chalasani, R.; Vasudevan, S., Cyclodextrin-functionalized Fe₃O₄@ TiO₂: reusable, magnetic nanoparticles for photocatalytic degradation of endocrine-disrupting chemicals in water supplies. *ACS Nano* **2013**, *7* (5), 4093-4104.
37. Gondal, M. A.; Sadullah, M. S.; Qahtan, T. F.; Dastageer, M. A.; Baig, U.; McKinley, G. H., Fabrication and wettability study of WO₃ coated photocatalytic membrane for oil-water separation: a comparative study with ZnO coated membrane. *Scientific Reports* **2017**, *7* (1), 1-10.
38. Rajeswari, A.; Vismaiya, S.; Pius, A., Preparation, characterization of nano ZnO-blended cellulose acetate-polyurethane membrane for photocatalytic degradation of dyes from water. *Chemical Engineering Journal* **2017**, *313*, 928-937.
39. Zhang, L.; He, Y.; Ma, L.; Chen, J.; Fan, Y.; Zhang, S.; Shi, H.; Li, Z.; Luo, P., Hierarchically stabilized PAN/ β -FeOOH nanofibrous membrane for efficient water purification with excellent antifouling performance and robust solvent resistance. *ACS Applied Materials & Interfaces* **2019**, *11* (37), 34487-34496.
40. Etman, A. S.; Abdelhamid, H. N.; Yuan, Y.; Wang, L.; Zou, X.; Sun, J., Facile water-based strategy for synthesizing MoO_{3-x} nanosheets: efficient visible light photocatalysts for dye degradation. *ACS Omega* **2018**, *3* (2), 2193-2201.
41. Sonkusare, V. N.; Chaudhary, R. G.; Bhusari, G. S.; Mondal, A.; Potbhare, A. K.; Mishra, R. K.; Juneja, H. D.; Abdala, A. A., Mesoporous octahedron-shaped tricobalt tetroxide nanoparticles for photocatalytic degradation of toxic dyes. *ACS Omega* **2020**, *5* (14), 7823-7835.
42. Orooji, Y.; Mohassel, R.; Amiri, O.; Sobhani, A.; Salavati-Niasari, M., Gd₂ZnMnO₆/ZnO nanocomposites: green sol-gel auto-combustion synthesis, characterization and photocatalytic degradation of different dye pollutants in water. *Journal of Alloys and Compounds* **2020**, *835*, 155240.
43. McCullagh, C.; Skillen, N.; Adams, M.; Robertson, P. K., Photocatalytic reactors for environmental remediation: a review. *Journal of Chemical Technology & Biotechnology* **2011**, *86* (8), 1002-1017.
44. Zhang, H.; Wan, Y.; Luo, J.; Darling, S. B., Drawing on Membrane Photocatalysis for Fouling Mitigation. *ACS Applied Materials & Interfaces* **2021**, *13* (13), 14844-14865.
45. Zhang, H.; Mane, A. U.; Yang, X.; Xia, Z.; Barry, E. F.; Luo, J.; Wan, Y.; Elam, J. W.; Darling, S. B., Visible - light - activated photocatalytic films toward self - cleaning membranes. *Advanced Functional Materials* **2020**, *30* (34), 2002847.
46. Guo, J.; Yan, D. Y.; Lam, F. L.-Y.; Deka, B. J.; Lv, X.; Ng, Y. H.; An, A. K., Self-cleaning BiOBr/Ag photocatalytic membrane for membrane regeneration under visible light in membrane distillation. *Chemical Engineering Journal* **2019**, *378*, 122137.
47. Liu, Y.; Shen, L.; Lin, H.; Yu, W.; Xu, Y.; Li, R.; Sun, T.; He, Y., A novel strategy based on magnetic field assisted preparation of magnetic and photocatalytic membranes with improved performance. *Journal of Membrane Science* **2020**, *612*, 118378.

48. Bortot Coelho, F. E.; Gionco, C.; Paganini, M. C.; Calza, P.; Magnacca, G., Control of Membrane Fouling in Organics Filtration Using Ce-Doped Zirconia and Visible Light. *Nanomaterials* **2019**, *9* (4), 534.
49. Heu, R.; Ateia, M.; Yoshimura, C., Photocatalytic Nanofiltration Membrane Using Zr-MOF/GO Nanocomposite with High-Flux and Anti-Fouling Properties. *Catalysts* **2020**, *10* (6), 711.
50. Barmeh, A.; Nilforoushan, M. R.; Otraj, S., Wetting and photocatalytic properties of Ni-doped TiO₂ coating on glazed ceramic tiles under visible light. *Thin Solid Films* **2018**, *666*, 137-142.
51. Zhang, X.; Jin, M.; Liu, Z.; Nishimoto, S.; Saito, H.; Murakami, T.; Fujishima, A., Preparation and photocatalytic wettability conversion of TiO₂-based superhydrophobic surfaces. *Langmuir* **2006**, *22* (23), 9477-9479.
52. Upadhaya, D.; Kumar, P.; Purkayastha, D. D., Tuning the wettability and photocatalytic efficiency of heterostructure ZnO-SnO₂ composite films with annealing temperature. *Materials Science in Semiconductor Processing* **2019**, *95*, 28-34.
53. De Gennes, P.-G.; Brochard-Wyart, F.; Quéré, D., *Capillarity and wetting phenomena: drops, bubbles, pearls, waves*. Springer Science & Business Media: 2013.
54. Coulson, J. M.; Richardson, J. F.; Backhurst, J. R.; Harker, J. H., *Chemical Engineering: Fluid Flow, Heat Transfer and Mass Transfer*. Pergamon press: 1954.
55. Bernhardt, I. C., *Particle size analysis: Classification and sedimentation methods*. Springer Science & Business Media: 1994; Vol. 5.
56. Tuteja, A.; Choi, W.; Mabry, J. M.; McKinley, G. H.; Cohen, R. E., Robust omniphobic surfaces. *Proceedings of the National Academy of Sciences* **2008**, *105* (47), 18200-18205.
57. Ezazi, M.; Shrestha, B.; Kim, S. I.; Jeong, B.; Gorney, J.; Hutchison, K.; Lee, D. H.; Kwon, G., Selective Wettability Membrane for Continuous Oil– Water Separation and In Situ Visible Light - Driven Photocatalytic Purification of Water. *Global Challenges*, 2000009.
58. Li, Y.; He, S.; Zhou, Z.; Zhou, S.; Huang, S.; Fane, A. G.; Zheng, C.; Zhang, Y.; Zhao, S., Carboxylated Nanodiamond-enhanced photocatalytic membranes with improved antifouling and self-cleaning properties. *Industrial & Engineering Chemistry Research* **2020**, *59* (8), 3538-3549.
59. Darcy, H., *Les fontaines publiques de la ville de Dijon: exposition et application*. Victor Dalmont: 1856.
60. Camin, D. L.; Forziati, A. F.; Rossini, F. D., Physical properties of n-hexadecane, n-decylcyclopentane, n-decylcyclohexane, 1-hexadecene and n-decylbenzene. *The Journal of Physical Chemistry* **1954**, *58* (5), 440-442.
61. Mamane, H.; Horovitz, I.; Lozzi, L.; Di Camillo, D.; Avisar, D., The role of physical and operational parameters in photocatalysis by N-doped TiO₂ sol - gel thin films. *Chemical Engineering Journal* **2014**, *257*, 159-169.
62. Mills, A.; Wang, J.; Ollis, D. F., Dependence of the kinetics of liquid-phase photocatalyzed reactions on oxygen concentration and light intensity. *Journal of Catalysis* **2006**, *243* (1), 1-6.
63. Emeline, A. V.; Ryabchuk, V.; Serpone, N., Factors affecting the efficiency of a photocatalyzed process in aqueous metal-oxide dispersions: Prospect of distinguishing between two kinetic models. *Journal of Photochemistry and Photobiology A: Chemistry* **2000**, *133* (1-2), 89-97.
64. Mills, A.; Le Hunte, S., An overview of semiconductor photocatalysis. *Journal of photochemistry and photobiology A: Chemistry* **1997**, *108* (1), 1-35.

65. Wetterer, S.; Lavrich, D.; Cummings, T.; Bernasek, S.; Scoles, G., Energetics and kinetics of the physisorption of hydrocarbons on Au (111). *The Journal of Physical Chemistry B* **1998**, *102* (46), 9266-9275.
66. Pelizzetti, E.; Minero, C.; Maurino, V.; Hidaka, H.; Serpone, N.; Terzian, R., Photocatalytic degradation of dodecane and of some dodecyl derivatives. *Annali Di Chimica* **1990**, *80* (1-2), 81-87.
67. Sturini, M.; Soana, F.; Albini, A., Reaction paths in the titanium dioxide photocatalysed degradation of dodecane and some of its derivatives. *Tetrahedron* **2002**, *58* (15), 2943-2950.
68. Cooper, J.; Dooley, R. *Release of the IAPWS formulation 2008 for the viscosity of ordinary water substance*; The international association for the properties of water and steam 2008.

Chapter 4: Delamination-Free In-Air and Underwater Oil-Repellent Filters for Oil-Water Separation: Gravity-Driven and Cross-Flow Operations

This chapter is adapted from **Paper P3**.

Abstract: Separating oil-water mixtures is critical in a variety of practical applications, including the treatment of industrial wastewater, oil spill cleanups, as well as the purification of petroleum products. Among various methodologies that have been utilized, membranes are the most attractive technology for separating oil-water emulsions. In recent years, selective wettability membranes have attracted particular attention for oil-water separations. The membrane surfaces with hydrophilic and in-air oleophobic wettability have demonstrated enhanced effectiveness for oil-water separations in comparison with underwater oleophobic membranes. However, developing a hydrophilic and in-air oleophobic surface for a membrane is not a trivial task. The coating delamination process is a critical challenge when applying these membranes for separations. Inspired by the above, in this study, we utilize poly(ethylene glycol)diacrylate (PEGDA) and 1H,1H,2H,2H-heptadecafluorodecyl acrylate (F-acrylate) to fabricate a hydrophilic and in-air oleophobic coating on a filter. We utilize methacryloxypropyl trimethoxysilane (MEMO) as an adhesion promoter to enhance the adhesion of the coating to the filter. The filter demonstrates robust oil repellency preventing oil adhesion and oil fouling. Utilizing the filter, gravity-driven and continuous separations of surfactant-stabilized oil-water emulsions are demonstrated. Finally, we demonstrate that the filter can be reused multiple times upon rinsing for further oil-water separations.

4.1. Introduction

Oil-water separation is a crucial step in a wide variety of industries.^{1,2} For example, 140,000 L of oil-contaminated water is produced during conventional mining operations on a daily basis.³ Additionally, oil leakage and spillage during marine transportation not only pose a threat to the marine environment and ecosystem but are a waste of valuable natural resources.^{4,5} Typically, an oil-water mixture can be classified into three categories based on the dispersed phase size (diameter, d)- free oil-water if $d > 150 \mu\text{m}$, as a dispersion if $20 \mu\text{m} < d < 150 \mu\text{m}$, or as an emulsion if $d < 20 \mu\text{m}$.⁶ Oil-water emulsions are stable in the presence of the adsorbed interface-active chemicals (e.g., surfactant).⁷ Spontaneous separation of stable oil-water emulsions can be impractically time-consuming. Further, the separation process becomes more challenging with the decrease in the size of the dispersed phase.⁸

There have been extensive efforts devoted to developing effective separation technologies for oil-water emulsions.⁸ Membrane-based technologies are the most attractive because they can separate oil and water without requiring chemical additives⁹⁻¹⁴; thus, they are relatively energy-saving and applicable to a broad range of industrial effluents.¹⁵⁻¹⁷ The working principle and operation of these technologies are simple. A membrane can regulate the transportation of two phases (e.g., oil and water) by allowing the selective passage of one phase while inhibiting the permeation of another phase.^{18,19} Various methods have been employed to enable the permeation of one phase through a membrane while repelling another phase. For example, a careful modulation of the applied pressure can overcome the hydraulic resistance of one phase while being insufficient for another phase.^{11, 14, 20, 21} Additionally, we^{20, 21}, and others²²⁻²⁴ have demonstrated that a water-in-oil emulsion can be demulsified upon applying an electric field due to the coalescence of the dispersed water droplets. The resulting free oil and water can be readily separated under gravity.

While membranes have become an industry benchmark to compare the performance of conventional separation technologies, they are limited by fouling when continuously operated.^{13, 14, 25-27} When a membrane is subjected to an oil-water mixture, oils, and organic substances are deposited onto its surface. This membrane fouling can result in a decrease in permeability over time²⁸. To compensate for this compromised performance, membrane operation often requires an increase in the applied transmembrane pressure (i.e., TMP, the pressure gradient generated across the two opposite membrane sides²⁹), which results in an increase in the energy consumption.³⁰ In some instances, the oil-water mixture treatment system becomes oversized to compensate for the permeate flux loss.³⁰ Further, due to fouling, membranes undergo periodic cleaning protocols that include backwashing, forward washing, and chemically enhanced cleaning to restore membrane permeability.³¹ Although these cleaning protocols allow a membrane to restore its inherent

permeability and selectivity, they may shorten the membrane's lifespan due to mechanical or chemical damage.^{32, 33}

The development of fouling-resistant membranes has been an active research topic for decades.^{34,}

³⁵ A membrane with hydrophilic (i.e., water contact angle, $\theta_{\text{water}} < 90^\circ$) or superhydrophilic ($\theta_{\text{water}} = 0^\circ$) wettability can retain a hydration layer on its surface when subjected to water, which can reduce the adhesion of organic substances such as oil.^{20, 36} While these membranes show resistance to oil fouling, they become vulnerable when a hydration layer disappears.³⁷ For example, the hydration layer can be evaporated or compromised due to a large exerted drag force (e.g., applied pressure), which results in direct contact and deposition of an oily phase on the membrane surface.^{38, 39}

Hydrophilic and in-air oleophobic (i.e., oil contact angle, $\theta_{\text{oil}} > 90^\circ$) membranes can overcome this limitation by providing oil repellency, not only underwater but also in the air^{20, 40}. This enables them to exhibit unique features in oil-water separations. For example, there is no need to prewet the membrane to introduce a hydration layer. Additionally, water-in-oil emulsions can be separated without prewetting as long as the breakthrough pressure for oil (P_b , i.e., the lowest applied pressure required to force a liquid permeation through a porous filter) is higher than the operating pressure. Fabricating a hydrophilic and in-air oleophobic membrane requires one to reconcile two conflicting design criteria. It should possess low solid surface energy to repel oil, while water should wet the surface. Given that the water surface tension ($\gamma_{\text{lv}} = 72.1 \text{ mN m}^{-1}$, $T = 22 \text{ }^\circ\text{C}$) is higher than that of oils ($\gamma_{\text{lv}} = 20\text{-}30 \text{ mN m}^{-1}$, $T = 22 \text{ }^\circ\text{C}$), a large volume of reports^{9, 41-46} have utilized materials composed of a low surface energy component along with a hydrogen-bond-capable hydrophilic moiety as the membrane coating to achieve selective wettability for water over oil^{20, 47-51}. For example, Brown et al.⁵² utilized a fluorosurfactant as a low surface energy material

and poly(diallyl dimethylammonium chloride) (PDDA) for hydrophilic moieties. Yang et al.⁴⁹ fabricated a membrane coated with a mixture of PDDA, chitosan, and perfluorooctanoic acid (PFOA). These surfaces often exhibit selective reconfiguration of the coating components. Upon contact with water, a hydrophilic component will expand to the surface for enthalpic gain, while a low surface energy material (e.g., fluorinated moiety) minimizes its contact with water.^{20, 47} When oil comes into contact, the surface reverts back to its inherent configuration to lower the overall free energy.

Utilizing surface reconfiguration, herein, we report on a superhydrophilic and in-air oleophobic filter by grafting a composite mixture of poly(ethylene glycol)diacrylate (PEGDA) and 1H,1H,2H,2H-heptadecafluorodecyl acrylate (F-acrylate) via silane chemistry. This enables the resulting coating (F-PEGDA) to firmly attach to the filter surface. The filter exhibits ultralow oil adhesion forces, both in air and underwater, which results in resistance to oil fouling during oil-water separation. Utilizing this filter, separation of surfactant-stabilized oil-in-water and water-in-oil emulsions is demonstrated. Finally, we demonstrate that the filter can be reused multiple times upon cleansing for further oil-water separations.

4.2. Experimental procedure

4.2.1. Grafting MEMO on the filter surface.

The filters with pore size of 6 μm (Whatman Grade 3, Whatman, Marlborough, MA, US) and 2 μm (Whatman Grade 602h) were rinsed with DI water followed by drying at room temperature. They were dip-coated in a 10 wt.% methacryloxypropyl trimethoxysilane (MEMO) solution in methanol for 30 min. Subsequently, the dip-coated filters were heated using a hot plate at 60° C for 1 h. Finally, the filters were thoroughly rinsed using DI water and ethanol to remove any unreacted MEMO molecules.

4.2.2. Coating F-PEGDA on filter.

A solution of F-PEGDA was prepared by adding PEGDA, F-acrylate, and Darocur 1173 (Photo-initiator) to water with an overall concentration of 30 mg ml^{-1} . The MEMO-grafted filters were then dip-coated in F-PEGDA solution for 30 min. Varying compositions of PEGDA and F-acrylate (i.e., 0, 20, 40, 60, 80, and 100 wt.% of F-acrylate) were utilized. Note that the concentration of Darocur 1173 was maintained at 5.0 wt.% with respect to the PEGDA and F-acrylate mixture. Consequently, the filters were removed and exposed to UV light (100 W, $\lambda = 365 \text{ nm}$, Analytikjena, Upland, CA, USA) for 5 min.

4.2.3. Measuring pore size of filters.

A capillary flow porometer (Particle Technology Labs, Downers Grove, IL, USA) was utilized to measure the nominal size and the distribution of the filter pores, as described elsewhere⁵³. A commercial wetting liquid (Porefil) was utilized to wet the filter. The nitrogen gas pressure and flow were controlled and recorded using a pressure transducer and a flow meter, respectively.

4.2.4. Determining the nominal pore size of the mesh.

Filter retention analysis^{9, 54} was utilized to determine the nominal pore size of the mesh. We sequentially fed monodisperse SiO_2 particles with various diameters to the mesh in the order of the lowest to the highest diameter. We calculated the proportion of the particles retained on the mesh for each diameter according to $\%R = M_R/M_T$, where M_R and M_T are the mass of SiO_2 retained on the mesh and the total mass of that introduced to the mesh, respectively. We assigned the diameter of SiO_2 as the nominal pore size of the mesh if $\%R$ exceeds 50% for that particular diameter. Note that we used SiO_2 particles with diameters of 120, 150, 200, 300, 400, 500, 600, and 750 nm and prepared suspensions in ethanol with a concentration of 50 mg mL^{-1} . We measured the $\%R$ as 66, 69, and 71%, with the SiO_2 possessing a diameter of 400 nm for meshes

coated with N-TiO₂/F-SiO₂ mixture with 50, 75, and 100 wt% of N-TiO₂, respectively. Therefore, 400 nm was assigned as the nominal pore size of meshes.

4.2.5. Contact angle measurement.

A Ramé-Hart 200-F1 goniometer (Ramé-Hart, Succasunna, NJ, USA) was employed to measure the advancing and receding contact angles of liquid droplets ($\approx 5 \mu\text{L}$) on the filter surfaces. The initial advancing contact angle for water was measured based on the instantaneous value observed when a water droplet first contacted a filter surface, while the initial receding water contact angle was measured by gradually withdrawing a small volume of water from the same droplet. The time-dependent advancing and receding water contact angle measurements were conducted in a controlled environment ($T = 22^\circ \pm 1^\circ$, relative humidity = $79\% \pm 4\%$) to minimize the evaporation effect. A sessile water droplet was placed on a filter surface, followed by periodic measurements of contact angles. The measurements were conducted three times to ensure the accuracy of the values. The typical error in the goniometry was $\pm 2^\circ$.

4.2.6. Zeta potential measurements.

Zeta potential measurements were conducted using a Brookhaven ZetaPALS instrument, Holtsville, NY, USA.⁵⁵ The electrophoretic velocity was calculated using a laser light-scattering phase analyzer. Then, the Smoluchowski model was utilized to calculate the zeta potential values.

4.2.7. Synthesis of oil-water emulsions.

An optical profiler (Veeco Wyko NT 1100) was utilized to measure the root mean square (RMS) surface roughness of coated meshes. The scan rate was set to 50 nm s^{-1} . The scanned area was $5 \mu\text{m} \times 5 \mu\text{m}$.

4.2.8. Dispersed phase size measurements:

The average size of the dispersed phase in an emulsion was characterized using dynamic light scattering (DLS) (ZetaPALS, Brookhaven Instruments, Holtsville, NY, USA).

4.2.9. Filter surface topology characterization

The PEGDA-coated filter surface's morphology was characterized using an SEM (FEI Versa 3D DualBeam, Hillsboro, OR, USA). A thin layer of gold (≈ 7 nm) was applied to the filter surface.

4.2.10. Underwater adhesion force measurements

A small piece of a filter (4 cm^2) was attached to the bottom of the container. The container was filled with DI water. Subsequently, a needle tip holding a droplet of n-hexadecane ($\approx 5 \mu\text{L}$) was immersed in the water (3 cm below the water surface). Then, the entire container was gradually elevated at a constant speed (6.0 mm min^{-1}) until the filter contacted the oil droplet. Subsequently, the container was gradually descended to detach the oil droplet from the filter. The force between the oil and filter surface was recorded using Data-Physics DCAT 11 (Data Physics, Filderstadt, Germany). The adhesion force was determined by force at the detachment point.

4.2.11. Thermogravimetric analyses (TGA).

PerkinElmer PYRIS 1 (PerkinElmer, Waltham, MA, USA) was utilized for TGA measurements. A sample ($\approx 50 \text{ mg}$) was heated to $110 \text{ }^\circ\text{C}$ at a rate of $5 \text{ }^\circ\text{C}$ per minute, then the temperature was maintained for 60 min. The TGA data were compared with the data for DI water and as-obtained n-hexadecane to measure the purity of the permeate or retentate after the separation.

4.2.12. Continuous separation apparatus.

We utilized a custom-made apparatus^{9, 10} for the continuous separation experiments. The apparatus consisted of a cross-flow cell CF042A, Sterlitech, Kent, WA, USA) connected to a container that stored the feed emulsion, a peristaltic pump (Model 2002, Vector, Minneapolis, MN, USA), a

differential pressure gauge (DPG409-500DWU, OMEGA, Stamford, CT, USA), and a permeate tank. A filter (surface area $\approx 42 \text{ cm}^2$) was mounted to the cell. The feed oil-water emulsion was supplied from one side (feed-in) of the apparatus while the permeate was collected at the opposite side of the apparatus. Note that the raffinate was readded to the feed emulsion storage container.

4.3. Results and discussion

4.3.1. Fabrication of a hydrophilic and in-air oleophobic filter.

We fabricated a hydrophilic and in-air oleophobic filter by coating it with F-PEGDA, utilizing filters with nominal pore sizes of $6.0 \mu\text{m}$ and $2.0 \mu\text{m}$ (**Experimental procedure**). Note that we utilized varying compositions of PEGDA and F-acrylate, while the photo-initiator concentration remained at 5.0 wt.% with respect to the mass of the PEGDA and F-acrylate mixture. The filters were irradiated by a long-wavelength ultraviolet (UV) light, which resulted in the grafting of F-PEGDA to the MEMO-treated filter surface (**Figure 4.1a**).

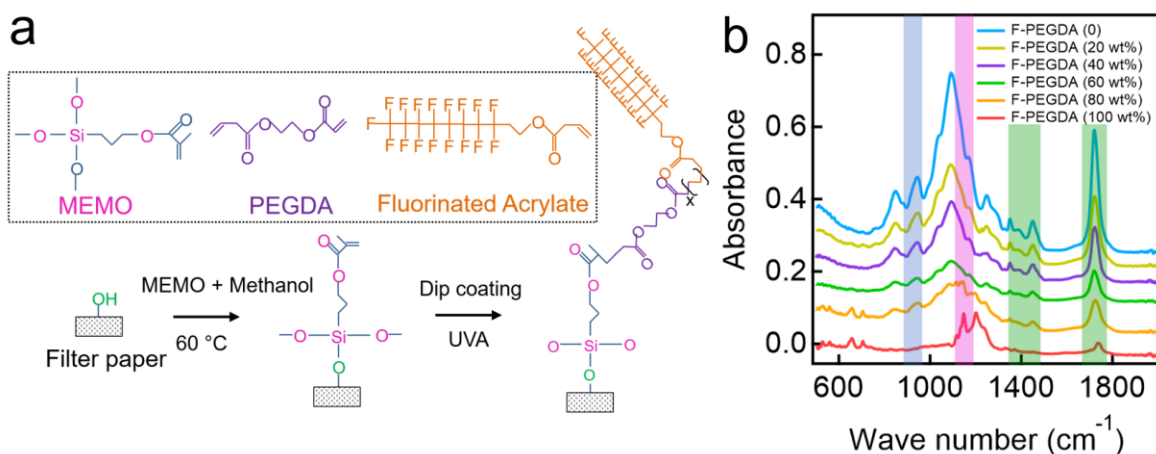


Figure 4.1. Schematic demonstrating the grafting of the filter surface with MEMO and the subsequent coating with F-PEGDA. (b) FT-IR survey spectra of F-PEGDA prepared with varied compositions of F-acrylate.

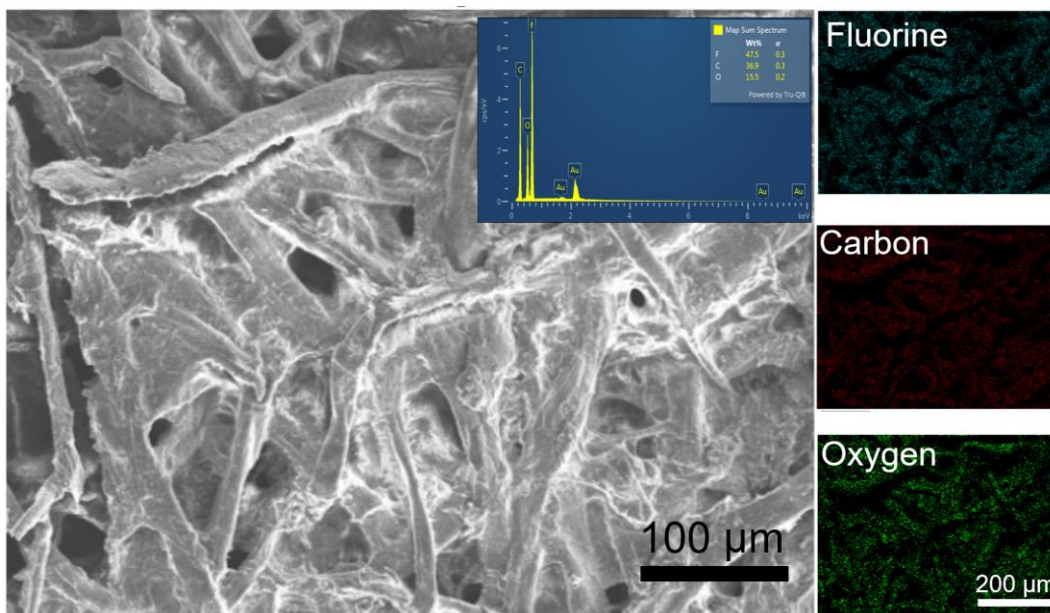


Figure 4.2. SEM image showing the morphology of the filter after coating with F-PEGDA (20 wt.%). Inset shows the elemental EDS spectrum and the elemental mappings for fluorine, carbon and oxygen.

To verify the chemical structure of F-PEGDA, the FT-IR analysis was conducted using a Perkin Elmer Spectrum 400 Spectrometer. The FT-IR spectra were recorded at a resolution of 4 cm^{-1} for 16 scans. **Figure 4.1b** demonstrates the survey spectra of F-PEGDA prepared with varied compositions of F-acrylate. Peaks appearing at $\approx 1205\text{ cm}^{-1}$ and 1149 cm^{-1} (pink shade) confirm the presence of fluorine moieties ($-\text{CF}_2$).⁵⁶ The fluorine moieties are critical for lowering the overall solid surface free energy. Note that these peaks become more prominent as the F-acrylate concentration increases in the F-PEGDA. Peaks corresponding to the hydroxyl group ($-\text{OH}$, 948 cm^{-1} , blue shade) and carbonyl group ($-\text{CO}$, $1440\text{--}1395\text{ cm}^{-1}$ and 1720 cm^{-1} , green shades) are also shown in FT-IR spectra.^{57, 58}

We analyzed the filter surface's morphology using scanning electron microscopy (SEM) (**Figure 4.2**). It was clear that the surface morphology remained nearly unaffected after coating with F-PEGDA. Additionally, the uniform coating of F-PEGDA on the filter surface was verified by the

energy-dispersive spectroscopy (EDS) analysis. The EDS elemental mapping demonstrated a uniform coverage of fluorine (F) across the filter surface (**Figure 4.2**, insets).

4.3.2. Pore size measurement

It is critical to ensure that the F-PEGDA coating has a negligible effect on the pore size of the filters. We measured the nominal pore size of the filters after coating with F-PEGDA (**Table 4. 1**). The results indicated that filters coated with F-PEGDA with a higher PEGDA composition demonstrate more decreased pore sizes. For example, the filter coated with F-PEGDA with 20 wt.% F-acrylate (F-PEGDA (20 wt.%)) exhibited a pore size of $5.0 \mu\text{m} \pm 0.5 \mu\text{m}$, while the filter coated with F-PEGDA (80 wt.%) showed $5.5 \mu\text{m} \pm 0.5 \mu\text{m}$. We attributed this to an increase in the viscosity of the coating solution with an increase in the PEGDA composition (i.e., a decrease in the F-acrylate composition), which resulted in an increase in the coating thickness.

Table 4.1. The pore size of as-purchased filters and those coated with F-PEGDA with various F-acrylate compositions.

Filter	Pore size	
As-purchased	6.0 μm	2.0 μm
F-PEGDA (0)	$4.8 \pm 0.5 \mu\text{m}$	$0.9 \pm 0.2 \mu\text{m}$
F-PEGDA (5 wt.%)	$4.8 \pm 0.3 \mu\text{m}$	$0.9 \pm 0.1 \mu\text{m}$
F-PEGDA (10 wt.%)	$4.9 \pm 0.3 \mu\text{m}$	$1.0 \pm 0.1 \mu\text{m}$
F-PEGDA (15 wt.%)	$5.0 \pm 0.4 \mu\text{m}$	$1.0 \pm 0.3 \mu\text{m}$
F-PEGDA (20 wt.%)	$5.0 \pm 0.3 \mu\text{m}$	$1.0 \pm 0.4 \mu\text{m}$
F-PEGDA (40 wt.%)	$5.2 \pm 0.5 \mu\text{m}$	$1.2 \pm 0.2 \mu\text{m}$
F-PEGDA (60 wt.%)	$5.3 \pm 0.5 \mu\text{m}$	$1.4 \pm 0.3 \mu\text{m}$
F-PEGDA (80 wt.%)	$5.5 \pm 0.4 \mu\text{m}$	$1.5 \pm 0.5 \mu\text{m}$
F-PEGDA (100 wt.%)	$5.6 \pm 0.1 \mu\text{m}$	$1.6 \pm 0.5 \mu\text{m}$

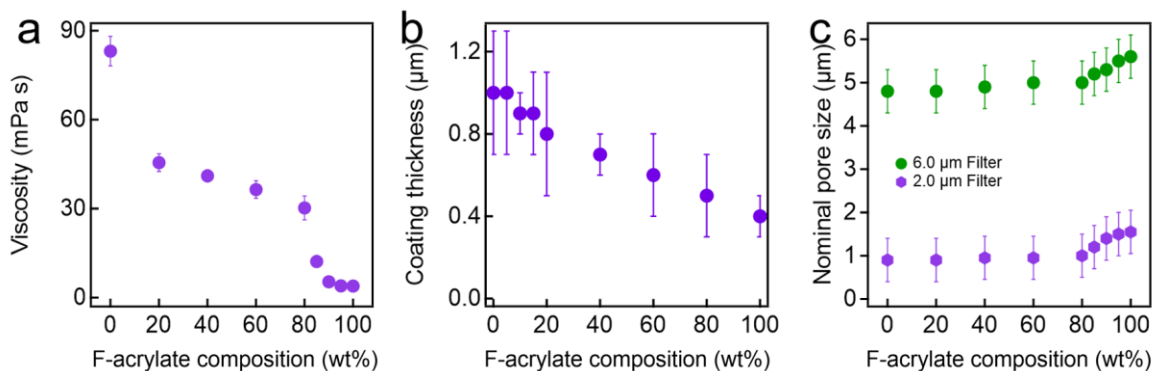


Figure 4.3. (a) The measured viscosity values of F-PEGDA solutions as a function of F-acrylate compositions. (b) The thickness of F-PEGDA coating as a function of F-acrylate compositions. (c) The nominal pore size of the resulting filters after F-PEGDA coating.

Figure 4.3a demonstrates a plot of the viscosity as a function of F-acrylate composition in the F-PEGDA solution. The viscosity of the solution increases with a decrease in the F-acrylate composition. We attribute this to a higher viscosity value of PEGDA in comparison to F-acrylate. We also found that an F-PEGDA coating solution with higher viscosity results in a coating with a higher thickness (**Figure 4.3b**). As a consequence, the effective pore size of a filter is also affected by the coating solution viscosity. **Figure 4.3c** shows that as F-acrylate composition decreases in the F-PEGDA coating solution, the nominal pore size of the resulting filter decreases as well. Based on these measurements, we anticipate that our F-PEGDA coating can be applied to a filter with a pore size of $\approx 1 \mu\text{m}$ or greater without resulting in a complete pore-clogging.

4.3.3. Wettability, surface energy, underwater oil adhesion force, and breakthrough pressure measurement

The wettability of our F-PEGDA-coated filters was analyzed by measuring the apparent contact angles for water (deionized (DI) water, $\gamma_{lv} = 72.1 \text{ mN m}^{-1}$, $T = 22 \text{ }^\circ\text{C}$) and oil (n-hexadecane, $\gamma_{lv} = 27.5 \text{ mN m}^{-1}$, $T = 22 \text{ }^\circ\text{C}$) in the air (**Figure 4.4**). The results showed that the filter (inherent nominal pore size = $6.0 \mu\text{m}$) coated with F-PEGDA with a higher F-acrylate composition exhibited higher oil apparent contact angles. When the composition reached 20 wt.%, the advancing ($\theta_{\text{oil,adv}}^*$)

($\theta_{oil,adv}^*$) and receding ($\theta_{oil,rec}^*$) ($\theta_{oil,rec}^*$) apparent contact angles for oil were measured as $131^\circ \pm 3^\circ$ and $108^\circ \pm 3^\circ$, respectively, while those for water remained at zero ($\theta_{water,adv}^* = 0$ and $\theta_{water,rec}^* = 0$). Further increases in the F-acrylate composition in F-PEGDA had a negligible effect on the oil's apparent contact angles, which can be attributed to the complete coverage of the filter surface by F-acrylate. When the F-acrylate composition reached 80 wt.% in the F-PEGDA coating, the value for $\theta_{water,adv}^*$ reached $25^\circ \pm 3^\circ$. We attributed this to the reduced presence of -OH moieties, which are responsible for inducing hydrophilicity and creating more fluorine moieties, which are responsible for omniphobic wettability.

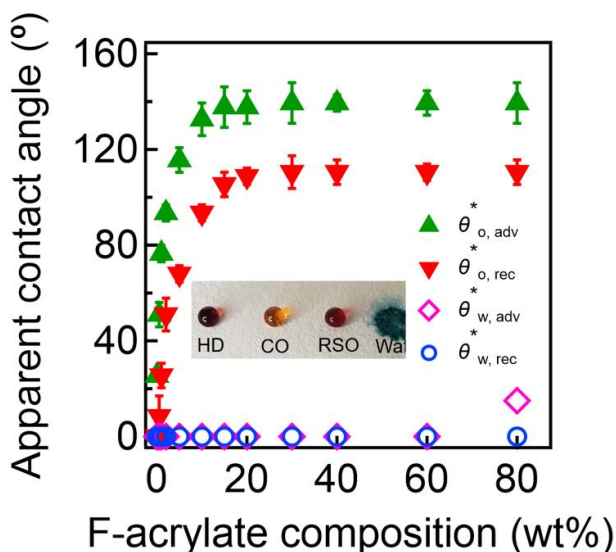


Figure 4.4. The measured apparent advancing and receding contact angles of water and oil (n-hexadecane) on F-PEGDA-coated filter surface with varied compositions of F-acrylate. A filter with a 6.0 μm inherent nominal pore size was used.

In previous reports, we²⁰ and others^{47, 59, 60} have shown that a water droplet can gradually wet the surface with hydrophilic and in-air oleophobic wettability due to surface reconfiguration. The required time for a water droplet to completely spread on a given reconfigurable surface is defined as the time of wetting (ToW).²⁰ When our F-PEGDA surface is subjected to water, it reconfigures by enabling the hydrophilic moieties (e.g., -OH groups) to emerge on the surface. This is a kinetic process that is manifested by the so-called Time of Wetting (ToW, see also main text). On our F-

PEGDA surfaces, a sessile water droplet exhibits a finite initial contact angle upon being placed. Then, it gradually wets the surface. **Table 4.2** lists the measured initial contact angle values for water on F-PEGDA surfaces. **Figure 4.5** shows the measured ToW values. It should be noted that a water droplet shows a final contact angle of $25^\circ \pm 3^\circ$ on the F-PEGDA (80 wt%) surface (also see **Figure 4.4**). We determined the final contact angle when it remained unchanged ($< 2^\circ$) for 10 mins.

Table 4.2. The measured initial contact angles for a sessile water droplet (5 μ l) on F-PEGDA surfaces with varying F-Acrylate compositions.

Surface	$\theta_{water,adv}^*(t=0)$	$\theta_{water,rec}^*(t=0)$
F-PEGDA (0)	$43^\circ \pm 3^\circ$	0°
F-PEGDA (5 wt%)	$62^\circ \pm 2^\circ$	0°
F-PEGDA (10 wt%)	$75^\circ \pm 3^\circ$	0°
F-PEGDA (15 wt%)	$82^\circ \pm 2^\circ$	0°
F-PEGDA (20 wt%)	$89^\circ \pm 4^\circ$	0°
F-PEGDA (40 wt%)	$95^\circ \pm 5^\circ$	$15^\circ \pm 4^\circ$
F-PEGDA (60 wt%)	$102^\circ \pm 2^\circ$	$25^\circ \pm 3^\circ$
F-PEGDA (80 wt%)	$110^\circ \pm 3^\circ$	$49^\circ \pm 4^\circ$

We also calculated the solid surface energy (γ_{sv}) values of the F-PEGDA surfaces. We have utilized the Owens and Wendt approach⁶¹ to calculate the solid surface energy (γ_{sv}) of F-PEGDA surfaces with varying F-acrylate compositions. Note that we fabricated a smooth surface of F-PEGDA by spincoating. Two probe liquids, n-hexadecane ($\gamma_{lv}^p=27.5$ mN/m) and water ($\gamma_{lv}^d=21.1$ mN/m and $\gamma_{lv}^p=51.0$ mN/m) were used as a non-polar liquid and a polar liquid, respectively. **Table 4.3** lists

the calculated solids surface energy values of F-PEGDA surfaces with varying F-acrylate compositions.

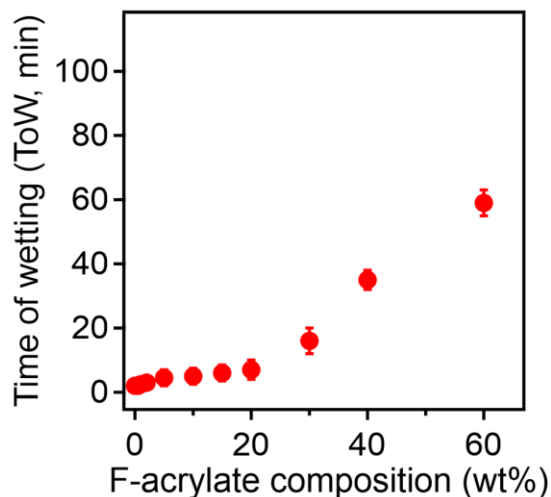


Figure 4.5. The measured ToW values for a sessile water droplet on the F-PEGDA surfaces with varying F-acrylate compositions.

Table 4.3. The calculated solid surface energy values of F-PEGDA surfaces.

Surface	γ_{sv}^p (mN m ⁻¹)	γ_{sv}^d (mN m ⁻¹)	γ_{sv} (mN m ⁻¹)
F-PEGDA (0)	39.5	35.2	74.7
F-PEGDA (5 wt%)	24.6	15.3	39.9
F-PEGDA (10 wt%)	13.8	13.2	27.0
F-PEGDA (15 wt%)	6.2	11.2	17.4
F-PEGDA (20 wt%)	3.1	10.1	13.2
F-PEGDA (40 wt%)	0.9	9.9	10.8
F-PEGDA (60 wt%)	0.5	9.9	10.4
F-PEGDA (80 wt%)	0.5	9.9	10.4

Similar to the results for the 6.0 μm filter (see **Figure 4.4** in the main text), the apparent contact angles of oil increase with an increase in the composition of F-acrylate (**Figure 4.6**). At 20 wt.% of F-acrylate composition, the advancing ($\theta_{\text{oil, adv}}^*$) and receding ($\theta_{\text{oil, rec}}^*$) apparent contact angles

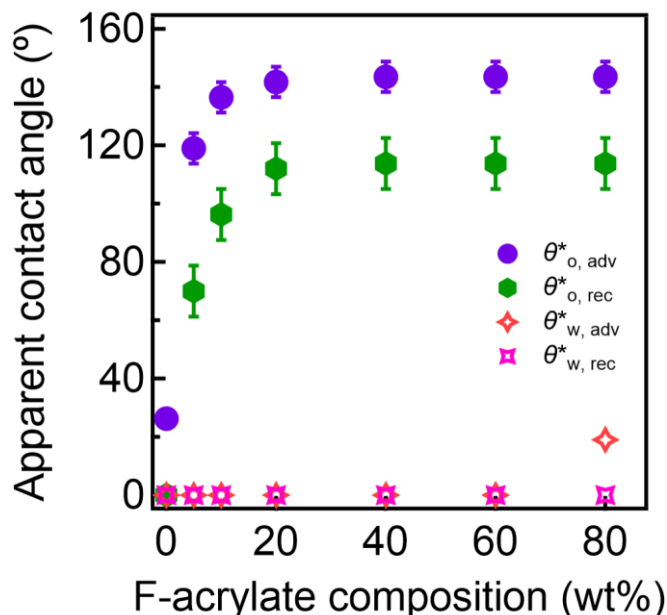


Figure 4.6. Advancing and receding apparent contact angles for water and oil (n-hexadecane) on F-PEGDA surface with varied compositions of F-acrylate for the filter with 2.0 μm of inherent nominal pore size.

for oil were measured as $135^\circ \pm 3^\circ$ and $111^\circ \pm 3^\circ$, respectively, while those for water remained zero ($\theta_{\text{water, adv}}^* = 0^\circ$ and $\theta_{\text{water, rec}}^* = 0^\circ$). When the F-acrylate composition becomes 80 wt.% in F-PEGDA coating, the value of $\theta_{\text{water, adv}}^*$ is measured as $18^\circ \pm 3^\circ$. Based on these results, a filter coated with 20 wt.% of F-acrylate (F-PEGDA (20 wt.%)) was utilized for the rest of the study.

We measured the adhesion force of a sessile oil droplet on the filters submerged in DI water using a high-precision microelectromechanical system (**Figure 4.7a**, see also **Experimental procedure**). The results showed that the adhesion force values were nearly constant ($\approx 1.32 \mu\text{N} \pm 0.10 \mu\text{N}$) on filters with an inherent nominal pore size of 6.0 μm , which were coated with F-PEGDA, irrespective of the F-acrylate composition. Note that the adhesion force value measured on the neat PEGDA-coated filter was slightly lower ($1.27 \mu\text{N} \pm 0.10 \mu\text{N}$), while that measured on

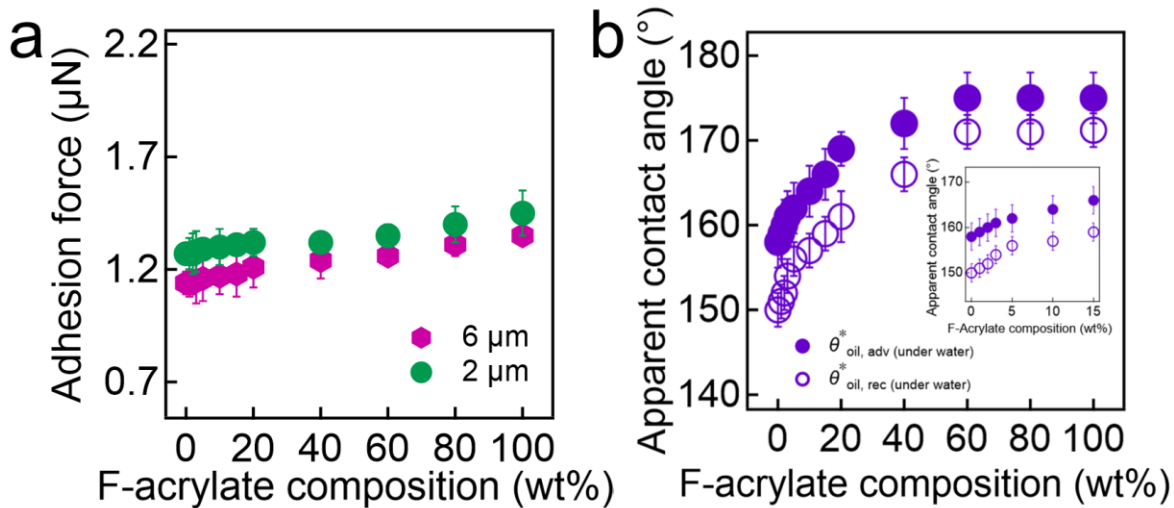


Figure 4.7. (a) The measured adhesion force of a sessile oil (n-hexadecane) droplet on the filter surfaces coated with F-PEGDA with various F-acrylate concentrations. (b) The measured apparent contact angles of an oil on the F-PEGDA (20 wt.%), which was prepared with MEMO before and after being submerged in water for 1 h. For comparison, the data for F-PEGDA (20 wt.%) prepared without MEMO are also shown.

the neat F-acrylate-coated filter was slightly higher ($1.45 \mu\text{N} \pm 0.10 \mu\text{N}$). The measured adhesion forces of an oil droplet on a filter with an inherent nominal pore size of $2.0 \mu\text{m}$ are also demonstrated in **Figure 4.7a**. This ultralow oil adhesion was a direct consequence of the underwater superoleophobic wettability (i.e., apparent oil contact angle $>150^\circ$ on a surface submerged in water). **Figure 4.7b** demonstrates a plot of advancing and receding apparent contact angles for oil (n-hexadecane) on filters coated with F-PEGDA with various F-acrylate compositions submerged in DI water. The results show that the filters coated with F-PEGDA exhibited very high underwater apparent oil contact angles (i.e., underwater superoleophobic wettability). Further, a filter coated with F-PEGDA with a lower F-acrylate composition exhibits a higher underwater oil contact angle. For example, a filter coated with F-PEGDA (20 wt.%) exhibited contact angles of $\theta_{\text{oil, adv (under water)}}^* = 169^\circ \pm 2^\circ$ and $\theta_{\text{oil, rec (under water)}}^* = 161^\circ \pm 3^\circ$, whereas the one coated with F-PEGDA (80 wt.%) exhibited $\theta_{\text{oil, adv (under water)}}^* = 174^\circ \pm 3^\circ$ and $\theta_{\text{oil, rec (under water)}}^* = 171^\circ \pm 2^\circ$. Additionally, the experimental results regarding water uptake by F-PEGDA-

coated filters are provided **Table 4.4**. The water uptake is calculated by subtracting the weight of an as-prepared filter from that of a wet filter.

Table 4.4. The measured weight values of F-PEGDA (20 wt%) coated filters and calculated water uptake.

Filter	Dry filter (mg)	Wet filter (mg)	Water uptake (mg)
6.0 μm	160	365	205
2.0 μm	162	381	219

Filters exhibiting hydrophilic and in-air oleophobic wettability do not need to undergo prewetting in order to introduce a hydration layer before conducting oil-water separation. This is because the in-air superoleophobic wettability plays a key role in resistance to oil adhesion on the surface by repelling it³⁸. In contrast, an in-air superoleophilic surface such as a neat PEGDA-coated filter or an unmodified filter allows oil to wet and adhere to the surface.

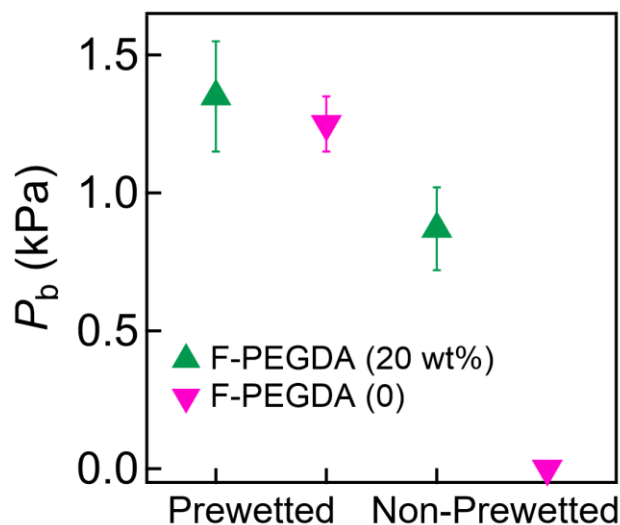


Figure 4.8. The breakthrough pressure of oil on prewetted and dry filters coated with F-PEGDA (20 wt.%). The data obtained from a filter coated with neat PEGDA are also provided for comparison.

We measured the breakthrough pressure (P_b) for oil of an F-PEGDA-coated filter. It was observed that filters coated with F-PEGDA (20 wt.%) and with neat PEGDA (i.e., F-PEGDA (0)) could both exhibit high P_b values for oil. For example, a filter coated with F-PEGDA (20 wt.%) exhibited $P_b = 1.35 \pm 0.2$ kPa, while another filter coated with neat PEGDA showed $P_b = 1.25 \pm 0.1$ kPa when they were prewetted (**Figure 4.8**). When the filters were dry, the neat PEGDA-coated filter immediately allowed oil to pass through ($P_b \approx 0$), whereas the filter coated with F-PEGDA (20 wt.%) maintained a breakthrough pressure of $P_b = 0.87 \pm 0.2$ kPa.

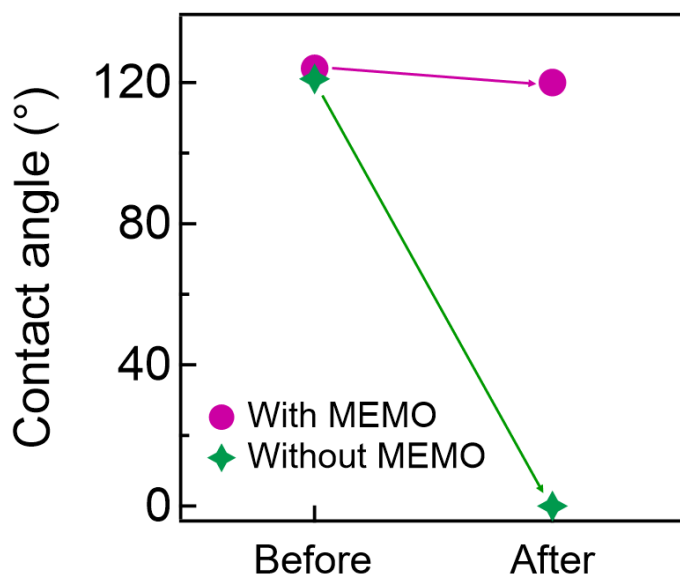


Figure 4.9. The measured apparent contact angles of an oil on the F-PEGDA (20 wt.%), which was prepared with MEMO before and after being submerged in water for 1 h. For comparison, the data for F-PEGDA (20 wt.%) prepared without MEMO are also shown.

4.3.4. Coating robustness measurement

Filters grafted with MEMO can prevent delamination of the F-PEGDA coating from the surface after being submerged in water. To test this, we measured the apparent contact angles of in-air oil on a filter coated with F-PEGDA after being submerged in DI water for 1 h. For comparison, we conducted the same experiment using a filter without MEMO grafting. The results showed that the apparent contact angles of oil remained almost unchanged on the filters coated with MEMO and F-PEGDA, while those on the filter without MEMO grafting equaled zero (**Figure 4.9**). This was the direct consequence of the delamination of the F-PEGDA coating from the filter surface. Grafting MEMO to a filter surface can prevent the delamination of F-PEGDA coating. **Figure 4.10a** and **4.10b** show SEM images with the EDS data (e.g., elemental mapping) of a filter coated with F-PEGDA (20 wt.%) without MEMO grafting before and after submersion in water for 1 hour, respectively. The results show that the Fluorine (F) element nearly disappeared after 1 hour of submersion, indicating that the F-PEGDA coating is delaminated (see **Figure 4.10b**). Consequently, the oil droplet contacts the underlying filter surface and completely wets it due to the absence of fluorine on the filter surface.

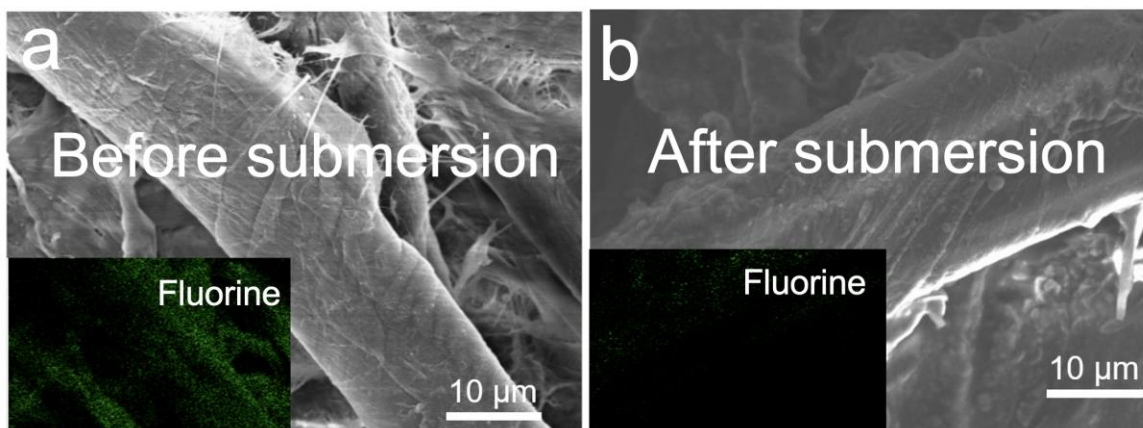


Figure 4.10. (a-b) SEM images and the EDS data (elemental mapping) showing a filter surface coated with F-PEGDA without MEMO before (a) and after submersion in water for 1 hour (b).

4.3.5. Gravity assisted oil-water separation

Using our hydrophilic and in-air oleophobic filter, we separated oil-water mixtures under gravity. Here, we utilized a surfactant-stabilized oil-in-water emulsion (10 vol% n-hexadecane in water) and a water-in-oil emulsion (90 vol% water in n-hexadecane). **Figure 4.11a** and **4.11b** show that the average size of the oil droplets dispersed in water is $\approx 19 \mu\text{m}$, whereas the average size of the water droplets dispersed in the oil phase is $\approx 16 \mu\text{m}$. The separation apparatus consisted of two vertical tubes and a filter coated with F-PEGDA (20 wt.%), which was sandwiched between them.

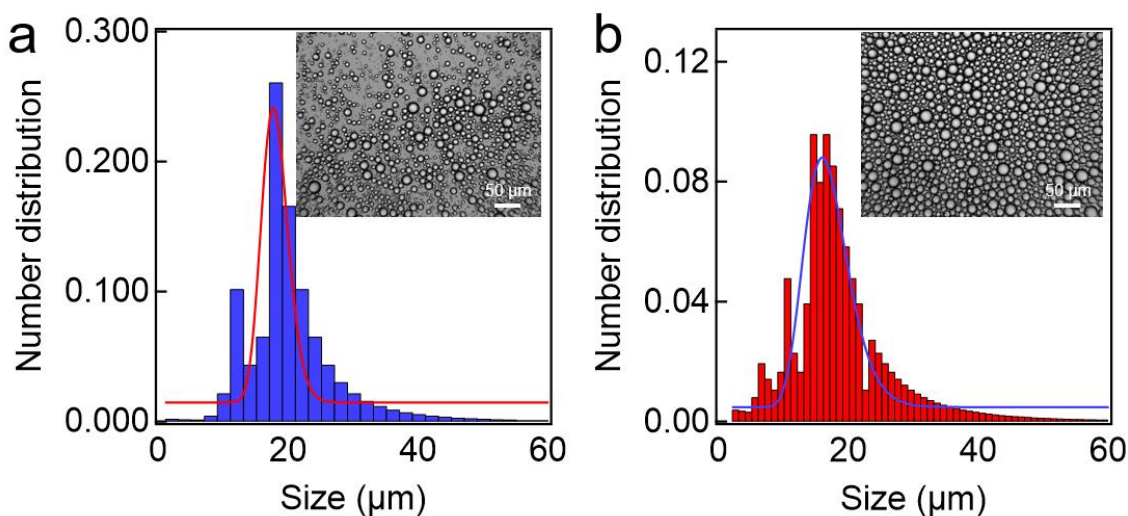


Figure 4.11. (a) SDS-stabilized oil-in-water emulsion and (b) dispersed water droplets in Tween 80-stabilized water-in-oil emulsion. The insets show the optical microscopy images of dispersed phases.

Here, we utilized a filter with an inherent nominal pore size of $6.0 \mu\text{m}$. Upon introducing an emulsion (15 mL) into an upper tube, a filter allows the water-rich phase to permeate through, while the oil-rich phase is retained above it within $11.2 \pm 2 \text{ min}$ (**Figure 4.12a**). We also calculated the flux ($J = \Delta m(A\rho\Delta t)^{-1}$, where Δm is the mass change of the water-rich permeate in a given time interval (i.e., $\Delta t = 1 \text{ min}$), A is the projected area of the filter surface, and ρ is the permeate density) values by periodically measuring the volume of the water-rich permeate through filters prewetted with water for 30 min. The results for the oil-in-water emulsion showed that the permeate flux

gradually declined from $J(t = 0) = 261 \pm 10 \text{ L m}^{-2} \text{ h}^{-1}$ and reached $J(t = 10 \text{ min}) = 245 \pm 10 \text{ L m}^{-2} \text{ h}^{-1}$. This can be attributed to the decreased height of the emulsion column as the water-rich phase permeated through the filter, which resulted in a decrease in the exerted pressure. The filter also separated the water-in-oil emulsion in $13.1 \pm 2 \text{ min}$. Similarly, the permeate flux values were determined as $J(t = 0) = 242 \pm 10 \text{ L m}^{-2} \text{ h}^{-1}$ and $J(t = 10 \text{ min}) = 225 \pm 10 \text{ L m}^{-2} \text{ h}^{-1}$. Note that almost all water droplets dispersed in an emulsion can come into contact with the filter surface under gravity. For comparison, we conducted the same experiments using a filter coated with F-PEGDA (0) after prewetting with water for 30 min. The results showed that the filter could separate both oil-in-water and water-in-oil emulsions in $11.9 \pm 2 \text{ min}$ and $13.5 \pm 2 \text{ min}$, respectively (**Figure 4.12a**). The permeate flux values were measured as $J(t = 10 \text{ min}) = 239 \pm 10 \text{ L m}^{-2} \text{ h}^{-1}$ and $J(t = 10 \text{ min}) = 219 \pm 10 \text{ L m}^{-2} \text{ h}^{-1}$ for the separation of the oil-in-water and water-in-oil emulsions, respectively.

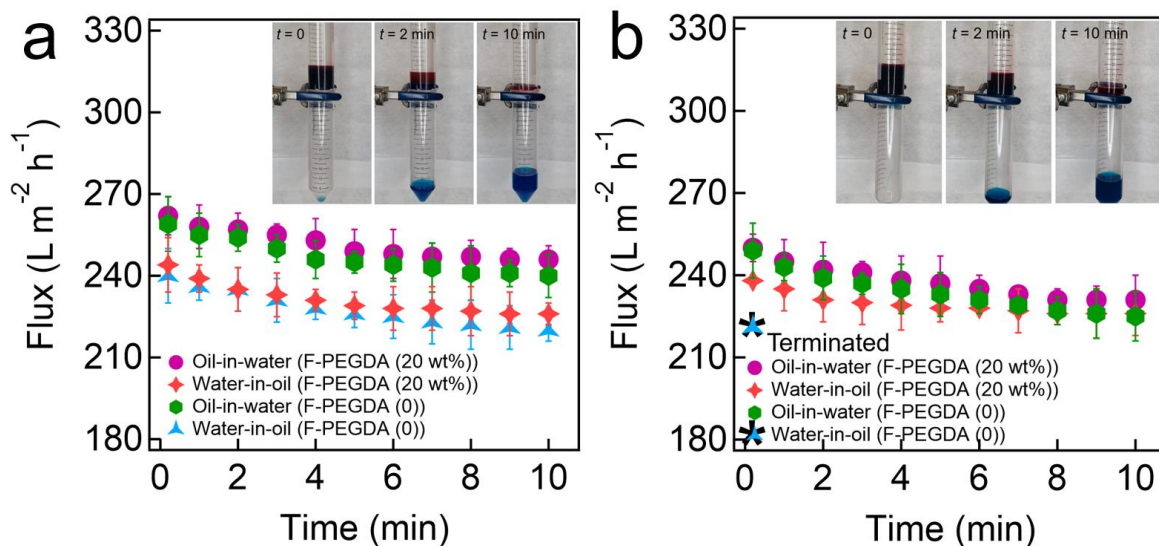


Figure 4.12. (a-b) Time-dependent flux measurements during the separation of oil-water mixtures under gravity by (a) prewetted and (b) dry filters coated with F-PEGDA (20 wt.%) and neat PEGDA. The inset shows images of the oil-water separation experiments with oil-in-water emulsions by utilizing a filter coated with F-PEGDA (20 wt.%).

When a filter coated with F-PEGDA (0) is subjected to a water-in-oil emulsion without prewetting, both oil and water immediately pass through. Note that the filter exhibited similar separation performance for the oil-in-water emulsion (**Figure 4.12b**). This is attributed to the water as a continuous medium in the emulsion, which provides a hydration layer on the filter surface and prevents oil droplets from permeating. The filter coated with F-PEGDA (20 wt.%) exhibited similar water-rich permeate flux values for both oil-in-water and water-in-oil emulsions ($J(t = 10 \text{ min}) = 231 \pm 10 \text{ L m}^{-2} \text{ h}^{-1}$ and $J(t = 10 \text{ min}) = 222 \pm 20 \text{ L m}^{-2} \text{ h}^{-1}$). **Figure 4.13** shows the TGA plots of the permeates and retentates after the separation experiments for oil-in-water and water-in-oil emulsions using a filter coated with F-PEGDA (20 wt.%).

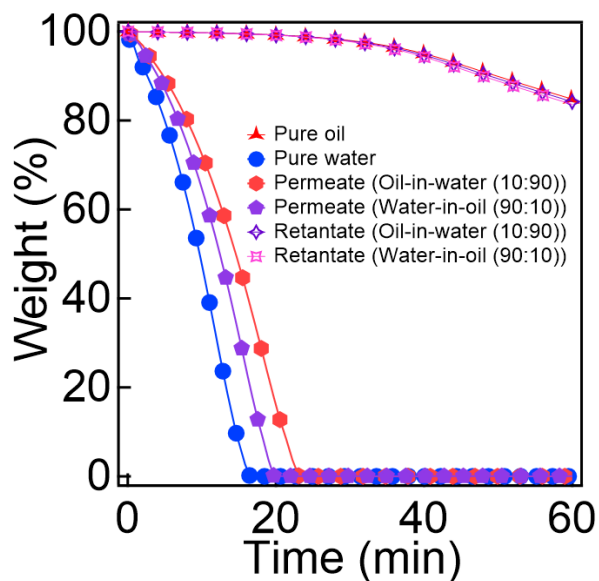


Figure 4.13. The TGA plots of the permeate and retentates after the separation of both oil-in-water and water-in-oil emulsions using a filter coated with F-PEGDA (20 wt.%). The TGA data for pure water and oil are also shown for comparison.

The results showed that our filter could separate both oil-in-water and water-in-oil emulsions with very high efficiency (>98%). Please note that our F-PEGDA filter surfaces after the separation remained clean (i.e., no fouling). We attributed this to a combinatorial effect of fouling resistance due to hydrophilic wettability and a relatively lower surfactant concentration (0.03 wt.%, See

Experimental Procedure). It is anticipated that our F-PEGDA-coated filter surface may suffer from a cake layer when it is subjected to emulsions stabilized by high-concentration surfactants⁶²⁻⁶⁴. Additionally, it should be noted that the surfactants used in this study were either anionic (sodium dodecyl sulfate for the oil-in-water emulsion) or nonionic (Tween 80 for the water-in-oil emulsion). Given that the zeta potential (ξ) value of our F-PEGDA (20 wt.%) -coated filter surface was measured as $-0.83 \text{ mV} \pm 0.19 \text{ mV}$, it is anticipated that our filter may be fouled by emulsions stabilized with cationic or amphoteric surfactants.^{62, 65, 66}

4.3.6. Continuous oil-water separation

Finally, we continuously separated an oil-in-water emulsion utilizing a cross-flow apparatus (**Experimental procedure**). An emulsion (total volume = 20 L) was gradually introduced into a cell in which a filter (inherent nominal pore size = $6.0 \mu\text{m}$) coated with F-PEGDA (20 wt.%) was mounted. We measured the volume of the water-rich permeates every 5 min for the entire 60

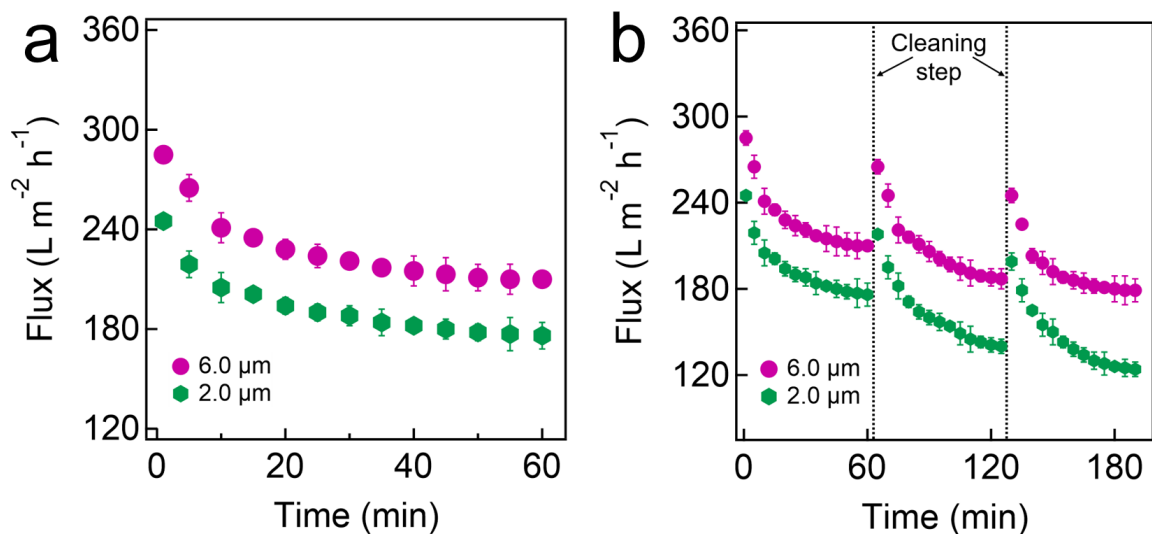


Figure 4.14. (a) Time-dependent flux measurements during the continuous separation of oil-water mixtures using prewetted filters with various inherent nominal pore sizes, which were coated with F-PEGDA (20 wt.%). The inset demonstrates the separation experiment using a cross-flow apparatus. (b) Time-dependent flux measurements during the continuous separation of oil-in-water emulsion with cleaning steps in between.

min of operation. The TMP value was maintained at $0.90 \text{ kPa} \pm 0.20 \text{ kPa}$. The results showed that $J(t = 0) = 285 \pm 10 \text{ L m}^{-2} \text{ h}^{-1}$, after which it declined and reached $J(t = 60 \text{ min}) = 210 \pm 10 \text{ L m}^{-2} \text{ h}^{-1}$ (Figure 4.14a).

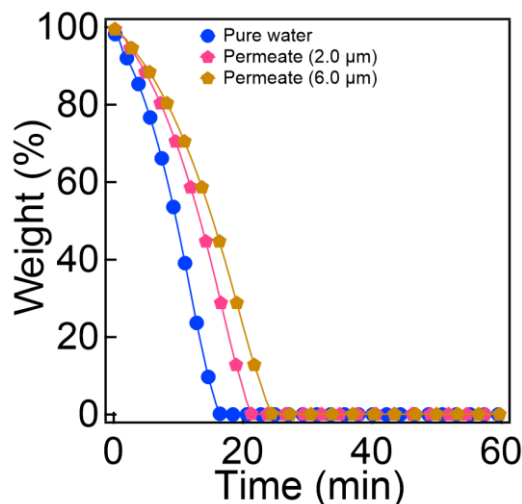


Figure 4.15. TGA analysis of the permeates and pure water for cross-flow apparatus-based separation.

We conducted the same experiments using a filter with an inherent nominal pore size of $2.0 \mu\text{m}$. The results showed that $J(t = 0) = 245 \pm 10 \text{ L m}^{-2} \text{ h}^{-1}$, after which it declined over time and reached $J(t = 60 \text{ min}) = 176 \pm 10 \text{ L m}^{-2} \text{ h}^{-1}$. Unlike the flux decline during batch separation, which was primarily caused by a decrease in the exerted pressure (see Figure 4.12a-b), the continuous separation was conducted at a constant TMP. Therefore, we attributed the flux decline to the oil droplet accumulation above the membrane surface.⁴ Although our filter exhibits very low oil adhesion force, oil can still accumulate on the surfaces and pore walls due to transmembrane pressure. The accumulation of oil can cause pore blockages. As a consequence, the volume of water passing through the filter in a given period of time (i.e., permeate flux) decreases. This results in a decline in the flux. We cleaned the filter by first rinsing it with ethanol for 10 s, followed by washing it with DI water for 30 s (flow rate $\approx 20.0 \text{ L min}^{-1}$). The cleansed filter was subjected to

the same separation experiments. The results showed that the filter nearly recovered its inherent flux values (**Figure 4.14b**).

Figure 4.15 shows the TGA plots of the water-rich permeates through the filters with 2.0 μm and 6.0 μm of inherent nominal pore size coated with F-PEGDA (20 wt.%) after continuous separation of oil-in-water emulsion using a cross-flow cell. It is observed that a 2.0 μm pore size filter was able to separate oil and water at a high efficiency of $\approx 98\%$, while the one with a 6.0 μm of pore size demonstrated a separation efficiency of $\approx 96\%$. **Figure 4.16** shows the measured flux values for the water-rich permeates during the continuous separation of oil-in-water emulsion utilizing F-

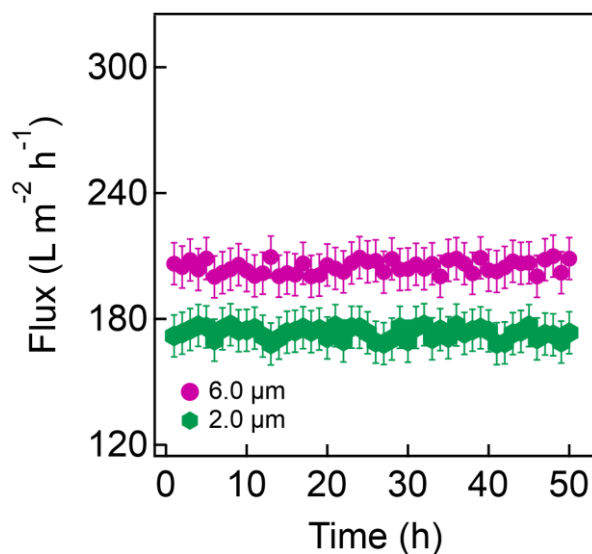


Figure 4.16. Measured flux values for the water-rich permeates as a function of time.

PEGDA (20wt%) coated filters. The results show that the flux values were maintained at 204 ± 4 $\text{L m}^{-2} \text{h}^{-1}$ (6.0 μm filter) and 172 ± 5 $\text{L m}^{-2} \text{h}^{-1}$ (2.0 μm filter) over 50 hours of continuous separation.

4.4. Conclusions

In this work, we prepared robust hydrophilic and in-air oleophobic F-PEGDA-coated filters to separate oil-water mixtures. We utilized MEMO as an adhesion promoter to enhance coating adhesion to the filter. The prepared surfaces were then subjected to fouling conditions

representative of conventional oil-water separation applications. The results of the study demonstrated that the F-PEGDA-coated filter showed low oil adhesion forces and was able to withstand fouling conditions without delamination. Subsequently, gravity-driven oil-water separations were conducted by utilizing oil-in-water and water-in-oil emulsions. The F-PEGDA-coated filter was able to separate both emulsions and maintained high flux values, while the filter with underwater oleophobicity failed to separate the water-in-oil emulsion, highlighting the advantages of in-air oleophobicity. Further, the F-PEGDA surface demonstrated good reusability upon cleansing.

4.5. References

1. Cheryan, M.; Rajagopalan, N., Membrane processing of oily streams. Wastewater treatment and waste reduction. *Journal of membrane science* **1998**, *151* (1), 13-28.
2. Yuan, J.; Liu, X.; Akbulut, O.; Hu, J.; Suib, S. L.; Kong, J.; Stellacci, F., Superwetting nanowire membranes for selective absorption. *Nature nanotechnology* **2008**, *3* (6), 332-336.
3. Guerin, T. F., Heavy equipment maintenance wastes and environmental management in the mining industry. *Journal of environmental management* **2002**, *66* (2), 185-199.
4. Chen, P.-C.; Xu, Z.-K., Mineral-coated polymer membranes with superhydrophilicity and underwater superoleophobicity for effective oil/water separation. *Scientific reports* **2013**, *3* (1), 1-6.
5. Lian, Z.; Xu, J.; Wang, Z.; Yu, Z.; Weng, Z.; Yu, H., Nanosecond laser-induced underwater superoleophobic and underoil superhydrophobic mesh for oil/water separation. *Langmuir* **2018**, *34* (9), 2981-2988.
6. Ali, N.; Bilal, M.; Khan, A.; Ali, F.; Iqbal, H. M., Design, engineering and analytical perspectives of membrane materials with smart surfaces for efficient oil/water separation. *TrAC Trends in Analytical Chemistry* **2020**, *127*, 115902.
7. Chen, C.; Weng, D.; Mahmood, A.; Chen, S.; Wang, J., Separation mechanism and construction of surfaces with special wettability for oil/water separation. *ACS applied materials & interfaces* **2019**, *11* (11), 11006-11027.
8. Fakhru'l-Razi, A.; Pendashteh, A.; Abdullah, L. C.; Biak, D. R. A.; Madaeni, S. S.; Abidin, Z. Z., Review of technologies for oil and gas produced water treatment. *Journal of hazardous materials* **2009**, *170* (2-3), 530-551.
9. Ezazi, M.; Shrestha, B.; Kim, S. I.; Jeong, B.; Gorney, J.; Hutchison, K.; Lee, D. H.; Kwon, G., Selective Wettability Membrane for Continuous Oil– Water Separation and In Situ Visible Light - Driven Photocatalytic Purification of Water. *Global Challenges* **2020**, *4* (10), 2000009.
10. Shrestha, B.; Ezazi, M.; Kwon, G., Engineered Nanoparticles with Decoupled Photocatalysis and Wettability for Membrane-Based Desalination and Separation of Oil-Saline Water Mixtures. *Nanomaterials* **2021**, *11* (6), 1397.
11. Baig, U.; Matin, A.; Gondal, M.; Zubair, S., Facile fabrication of superhydrophobic, superoleophilic photocatalytic membrane for efficient oil-water separation and removal of hazardous organic pollutants. *Journal of cleaner production* **2019**, *208*, 904-915.
12. Gondal, M. A.; Sadullah, M. S.; Qahtan, T. F.; Dastageer, M. A.; Baig, U.; McKinley, G. H., Fabrication and wettability study of WO₃ coated photocatalytic membrane for oil-water separation: a comparative study with ZnO coated membrane. *Scientific Reports* **2017**, *7* (1), 1-10.
13. Jiang, C.; Liu, W.; Yang, M.; Liu, C.; He, S.; Xie, Y.; Wang, Z., Robust multifunctional superhydrophobic fabric with UV induced reversible wettability, photocatalytic self-cleaning property, and oil-water separation via thiol-ene click chemistry. *Applied Surface Science* **2019**, *463*, 34-44.
14. Zhang, L.; Zhong, Y.; Cha, D.; Wang, P., A self-cleaning underwater superoleophobic mesh for oil-water separation. *Scientific reports* **2013**, *3* (1), 1-5.
15. Henthorne, L., *Evaluation of Membrane Pretreatment for Seawater Reverse Osmosis Desalination*. US Department of the Interior, Bureau of Reclamation, Technical Service ...: 2007.
16. Duraisamy, R. T.; Beni, A. H.; Henni, A., State of the art treatment of produced water. *Water Treatment* **2013**, 199-222.

17. Mohammad, A. W.; Teow, Y.; Ang, W.; Chung, Y.; Oatley-Radcliffe, D.; Hilal, N., Nanofiltration membranes review: Recent advances and future prospects. *Desalination* **2015**, *356*, 226-254.
18. Yuan, X.; Li, W.; Liu, H.; Han, N.; Zhang, X., A novel PVDF/graphene composite membrane based on electrospun nanofibrous film for oil/water emulsion separation. *Composites Communications* **2016**, *2*, 5-8.
19. Padaki, M.; Murali, R. S.; Abdullah, M. S.; Misdan, N.; Moslehyani, A.; Kassim, M.; Hilal, N.; Ismail, A., Membrane technology enhancement in oil–water separation. A review. *Desalination* **2015**, *357*, 197-207.
20. Kota, A. K.; Kwon, G.; Choi, W.; Mabry, J. M.; Tuteja, A., Hygro-responsive membranes for effective oil–water separation. *Nature communications* **2012**, *3* (1), 1-8.
21. Kwon, G.; Post, E.; Tuteja, A., Membranes with selective wettability for the separation of oil–water mixtures. *MRS Communications* **2015**, *5* (3), 475-494.
22. Ichikawa, T.; Nakajima, Y., Rapid demulsification of dense oil-in-water emulsion by low external electric field.: II. Theory. *Colloids and Surfaces A: Physicochemical and Engineering Aspects* **2004**, *242* (1-3), 27-37.
23. Ren, B.; Kang, Y., Demulsification of oil-in-water (O/W) emulsion in bidirectional pulsed electric field. *Langmuir* **2018**, *34* (30), 8923-8931.
24. Hano, T.; OHTAKE, T.; TAKAGI, K., Demulsification kinetics of W/O emulsion in an AC electric field. *Journal of chemical engineering of Japan* **1988**, *21* (4), 345-351.
25. Guo, J.; Yan, D. Y.; Lam, F. L.-Y.; Deka, B. J.; Lv, X.; Ng, Y. H.; An, A. K., Self-cleaning BiOBr/Ag photocatalytic membrane for membrane regeneration under visible light in membrane distillation. *Chemical Engineering Journal* **2019**, *378*, 122137.
26. Nishimoto, S.; Tomoishi, S.; Kameshima, Y.; Fujii, E.; Miyake, M., Self-cleaning efficiency of titanium dioxide surface under simultaneous UV irradiation of various intensities and water flow. *Journal of the Ceramic Society of Japan* **2014**, *122* (1426), 513-516.
27. Zhang, H.; Mane, A. U.; Yang, X.; Xia, Z.; Barry, E. F.; Luo, J.; Wan, Y.; Elam, J. W.; Darling, S. B., Visible - light - activated photocatalytic films toward self - cleaning membranes. *Advanced Functional Materials* **2020**, *30* (34), 2002847.
28. Qahtan, T. F.; Gondal, M. A.; Dastageer, M. A.; Kwon, G.; Ezazi, M.; Al-Kuban, M. Z., Thermally Sensitized Membranes for Crude Oil–Water Remediation under Visible Light. *ACS Applied Materials & Interfaces* **2020**, *12* (43), 48572-48579.
29. Defrance, L.; Jaffrin, M., Comparison between filtrations at fixed transmembrane pressure and fixed permeate flux: application to a membrane bioreactor used for wastewater treatment. *Journal of Membrane Science* **1999**, *152* (2), 203-210.
30. Cheryan, M., *Ultrafiltration handbook*. Technomic Publishing Co. Inc.: 1986.
31. Zhang, W.; Luo, J.; Ding, L.; Jaffrin, M. Y., A review on flux decline control strategies in pressure-driven membrane processes. *Industrial & Engineering Chemistry Research* **2015**, *54* (11), 2843-2861.
32. Wang, Z.; Ma, J.; Tang, C. Y.; Kimura, K.; Wang, Q.; Han, X., Membrane cleaning in membrane bioreactors: a review. *Journal of Membrane Science* **2014**, *468*, 276-307.
33. Zsirai, T.; Buzatu, P.; Aerts, P.; Judd, S., Efficacy of relaxation, backflushing, chemical cleaning and clogging removal for an immersed hollow fibre membrane bioreactor. *Water Research* **2012**, *46* (14), 4499-4507.

34. Panchanathan, D.; Kwon, G.; Qahtan, T. F.; Gondal, M. A.; Varanasi, K. K.; McKinley, G. H., Kinetics of photoinduced wettability switching on nanoporous titania surfaces under oil. *Advanced Materials Interfaces* **2017**, *4* (21), 1700462.
35. Liu, Y.; Su, Y.; Li, Y.; Zhao, X.; Jiang, Z., Improved antifouling property of PVDF membranes by incorporating an amphiphilic block-like copolymer for oil/water emulsion separation. *RSC Advances* **2015**, *5* (27), 21349-21359.
36. Kwon, G.; Kota, A. K.; Li, Y.; Sohani, A.; Mabry, J. M.; Tuteja, A., On - demand separation of oil - water mixtures. *Advanced materials* **2012**, *24* (27), 3666-3671.
37. Yong, J.; Chen, F.; Yang, Q.; Huo, J.; Hou, X., Superoleophobic surfaces. *Chemical Society Reviews* **2017**, *46* (14), 4168-4217.
38. Tuteja, A.; Choi, W.; Ma, M.; Mabry, J. M.; Mazzella, S. A.; Rutledge, G. C.; McKinley, G. H.; Cohen, R. E., Designing superoleophobic surfaces. *Science* **2007**, *318* (5856), 1618-1622.
39. Zhu, X.; Tu, W.; Wee, K.-H.; Bai, R., Effective and low fouling oil/water separation by a novel hollow fiber membrane with both hydrophilic and oleophobic surface properties. *Journal of membrane science* **2014**, *466*, 36-44.
40. Li, C.; Boban, M.; Snyder, S. A.; Kobaku, S. P.; Kwon, G.; Mehta, G.; Tuteja, A., Paper - based surfaces with extreme wettabilities for novel, open - channel microfluidic devices. *Advanced Functional Materials* **2016**, *26* (33), 6121-6131.
41. Jiang, L.; Tang, Z.; Park-Lee, K. J.; Hess, D. W.; Breedveld, V., Fabrication of non-fluorinated hydrophilic-oleophobic stainless steel mesh for oil-water separation. *Separation and Purification Technology* **2017**, *184*, 394-403.
42. Rohrbach, K.; Li, Y.; Zhu, H.; Liu, Z.; Dai, J.; Andreasen, J.; Hu, L., A cellulose based hydrophilic, oleophobic hydrated filter for water/oil separation. *Chemical Communications* **2014**, *50* (87), 13296-13299.
43. Wang, Y.; You, C.; Kowall, C.; Li, L., A Nanometer-Thick, Mechanically Robust, and Easy-to-Fabricate Simultaneously Oleophobic/Hydrophilic Polymer Coating for Oil–Water Separation. *Industrial & Engineering Chemistry Research* **2018**, *57* (45), 15395-15399.
44. Kordjazi, S.; Kamyab, K.; Hemmatinejad, N., Super-hydrophilic/oleophobic chitosan/acrylamide hydrogel: an efficient water/oil separation filter. *Advanced Composites and Hybrid Materials* **2020**, *3*, 167-176.
45. Guo, W.; Zhang, Q.; Xiao, H.; Xu, J.; Li, Q.; Pan, X.; Huang, Z., Cu mesh's super-hydrophobic and oleophobic properties with variations in gravitational pressure and surface components for oil/water separation applications. *Applied surface science* **2014**, *314*, 408-414.
46. Wu, Z.; Zhang, T.; Zhang, H.; Liu, R.; Chi, H.; Li, X.; Wang, S.; Zhao, Y., One-pot fabrication of hydrophilic-oleophobic cellulose nanofiber-silane composite aerogels for selectively absorbing water from oil–water mixtures. *Cellulose* **2021**, *28* (3), 1443-1453.
47. Brown, P.; Atkinson, O.; Badyal, J., Ultrafast oleophobic–hydrophilic switching surfaces for antifogging, self-cleaning, and oil–water separation. *ACS applied materials & interfaces* **2014**, *6* (10), 7504-7511.
48. Pan, S.; Guo, R.; Xu, W., Durable superoleophobic fabric surfaces with counterintuitive superwettability for polar solvents. *AIChE Journal* **2014**, *60* (8), 2752-2756.
49. Yang, J.; Zhang, Z.; Xu, X.; Zhu, X.; Men, X.; Zhou, X., Superhydrophilic–superoleophobic coatings. *Journal of Materials Chemistry* **2012**, *22* (7), 2834-2837.
50. Sawada, H.; Ikematsu, Y.; Kawase, T.; Hayakawa, Y., Synthesis and surface properties of novel fluoroalkylated flip-flop-type silane coupling agents. *Langmuir* **1996**, *12* (15), 3529-3530.

51. Rambabu, G.; Bhat, S. D., Simultaneous tuning of methanol crossover and ionic conductivity of sPEEK membrane electrolyte by incorporation of PSSA functionalized MWCNTs: a comparative study in DMFCs. *Chemical Engineering Journal* **2014**, *243*, 517-525.
52. Brown, P. S.; Bhushan, B., Mechanically durable, superoleophobic coatings prepared by layer-by-layer technique for anti-smudge and oil-water separation. *Scientific reports* **2015**, *5* (1), 1-9.
53. Shaulsky, E.; Nejati, S.; Boo, C.; Perreault, F.; Osuji, C. O.; Elimelech, M., Post-fabrication modification of electrospun nanofiber mats with polymer coating for membrane distillation applications. *Journal of Membrane Science* **2017**, *530*, 158-165.
54. Bernhardt, I. C., *Particle size analysis: Classification and sedimentation methods*. Springer Science & Business Media: 1994; Vol. 5.
55. Barati, R.; Johnson, S. J.; McCool, S.; Green, D. W.; Willhite, G. P.; Liang, J. T., Polyelectrolyte complex nanoparticles for protection and delayed release of enzymes in alkaline pH and at elevated temperature during hydraulic fracturing of oil wells. *Journal of Applied Polymer Science* **2012**, *126* (2), 587-592.
56. Kumar, V.; Pulpytel, J.; Mannelli, I.; Rossi, F.; Rauscher, H.; Arefi-Khonsari, F. In *Low surface energy fluorocarbon coatings via plasma polymerization process: process optimization and protein repellent study*, International Symposium on Plasma Chemistry, 2009.
57. Browning, M.; Cereceres, S.; Luong, P.; Cosgriff - Hernandez, E., Determination of the in vivo degradation mechanism of PEGDA hydrogels. *Journal of Biomedical Materials Research Part A* **2014**, *102* (12), 4244-4251.
58. Zhang, X.; Yang, D.; Nie, J., Chitosan/polyethylene glycol diacrylate films as potential wound dressing material. *International journal of biological macromolecules* **2008**, *43* (5), 456-462.
59. Lee, H.; Alcaraz, M. L.; Rubner, M. F.; Cohen, R. E., Zwitter-wettability and antifogging coatings with frost-resisting capabilities. *ACS nano* **2013**, *7* (3), 2172-2185.
60. Pan, Y.; Huang, S.; Li, F.; Zhao, X.; Wang, W., Coexistence of superhydrophilicity and superoleophobicity: theory, experiments and applications in oil/water separation. *Journal of materials chemistry A* **2018**, *6* (31), 15057-15063.
61. Owens, D. K.; Wendt, R., Estimation of the surface free energy of polymers. *Journal of applied polymer science* **1969**, *13* (8), 1741-1747.
62. Banchik, L. D. *Advances in membrane-based oil/water separation*. Massachusetts Institute of Technology, 2017.
63. Chang, I.-S.; Chung, C.-M.; Han, S.-H., Treatment of oily wastewater by ultrafiltration and ozone. *Desalination* **2001**, *133* (3), 225-232.
64. Tummons, E. N.; Chew, J. W.; Fane, A. G.; Tarabara, V. V., Ultrafiltration of saline oil-in-water emulsions stabilized by an anionic surfactant: Effect of surfactant concentration and divalent counterions. *Journal of Membrane Science* **2017**, *537*, 384-395.
65. Wu, J.; Wei, W.; Li, S.; Zhong, Q.; Liu, F.; Zheng, J.; Wang, J., The effect of membrane surface charges on demulsification and fouling resistance during emulsion separation. *Journal of Membrane Science* **2018**, *563*, 126-133.
66. Yang, Z.; Tarabara, V. V.; Bruening, M. L., Adsorption of anionic or cationic surfactants in polyanionic brushes and its effect on brush swelling and fouling resistance during emulsion filtration. *Langmuir* **2015**, *31* (43), 11790-11799.

Chapter 5: Reversible adsorption and desorption of PFAS on inexpensive graphite adsorbents via alternating electric field

This chapter is adapted from **Paper P4**.

Abstract: Per- and polyfluoroalkyl substances (PFAS) have been extensively utilized in practical applications that include surfactants, lubricants, and firefighting foams due to their thermal stability and chemical inertness. Recent studies have revealed that PFAS were detected in groundwater and even drinking water systems which can cause severe environmental and health issues. While adsorbents with a large specific surface area have demonstrated effective removal of PFAS from water, their capability in desorbing the retained PFAS has been often neglected despite its critical role in regeneration for reuse. Further, they have demonstrated a relatively lower adsorption capacity for PFAS with a short fluoroalkyl chain length. To overcome these limitations, electric field-aided adsorption has been explored. In this work, reversible adsorption and desorption of PFAS dissolved in water upon alternating voltage is reported. An inexpensive graphite adsorbent is fabricated by using a simple press, resulting in a mesoporous structure with a BET surface area of $132.9 \pm 10.0 \text{ m}^2 \text{ g}^{-1}$. Electric field-aided adsorption and desorption experiments are conducted by using a custom-made cell consisting of two graphite electrodes placed in parallel in a polydimethylsiloxane container. Unlike the conventional sorption process, a graphite electrode exhibits a higher adsorption capacity for PFAS with a short fluoroalkyl chain (perfluoropentanoic acid, PFPA) in comparison to that with a long fluoroalkyl chain (perfluorooctanoic acid, PFOA). Upon alternating the voltage to a negative value, the retained PFPA or PFOA is released into the surrounding water. Finally, we engineered a device module mounted to a gravity-assisted apparatus to demonstrate electrosorption of PFAS and collection of high purity water.

5.1. Introduction

Per- and polyfluoroalkyl substances (PFAS)¹⁻⁶ are a group of organofluorine compounds that possess functional groups such as carboxylic acid and sulfonic acid attached at one end while a fluoroalkyl chain is attached to the other end. Due to fluoroalkyl chain's excellent thermal stability^{7, 8} and chemical durability^{8, 9}, PFAS have been used in a wide range of practical applications, including surfactants^{10, 11}, lubricants^{12, 13}, firefighting foams^{14, 15}, and insulations.^{16, 17} Extensive usage of PFAS over past decades has resulted in unexpected environmental contamination.^{5, 18, 19} A recent study²⁰ has revealed that groundwater near a PFAS manufacturing facility was contaminated by more than 20 different types of PFAS. Further, PFAS have been detected in drinking water systems²¹⁻²³ which has raised health concerns because they can

accumulate in the human body.^{24, 25} Thus, environmental agencies have made regulatory actions to hamper the production of PFAS²⁶, and major manufacturing companies have voluntarily agreed to phase out the PFAS.²⁷ While these actions have resulted in a decrease in the total amount of PFAS manufacturing in past years²⁸, and there has been a drastic increase in the production of PFAS with a short fluoroalkyl chain (e.g., (CF₂)₅ or shorter).²⁹ This is because most regulations have targeted PFAS with a long fluoroalkyl chain³⁰ such as perfluorooctanoic acid (PFOA) and perfluorooctanesulfonic acid (PFOS).³¹

Remediation of PFAS contaminated water has been tested by various technologies.^{3, 32-34} Conventional coagulation or flocculation has demonstrated a limited performance due to the chemical inertness of PFAS, which makes the adsorption to the coagulant ineffective.^{3, 32} While physico-chemical processes such as plasma-based oxidation³³ and chemical oxidation³⁴ can decompose PFAS, and they often result in secondary pollution by fragmented parts after the process.³³ Membrane-based technologies⁶ (e.g., reverse osmosis and nanofiltration) are relatively effective in removing PFAS from water by size exclusion. However, they often require high operating pressure to collect water-rich permeate.⁶

Sorption is perhaps the most promising technology to remove PFAS from water. Various adsorbents, including metal-organic frameworks (MOF)^{35, 36}, zeolites^{37, 38}, activated carbons^{39, 40}, and anion exchange resins⁴¹⁻⁴³, have been utilized. Carbonaceous adsorbents^{39, 40, 44-46} (e.g., activated carbon, graphene, carbon nanotubes) are attractive due to their chemical durability and thermal stability⁴⁷, and a large specific surface area that can accelerate the adsorption kinetics.⁴⁸ However, most carbonaceous adsorbents exhibit a relatively low adsorption capacity (i.e., the amount of contaminant taken up by the unit mass of adsorbent)⁴⁹ for PFAS with a short fluoroalkyl

chain length.⁵⁰⁻⁵⁴ Further, these absorbents often suffer from a decrease in the adsorption capacity over time because the residual PFAS remains even after the regeneration process.⁵⁵

Electric-field aided sorption (i.e., electrosorption) is an emerging technology to remove ionized contaminants from water. When an external electric field is applied across the electrodes submerged in water, the ionized contaminants are attracted and adsorb to an electrode surface with an opposite charge.^{44, 45, 56, 57} Thus, PFAS dissolved in water can adsorb to an anode upon application of an electric field. For example, Li et al.⁴⁴ demonstrated that PFOA adsorbed to a multiwalled carbon nanotube electrode upon application of voltage ($V = 0.6$ V), resulting in a 150-fold increase in adsorption capacity compared to that without an electric field. Niu et al.⁴⁵ reported that the adsorption rate and capacity for PFOA to a carbon nanotube/graphene anode became 12 times and 3 times higher than the results of adsorption without an electric field. Recently, Saeidi et al.⁴⁶ demonstrated reversible adsorption and desorption for PFOA and perfluorobutanoic acid upon reversing the voltage across the activated carbon electrode.

Herein, we demonstrate an inexpensive graphite adsorbent that enables reversible adsorption and desorption of PFAS with both short and long fluoroalkyl chain lengths (perfluoropentanoic acid (PFPA) and PFOA) in water upon alternating the voltage. The PFAS readily adsorbs to the graphite adsorbent upon application of a positive voltage within ≈ 10 s. We demonstrate that the adsorbed PFAS can be released into water with a high desorption efficiency of $\approx 96\%$ and $\approx 94\%$ for PFPA and PFOA, respectively, upon alternating voltage to a negative value. We also establish a quantitative relation to describe the kinetics of electrosorption for PFAS on a graphite adsorbent surface by utilizing a pseudo-second-order kinetic model. Finally, we engineer a device module that can be mounted to a gravity-assisted apparatus and demonstrate electrosorption of PFAS and collection of high purity water.

5.2. Experimental procedure

5.2.1. Materials.

Graphite powder (particle size < 20 μm), PFPA, perfluorohexanoic acid (PFHxA), perfluoroheptanoic acid (PFHtA), PFOA, perfluorononanoic acid (PFNA), and perfluorodecanoic acid (PFDA) were purchased from Sigma Aldrich. Teflonized acetylene black was purchased from Denka Co. Ltd. polydimethylsiloxane (PDMS) Sylgard 184 was purchased from Dow Corning.

5.2.2. Fabrication of graphite adsorbents.

We fabricated graphite adsorbents by mixing the graphite powder and teflonized acetylene black (conductive binder) at a ratio of 4:1 by weight. The mixture was pressed utilizing a vice to a final thickness of 0.2 cm. The resulting graphite film was then cut into the squares ($2.5 \times 2.5 \text{ cm}^2$) utilizing a blade, followed by drying in an oven at 100 $^{\circ}\text{C}$ for 24 hours.

5.2.3. Characterization of graphite adsorbents.

5.2.3.1. Surface morphology, surface area, and pore size distribution

The surface morphology of a graphite adsorbent was analyzed by scanning electron microscopy (SEM, FEI Versa 3D DualBeam). A graphite adsorbent was cut into a small piece size $\approx 1.0 \text{ cm} \times 1.0 \text{ cm}$. Then it was attached to a mount with the aid of carbon tape. SEM images were obtained at an accelerating voltage of 10 kV. Please note that metal sputtering was not involved. The Brunauer Emmett and Teller (BET) surface area and pore size distribution (PSD) were analyzed by measuring the isotherms of nitrogen (N_2) adsorption-desorption utilizing a BET analyzer (TriStar II 3020 surface analyzer) at $-196.15 \text{ }^{\circ}\text{C}$. The pore size distribution was measured by using the BJH methodology to the desorption section of the isotherms of nitrogen at $-196.15 \text{ }^{\circ}\text{C}$, assuming the pores to be cylindrical in shape.⁵⁸

5.2.3.2. Electrochemical analyses

The electrochemical analyses were performed by utilizing a three-electrode cell setup (Model 760E Series Bipotentiostat workstation). The setup included a square-shaped graphite adsorbent ($2.5 \times 2.5 \text{ cm}^2$, thickness = 0.2 cm), platinum (Pt), an Ag/AgCl as a working electrode, a counter electrode, and a reference electrode, respectively. Utilizing this setup, we performed cyclic voltammetry to measure the capacitance of our graphite adsorbent. The cyclic voltammetry was performed at 10 mV s^{-1} scan rates with the cyclic voltage of -0.6 V and + 0.6 V. Please note that electrodes were conditioned by running 100 cyclic voltammetry with a scan rate of 20 mV s^{-1} and cyclic voltage of -0.6 V and +0.6 V. Also, we carried out the electrochemical impedance spectroscopy (EIS) to measure the conductivity dynamics of PFAS dissolved in water by applying 10 mV amplitude sinusoidal potential perturbation scanned over a frequency range from 200 kHz to 10 MHz at open circuit potential. Please note that all measurements were conducted at a constant temperature ($T = 25.0 \text{ }^\circ\text{C} \pm 1.4 \text{ }^\circ\text{C}$). The specific capacitance (C) was calculated by⁵⁹:

$$\text{(Equation 5.1)} \quad C = \int \frac{IdV}{2UVm}$$

5.2.4. Reversible adsorption and desorption of PFAS.

The adsorption experiments for PFAS on a graphite adsorbent were conducted by utilizing a custom-made cell consisting of two graphite adsorbents ($2.5 \times 2.5 \times 0.2 \text{ cm}^3$) placed in parallel at a distance = 0.5 cm in a PDMS container. Please note that we fabricated two PDMS containers with dimensions of $2.5 \times 2.5 \times 1.2 \text{ cm}^3$ and $3.0 \times 3.0 \times 3.0 \text{ cm}^3$. A power supply (TP3016M, Tekpower) was connected to the electrodes. A 20 mL of deionized (DI) water dissolved with PFAS (e.g., PFPA, PFH_xA, PFHtA, PFOA, PFNA, and PFDA) was injected at the inlet of the cell with a flow rate of $\approx 3 \text{ mL min}^{-1}$ by a syringe pump (KDS-230, KD Scientific). While injecting PFAS solution, a positive voltage (V) was applied across the electrodes. The solution was collected at the

outlet of the cell. The temperature was maintained at $T = 22.0 \text{ }^{\circ}\text{C} \pm 1.4 \text{ }^{\circ}\text{C}$. The desorption experiments were conducted by utilizing the same custom-made cell. A 20 mL of DI water was injected at the inlet of the cell with a flow rate of $\approx 3 \text{ mL min}^{-1}$ while applying a negative voltage across the graphite electrodes that were adsorbed with PFAS. The DI water containing desorbed PFAS was collected at the outlet of the cell at $T = 22.0 \text{ }^{\circ}\text{C} \pm 1.4 \text{ }^{\circ}\text{C}$. The adsorption capacity (α) is defined as⁴⁹:

$$\text{(Equation 5.2)} \quad \alpha = (C_o - C_t)Q/m$$

where C_o and C_t (in ppm) are the concentration of PFAS solution at $t = 0$ and t , respectively. Q and m are the volume of the solution collected at the outlet of the cell and the mass of the anode, respectively.

The adsorption rate (R_a) was measured by⁴⁹:

$$\text{(Equation 5.3)} \quad R_a = (C_o - C_t)Q/tA$$

where t and A are the time and the total surface area of the anode.

5.2.5. Fabrication of a device module for electrosorption of PFAS and gravity-assisted collection of high purity water.

The device module was fabricated by alternatively stacking two pairs of graphite electrodes (two anodes and two cathodes) with a circular shape (diameter = 2.0 cm and thickness = 0.3 cm). Please note that nylon mesh was utilized as the spacer between the electrodes. The stacked electrodes were sandwiched between two cylindrical tubes (diameter = 2.0 cm and length = 15 cm) to form a gravity-assisted separation apparatus. Of note, the device module and tubes were sealed with a silicone sealant to prevent leakage.

5.2.6. PFAS concentration measurements.

The concentration of PFAS was assessed by measuring the electrical conductivity of the solution. We measured the electrical conductivity by submerging two probes of a multimeter (Gardner Bender GDT-3190) with an offset distance of 2.0 cm in a PFAS solution. The multimeter measured the values of electrical resistance (R). The electrical resistivity (r) was then calculated by using the equation $R = rL/A$. Here, L and A are the offset distance between two probes (i.e., 2.0 cm) and the surface area of the probe (i.e., 1.5 cm²), respectively. The electrical conductivity (s) of the PFAS solution was obtained by the equation $s = 1/r$. The electrical conductivity values were compared with a calibration curve of the electrical conductivity as a function of PFAS concentration.

5.3. Results and discussion

5.3.1. Characterization of surface morphology, surface area, and pore size distribution of graphite adsorbents

We characterized the surface morphology of a graphite adsorbent by SEM (**Figure 5.1**). It shows that graphite adsorbent possesses interconnected and overlapped planar sheets. Please note that such stacked sheets enable a large surface area for transport and diffusion of ionized species.

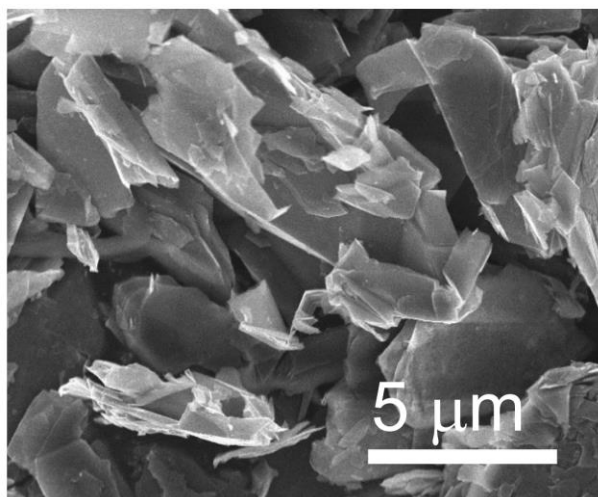


Figure 5.1. Scanning electron microscopy (SEM) image of a graphite adsorbent.

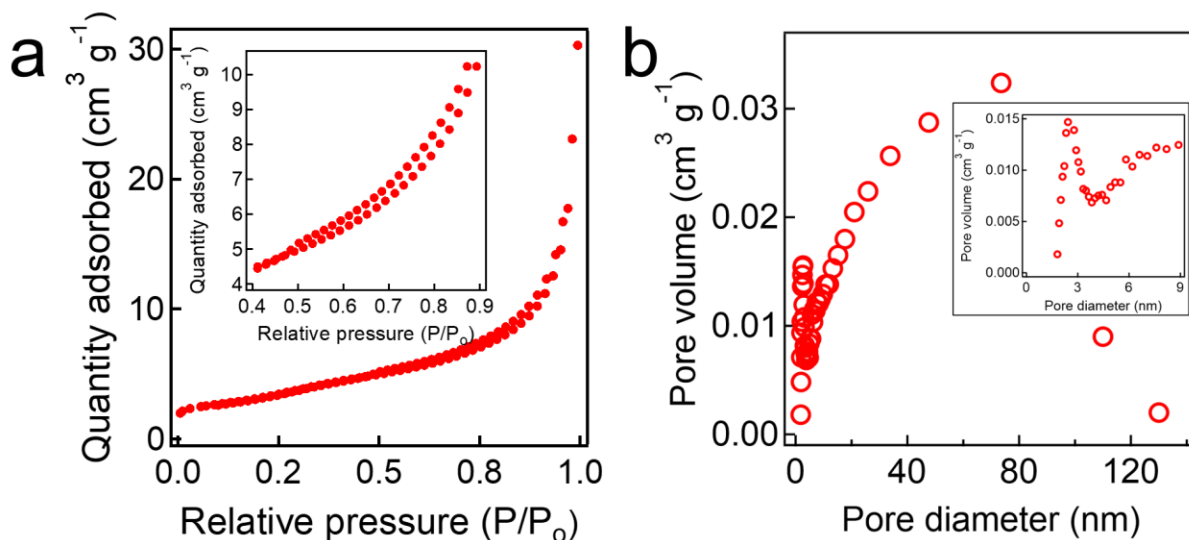


Figure 5.2. (a) Brunauer Emmett and Teller (BET) plot obtained by utilizing N₂ adsorption-desorption isotherms at -196.15 °C. Inset shows isotherms in the relative pressure (P/P_0) range of 0.55-0.85. (b) Pore size distribution (PSD) data of a graphite adsorbent. Inset shows the PSD data of the pore diameter range of 2.0-10.0 nm.

The BET surface area was measured as approximately $132.9 \pm 10.0 \text{ m}^2 \text{ g}^{-1}$ which is comparable to those reported in the literature.^{45, 60, 61} The BET measurements also show that our graphite adsorbent exhibits a type IV isotherm with a hysteresis loop in the relative pressure (i.e., P/P_0 , P_0 is the saturation pressure of N₂ at -195.15 °C) range of 0.4 – 0.9 indicating that it possesses mesopores⁶² (i.e., pores size = 2.0 – 50.0 nm) (**Figure 5.2a**). This was further corroborated by the pore size distribution (PSD) (**Figure 5.2b**). The average pore size was measured at 18 nm, and a total pore volume was measured as $0.1645 \text{ cm}^3 \text{ g}^{-1}$. A large surface area along with a wide range of pore size (e.g., 3.0 nm – 130.0 nm) makes our graphite adsorbent suitable for an electrode in the electrosorption for PFAS as it helps relieve steric hindrance for adsorption of PFAS molecules. This has been verified in previous reports. For example, Cao et al.⁶³ have demonstrated that a silica gel with a widened pore size (i.e., 6 nm) can facilitate the PFAS diffusion. Similarly, Sasi et al.⁶⁴ have shown that an adsorbent with a wide range of pore sizes (e.g., mesopore, 2 nm – 50 nm) with an average pore size of 9 nm can overcome the steric hindrance. An adsorbent with a wide range

of pore sizes can take advantage of both large and small pores. Pores of large size can facilitate the diffusion of PFAS molecules, while small pores can contribute to a larger surface area that can provide adsorption sites. In contrast, an adsorbent with a narrow pore size distribution may compromise either its diffusion kinetics or the surface area. For example, when an adsorbent possesses a small pore size with narrow distribution, it may suffer from steric hindrance and exhibit slow diffusion kinetics. If an adsorbent possesses large pores with narrow distribution, its surface area is low which can limit its adsorption capacity.

5.3.2. Electrochemical analysis

Electrosorption for PFAS can be facilitated when an electrode (i.e., anode) exhibits a high specific capacitance (i.e., capacitance per unit mass).⁶⁵ We measured a specific capacitance (C) of our graphite adsorbent (electrode) by conducting cyclic voltammetry (CV) measurements at a scan rate of 10 mV s^{-1} (see **Experimental procedure**). **Figures 5.3a** and **b** show the measured CV curves for PFPA and PFOA, respectively, by applying a cyclic voltage between -1.2 V and $+1.2 \text{ V}$. Here, we utilized PFPA and PFOA as representative PFAS with a short and a long fluoroalkyl

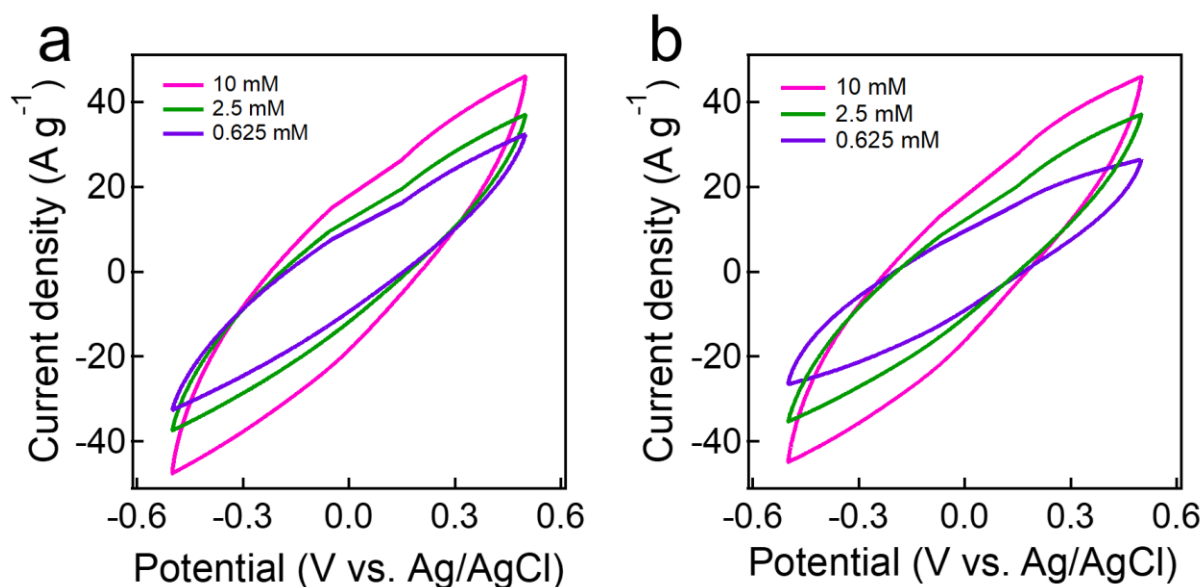


Figure 5.3. (a)-(b). Cyclic voltammetry measurements of graphite adsorbent (electrode) for PFPA (a) and PFOA (b) solutions with varying concentrations at a scan rate of 10 mV s^{-1} . The temperature was maintained at $25.0 \text{ }^\circ\text{C} \pm 1.4 \text{ }^\circ\text{C}$ during the measurements.

chain length, respectively. The specific capacitance values were determined by calculating the enclosed area of a CV curve (Equation 5.1). **Table 5.1** lists the specific capacitance values for PFPA and PFOA with varied concentrations. The results show that the C values for PFPA are higher than those of PFOA at a given concentration. This can be attributed to a higher resistivity and lower polarization of PFOA in comparison to PFPA.⁶⁶ Also, it was observed that the C values are higher for solutions with higher concentrations. This was attributed to the fact that a larger number of PFAS can participate in the electrical double layer on a graphite electrode surface.⁶⁷

Table 5.1. Specific capacitance values calculated for PFPA and PFOA at varied concentrations.

Concentration (mM)	PFPA (F g ⁻¹)	PFOA (F g ⁻¹)
10	45.44	43.37
2.5	30.25	29.06
0.625	24.08	23.91

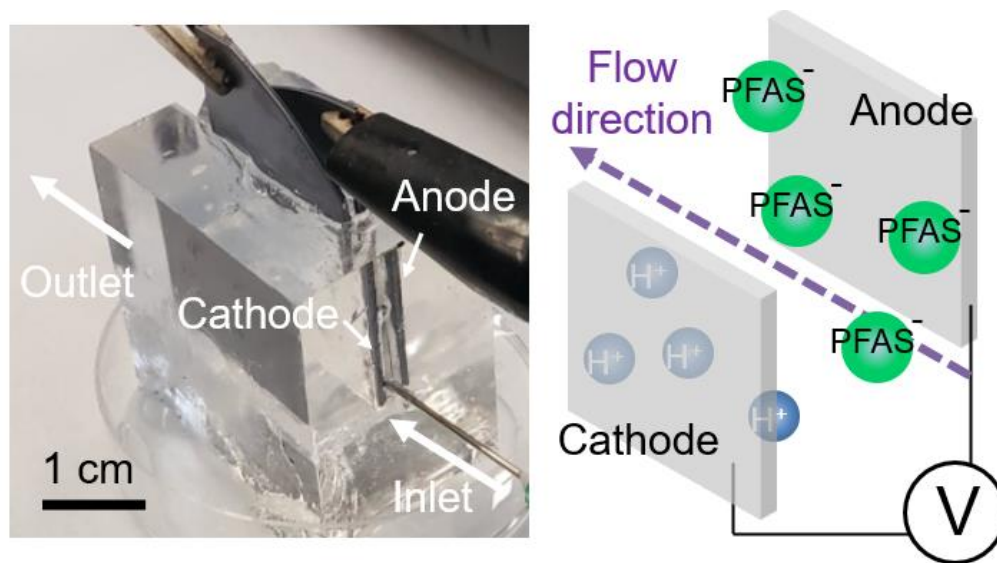


Figure 5.4. Photographs of the custom-made cell for electrosorption of PFAS.

5.3.3. Reversible adsorption and desorption of PFAS upon alternating electric field

We utilized a custom-made cell (Figure 5.4, see also Experimental procedure) to conduct adsorption and desorption experiments. The adsorption capacity (α , i.e., mass of the adsorbed PFAS on one gram of anode, Equation 5.2) was measured at varied voltage. The results show that a higher value of α was obtained upon applying a higher voltage. For example, the α value for PFPA at $V = +0.8$ V is 3.6 mg g^{-1} while $\alpha = 13.1 \text{ mg g}^{-1}$ at $V = +1.4$ V (Figure 5.5a). This can be attributed to an increase in the charge density on the electrode surface. Also, the α value for PFPA is higher than that for PFOA at a given applied voltage. For example, the α value for PFPA is 10.2 mg g^{-1} while $\alpha = 2.15 \text{ mg g}^{-1}$ for PFOA at $V = +1.2$ V, which can be attributed to higher mobility and a higher diffusion coefficient for PFPA due to its higher polarity along with its lower molecular weight.⁶⁸ Please note that the α values for PFHxA, PFHtA, PFNA, and PFDA are provided in

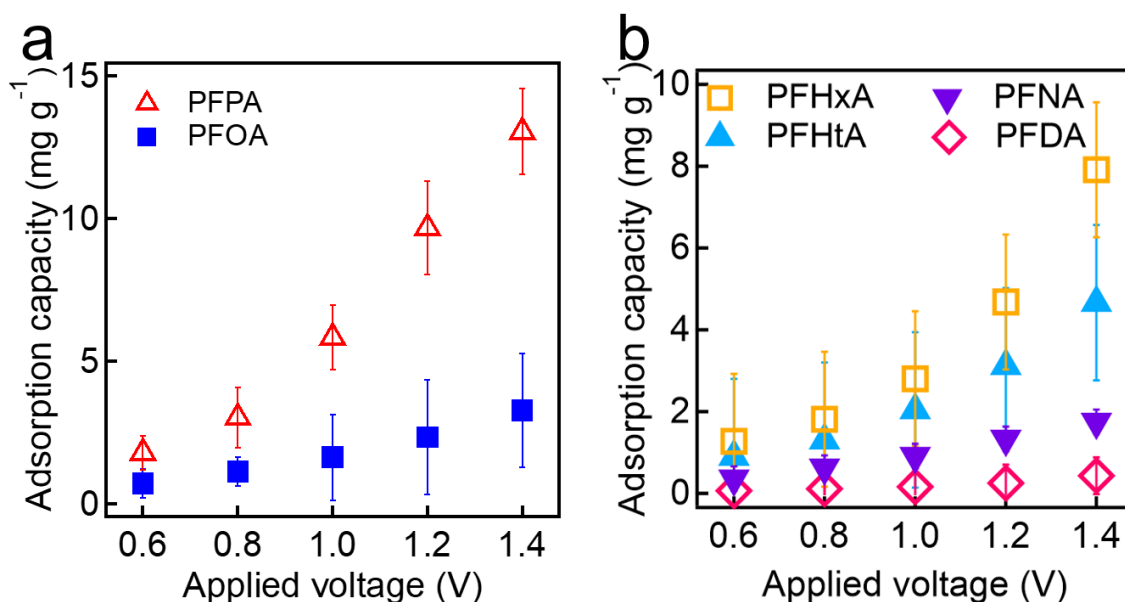


Figure 5.5. (a) The measured adsorption capacity for PFPA and PFOA aqueous solutions ($C_0 = 0.01$ M for both solutions) at varied applied voltages, (b) The measured adsorption capacity values for PFHxA, PFHtA, PFNA, and PFDA aqueous solutions at varied voltages. Note that the concentration (C_0) for each solution was 0.01 M. The adsorption capacity values are lower for PFAS with a longer fluoroalkyl chain.

Figure 5.5b). It should be noted that the α values for PFPA or PFOA without applying voltage were almost 50-fold higher compared to those without applying voltage (Table 5.2).

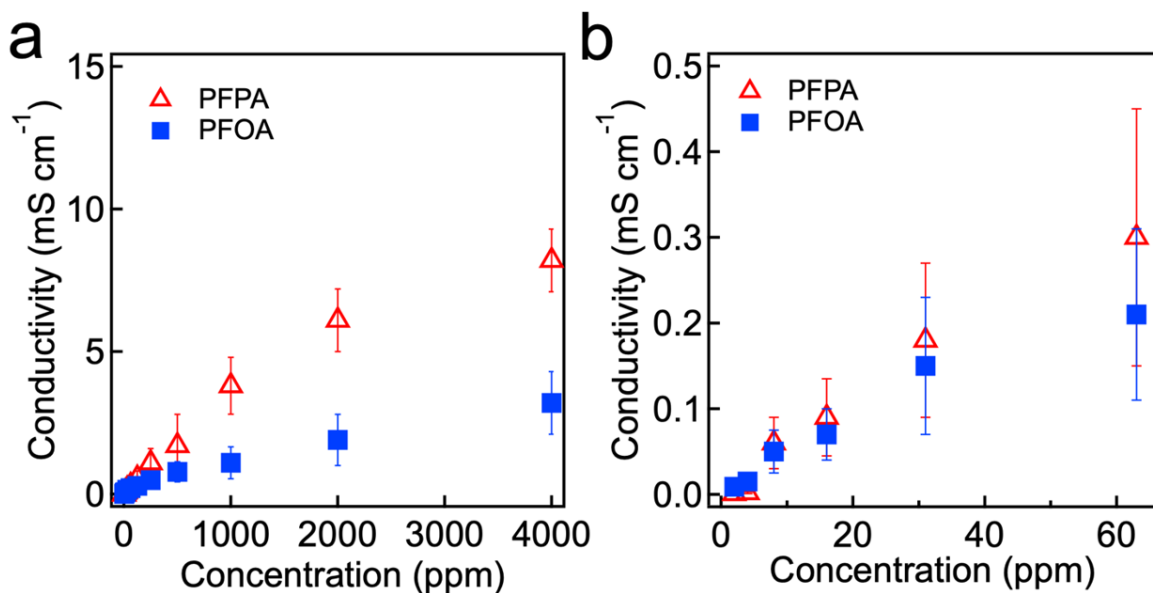


Figure 5.6. (a) and (b). The calibration curves established by calculating the electrical conductivity of DI water dissolved with PFPA (a) and PFOA (b) as a function of concentrations.

Table 5.2. The adsorption capacity (α) values of our graphite electrode for PFPA, PFH_xA, PFHtA, PFOA, PFNA, and PFDA upon application of voltage ($V = +1.2$ V). Note that all solutions are at the same concentrations ($C_0 = 0.01$ M). For comparison, the adsorption capacity values measured without application of voltage (i.e., conventional sorption) are also shown.

PFAS	Adsorption capacity (mg g ⁻¹)	
	With voltage	Without voltage
PFPA	10.20	0.20
PFH _x A	4.87	0.12
PFHtA	3.36	0.07
PFOA	2.15	0.04
PFNA	1.56	0.031
PFDA	0.75	0.028

The concentration of PFAS in water can affect the adsorption capacity at a given applied voltage. The results show that the α values decrease with a decrease in the concentration (**Figure 5.7**). For example, the α value for PFPA solution with a concentration of $C_o = 4000$ ppm was measured as 17.08 mg g^{-1} while that for a solution with $C_o = 2000$ ppm is 9.80 mg g^{-1} at $V = +1.2 \text{ V}$. This is a consequence of a decrease in the capacitance which can result in a lower mass transfer rate for PFAS (see also **Figure 5.3a**).⁶⁶ We have also conducted Langmuir isotherm studies (**Figure 5.7** and **Table 5.3**). The results show that Langmuir isotherm for PFOA reasonably matches well with the experimental data while that for PFPA deviates at a higher concentration. Such a discrepancy of PFPA isotherm can be attributed to its lower molecular weight, which in turn results in higher ionic strength. Consequently, it is possible that PFPA exhibits multilayer deposition at a higher concentration.

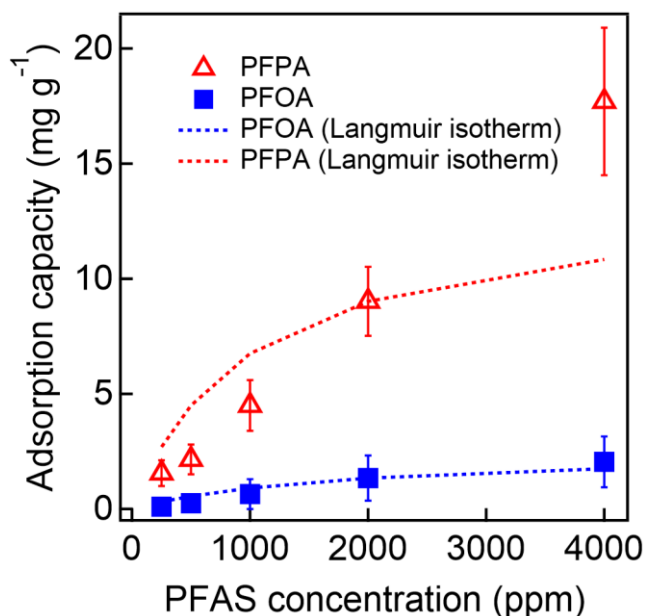


Figure 5.7. The measured adsorption capacity for PFPA and PFOA aqueous solutions ($C_o = 0.01 \text{ M}$ for both solutions) at varied concentrations ($V = \pm 1.2 \text{ V}$).

Table 5.3. Langmuir isotherm parameters for PFPA and PFOA adsorption.

PFAS	q_m (mg g ⁻¹)	b (ml mg ⁻¹)	R^2
PFPA	13.58	0.99	0.85
PFOA	2.52	0.57	0.99

Our electrosorption technique enables reversible adsorption and desorption of PFAS by alternating the applied voltage. A 20 mL of PFPA (or PFOA) solution with an initial concentration (C_0) of 30 ppm was poured into a custom-made cell. We continuously measured the electrical conductivity values of the solution by recording them. The measured values were compared to those in a calibration curve (see **Figure 5.6**) to determine the concentrations. Please note that the voltage was alternated between +1.2 V and -1.2 V every 10 s. The results show that PFOA concentration becomes 17.6 ± 2.4 ppm and 28.1 ± 2.1 ppm at $V = +1.2$ V (adsorption) and $V = -1.2$ V (desorption), respectively (**Figure 5.8**). Similarly, PFPA concentration was measured as 9.8 ± 2.5 ppm and 29.3 ± 1.7 ppm at $V = +1.2$ V and $V = -1.2$ V, respectively. These results indicate that our graphite electrode can adsorb and desorb PFAS upon alternating the voltage. The adsorption and desorption efficiency per cycle is provided in **Figure 5.9**. Please note that such on-demand reversibility is critical for regenerating the electrode.

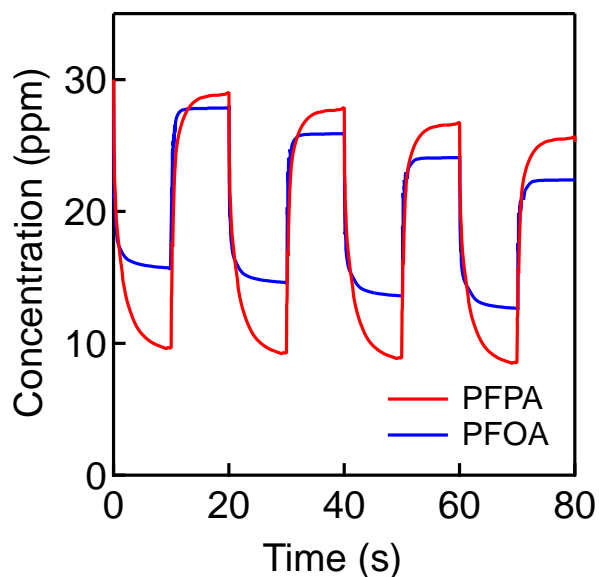


Figure 5.8. The measured concentration of PFPA and PFOA aqueous solutions upon reversible adsorption and desorption ($C_0 = 30$ ppm for both solutions) on graphite electrode by alternating the applied voltage between +1.2 V and -1.2 V. Note that the voltage alternated every 10 s.

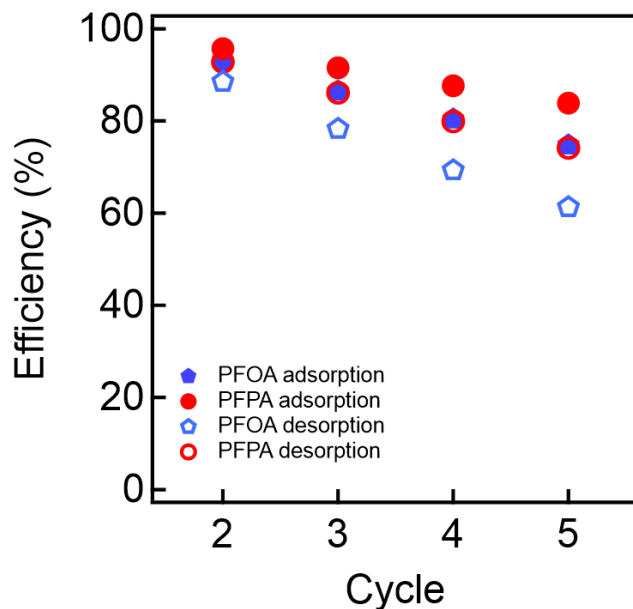


Figure 5.9. The measured adsorption and desorption efficiency as a function of cycles.

5.3.4. Kinetics of the reversible electrosorption for PFAS

We investigated the kinetics of electrosorption for PFAS. **Figure 5.10a** shows the time-dependent change in the concentration of PFOA and PFPA solutions at $V = +1.2$ V. Note that we utilized the same concentration values (different molar concentrations) that are shown in **Figure 5.8**. The results show that the concentration of PFOA and PFPA solutions rapidly decreased and reached constant values of 0.0426 ± 0.004 mM and 0.03714 ± 0.006 mM, respectively, after ≈ 5 s of voltage application, indicating that the equilibrium condition was attained. Electrosorption is a kinetic process that can be described by a pseudo-second-order kinetic model, which is given as:

$$\text{(Equation 5.4)} \quad C(t) = C_0 - \frac{k_1 q_e^2 t}{1 + k_1 q_e t}$$

where $C(t)$ and C_0 are the concentration of PFAS in a solution at time t and $t = 0$ (i.e., the initial concentration). q_e is the amount of PFAS adsorbed on the electrode at equilibrium, and k_1 is the adsorption rate constant. By fitting Equation 5.4 to the experimentally measured values (**Figure 5.10a**), we obtained the k_1 values for PFPA and PFOA as 84.44 s^{-1} and 101.30 s^{-1} , respectively. This indicates that the adsorption rate for PFPA is higher than that of PFOA, which can be

attributed to the higher mobility of the PFPA in comparison to PFOA due to its lower molecular weight.⁶⁸

Upon alternating the voltage ($V = -1.2$ V), the concentration of PFPA and PFOA started to increase and reached constant values of 0.111 ± 0.004 mM and 0.106 ± 0.004 mM, respectively, after ≈ 10 s of voltage application (**Figure 5.10b**). This can also be described by the pseudo-second order kinetic model, which is given as:

$$\text{(Equation 5.5)} \quad C(t) = C_f + \frac{k_2 q'_e{}^2 t}{1 + k_2 q'_e t}$$

where C_f is the concentration of PFAS in a solution after the adsorption experiment, q'_e is the amount of PFAS desorbed from the electrode at equilibrium, and k_2 is a desorption rate constant.

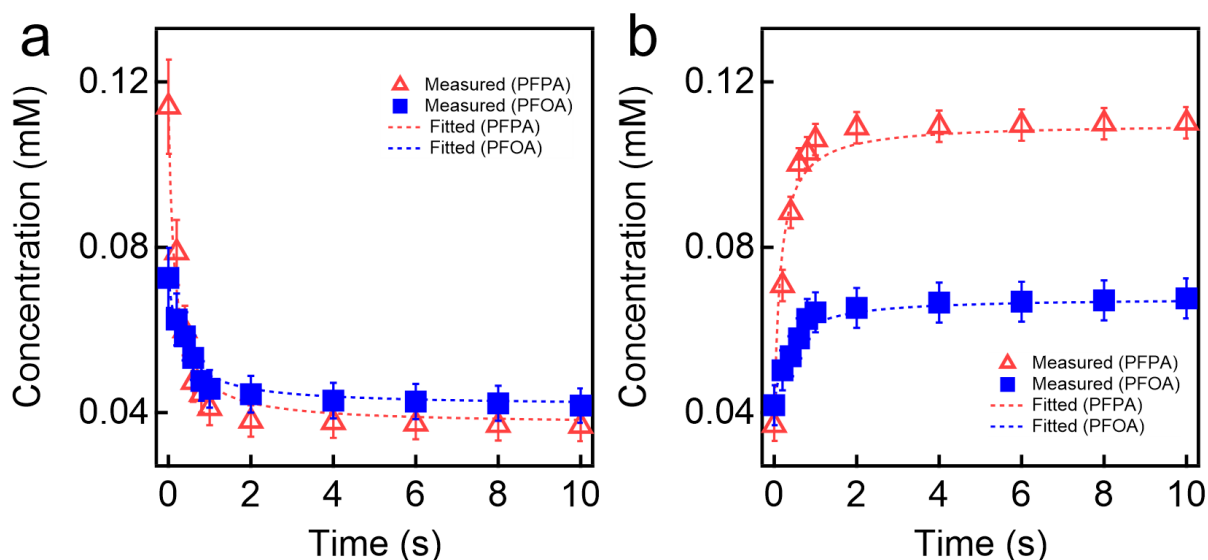


Figure 5.10. (a) and (b) The measured concentrations for PFPA and PFOA aqueous solutions upon applying voltage of $V = +1.2$ V (a) or $V = -1.2$ V (b). The fitted values of concentration utilizing pseudo-second order kinetic model for adsorption (Equation 5.4) and desorption (Equation 5.5) are also provided.

We determined the k_2 values as 90.68 s^{-1} and 118.6 s^{-1} for PFPA and PFOA, respectively, by fitting Equation 5.5 to the experimentally measured values (**Figure 5.10b**). The time-dependent

adsorption and desorption of PFPA and PFOA at varied voltages are provided in **Figure 5.11a** and **Figure 5.11b**, respectively.

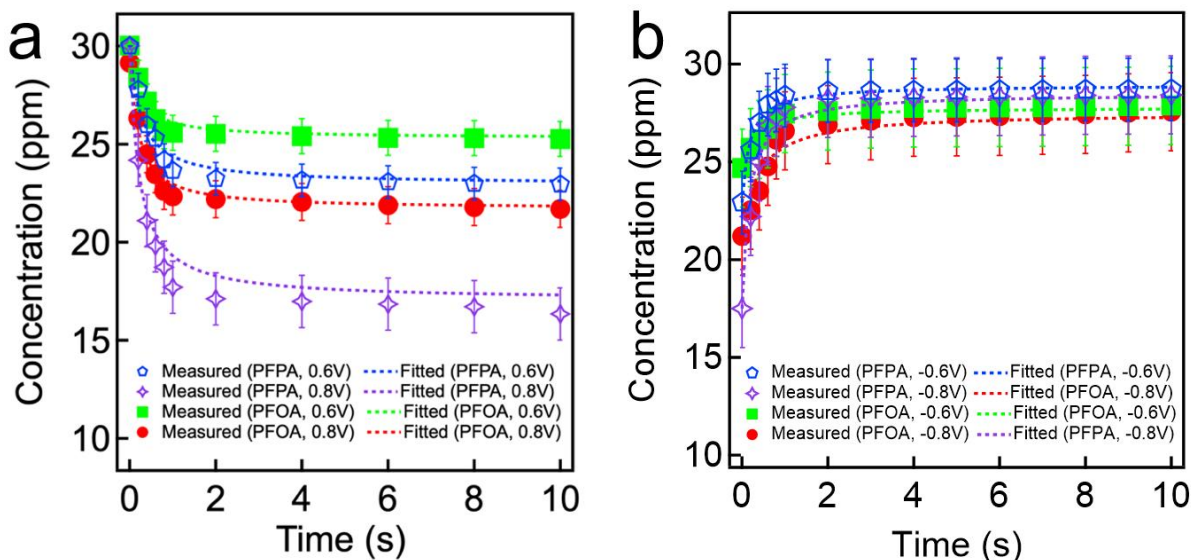


Figure 5.11. (a) The measured concentrations for PFPA and PFOA aqueous solutions upon applying voltage of $V = +0.6$ V or $V = +0.8$ V. The fitted values of concentration utilizing pseudo-second order kinetic model for adsorption (Equation 5.4) are also provided. The rate constants for adsorption (k_1) are determined as $k_1 = 0.3424$ s⁻¹ ($V = +0.6$ V) and $k_1 = 0.5521$ s⁻¹ ($V = +0.8$ V) for PFPA. For PFOA, we found $k_1 = 0.6723$ s⁻¹ ($V = +0.6$ V) and $k_1 = 1.012$ s⁻¹ ($V = +0.8$ V). (b) The measured concentrations for PFPA and PFOA aqueous solutions upon applying voltage of $V = -0.6$ V or $V = -0.8$ V. The fitted values of concentration utilizing pseudo-second order kinetic model for desorption (Equation 5.5) are also provided. The rate constants for desorption (k_2) are determined as $k_2 = 0.5553$ s⁻¹ ($V = -0.6$ V) and $k_2 = 0.9591$ s⁻¹ ($V = -0.8$ V) for PFPA. For PFOA, we found $k_2 = 0.417$ s⁻¹ ($V = -0.6$ V) and $k_2 = 1.19$ s⁻¹ ($V = -0.8$ V).

5.3.5. Electrosorption of PFAS and gravity-assisted collection of high purity water

The module for electrosorption for PFAS and gravity-assisted collection of clean water consists of two pairs of alternatively stacked graphite electrodes (two anodes and two cathodes) with a circular shape that is separated by nylon mesh as a spacer. We found that a spacer with a width of 0.2 cm can result in the highest adsorption rate for both PFPA and PFOA (**Figure 5.12** and Equation 5.3). The module was sandwiched between two cylindrical tubes to form a gravity-assisted apparatus (**Figure 5.13**). Upon pouring PFOA solution ($C_0 = 10$ ppm, 10 mL) into the upper tube, it started to permeate through the module under gravity, and the permeate was collected in the bottom tube.

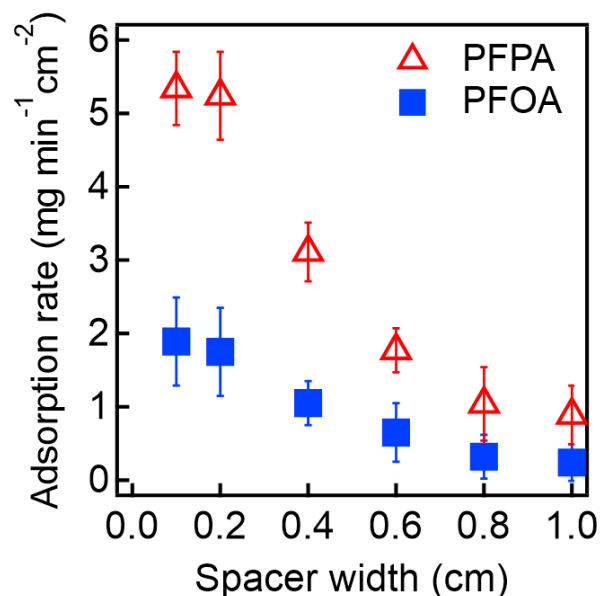


Figure 5.12. The measured adsorption rate (R_a) values of the module for PFPA and PFOA aqueous solutions ($C_o=0.01$ M) as a function of the spacer width. It is observed that a spacer width of 0.2 cm exhibits the highest R_a values for both PFPA and PFOA.

A voltage of $V = +1.2$ V was continuously applied across a cathode and an anode during permeation. Please note that the entire solution passes through the module in approximately $300 \text{ s} \pm 12 \text{ s}$. The concentration of PFOA in the permeate was measured as 1.1 ± 0.1 ppm. We conducted the same experiments using PFOA solution with varying concentrations (e.g., $C_o = 20$ ppm and C_o

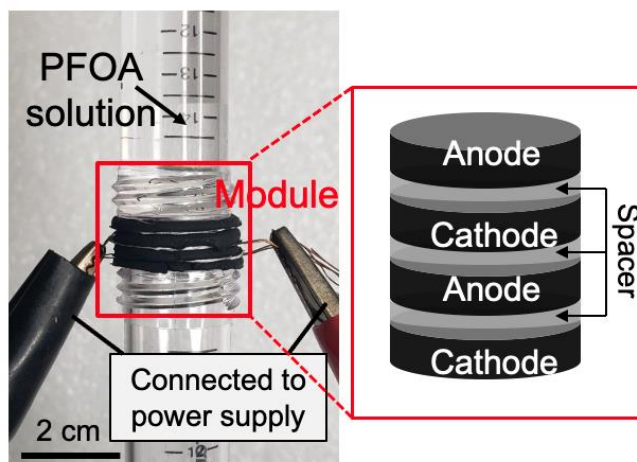


Figure 5.13. Photographs showing a device module utilized for gravity-assisted electroadsorption for PFOA from water.

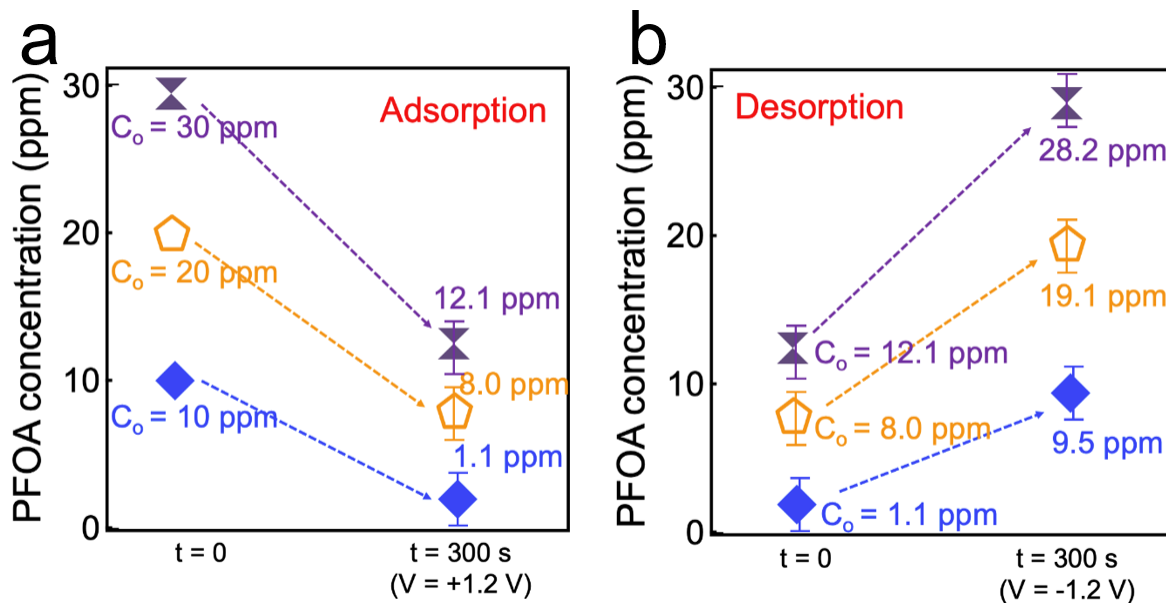


Figure 5.14. (a) The measured concentrations of PFOA in the permeate after introducing 10 mL of feed PFOA solutions with varying concentrations ($C_o = 30$ ppm, 20 ppm, and 10 ppm) to the device module. (b) The measured concentrations of PFOA after desorption for solutions with varying initial concentrations ($C_o = 30$ ppm, 20 ppm, and 10 ppm) utilizing the device module.

= 30 ppm). The results show that the permeate contains $8.0 \text{ ppm} \pm 1.0 \text{ ppm}$ ($C_o = 20$ ppm) and $12.1 \text{ ppm} \pm 2.2 \text{ ppm}$ ($C_o = 30$ ppm), respectively (**Figure 5.14a**).

We conducted desorption experiments by submerging the module in DI water and applying a voltage of $V = -1.2$ V for 300 s. The results show that the water contained 9.45 ppm of PFOA ($C_o = 10$ ppm), indicating that nearly all PFOA was released from graphite anodes. Please note that the water contained 19.1 ppm ($C_o = 20$ ppm) and 28.2 ppm ($C_o = 30$ ppm) of PFOA after desorption experiments (**Figure 5.14b**). The experimental data of adsorption and desorption for PFPA solutions by using the device module are provided in **Figures 5.15a** and **15b**, respectively. We believe that our module has the potential for a portable water purification device that can remove the dissolved contaminants and generate clean water at a low voltage (e.g., 1.2V).

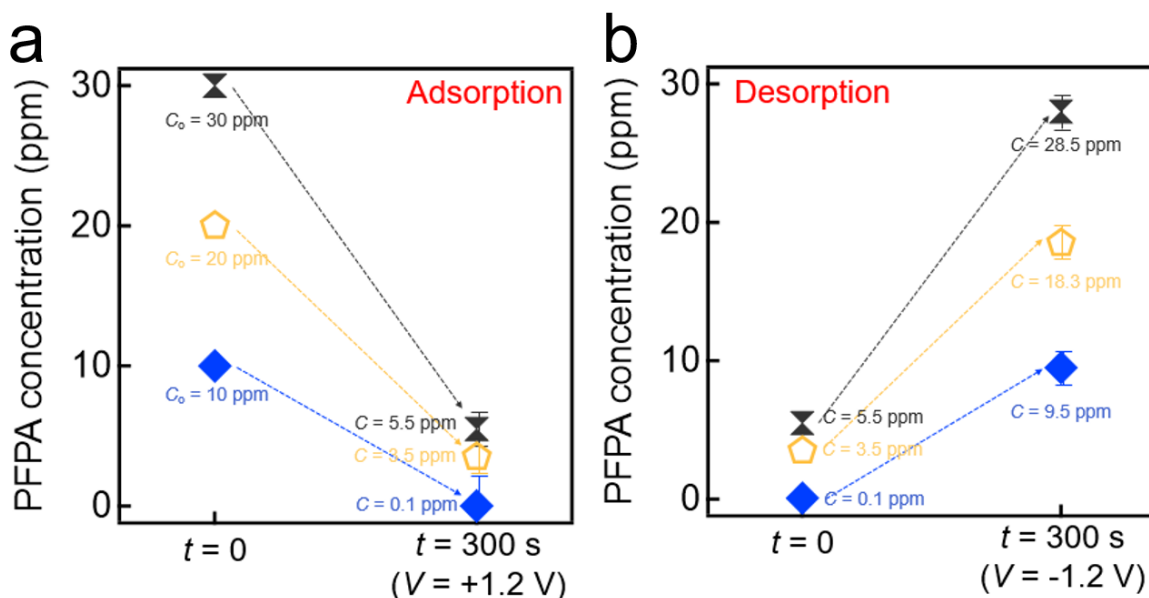


Figure 5.15. (a) The measured concentrations of PFPA in the permeate after introducing 10 mL of feed PFPA solutions with varied concentrations ($C_0 = 30$ ppm, 20 ppm, and 10 ppm) to the device module. (b) The measured concentrations of PFPA after desorption for solutions with varied initial concentrations ($C_0 = 30$ ppm, 20 ppm, and 10 ppm) utilizing the device

5.4. Conclusions

We demonstrated reversible adsorption and desorption of PFAS in water by an electric-field aided process utilizing an inexpensive graphite adsorbent as the electrode. A large BET surface area along with mesopores of graphite enabled a large adsorption capacity for PFAS with both short and long fluoroalkyl chain lengths (e.g., PFPA and PFOA, respectively) upon application of the voltage. We demonstrated that an adsorption capacity value increases with an increase in the applied voltage as well as with the increase in the PFAS concentration. We also showed multiple adsorption-desorption cycles by alternating the voltage that can result in highly efficient adsorption and desorption of PFAS from the graphite electrode surface. The kinetics of electric-field aided adsorption and desorption of PFAS in water were investigated by utilizing a pseudo-second-order model. Finally, a device module was engineered that can be mounted to a gravity-assisted apparatus for electrosorption of PFAS and obtaining water with high purity.

5.5. References

1. Buck, R. C.; Franklin, J.; Berger, U.; Conder, J. M.; Cousins, I. T.; De Voogt, P.; Jensen, A. A.; Kannan, K.; Mabury, S. A.; van Leeuwen, S. P., Perfluoroalkyl and polyfluoroalkyl substances in the environment: terminology, classification, and origins. *Integrated environmental assessment and management* **2011**, 7 (4), 513-541.
2. Sunderland, E. M.; Hu, X. C.; Dassuncao, C.; Tokranov, A. K.; Wagner, C. C.; Allen, J. G., A review of the pathways of human exposure to poly-and perfluoroalkyl substances (PFASs) and present understanding of health effects. *Journal of exposure science & environmental epidemiology* **2019**, 29 (2), 131-147.
3. Rahman, M. F.; Peldszus, S.; Anderson, W. B., Behaviour and fate of perfluoroalkyl and polyfluoroalkyl substances (PFASs) in drinking water treatment: A review. *Water Research* **2014**, 50, 318-340.
4. Post, G. B.; Cohn, P. D.; Cooper, K. R., Perfluorooctanoic acid (PFOA), an emerging drinking water contaminant: a critical review of recent literature. *Environmental Research* **2012**, 116, 93-117.
5. Ahrens, L.; Bundschuh, M., Fate and effects of poly - and perfluoroalkyl substances in the aquatic environment: A review. *Environmental toxicology and chemistry* **2014**, 33 (9), 1921-1929.
6. Kucharzyk, K. H.; Darlington, R.; Benotti, M.; Deeb, R.; Hawley, E., Novel treatment technologies for PFAS compounds: A critical review. *Journal of environmental management* **2017**, 204, 757-764.
7. Krafft, M. P.; Riess, J. G., Selected physicochemical aspects of poly-and perfluoroalkylated substances relevant to performance, environment and sustainability—Part one. *Chemosphere* **2015**, 129, 4-19.
8. Merino, N.; Qu, Y.; Deeb, R. A.; Hawley, E. L.; Hoffmann, M. R.; Mahendra, S., Degradation and removal methods for perfluoroalkyl and polyfluoroalkyl substances in water. *Environmental Engineering Science* **2016**, 33 (9), 615-649.
9. Haukås, M.; Berger, U.; Hop, H.; Gulliksen, B.; Gabrielsen, G. W., Bioaccumulation of per-and polyfluorinated alkyl substances (PFAS) in selected species from the Barents Sea food web. *Environmental Pollution* **2007**, 148 (1), 360-371.
10. Moody, C. A.; Field, J. A., Perfluorinated surfactants and the environmental implications of their use in fire-fighting foams. *Environmental science & technology* **2000**, 34 (18), 3864-3870.
11. Schultz, M. M.; Barofsky, D. F.; Field, J. A., Fluorinated alkyl surfactants. *Environmental Engineering Science* **2003**, 20 (5), 487-501.
12. Glüge, J.; Scheringer, M.; Cousins, I. T.; DeWitt, J. C.; Goldenman, G.; Herzke, D.; Lohmann, R.; Ng, C. A.; Trier, X.; Wang, Z., An overview of the uses of per-and polyfluoroalkyl substances (PFAS). *Environmental Science: Processes & Impacts* **2020**, 22 (12), 2345-2373.
13. Zhu, H.; Kannan, K., A pilot study of per-and polyfluoroalkyl substances in automotive lubricant oils from the United States. *Environmental Technology & Innovation* **2020**, 19, 100943.
14. Backe, W. J.; Day, T. C.; Field, J. A., Zwitterionic, cationic, and anionic fluorinated chemicals in aqueous film forming foam formulations and groundwater from US military bases by nonaqueous large-volume injection HPLC-MS/MS. *Environmental science & technology* **2013**, 47 (10), 5226-5234.
15. Baduel, C.; Paxman, C. J.; Mueller, J. F., Perfluoroalkyl substances in a firefighting training ground (FTG), distribution and potential future release. *Journal of hazardous materials* **2015**, 296, 46-53.

16. Kissa, E., *Fluorinated surfactants and repellents*. CRC Press: 2001; Vol. 97.
17. Rayne, S.; Forest, K., Perfluoroalkyl sulfonic and carboxylic acids: A critical review of physicochemical properties, levels and patterns in waters and wastewaters, and treatment methods. *Journal of Environmental Science and Health Part A* **2009**, *44* (12), 1145-1199.
18. Xiao, F., Emerging poly-and perfluoroalkyl substances in the aquatic environment: A review of current literature. *Water research* **2017**, *124*, 482-495.
19. Kannan, K., Perfluoroalkyl and polyfluoroalkyl substances: current and future perspectives. *Environmental chemistry* **2011**, *8* (4), 333-338.
20. Pétré, M.-A.; Genereux, D. P.; Koropecykj-Cox, L.; Knappe, D. R.; Duboscq, S.; Gilmore, T. E.; Hopkins, Z. R., Per-and Polyfluoroalkyl Substance (PFAS) Transport from Groundwater to Streams near a PFAS Manufacturing Facility in North Carolina, USA. *Environmental Science & Technology* **2021**.
21. Gellrich, V.; Brunn, H.; Stahl, T., Perfluoroalkyl and polyfluoroalkyl substances (PFASs) in mineral water and tap water. *Journal of Environmental Science and Health, Part A* **2013**, *48* (2), 129-135.
22. Hu, X. C.; Andrews, D. Q.; Lindstrom, A. B.; Bruton, T. A.; Schaidler, L. A.; Grandjean, P.; Lohmann, R.; Carignan, C. C.; Blum, A.; Balan, S. A., Detection of poly-and perfluoroalkyl substances (PFASs) in US drinking water linked to industrial sites, military fire training areas, and wastewater treatment plants. *Environmental science & technology letters* **2016**, *3* (10), 344-350.
23. Rumsby, P. C.; McLaughlin, C. L.; Hall, T., Perfluorooctane sulphonate and perfluorooctanoic acid in drinking and environmental waters. *Philosophical Transactions of the Royal Society A: Mathematical, Physical and Engineering Sciences* **2009**, *367* (1904), 4119-4136.
24. Olsen, G. W.; Butenhoff, J. L.; Zobel, L. R., Perfluoroalkyl chemicals and human fetal development: an epidemiologic review with clinical and toxicological perspectives. *Reproductive Toxicology* **2009**, *27* (3-4), 212-230.
25. Chain, E. P. o. C. i. t. F.; Knutsen, H. K.; Alexander, J.; Barregård, L.; Bignami, M.; Brüschweiler, B.; Ceccatelli, S.; Cottrill, B.; Dinovi, M.; Edler, L., Risk to human health related to the presence of perfluorooctane sulfonic acid and perfluorooctanoic acid in food. *EFSA journal* **2018**, *16* (12), e05194.
26. ITRC, PFAS Technical and Regulatory Guidance Document and Fact Sheets PFAS-1. Interstate Technology & Regulatory Council Washington, DC: 2020.
27. Sulfonates, P., Perfluoroalkyl Sulfonates; Significant New Use Rule. *Federal Register* **2002**, *67* (236), 72854-72867.
28. Control, C. f. D.; Prevention, Fourth national report on human exposure to environmental chemicals, updated tables, January 2019. *Atlanta, GA: US Department of Health and Human Services, Centers for Disease Control and Prevention.[Google Scholar]* **2019**.
29. Zhao, P.; Xia, X.; Dong, J.; Xia, N.; Jiang, X.; Li, Y.; Zhu, Y., Short-and long-chain perfluoroalkyl substances in the water, suspended particulate matter, and surface sediment of a turbid river. *Science of the Total Environment* **2016**, *568*, 57-65.
30. Brendel, S.; Fetter, É.; Staude, C.; Vierke, L.; Biegel-Engler, A., Short-chain perfluoroalkyl acids: environmental concerns and a regulatory strategy under REACH. *Environmental Sciences Europe* **2018**, *30* (1), 1-11.
31. Co - operation, O. f. E.; Development, Synthesis paper on per - and polyfluorinated chemicals (PFCs). Environment, health and safety, environment directorate, OECD/UNEP Global PFC Group. **2013**.

32. Quiñones, O.; Snyder, S. A., Occurrence of perfluoroalkyl carboxylates and sulfonates in drinking water utilities and related waters from the United States. *Environmental science & technology* **2009**, *43* (24), 9089-9095.
33. Nzeribe, B. N.; Crimi, M.; Mededovic Thagard, S.; Holsen, T. M., Physico-chemical processes for the treatment of per-and polyfluoroalkyl substances (PFAS): A review. *Critical Reviews in Environmental Science and Technology* **2019**, *49* (10), 866-915.
34. Bruton, T. A.; Sedlak, D. L., Treatment of aqueous film-forming foam by heat-activated persulfate under conditions representative of in situ chemical oxidation. *Environmental Science & Technology* **2017**, *51* (23), 13878-13885.
35. Barpaga, D.; Zheng, J.; Han, K. S.; Soltis, J. A.; Shutthanandan, V.; Basuray, S.; McGrail, B. P.; Chatterjee, S.; Motkuri, R. K., Probing the Sorption of Perfluorooctanesulfonate Using Mesoporous Metal–Organic Frameworks from Aqueous Solutions. *Inorganic chemistry* **2019**, *58* (13), 8339-8346.
36. Yang, Y.; Zheng, Z.; Ji, W.; Xu, J.; Zhang, X., Insights to perfluorooctanoic acid adsorption micro-mechanism over Fe-based metal organic frameworks: Combining computational calculation with response surface methodology. *Journal of hazardous materials* **2020**, *395*, 122686.
37. Ochoa-Herrera, V.; Sierra-Alvarez, R., Removal of perfluorinated surfactants by sorption onto granular activated carbon, zeolite and sludge. *Chemosphere* **2008**, *72* (10), 1588-1593.
38. Van den Bergh, M.; Krajnc, A.; Voorspoels, S.; Tavares, S. R.; Mullens, S.; Beurroies, I.; Maurin, G.; Mali, G.; De Vos, D. E., Highly selective removal of perfluorinated contaminants by adsorption on all - silica zeolite Beta. *Angewandte Chemie* **2020**, *132* (33), 14190-14194.
39. McCleaf, P.; Englund, S.; Östlund, A.; Lindegren, K.; Wiberg, K.; Ahrens, L., Removal efficiency of multiple poly-and perfluoroalkyl substances (PFASs) in drinking water using granular activated carbon (GAC) and anion exchange (AE) column tests. *Water research* **2017**, *120*, 77-87.
40. Zeng, C.; Atkinson, A.; Sharma, N.; Ashani, H.; Hjelmstad, A.; Venkatesh, K.; Westerhoff, P., Removing per - and polyfluoroalkyl substances from groundwaters using activated carbon and ion exchange resin packed columns. *AWWA Water Science* **2020**, *2* (1), e1172.
41. Haddad, M.; Oie, C.; Duy, S. V.; Sauvé, S.; Barbeau, B., Adsorption of micropollutants present in surface waters onto polymeric resins: Impact of resin type and water matrix on performance. *Science of The Total Environment* **2019**, *660*, 1449-1458.
42. Taleb, F.; ben Mosbah, M.; Elaloui, E.; Moussaoui, Y., Adsorption of ibuprofen sodium salt onto Amberlite resin IRN-78: Kinetics, isotherm and thermodynamic investigations. *Korean Journal of Chemical Engineering* **2017**, *34* (4), 1141-1148.
43. Yu, Q.; Deng, S.; Yu, G., Selective removal of perfluorooctane sulfonate from aqueous solution using chitosan-based molecularly imprinted polymer adsorbents. *Water Research* **2008**, *42* (12), 3089-3097.
44. Li, X.; Chen, S.; Quan, X.; Zhang, Y., Enhanced adsorption of PFOA and PFOS on multiwalled carbon nanotubes under electrochemical assistance. *Environmental science & technology* **2011**, *45* (19), 8498-8505.
45. Niu, Z.; Wang, Y.; Lin, H.; Jin, F.; Li, Y.; Niu, J., Electrochemically enhanced removal of perfluorinated compounds (PFCs) from aqueous solution by CNTs-graphene composite electrode. *Chemical Engineering Journal* **2017**, *328*, 228-235.

46. Saeidi, N.; Kopinke, F.-D.; Georgi, A., Controlling adsorption of perfluoroalkyl acids on activated carbon felt by means of electrical potentials. *Chemical Engineering Journal* **2021**, *416*, 129070.
47. Liu, L.; Liu, Y.; Gao, B.; Ji, R.; Li, C.; Wang, S., Removal of perfluorooctanoic acid (PFOA) and perfluorooctane sulfonate (PFOS) from water by carbonaceous nanomaterials: A review. *Critical Reviews in Environmental Science and Technology* **2020**, *50* (22), 2379-2414.
48. Marsh, H.; Reinoso, F. R., *Activated carbon*. Elsevier: 2006.
49. Han, J.; Yan, T.; Shen, J.; Shi, L.; Zhang, J.; Zhang, D., Capacitive deionization of saline water by using MoS₂-graphene hybrid electrodes with high volumetric adsorption capacity. *Environmental science & technology* **2019**, *53* (21), 12668-12676.
50. Du, Z.; Deng, S.; Bei, Y.; Huang, Q.; Wang, B.; Huang, J.; Yu, G., Adsorption behavior and mechanism of perfluorinated compounds on various adsorbents—A review. *Journal of hazardous materials* **2014**, *274*, 443-454.
51. Chularueangaksorn, P.; Tanaka, S.; Fujii, S.; Kunacheva, C., Adsorption of perfluorooctanoic acid (PFOA) onto anion exchange resin, non-ion exchange resin, and granular-activated carbon by batch and column. *Desalination and water treatment* **2014**, *52* (34-36), 6542-6548.
52. Appleman, T. D.; Higgins, C. P.; Quiñones, O.; Vanderford, B. J.; Kolstad, C.; Zeigler-Holady, J. C.; Dickenson, E. R., Treatment of poly-and perfluoroalkyl substances in US full-scale water treatment systems. *Water research* **2014**, *51*, 246-255.
53. Gagliano, E.; Sgroi, M.; Falciglia, P. P.; Vagliasindi, F. G.; Roccaro, P., Removal of poly-and perfluoroalkyl substances (PFAS) from water by adsorption: Role of PFAS chain length, effect of organic matter and challenges in adsorbent regeneration. *Water research* **2020**, *171*, 115381.
54. Li, F.; Duan, J.; Tian, S.; Ji, H.; Zhu, Y.; Wei, Z.; Zhao, D., Short-chain per-and polyfluoroalkyl substances in aquatic systems: Occurrence, impacts and treatment. *Chemical Engineering Journal* **2020**, *380*, 122506.
55. Militao, I. M.; Roddick, F. A.; Bergamasco, R. N.; Fan, L., Removing PFAS from aquatic systems using natural and renewable material-based adsorbents: A review. *Journal of Environmental Chemical Engineering* **2021**, 105271.
56. Wang, S.; Li, X.; Zhang, Y.; Quan, X.; Chen, S.; Yu, H.; Zhao, H., Electrochemically enhanced adsorption of PFOA and PFOS on multiwalled carbon nanotubes in continuous flow mode. *Chinese science bulletin* **2014**, *59* (23), 2890-2897.
57. Kim, K.; Baldaguez Medina, P.; Elbert, J.; Kayiwa, E.; Cusick, R. D.; Men, Y.; Su, X., Molecular Tuning of Redox - Copolymers for Selective Electrochemical Remediation. *Advanced Functional Materials* **2020**, 2004635.
58. Barrett, E. P.; Joyner, L. G.; Halenda, P. P., The determination of pore volume and area distributions in porous substances. I. Computations from nitrogen isotherms. *Journal of the American Chemical society* **1951**, *73* (1), 373-380.
59. Wang, Z.; Dou, B.; Zheng, L.; Zhang, G.; Liu, Z.; Hao, Z., Effective desalination by capacitive deionization with functional graphene nanocomposite as novel electrode material. *Desalination* **2012**, *299*, 96-102.
60. Mahmoud, A. E. D.; Stolle, A.; Stelter, M., Sustainable synthesis of high-surface-area graphite oxide via dry ball milling. *ACS Sustainable Chemistry & Engineering* **2018**, *6* (5), 6358-6369.

61. Li, H.-Q.; Wang, Y.-G.; Wang, C.-X.; Xia, Y.-Y., A competitive candidate material for aqueous supercapacitors: High surface-area graphite. *Journal of Power Sources* **2008**, *185* (2), 1557-1562.
62. Sing, K., Reporting physisorption data for gas/solid systems with special reference to the determination of surface area and porosity (Provisional). *Pure and applied chemistry* **1982**, *54* (11), 2201-2218.
63. Cao, D.; Hu, M.; Han, C.; Yu, J.; Cui, L.; Liu, Y.; Wang, H.; Cai, Y.; Kang, Y.; Zhou, Y., Proton sponge-functionalized silica as high performance adsorbents for solid-phase extraction of trace perfluoroalkyl sulfonates in the environmental water samples and their direct analysis by MALDI-TOF-MS. *Analyst* **2012**, *137* (9), 2218-2225.
64. Sasi, P. C.; Alinezhad, A.; Yao, B.; Kubátová, A.; Golovko, S. A.; Golovko, M. Y.; Xiao, F., Effect of granular activated carbon and other porous materials on thermal decomposition of per- and polyfluoroalkyl substances: Mechanisms and implications for water purification. *Water Research* **2021**, *200*, 117271.
65. Suss, M.; Porada, S.; Sun, X.; Biesheuvel, P.; Yoon, J.; Presser, V., Water desalination via capacitive deionization: what is it and what can we expect from it? *Energy & Environmental Science* **2015**, *8* (8), 2296-2319.
66. Rica, R.; Ziano, R.; Salerno, D.; Mantegazza, F.; Brogioli, D., Thermodynamic relation between voltage-concentration dependence and salt adsorption in electrochemical cells. *Physical review letters* **2012**, *109* (15), 156103.
67. Zhang, D.; Wen, X.; Shi, L.; Yan, T.; Zhang, J., Enhanced capacitive deionization of graphene/mesoporous carbon composites. *Nanoscale* **2012**, *4* (17), 5440-5446.
68. Dyatkin, B.; Osti, N. C.; Gallegos, A.; Zhang, Y.; Mamontov, E.; Cummings, P. T.; Wu, J.; Gogotsi, Y., Electrolyte cation length influences electroadsorption and dynamics in porous carbon supercapacitors. *Electrochimica Acta* **2018**, *283*, 882-893.

Chapter 6: Electrosorption-driven remediation of PFAS-contaminated water with Engineered MXene/PEDOT:PSS Adsorbents

Abstract: Per- and polyfluoroalkyl substances (PFAS) are a group of chemicals that have been used in a wide range of applications. Recent studies have revealed that PFAS are persistent and accumulative both in the environment and the human body. The technologies that are currently in use for PFAS removal from water rely on physisorption. While it is effective for removing PFAS with a longer fluoroalkyl chain (e.g., $(\text{CH}_2)_7$ or longer), its efficacy for those with a shorter chain (e.g., $(\text{CH}_2)_6$ or shorter) is an issue. Electric-field aided sorption (i.e., electrosorption) has been explored as an alternative to overcome such limitations. Herein, we demonstrate electrosorption of PFAS with varied fluoroalkyl chains by utilizing MXene-PEDOT:PSS adsorbent. Intercalation of PEDOT:PSS to the MXene help enhance the capacitive property of MXene, increasing the electrosorption of PFAS. Using the adsorbent, we demonstrate electrosorption of PFAS with varied fluoroalkyl chain lengths from water upon applying a voltage of $V = 1.0$ V. Also, the adsorbent can desorb the PFAS from its surface when applying a voltage of $V = -1.0$ V, which regenerates the adsorbent for further operations. Finally, a pseudo-second-order kinetic model that describes the reversible electrosorption of PFAS from MXene-PEDOT:PSS adsorbent is proposed.

6.1. Introduction

Perfluoroalkyl substances (PFAS), as a group of organofluorine materials¹⁻⁶, have been employed extensively in a range of practical applications, including lubricants⁷, surfactants^{8, 9}, and firefighting foams.¹⁰⁻¹² PFAS can exhibit excellent chemical and thermal stability, which can be attributed to their fluoroalkyl chains with a strong carbon-fluorine bond.¹³⁻¹⁵ The widespread utilization of PFAS has resulted in their ingress into the environment (e.g., surface and groundwaters, soils)^{5, 16, 17}. Recently, PFAS has been detected in the drinking water which has raised serious health concerns.^{11, 18} It has been revealed that PFAS accumulation in the body can cause several health disorders including cancer, high blood pressure, and weak immune system.^{19,}
²⁰ Thus, the government and environmental agencies have implemented regulations to decrease the manufacturing of PFAS. For example, the United States Environmental Protection Agency (US EPA) has entered into an agreement with PFAS manufacturers over the voluntary "phase-out" of certain PFAS types by January 2024.²¹ Despite these efforts, a drastic increase in the production of short-chain PFAS (i.e., $-(\text{CH}_2)_6-$ and shorter) has been reported.²² Given that the short-chain

PFAS are more persistent and mobile²³ as well as challenging to remove²⁴ compared to those with long-chain, there is a dire need for developing remediation technologies that can enable the removal of PFAS with long as well as short-chain lengths.

Various technologies for remediating PFAS-contaminated water have been implemented.^{3, 25-27} Electrochemical or plasma-based oxidation processes can degrade PFAS dissolved in water.^{3, 25} For example, Zhuo et al.,²⁸ demonstrated electrochemical oxidation of perfluorooctanoic acid (PFOA) in water. The process results in approximately 90 % removal of PFOA. Singh et al.,²⁹ demonstrated that Argon plasma treatment could result in the decomposition of PFOA and perfluorooctane sulfonic acid (PFOS) with very high efficiency. While these destructive technologies are effective for long-chain PFAS, their performance in the removal of short-chain PFAS is limited.²⁴ Also, these processes can produce byproducts resulting in secondary pollution.²⁹ Adsorption is a non-destructive technology to decontaminate the water from PFAS.³⁰⁻³³ For example, McCleaf et al.³⁴ have demonstrated that the activated carbons can remove various PFAS from water with a reasonable (>70%) removal efficiency. Various reports have shown that ion exchange resins can demonstrate a high-efficiency removal of PFAS from water.³⁵ Despite their relatively lower cost of operation and lower energy consumption, adsorption-based technologies can be limited by poor removal efficiency for short-chain PFAS.³⁶ Also, most adsorbents undergo a decrease in the adsorption capacity over time due to the residual PFAS that remains even after the regeneration process.³⁷

Electric-field aided sorption (i.e., electrosorption) has been identified as a promising technology that can overcome the abovementioned limitations of the conventional adsorption process.³⁸ Upon application of electric field across the two electrodes (i.e., adsorbents), anionic PFAS gets attracted and adsorbed to an anode surface.³⁸⁻⁴¹ Considering that electrosorption employs the electrostatic

and coulombic force of attraction between an electrode and ionized species, it can effectively remove PFAS with both long and short fluoroalkyl chain lengths. In contrast, conventional adsorbents primarily rely on hydrophobic interaction with PFAS, which makes them less effective for removing short-chain PFAS.^{41,42}

An effective electrosorption process requires the adsorbent to fulfill the following design criteria. First, it should possess a large specific surface area that serves as adsorption sites. Also, it should exhibit durability against chemically and thermally aggressive environments.³⁸⁻⁴¹ Furthermore, it should demonstrate high capacitance and electrical conductivity. Recently, a new class of two-dimensional metal carbide, carbonitride, and nitride (i.e., MXene) has emerged as a competitive adsorbent for the electrosorption process due to MXene's high capacitance and electrical conductivity.⁴³ The layered structure of MXene allows the dissolved ions to be readily inserted and adsorbed to the surface (i.e., ion intercalation).⁴⁴

The electrochemical performance of MXene can be improved by increasing the interfacial area between the MXene surface and the electrolyte or by decreasing the ion diffusion length.⁴⁵ Recently, poly(3,4-ethylenedioxythiophene) polystyrene sulfonate (PEDOT:PSS) has been employed in MXene due to its elasticity and facile fabrication process^{46,47}.⁴⁵ The resulting MXene-PEDOT adsorbent exhibited enhanced specific surface area and high volumetric capacitance. However, PSS is an insulator that impedes charge transport on the polymer. Previous reports have shown that strong acid treatment can remove the insulating PSS from the MXene-PEDOT:PSS resulting in increased electrical conductivity.⁴⁵

Herein, we report electrosorption of PFAS with varied fluoroalkyl chain lengths by utilizing Mxene-PEDOT:PSS adsorbent upon application of electric voltage. The adsorbent is fabricated by facile mixing of MXene, and PEDOT:PSS. Using the adsorbent, we demonstrate electrosorption

of PFAS with varied fluoroalkyl chain lengths from water upon applying a voltage of $V = 1.0$ V. Also, the adsorbent can desorb the PFAS from its surface when applying a voltage of $V = -1.0$ V, which regenerates the adsorbent for further operations. Finally, a pseudo-second-order kinetic model that describes the reversible electrosorption of PFAS from MXene-PEDOT:PSS adsorbent is proposed.

6.2. Experimental procedure

6.2.1. Synthesis of MXene.

A 1.98 g of lithium fluoride (LiF) was added to 30 ml of 6 M hydrochloric acid (HCl). The solution was stirred for 5 mins to dissolve the LiF. Subsequently, 3.0 g of MAX ($M_{n+1}AX_n$, where $n = 1$ to 3, and M is an early transition metal, A is an A-group (mostly IIIA and IVA, or groups 13 and 14) element and X is either carbon and/or nitrogen phase titanium aluminum carbide) was gradually added to the solution over the course of 10 mins to avoid initial overheating of the solution. The solution was then held at 40 °C for 45 hours, followed by washing through 5 cycles of DI water addition, centrifugation (5 mins for each cycle), and decanting until the supernatant reached a pH of approximately 6.0. The final product (MXene) was filtered, followed by drying in ambient conditions for 24 hours.

6.2.2. Preparation of MXene-PEDOT:PSS adsorbent.

The MXene was first dispersed in DI water to reach a concentration of 1.5 mg ml⁻¹. A desirable quantity of PEDOT:PSS (Sigma Aldrich) was added to the dispersion to fabricate varied compositions of MXene and PEDOT PSS (95:5, 90:10, 80:20, 70:30, and 60:40, MXene: (PEDOT:PSS) by weight). The dispersion was stirred for 24 hours and was filtered using filter paper (Watman Grade 6, 2 μm) under negative pressure (600 torrs). The obtained a clay-like

MXene-PEDOT:PSS was applied to a glass slide with required thickness and was dried, followed by being soaked in H₂SO₄ for 24 hours and subsequently drying at 40 °C for 24 hours.

6.2.3. Characterization of surface morphology, chemistry, and interlayer spacing of MXene-PEDOT:PSS.

The surface morphology was characterized by scanning electron microscopy (SEM, FEI Versa 3D DualBeam) at an accelerating voltage of 10 kV. A PerkinElmer Spectrum 400 FTIR spectrometer was utilized in the attenuated total reflectance (ATR) mode in the wavenumber range of 600 cm⁻¹ – 4000 cm⁻¹ to analyze the chemical structure. The FTIR spectra were recorded at a resolution of 4 cm⁻¹ for 16 scans. The interlayer spacing was studied by powder X-ray diffraction (XRD) with a PANalytical Model X'Pert PRO diffractometer with Cu K α radiation ($k = 1.54 \text{ \AA}$) by scanning at a rate of 2° (2θ) min⁻¹.

6.2.4. Characterization of electrochemical properties of MXene-PEDOT:PSS.

Cyclic voltammetry measurements were performed on a Model 760E Series Bipotentiostat workstation with a three-electrode cell setup at room temperature ($\approx 22 \text{ }^\circ\text{C}$). The MXene-PEDOT:PSS (size = 2 cm \times 2 cm, thickness = 0.5 cm), a platinum (Pt) wire electrode, and an Ag/AgCl electrode were used as a working electrode, counter electrode, and reference electrode, respectively. The sweep potential range was adjusted from -1.4 V to +1.4 V (vs. Ag/AgCl electrode) and scanned at a rate of 10 mV s⁻¹. We chose this range based on previous reports.⁴⁸ The electrolytes were 0.01 M PFOA and PFBA-water mixture. Volumetric capacitance (C_v) is calculated utilizing following equation:

$$\text{(Equation 6.1)} \quad C_v = \rho \frac{\int Idv}{2mv\Delta V}$$

Where ρ is electrode density, I is the response current (A), V is the potential vs. reference electrode (V), m is mass (mg), v is the scan rate (mV s⁻¹), ΔV is the potential window (V).

6.2.5. Adsorption and desorption tests.

We utilized a custom-made batch separation cell for adsorption and desorption tests, which was reported in our previous work.⁴⁸ The feed solution was continuously fed into the channel between the two adsorbents at a constant flow rate of $\approx 3 \text{ ml min}^{-1}$. A total of 20 ml of solution was used. Note that all solutions concentration was 4 mg ml^{-1} . While a voltage was applied across the electrodes, electrical conductivity was monitored by a multimeter (Gardner Bender GDT-3190). The correlation of the electrical conductivity of a solution and the concentration of PFAS was established prior to the test. The adsorption capacity (α) was calculated by:

$$\text{(Equation 6.2)} \quad \alpha = \frac{(C_0 - C_t)Q}{m}$$

where C_0 and C_t (mg ml^{-1}) represent the initial and final PFAS concentrations, respectively. Q is the volume of the solution. M is the mass of electrode. Note that all experiments were conducted at room temperature ($\approx 22 \text{ }^\circ\text{C}$). The desorption experiments were conducted by utilizing the same custom-made cell. A 20 ml of DI water was injected at the inlet of the cell with a flow rate of $\approx 3 \text{ ml min}^{-1}$ while applying a negative voltage across the electrodes with adsorbed PFAS. The DI water containing desorbed PFAS was collected at the outlet of the cell at $T = 22.0 \pm 1.4 \text{ }^\circ\text{C}$.

6.3. Results and discussion

6.3.1. Characterization of surface and its morphology

Figure 6.1 illustrates the procedure of synthesizing MXene-PEDOT:PSS electrode for electrosorption of PFAS from water (see **Experimental procedure**). The resulting electrode's

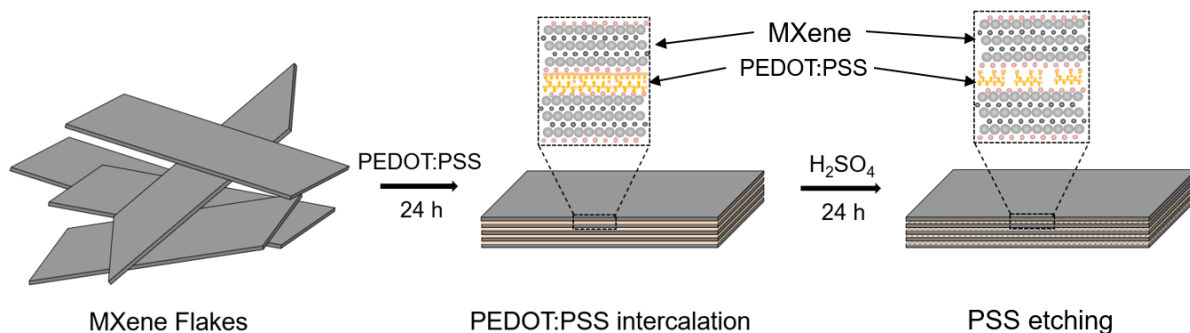


Figure 6.1. Schematic demonstrating the preparation of the MXene:PEDOT:PSS electrode for the electrosorption process.

surface morphology was analyzed by scanning electron microscopy (SEM) (**Figure 6.2**). The SEM image shows that the surface possesses an open-edged and layered structure. The layered structure demonstrates smoother morphology with an increase in the PEDOT:PSS concentration. By comparing the SEM image of MXene-PEDOT:PSS prepared without the acid etching process (**Figure 6.2** inset), it is clear that acid etching can enable an increased interlayer spacing which can be attributed to the dissolution of PSS.⁴⁵ To verify this, we conducted Fourier transform infrared (FT-IR) spectroscopy for as-prepared and acid-etched MXene-PEDOT:PSS (**Figure 6.3a**). Both spectra exhibit several characteristic peaks of MXene, including C–O ($\approx 1051\text{ cm}^{-1}$), C–F ($\approx 1090\text{ cm}^{-1}$), –OH ($\approx 1600\text{ cm}^{-1}$), and Ti–O ($\approx 665\text{ cm}^{-1}$). However, the spectrum of the

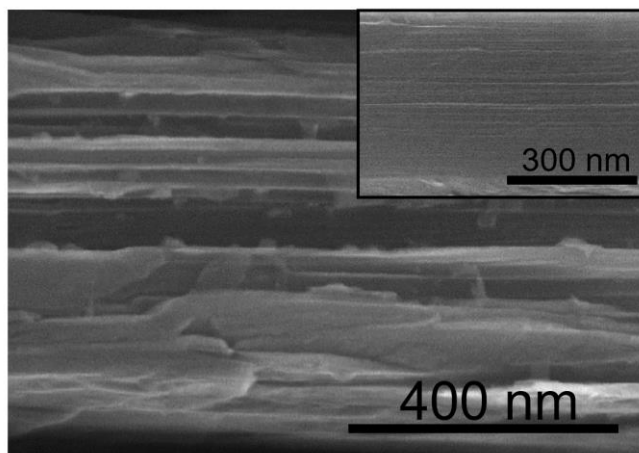


Figure 6.2. Cross-section morphology of the MXene intercalate with PEDOT:PSS. Inset shows the cross-sectional view of the MXene-PEDOT:PSS without acid etching.

electrode after acid etching exhibits diminished FT-IR bands at 1630 cm^{-1} , 1420 cm^{-1} , and 1170 cm^{-1} , which are mainly due to C-C and C=C stretching of the polymeric PSS indicating partial removal. This can be attributed to partial etching of PSS and PMMA from the electrode. Further,

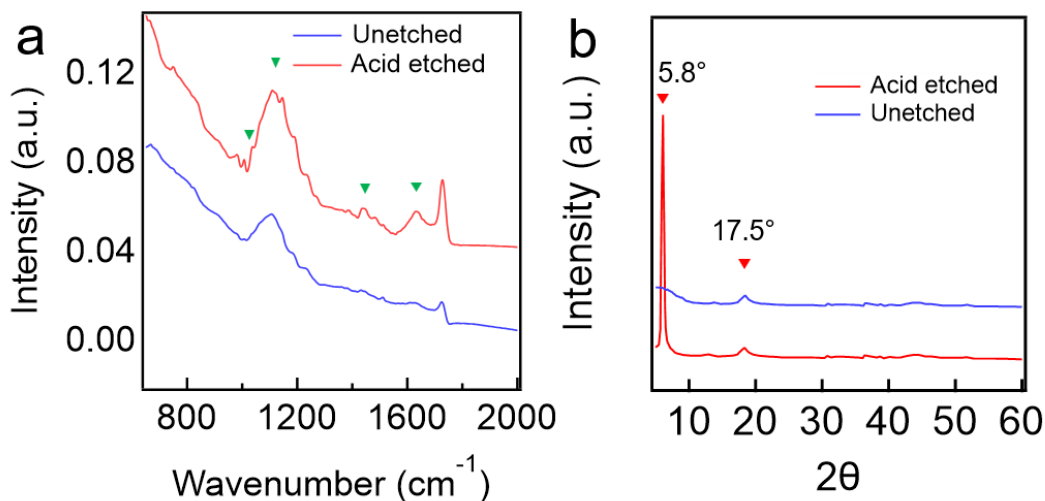


Figure 6.3. (a) Comparison of the FTIR spectra of acid-etched and unetched MXene-PEDOT:PSS. (b) Comparison of the XRD patterns of acid-etched and unetched MXene-PEDOT:PSS.

the FT-IR results demonstrate that PEDOT:PSS was intercalated between the MXene layers, which can expand the interlayer spacing and prevent the re-stacking of layers. Upon acid etching, the polymer (e.g., PSS) was dissolved, which results in a larger surface area for adsorption of anionic PFAS.

The change in the interlayer spacing was further confirmed by x-ray diffraction (XRD) (**Experimental procedure**). **Figure 6.3b** shows the XRD patterns of as-prepared MXene-PEDOT:PSS, and acid-etched MXene-PEDOT:PSS. An as-prepared MXene-PEDOT:PSS does not show the peak at $2\theta < 12^\circ$, indicating that PEDOT:PSS is intercalated. After acid treatment, it a peak appears at $2\theta = 5.8^\circ$, which corresponds to an interlayer spacing value of 15.2 \AA due to partial removal of PSS. Note that no notable diffraction peaks related to PEDOT:PSS were distinguished in the XRD patterns due to their amorphous structure.

6.3.2. Electrochemical characterization

We measured a volumetric capacitance (C_v) of MXene-PEDOT:PSS by conducting cyclic voltammetry (CV) measurements with a scan rate of 2 mV s^{-1} (**Experimental procedure**). Here we utilized MXene-PEDOT:PSS with varied PEDOT:PSS compositions. **Figure 6.4a** shows the measured CV plots for perfluorooctanoic acid (PFOA) solution (concentration = 0.1 M) by applying a cyclic voltage between -1.0 V and $+1.0 \text{ V}$. The shape of the CV curve is a slightly distorted rectangular shape. The distortion can be attributed to a high resistivity of the PFAS solution and polarization effects. It should be noted that a higher capacitance was obtained at a higher composition of MXene, indicating an excellent capacitive behavior. The intercalation and confinement of the polymer between MXene flakes enhanced the cationic intercalation, offering remarkable volumetric capacitance. An increase in polymer composition impedes charge transport within the electrode resulting in a decrease in capacitance.⁴⁵ Utilizing the measured CV plots, we calculated the C_v values by Equation 6.1. The results show that MXene-PEDOT:PSS with a higher PEDOT:PSS composition shows a lower C_v value (**Table 6.1**) at 20 mV s^{-1} . For example, MXene-

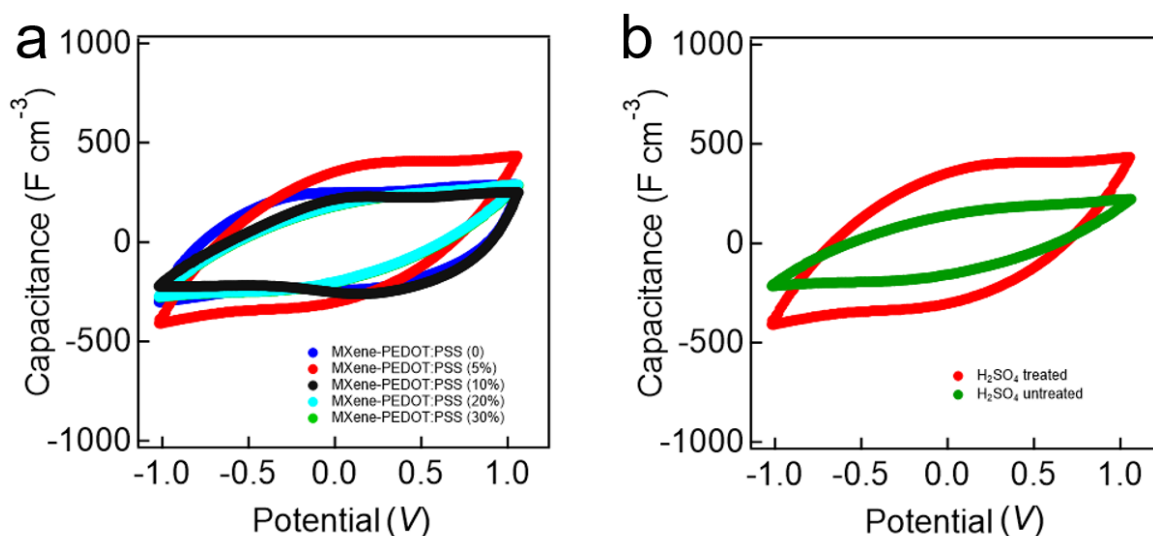


Figure 6.4. (a) Cyclic voltammetry (CV) curves of MXene-PEDOT:PSS electrodes with varied compositions. (b) CV curves for MXene-PEDOT:PSS (5 wt%) electrodes with and without H_2SO_4 treatment.

PEDOT:PSS (5 wt%) demonstrates the C_v value of 410 F cm^{-3} while that with 20 wt% shows $C_v = 114 \text{ F cm}^{-3}$. When MXene-PEDOT:PSS undergoes acid treatment, it shows a significantly higher C_v value (**Figure 6.4b**). An MXene-PEDOT:PSS (5 wt%) without acid treatment demonstrates the C_v value of 98 F cm^{-3} while that treated with acid shows $C_v = 410 \text{ F cm}^{-3}$. Note that the etched MXene-PEDOT:PSS shows a density of 3.72 g cm^{-3} , which is comparable to that of a neat MXene (3.95 g cm^{-3}). The capacitance values of MXene-PEDOT:PSS (5 wt%) at different scan rates are provided in **Figure 6.5**.

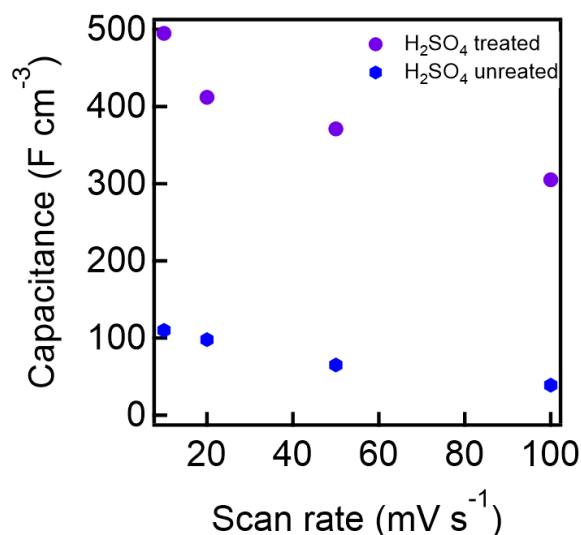


Figure 6.5. Capacitance of MXene-PEDOT:PSS (5%) at varied scan rate.

Table 6.1. Capacitance value for MXene-PEDOT:PSS electrodes with and without acid treatment.

Sample	Non-acid treated	Acid treated
MXene-PEDOT:PSS (0)	$252 \pm 5 \text{ F cm}^{-3}$	$252 \pm 11 \text{ F cm}^{-3}$
MXene-PEDOT:PSS (5 wt%)	$98 \pm 4 \text{ F cm}^{-3}$	$410 \pm 10 \text{ F cm}^{-3}$
MXene-PEDOT:PSS (10 wt%)	$54 \pm 3 \text{ F cm}^{-3}$	$298 \pm 6 \text{ F cm}^{-3}$
MXene-PEDOT:PSS (20 wt%)	$32 \pm 3 \text{ F cm}^{-3}$	$114 \pm 5 \text{ F cm}^{-3}$
MXene-PEDOT:PSS (30 wt%)	$18 \pm 4 \text{ F cm}^{-3}$	$95 \pm 5 \text{ F cm}^{-3}$

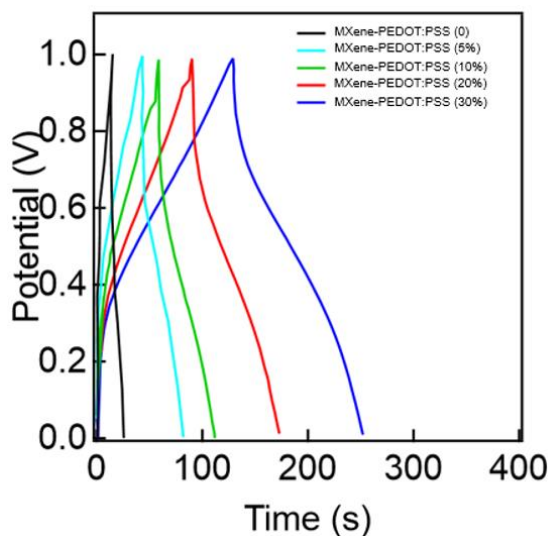


Figure 6.6. Gravimetric charge-discharge (GCD) curves of MXene-PEDOT:PSS electrodes with varied compositions.

To test MXene-PEDOT: PSS's reversibility of the redox reactions and low equivalent series resistance, we conducted a gravimetric charge-discharge (GCD) analysis (**Figure 6.6**). The measured GCD curves exhibit a triangular shape with linear lines⁴⁵ indicating reversibility of the redox reactions and low equivalent series resistance with negligible voltage drop. Based on the CV measurements, we utilized MXene-PEDOT:PSS (5 wt%) as the adsorbent for electrosorption of PFAS for the rest of this report.

6.3.3. Adsorption and desorption of PFAS

Electrosorption of PFAS using MXene-PEDOT:PSS was conducted by using a custom-made cell (**Figure 6.7** and see also **Experimental procedure**). In this setup, the PFAS solution in water is introduced at a flow rate of 3 ml min^{-1} to the electrodes (anode and cathode, MXene-PEDOT:PSS) separated by 5 mm.

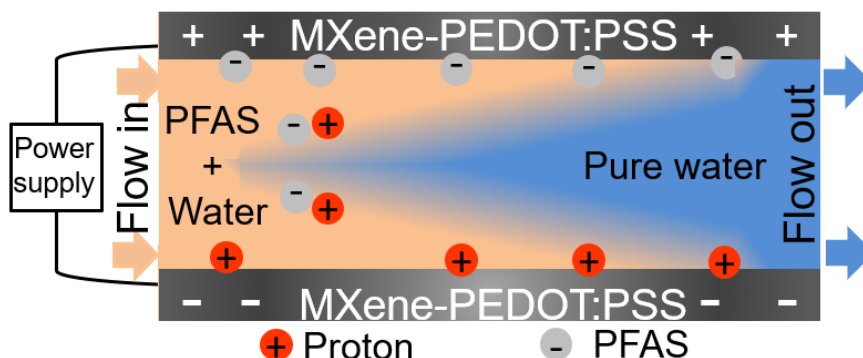


Figure 6.7. Schematic illustrating the working principle of the custom-made cell utilized for capacitive electrosorption and removal of PFAS.

Upon application of a voltage across the electrodes, anionic PFAS and the cations intercalate into the anode and cathode, respectively. Here we tested PFAS with different fluoroalkyl chain lengths, including perfluorobutyric acid (PFBA), perfluoropentanoic acid (PFPA), perfluorohexanoic acid (PFHxA), perfluorooctanoic acid (PFOA), and perfluorononaic acid (PFNA) at varied concentrations (e.g., 0.01 M, 0.005 M, 0.0025 M, 0.00125 M, and 0.000625 M). Please note that the applied voltage was $V = 1.0$ V. The concentration of PFAS following the electrosorption was determined by measuring the electrical conductivity and comparing it with the calibration curves of standard concentrations. An MXene-PEDOT:PSS shows a higher adsorption capacity (α , the mass of the adsorbed PFAS on one gram of MXene-PEDOT:PSS, see **Experimental procedure**) value for a PFAS with a shorter fluoroalkyl chain length at a given concentration (**Figure 6.8a**). For example, the α value for PFNA ($-(\text{CF}_2)_7\text{CF}_3$) was measured as $\alpha = 22.5 \text{ mg g}^{-1}$ while that for PFBA ($-(\text{CF}_2)_2\text{CF}_3$) was $\alpha = 59.4 \text{ mg g}^{-1}$, respectively, at a concentration of 0.01 M. This is a direct consequence of the difference in the molecular size (i.e., fluoroalkyl chain length) which results in the association of more PFBA anions with the charges on the anode surface compared to PFNA anions. Also, the results show that a PFAS solution with a higher concentration exhibits a higher

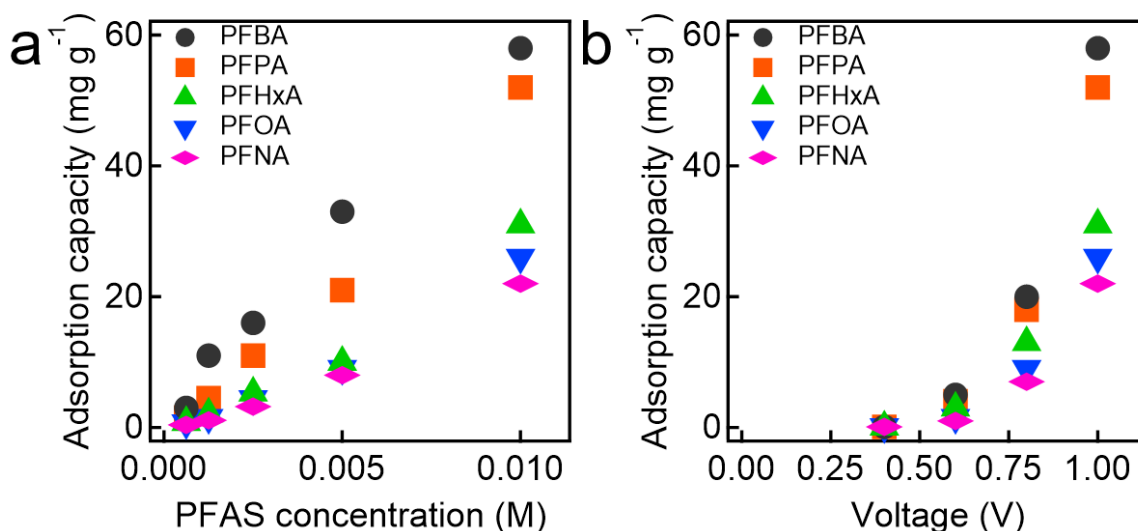


Figure 6.8. (a) Adsorption capacity for various PFAS with different concentrations at a given voltage of $V = 1.0$ V. (b) Adsorption capacity for various PFAS at different voltages when the concentration is 0.01 M.

α value. For example, the α value for PFNA at a concentration of 0.01 M was measured as $\alpha = 22.5$ mg g⁻¹ while that with a concentration of 0.0025 M was $\alpha = 4.2$ mg g⁻¹. This can be attributed to a higher mass transfer rate of anionic PFAS in an MXene-PEDOT:PSS with an increase in the overlapping effect.⁴⁹ We measured the adsorption capacity for PFAS solutions (concentration = 0.01 M) at different voltages (**Figure 6.8b**). The results show that the adsorption capacity for all PFAS increased at higher values of voltage. Further, at a given voltage, the adsorption capacity for a PFAS with a shorter fluoroalkyl chain length (e.g., PFBA) is significantly higher than that of a long chain PFAS (e.g., PFOA). This can be attributed to a higher mobility⁵⁰ of anionic PFBA compared to PFOA, which can contribute to a greater decrease in the electrical conductivity as the electrosorption process proceeds. We also measured the adsorption and desorption rate for PFBA and PFOA as representative short and long-chain PFAS, respectively. The result of the experiments is demonstrated in **Figures 6.9a** and **9b**. The results indicate a higher adsorption and

desorption rate for the long-chain PFBA compared with short-chain PFOA at all applied voltages.⁴⁸

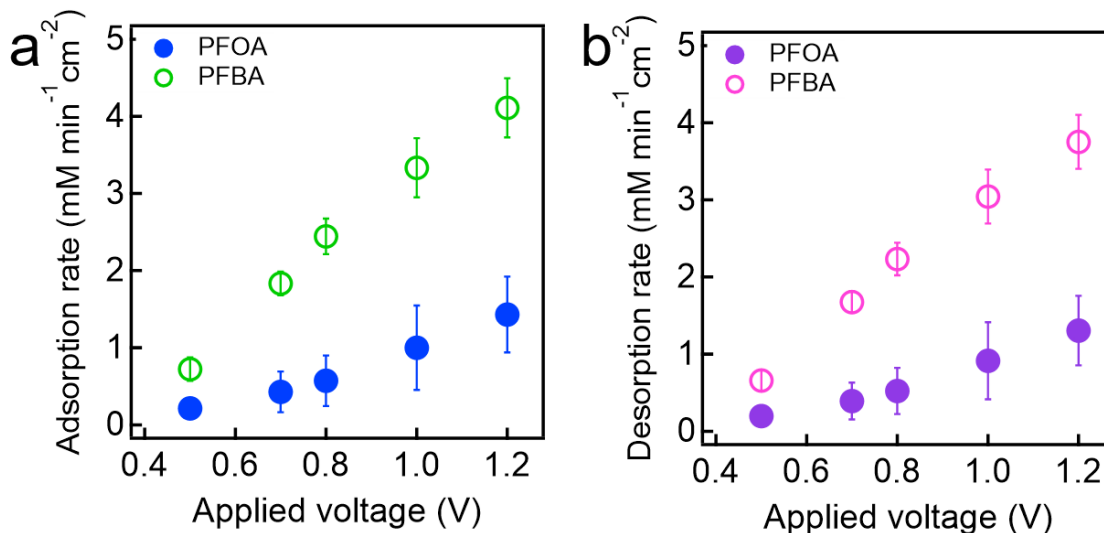


Figure 6.9. Adsorption (a) and desorption (b) rates for PFBA and PFOA at different voltages.

6.3.4. Kinetics of adsorption and desorption

Finally, we investigated the kinetics of electrosorption by MXene-PEDOT:PSS. Here we also utilized PFBA, PFPA, PFHxA, PFOA, and PFNA solutions (concentration = 0.01 M). Please note that the same custom-made cell was utilized for the kinetics studies as well. **Figure 6.10a** shows the time-dependent change in the concentration of the solutions upon application of a voltage of $V = +1.0$ V across the MXene-PEDOT:PSS electrodes. The results show that the concentration of the solutions rapidly decreases upon the application of voltage. For example, the concentration of PFBA and PFNA solutions reached a nearly constant value (0.0072 ± 0.0010 M and 0.0027 ± 0.0005 M, respectively) after 30 s of voltage application, which indicates that the equilibrium condition was attained. Please note that the electrosorption process can be described by the pseudo-second-order kinetic model, which is given as:

$$\text{(Equation 6.3)} \quad \sigma(t) = \sigma_o - \frac{k_2 q_e^2 t}{1 + k_2 q_e t}$$

where $\sigma(t)$ and σ_0 are the concentration of PFAS solution at time t and $t = 0$ (i.e., the initial concentration). q_e is the amount of PFAS adsorbed on the electrode at equilibrium, and k_2 is the adsorption rate constant. By fitting Equation 6.3 to the experimentally measured values, we obtained the k_2 values as 38.91 s^{-1} , 34.22 , 30.32 , 30.21 , and 10.66 s^{-1} for PFNA, PFOA, PFHxA, PFPA, and PFBA, respectively.

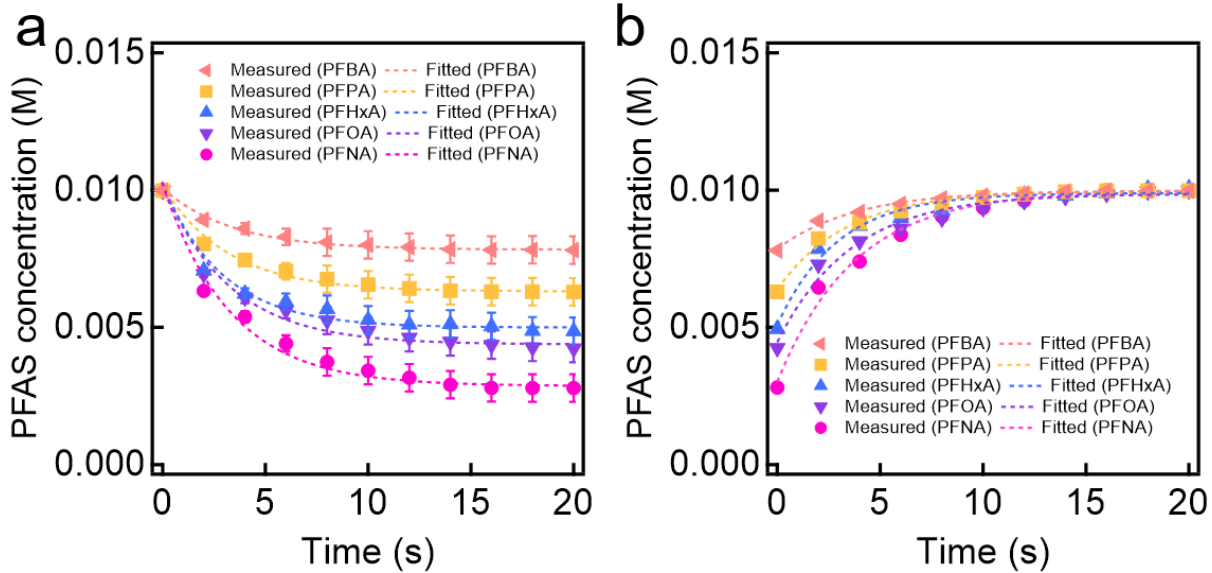


Figure 6.10. (a-b) Time-dependent plots demonstrating the change in the concentration of the PFAS solutions upon applying a voltage of (a) $V = +1.0 \text{ V}$ during the adsorption, and (b) $V = -1.0 \text{ V}$ during the desorption. The fitted values of concentration by pseudo-second order kinetic model are also provided.

When the applied voltage is reversed ($V = -1.0 \text{ V}$), the adsorbent starts to desorb the PFAS to the surrounding water. Consequently, the concentration of a solution started to increase and reached a constant value (**Figure 6.10b**). For example, the concentration of PFBA and PFNA solutions reached a constant value ($0.01 \pm 0.0010 \text{ M}$) after 20 s. The kinetics for the desorption process can also be described by a pseudo-second-order kinetic model:

$$\text{(Equation 6.4)} \quad \sigma(t) = \sigma_f + \frac{k_2' q_e'^2 t}{1 + k_2' q_e' t}$$

where σ_f is the concentration of a solution after the adsorption experiment, q_e' is the amount of PFAS desorbed from the electrode at equilibrium, and k_2' is a desorption rate constant. By fitting

the experimentally measured data, we determined the k_2' values as 42.91 s⁻¹, 37.22, 33.32, 31.92, and 12.92 s⁻¹ for PFNA, PFOA, PFH_xA, PFPA, and PFBA, respectively.

6.4. Conclusions

We demonstrated electrosorption of PFAS from water utilizing an MXene-PEDOT:PSS as an electrode. The electrode was fabricated by intercalating PEDOT:PSS in MXene layers followed by acid etching. The resulting MXene-PEDOT:PSS electrodes exhibited 410 F cm⁻³ as the volumetric capacitance, which can result in a higher adsorption capacity value for PFAS with both long and short fluoroalkyl chain lengths. Finally, the kinetics of electrosorption of PFAS in water was investigated by utilizing a pseudo-second-order model.

6.5. References

1. Buck, R. C.; Franklin, J.; Berger, U.; Conder, J. M.; Cousins, I. T.; De Voogt, P.; Jensen, A. A.; Kannan, K.; Mabury, S. A.; van Leeuwen, S. P., Perfluoroalkyl and polyfluoroalkyl substances in the environment: terminology, classification, and origins. *Integrated environmental assessment and management* **2011**, 7 (4), 513-541.
2. Sunderland, E. M.; Hu, X. C.; Dassuncao, C.; Tokranov, A. K.; Wagner, C. C.; Allen, J. G., A review of the pathways of human exposure to poly-and perfluoroalkyl substances (PFASs) and present understanding of health effects. *Journal of exposure science & environmental epidemiology* **2019**, 29 (2), 131-147.
3. Rahman, M. F.; Peldszus, S.; Anderson, W. B., Behaviour and fate of perfluoroalkyl and polyfluoroalkyl substances (PFASs) in drinking water treatment: A review. *Water research* **2014**, 50, 318-340.
4. Post, G. B.; Cohn, P. D.; Cooper, K. R., Perfluorooctanoic acid (PFOA), an emerging drinking water contaminant: a critical review of recent literature. *Environmental research* **2012**, 116, 93-117.
5. Ahrens, L.; Bundschuh, M., Fate and effects of poly - and perfluoroalkyl substances in the aquatic environment: A review. *Environmental toxicology and chemistry* **2014**, 33 (9), 1921-1929.
6. Kucharzyk, K. H.; Darlington, R.; Benotti, M.; Deeb, R.; Hawley, E., Novel treatment technologies for PFAS compounds: A critical review. *Journal of environmental management* **2017**, 204, 757-764.
7. Glüge, J.; Scheringer, M.; Cousins, I. T.; DeWitt, J. C.; Goldenman, G.; Herzke, D.; Lohmann, R.; Ng, C. A.; Trier, X.; Wang, Z., An overview of the uses of per-and polyfluoroalkyl substances (PFAS). *Environmental Science: Processes & Impacts* **2020**, 22 (12), 2345-2373.
8. Kissa, E., *Fluorinated surfactants and repellents*. CRC Press: 2001; Vol. 97.
9. Schultz, M. M.; Barofsky, D. F.; Field, J. A., Fluorinated alkyl surfactants. *Environmental Engineering Science* **2003**, 20 (5), 487-501.
10. Baduel, C.; Paxman, C. J.; Mueller, J. F., Perfluoroalkyl substances in a firefighting training ground (FTG), distribution and potential future release. *Journal of hazardous materials* **2015**, 296, 46-53.
11. Hu, X. C.; Andrews, D. Q.; Lindstrom, A. B.; Bruton, T. A.; Schaidler, L. A.; Grandjean, P.; Lohmann, R.; Carignan, C. C.; Blum, A.; Balan, S. A., Detection of poly-and perfluoroalkyl substances (PFASs) in US drinking water linked to industrial sites, military fire training areas, and wastewater treatment plants. *Environmental science & technology letters* **2016**, 3 (10), 344-350.
12. Moody, C. A.; Field, J. A., Perfluorinated surfactants and the environmental implications of their use in fire-fighting foams. *Environmental science & technology* **2000**, 34 (18), 3864-3870.
13. Krafft, M. P.; Riess, J. G., Selected physicochemical aspects of poly-and perfluoroalkylated substances relevant to performance, environment and sustainability—Part one. *Chemosphere* **2015**, 129, 4-19.
14. Merino, N.; Qu, Y.; Deeb, R. A.; Hawley, E. L.; Hoffmann, M. R.; Mahendra, S., Degradation and removal methods for perfluoroalkyl and polyfluoroalkyl substances in water. *Environmental Engineering Science* **2016**, 33 (9), 615-649.
15. Haukås, M.; Berger, U.; Hop, H.; Gulliksen, B.; Gabrielsen, G. W., Bioaccumulation of per-and polyfluorinated alkyl substances (PFAS) in selected species from the Barents Sea food web. *Environmental Pollution* **2007**, 148 (1), 360-371.

16. Xiao, F., Emerging poly-and perfluoroalkyl substances in the aquatic environment: A review of current literature. *Water research* **2017**, *124*, 482-495.
17. Kannan, K., Perfluoroalkyl and polyfluoroalkyl substances: current and future perspectives. *Environmental chemistry* **2011**, *8* (4), 333-338.
18. Rumsby, P. C.; McLaughlin, C. L.; Hall, T., Perfluorooctane sulphonate and perfluorooctanoic acid in drinking and environmental waters. *Philosophical Transactions of the Royal Society A: Mathematical, Physical and Engineering Sciences* **2009**, *367* (1904), 4119-4136.
19. Olsen, G. W.; Butenhoff, J. L.; Zobel, L. R., Perfluoroalkyl chemicals and human fetal development: an epidemiologic review with clinical and toxicological perspectives. *Reproductive Toxicology* **2009**, *27* (3-4), 212-230.
20. Chain, E. P. o. C. i. t. F.; Knutsen, H. K.; Alexander, J.; Barregård, L.; Bignami, M.; Brüschweiler, B.; Ceccatelli, S.; Cottrill, B.; Dinovi, M.; Edler, L., Risk to human health related to the presence of perfluorooctane sulfonic acid and perfluorooctanoic acid in food. *EFSA journal* **2018**, *16* (12), e05194.
21. ITRC, PFAS Technical and Regulatory Guidance Document and Fact Sheets PFAS-1. Interstate Technology & Regulatory Council Washington, DC: 2020.
22. Zhao, P.; Xia, X.; Dong, J.; Xia, N.; Jiang, X.; Li, Y.; Zhu, Y., Short-and long-chain perfluoroalkyl substances in the water, suspended particulate matter, and surface sediment of a turbid river. *Science of the Total Environment* **2016**, *568*, 57-65.
23. Li, F.; Duan, J.; Tian, S.; Ji, H.; Zhu, Y.; Wei, Z.; Zhao, D., Short-chain per-and polyfluoroalkyl substances in aquatic systems: Occurrence, impacts and treatment. *Chemical Engineering Journal* **2020**, *380*, 122506.
24. Ateia, M.; Maroli, A.; Tharayil, N.; Karanfil, T., The overlooked short-and ultrashort-chain poly-and perfluorinated substances: A review. *Chemosphere* **2019**, *220*, 866-882.
25. Quiñones, O.; Snyder, S. A., Occurrence of perfluoroalkyl carboxylates and sulfonates in drinking water utilities and related waters from the United States. *Environmental science & technology* **2009**, *43* (24), 9089-9095.
26. Nzeribe, B. N.; Crimi, M.; Mededovic Thagard, S.; Holsen, T. M., Physico-chemical processes for the treatment of per-and polyfluoroalkyl substances (PFAS): A review. *Critical Reviews in Environmental Science and Technology* **2019**, *49* (10), 866-915.
27. Bruton, T. A.; Sedlak, D. L., Treatment of aqueous film-forming foam by heat-activated persulfate under conditions representative of in situ chemical oxidation. *Environmental Science & Technology* **2017**, *51* (23), 13878-13885.
28. Zhuo, Q.; Xiang, Q.; Yi, H.; Zhang, Z.; Yang, B.; Cui, K.; Bing, X.; Xu, Z.; Liang, X.; Guo, Q., Electrochemical oxidation of PFOA in aqueous solution using highly hydrophobic modified PbO₂ electrodes. *Journal of Electroanalytical Chemistry* **2017**, *801*, 235-243.
29. Singh, R. K.; Fernando, S.; Baygi, S. F.; Multari, N.; Thagard, S. M.; Holsen, T. M., Breakdown products from perfluorinated alkyl substances (PFAS) degradation in a plasma-based water treatment process. *Environmental science & technology* **2019**, *53* (5), 2731-2738.
30. Haddad, M.; Oie, C.; Duy, S. V.; Sauv e, S.; Barbeau, B., Adsorption of micropollutants present in surface waters onto polymeric resins: Impact of resin type and water matrix on performance. *Science of The Total Environment* **2019**, *660*, 1449-1458.
31. Taleb, F.; ben Mosbah, M.; Elaloui, E.; Moussaoui, Y., Adsorption of ibuprofen sodium salt onto Amberlite resin IRN-78: Kinetics, isotherm and thermodynamic investigations. *Korean Journal of Chemical Engineering* **2017**, *34* (4), 1141-1148.

32. Wang, F.; Shih, K., Adsorption of perfluorooctanesulfonate (PFOS) and perfluorooctanoate (PFOA) on alumina: Influence of solution pH and cations. *water research* **2011**, *45* (9), 2925-2930.
33. Yu, Q.; Deng, S.; Yu, G., Selective removal of perfluorooctane sulfonate from aqueous solution using chitosan-based molecularly imprinted polymer adsorbents. *Water Research* **2008**, *42* (12), 3089-3097.
34. McCleaf, P.; Englund, S.; Östlund, A.; Lindegren, K.; Wiberg, K.; Ahrens, L., Removal efficiency of multiple poly-and perfluoroalkyl substances (PFASs) in drinking water using granular activated carbon (GAC) and anion exchange (AE) column tests. *Water research* **2017**, *120*, 77-87.
35. Dixit, F.; Dutta, R.; Barbeau, B.; Berube, P.; Mohseni, M., PFAS removal by ion exchange resins: A review. *Chemosphere* **2021**, *272*, 129777.
36. Han, J.; Yan, T.; Shen, J.; Shi, L.; Zhang, J.; Zhang, D., Capacitive deionization of saline water by using MoS₂-graphene hybrid electrodes with high volumetric adsorption capacity. *Environmental science & technology* **2019**, *53* (21), 12668-12676.
37. Militao, I. M.; Roddick, F. A.; Bergamasco, R. N.; Fan, L., Removing PFAS from aquatic systems using natural and renewable material-based adsorbents: A review. *Journal of Environmental Chemical Engineering* **2021**, 105271.
38. Li, X.; Chen, S.; Quan, X.; Zhang, Y., Enhanced adsorption of PFOA and PFOS on multiwalled carbon nanotubes under electrochemical assistance. *Environmental science & technology* **2011**, *45* (19), 8498-8505.
39. Wang, S.; Li, X.; Zhang, Y.; Quan, X.; Chen, S.; Yu, H.; Zhao, H., Electrochemically enhanced adsorption of PFOA and PFOS on multiwalled carbon nanotubes in continuous flow mode. *Chinese science bulletin* **2014**, *59* (23), 2890-2897.
40. Kim, K.; Baldaque Medina, P.; Elbert, J.; Kayiwa, E.; Cusick, R. D.; Men, Y.; Su, X., Molecular Tuning of Redox - Copolymers for Selective Electrochemical Remediation. *Advanced Functional Materials* **2020**, 2004635.
41. Niu, Z.; Wang, Y.; Lin, H.; Jin, F.; Li, Y.; Niu, J., Electrochemically enhanced removal of perfluorinated compounds (PFCs) from aqueous solution by CNTs-graphene composite electrode. *Chemical Engineering Journal* **2017**, *328*, 228-235.
42. Saeidi, N.; Kopinke, F.-D.; Georgi, A., Controlling adsorption of perfluoroalkyl acids on activated carbon felt by means of electrical potentials. *Chemical Engineering Journal* **2021**, *416*, 129070.
43. Zhang, J.; Seyedin, S.; Qin, S.; Wang, Z.; Moradi, S.; Yang, F.; Lynch, P. A.; Yang, W.; Liu, J.; Wang, X., Highly conductive Ti₃C₂T_x MXene hybrid fibers for flexible and elastic fiber - shaped supercapacitors. *Small* **2019**, *15* (8), 1804732.
44. Bao, W.; Tang, X.; Guo, X.; Choi, S.; Wang, C.; Gogotsi, Y.; Wang, G., Porous cryo-dried MXene for efficient capacitive deionization. *Joule* **2018**, *2* (4), 778-787.
45. Li, L.; Zhang, N.; Zhang, M.; Zhang, X.; Zhang, Z., Flexible Ti₃C₂T_x/PEDOT: PSS films with outstanding volumetric capacitance for asymmetric supercapacitors. *Dalton Transactions* **2019**, *48* (5), 1747-1756.
46. Zhang, M.; Yuan, W.; Yao, B.; Li, C.; Shi, G., Solution-processed PEDOT: PSS/graphene composites as the electrocatalyst for oxygen reduction reaction. *ACS applied materials & interfaces* **2014**, *6* (5), 3587-3593.

47. Liu, Y.; Weng, B.; Razal, J. M.; Xu, Q.; Zhao, C.; Hou, Y.; Seyedin, S.; Jalili, R.; Wallace, G. G.; Chen, J., High-performance flexible all-solid-state supercapacitor from large free-standing graphene-PEDOT/PSS films. *Scientific reports* **2015**, *5* (1), 1-11.
48. Shrestha, B.; Ezazi, M.; Ajayan, S.; Kwon, G., Reversible adsorption and desorption of PFAS on inexpensive graphite adsorbents via alternating electric field. *RSC Advances* **2021**, *11* (55), 34652-34659.
49. Yang, K.-L.; Ying, T.-Y.; Yiacoumi, S.; Tsouris, C.; Vittoratos, E. S., Electrosorption of ions from aqueous solutions by carbon aerogel: an electrical double-layer model. *Langmuir* **2001**, *17* (6), 1961-1969.
50. Dyatkin, B.; Osti, N. C.; Gallegos, A.; Zhang, Y.; Mamontov, E.; Cummings, P. T.; Wu, J.; Gogotsi, Y., Electrolyte cation length influences electrosorption and dynamics in porous carbon supercapacitors. *Electrochimica Acta* **2018**, *283*, 882-893.

Chapter 7: Dissertation Summary and Future Outlook

7.1. Dissertation Summary

Freshwater contamination is one of the crucial problems the world is facing right now.^{1,2} With rapid urbanization, population growth, and industrialization, the situation is getting worst.³⁻⁵ Agricultural and industrial wastewater are major sources of contamination. It is essential to treat the wastewater before it is discharged into the environment. General constituents of the wastewater can be classified into two types, namely dissolved and suspended contaminants.⁶⁻⁸ Various remediation technologies have been developed to treat these dissolved and suspended contaminants.^{9, 10} Membrane-based technology^{11, 12} is the most preferred one for treating suspended contaminant while electrosorption¹³ is an emerging technology for treating dissolved contaminants. My dissertation mainly focuses on improving these two technologies for better remediation of wastewater.

The first topic of my dissertation is the development of a photocatalytic coating with hydrophilic and oleophobic wettability by intercalating a mixture of visible light-responsive N-TiO₂ and low surface energy F-SiO₂ nanoparticles.¹⁴ The chemically heterogeneous surface with intercalating high surface energy (N-TiO₂) and low surface energy (F-SiO₂) regions along with photocatalysis can in-situ recover the flux upon visible light irradiation. We attributed this to the photocatalytic degradation of the surface adsorbed oil when placed under visible light irradiation. Further due to the decoupling of photocatalysis and wettability, photocatalytic degradation did not compromise the wettability or integrity of the membrane due to the robust chemistry of the adhesive. We also engineered an apparatus that enabled the continuous separation and desalination of a surfactant-stabilized oil-in-water emulsion that was dissolved with salt and the photocatalytic

degradation of organic substances that were adsorbed on the coated membrane surface when it was exposed to visible light irradiation.

In the second part of my dissertation, we utilized a photocatalytic mesh with selective wettability for water over oil to study the kinetics of the water-rich permeate flux as a result of the photocatalytic degradation of the surface-adsorbed oil under visible light illumination.¹⁵ A mathematical model was derived by integrating the Langmuir–Hinshelwood kinetics of photocatalysis and the Cassie–Baxter wettability analysis on a chemically heterogeneous surface into a permeate flux relation. The model demonstrated that it can predict the evolution of the water-rich permeate flux through the photocatalytic mesh with a goodness of fit of 0.92.

In the third part¹⁶, we developed robust hydrophilic and in-air oleophobic F-PEGDA-coated filters to separate oil-water mixtures utilizing MEMO as an adhesion promoter. F-PEGDA-coated filter showed significantly low oil adhesion forces and was able to withstand fouling conditions without delamination. The filter was able to separate both water-in-oil and oil-in-water emulsions and maintained high flux values under both gravity-assisted as well as continuous separation setup with high oil separation efficiency. Further, the F-PEGDA surface demonstrated good reusability upon cleansing.

In the fourth and fifth parts,¹⁷ we demonstrated reversible adsorption and desorption of PFAS in water by an electric-field aided process utilizing two different carbonaceous (graphite and MXene-PEDOT:PSS) electrodes. We demonstrated that an adsorption capacity value increases with an increased capacitance of the electrode material, applied voltage, the PFAS concentration. We also showed multiple adsorption–desorption cycles by alternating the voltage that can result in highly efficient adsorption and desorption of PFAS from the graphite electrode surface. The kinetics of electric-field aided adsorption and desorption of PFAS in water were also

investigated by utilizing a pseudo-second-order model. We also engineered a device module that can be mounted to a gravity-assisted apparatus for electrosorption of PFAS and obtaining water with high purity.

7.2. Future Outlook

7.2.1. Photocatalytic and selective wettable membrane for wastewater remediation

Membrane based wastewater remediation technologies have demonstrated that they are effective in removing suspended contaminants from the wastewater. Nevertheless, there still remains a few more challenges that need to be addressed. Kamali et al.¹⁸ established 17 criteria (treatment efficiency (TE), ease of implementation (EI), combination with other methods (CM), process stability (PS), and health and safety risks (HSR), economic (i.e., initial investments (II), operating costs (OC), maintenance costs (MC)), environmental (i.e., solid waste generation (SWG), release of chemical substances (RCS), CO₂ emission (CE), water reuse potential (WRP), potential to recover by-products (PRB)), social (i.e., odor impact (OI), noise impact (NI), visual impact (VI), and public acceptance (PA)) for an ideal membrane for wastewater treatment. Based on these criteria, an inexpensive membrane with robust antifouling characteristic is still lacking. To address this issues, photocatalytic membrane with selective wettability membranes have been proposed.¹⁹

In this dissertation, we also have developed such membranes with decoupled functionalities (i.e., selective wettability and photocatalysis). The membrane can exhibit recovery of the permeate flux upon visible light illumination after being fouled. While it is promising, the flux recovery rate can be further improved. Note that the current rate is approximately 27%. We attribute this to poor quantum yield of N-TiO₂ upon visible light irradiation.^{20, 21} We envision two pathways. First, we can employ a better quantum yield photocatalytic materials.²² Second, we can use UV light to enhance the photocatalytic efficeincy.²³

Also, we have developed robust in-air oleophobic and hydrophilic filter using commercially available materials with a simple copolymerization technique. While it shows selective wettability of water over oil, its wettability contrast can further be enhanced by using a lower surface energy material such as fluorinated polyhedral oligomeric silsesquioxanes (F-POSS)²⁴. This can result in a higher oil-water separation efficiency as it can repel oils with even lower surface tension. Further, our copolymerization technique can be tested for various porous media including mesh, fabric, paper, and foams.

7.2.2. Electric field aided sorption for wastewater remediation

The primary limitation of the adsorption-based remediation technologies is their poor selectivity to contaminants. Upon application of an electric field across the electrodes submerged into a contaminated water, all charged ions are attracted to an electrode with oppositely charged. This can result in a lower adsorption capacity for a target contaminant (e.g., PFAS). In this dissertation, we partly verified that a larger quantity of PFAS with longer fluoroalkyl chain length adsorbs to an electrode compared to that with a shorter chain length at a given voltage. Thus, we envision that selective PFAS electroadsorption can be achieved by careful modulation of electric field.

Another challenge is a relatively poor adsorption capacity which is in the order of milligram of PFAS per one gram of electrode material (graphite or MXene). Although this value is comparable or even higher than other adsorbent that are currently in use,^{25, 26} it can be further improved by increasing a surface area (i.e., porosity). We envision that this can be achieved by introducing nano- and micro-scale hierarchical topography to an adsorbent.

7.3. References

1. Desa, U., World population prospects 2019: Highlights. *New York (US): United Nations Department for Economic and Social Affairs* **2019**, *11* (1), 125.
2. Covich, A., Water in crisis: a guide to the world's fresh water resources. *Water and Ecosystems* **1993**, *40*, 55.
3. Tchobanoglous, G.; Burton, F. L.; Stensel, H. D., Wastewater engineering. *Management* **1991**, *7* (1), 4.
4. Droste, R. L.; Gehr, R. L., *Theory and practice of water and wastewater treatment*. John Wiley & Sons: 2018.
5. De Zuane, J., Drinking water quality standards and controls. **1990**.
6. Wang, X.; Jin, P.; Zhao, H.; Meng, L., Classification of contaminants and treatability evaluation of domestic wastewater. *Frontiers of Environmental Science & Engineering in China* **2007**, *1* (1), 57-62.
7. Guibal, E.; Van Vooren, M.; Dempsey, B. A.; Roussy, J., A review of the use of chitosan for the removal of particulate and dissolved contaminants. *Separation science and technology* **2006**, *41* (11), 2487-2514.
8. Ellis, T. G., Chemistry of wastewater. *Encyclopedia of life support system (EOLSS)* **2004**, *2*, 1-10.
9. Patterson, J. W., Industrial wastewater treatment technology. **1985**.
10. Liu, D. H.; Lipták, B. G., *Wastewater treatment*. CRC Press: 2020.
11. Tanudjaja, H. J.; Hejase, C. A.; Tarabara, V. V.; Fane, A. G.; Chew, J. W., Membrane-based separation for oily wastewater: A practical perspective. *Water research* **2019**, *156*, 347-365.
12. Konvensional, B. T., A review of oilfield wastewater treatment using membrane filtration over conventional technology. *Malays. J. Anal. Sci* **2017**, *21*, 643-658.
13. Lissaneddine, A.; Pons, M.-N.; Aziz, F.; Ouazzani, N.; Mandi, L.; Mousset, E., A critical review on the electrosorption of organic compounds in aqueous effluent—Influencing factors and engineering considerations. *Environmental Research* **2022**, *204*, 112128.
14. Shrestha, B.; Ezazi, M.; Kwon, G., Engineered nanoparticles with decoupled photocatalysis and wettability for membrane-based desalination and separation of oil-saline water mixtures. *Nanomaterials* **2021**, *11* (6), 1397.
15. Shrestha, B.; Ezazi, M.; Rad, S. V.; Kwon, G., Predicting kinetics of water-rich permeate flux through photocatalytic mesh under visible light illumination. *Scientific reports* **2021**, *11* (1), 1-9.
16. Shrestha, B.; Ezazi, M.; Kwon, G., Delamination-Free In-Air and Underwater Oil-Repellent Filters for Oil-Water Separation: Gravity-Driven and Cross-Flow Operations. *Energies* **2021**, *14* (21), 7429.
17. Shrestha, B.; Ezazi, M.; Ajayan, S.; Kwon, G., Reversible adsorption and desorption of PFAS on inexpensive graphite adsorbents via alternating electric field. *RSC Advances* **2021**, *11* (55), 34652-34659.
18. Kamali, M.; Suhas, D.; Costa, M. E.; Capela, I.; Aminabhavi, T. M., Sustainability considerations in membrane-based technologies for industrial effluents treatment. *Chemical Engineering Journal* **2019**, *368*, 474-494.
19. Nasrollahi, N.; Ghalamchi, L.; Vatanpour, V.; Khataee, A., Photocatalytic-membrane technology: a critical review for membrane fouling mitigation. *Journal of Industrial and Engineering Chemistry* **2021**, *93*, 101-116.

20. Rizzo, L.; Koch, J.; Belgiorno, V.; Anderson, M., Removal of methylene blue in a photocatalytic reactor using polymethylmethacrylate supported TiO₂ nanofilm. *Desalination* **2007**, *211* (1-3), 1-9.
21. Nakata, K.; Fujishima, A., TiO₂ photocatalysis: Design and applications. *Journal of photochemistry and photobiology C: Photochemistry Reviews* **2012**, *13* (3), 169-189.
22. Yoon, T. P.; Ischay, M. A.; Du, J., Visible light photocatalysis as a greener approach to photochemical synthesis. *Nature chemistry* **2010**, *2* (7), 527-532.
23. Serpone, N., Photocatalysis. *Kirk - Othmer Encyclopedia of Chemical Technology* **2000**.
24. Mabry, J. M.; Vij, A.; Iacono, S. T.; Viers, B. D., Fluorinated polyhedral oligomeric silsesquioxanes (F - POSS). *Angewandte Chemie International Edition* **2008**, *47* (22), 4137-4140.
25. Gagliano, E.; Sgroi, M.; Falciglia, P. P.; Vagliasindi, F. G.; Roccaro, P., Removal of poly-and perfluoroalkyl substances (PFAS) from water by adsorption: Role of PFAS chain length, effect of organic matter and challenges in adsorbent regeneration. *Water research* **2020**, *171*, 115381.
26. Li, X.; Chen, S.; Quan, X.; Zhang, Y., Enhanced adsorption of PFOA and PFOS on multiwalled carbon nanotubes under electrochemical assistance. *Environmental science & technology* **2011**, *45* (19), 8498-8505.

Paper P1

Engineered nanoparticles with decoupled photocatalysis and wettability for membrane-based desalination and separation of oil-saline water mixtures

Reproduced with permission from [**Shrestha, Bishwash**, Mohammadamin Ezazi, and Gibum Kwon], [Nanomaterials]; published by [Multidisciplinary Digital Publishing Institute], [2021].



Article

Engineered Nanoparticles with Decoupled Photocatalysis and Wettability for Membrane-Based Desalination and Separation of Oil-Saline Water Mixtures

Bishwash Shrestha [†], Mohammadamin Ezazi [†] and Gibum Kwon ^{*†}

Department of Mechanical Engineering, University of Kansas, Lawrence, KS 66045, USA; bishwashs@ku.edu (B.S.); aminezazi@ku.edu (M.E.)

* Correspondence: gbkwon@ku.edu

† Equal contributions.



Citation: Shrestha, B.; Ezazi, M.; Kwon, G. Engineered Nanoparticles with Decoupled Photocatalysis and Wettability for Membrane-Based Desalination and Separation of Oil-Saline Water Mixtures. *Nanomaterials* **2021**, *11*, 1397. <https://doi.org/10.3390/nano11061397>

Academic Editor: Gheorghe Nechifor

Received: 8 May 2021

Accepted: 22 May 2021

Published: 25 May 2021

Publisher's Note: MDPI stays neutral with regard to jurisdictional claims in published maps and institutional affiliations.



Copyright: © 2021 by the authors. Licensee MDPI, Basel, Switzerland. This article is an open access article distributed under the terms and conditions of the Creative Commons Attribution (CC BY) license (<https://creativecommons.org/licenses/by/4.0/>).

Abstract: Membrane-based separation technologies are the cornerstone of remediating unconventional water sources, including brackish and industrial or municipal wastewater, as they are relatively energy-efficient and versatile. However, membrane fouling by dissolved and suspended substances in the feed stream remains a primary challenge that currently prevents these membranes from being used in real practices. Thus, we directly address this challenge by applying a superhydrophilic and oleophobic coating to a commercial membrane surface which can be utilized to separate and desalinate an oil and saline water mixture, in addition to photocatalytically degrading the organic substances. We fabricated the photocatalytic membrane by coating a commercial membrane with an ultraviolet (UV) light-curable adhesive. Then, we sprayed it with a mixture of photocatalytic nitrogen-doped titania (N-TiO₂) and perfluoro silane-grafted silica (F-SiO₂) nanoparticles. The membrane was placed under a UV light, which resulted in a chemically heterogeneous surface with intercalating high and low surface energy regions (i.e., N-TiO₂ and F-SiO₂, respectively) that were securely bound to the commercial membrane surface. We demonstrated that the coated membrane could be utilized for continuous separation and desalination of an oil-saline water mixture and for simultaneous photocatalytic degradation of the organic substances adsorbed on the membrane surface upon visible light irradiation.

Keywords: photocatalytic nanoparticles; wettability; perfluorinated silica nanoparticles; oil-water separation; membrane fouling

1. Introduction

Modulating the surface wettability plays a vital role in a solid-liquid system and has found increasing interest in practical applications, including self-cleaning [1,2], microfluidics [3,4], and liquid separation [5,6]. Based on the contact angle (θ) for high (e.g., water) and low surface tension liquids (e.g., oil), a surface can be grouped into four wettability classifications: omniphobic ($\theta_{\text{water}} > 90^\circ$ and $\theta_{\text{oil}} > 90^\circ$), hydrophobic and oleophilic ($\theta_{\text{water}} > 90^\circ$ and $\theta_{\text{oil}} < 90^\circ$), hydrophilic and oleophobic ($\theta_{\text{water}} < 90^\circ$ and $\theta_{\text{oil}} > 90^\circ$), and omniphilic ($\theta_{\text{water}} < 90^\circ$ and $\theta_{\text{oil}} < 90^\circ$) [7,8]. We [9–11] and others [12–14] have demonstrated that a low surface energy coating, in conjunction with the surface texture, can result in a non-wetting Cassie-Baxter state with air trapped between the contacting liquid and the solid surface.

Organofluorine is perhaps the most prevalent material for lowering the overall surface free energy and rendering the surface repellent to liquids [10]. It has been extensively employed to fabricate not only a surface with omniphobic [15,16] or superomniphobic wettability (i.e., $\theta_{\text{water}}^* > 150^\circ$ and $\theta_{\text{oil}}^* > 150^\circ$) [9,17,18] but also those with selective (i.e., hydrophobic and oleophilic or hydrophilic and oleophobic) wettability [19–22]. For example, Mertens et al. [19] utilized a combination of photolithography and oxygen plasma

treatment to fabricate a nanocrystalline diamond surface with hydrophobic and hydrophilic arrays. Howarter et al. [20] grafted a perfluorinated polyethylene glycol on a silicon surface which could exhibit hydrophilic and oleophobic wettability.

The utility of surfaces with selective wettability can be further extended by incorporating them with photocatalytic nanoparticles that can degrade organic substances upon light irradiation [23–25]. Such a photocatalytic surface with selective wettability has demonstrated the potential for a wide range of practical applications, including anti-fouling [26,27], self-cleaning [28,29], and bactericidal coating [30]. Recent studies [31–34] have revealed that membranes with selective wettability can further benefit by incorporating photocatalytic nanoparticles that can radically transform physical filtration into chemically reactive processes. Thus, it can progressively eliminate the inherent shortcomings of conventional membrane-based filtration, such as pollutant degradation and membrane fouling [23]. Zhao et al. [35] reported on a polyacrylonitrile membrane coated with a fluorinated agent and photocatalytic ZnO. The membrane exhibited remediation of wastewater upon ultraviolet (UV) light irradiation and resistance to fouling. Luster et al. [36] fabricated an N-doped, TiO₂-coated alumina membrane and demonstrated the photocatalytic degradation of carbamazepine (CBZ) as a model pollutant under simulated solar irradiation. Further, Coelho et al. [26] coated a filter paper with zirconia-doped cerium to prepare a photocatalytic membrane. The membrane demonstrated flux recovery by photocatalytic degradation of humic acid as a foulant.

Before these photocatalytic membranes with desired wettability can be utilized for practical applications, they need to fulfill the following three conditions [37,38]. First, the membrane's wettability must remain unchanged by a photocatalytic reaction. Similarly, its physical and chemical integrity must not be affected by a photocatalytic reaction, particularly if the membrane is organic. Lastly, the coating (e.g., photocatalytic nanoparticles) needs to remain undetached when a high hydraulic shear force is exerted.

In this work, we engineered a visible light-responsive photocatalytic coating with superhydrophilic and oleophobic wettability both in air and underwater by utilizing nitrogen-doped titania (N-TiO₂) and perfluoro silane-grafted silica (F-SiO₂) nanoparticles. The coating was sprayed onto a commercial membrane surface with a UV-curable adhesive. Subsequent irradiation of UV light resulted in a chemically heterogeneous surface with intercalating high surface energy (N-TiO₂) and low surface energy (F-SiO₂) regions that were securely bound to the surface. Both the wettability and the integrity of the membrane remained unaffected throughout the photocatalytic degradation process of the organic substances when exposed to visible light irradiation. This can be attributed to the robust chemistry of the cured adhesive that protected the perfluoro silane molecules grafted to the SiO₂ nanoparticles, as well as the underlying membrane from the reactive radical species generated when it was exposed to visible light irradiation. Thus, the coated membrane can be utilized for continuous separation and desalination of an oil-saline water mixture and simultaneous photocatalytic degradation of the organic substances adsorbed on the membrane surface upon visible light irradiation.

2. Materials and Methods

2.1. Chemicals

Titanium butoxide (TBOT), tetraethyl orthosilicate (TEOS), triethylamine (TEA), sodium dodecyl sulfate (SDS), and sodium chloride (NaCl) were purchased from Millipore Sigma, St. Louis, MO, USA. The 1H,1H,2H,2H-perfluorodecyl trichlorosilane (perfluoro silane) was purchased from Alfa Aesar, Lancashire, UK. Ethanol, acetone, isopropyl alcohol, hydrochloric acid (HCl), nitric acid (HNO₃), and n-hexadecane were purchased from Fisher Chemical, Fairlawn, NJ, USA. The Norland ultraviolet (UV) light-curable optical adhesive (NOA 61) was purchased from Norland Products Inc, Cranbury, NJ, USA. The commercial TRISEP ACM5 membrane was purchased from Sterlitech, Kent, WA, USA.

2.2. Synthesis of N-TiO₂ Nanoparticles

Titanium butoxide (TBOT, 5.0 g) was added dropwise to isopropyl alcohol (79 g), followed by the addition of deionized (DI) water (910 g). Nitric acid (HNO₃, 0.01 M) was added to the solution to adjust the pH to 2. Subsequently, triethylamine was added dropwise to the solution. Please note that the molar ratios of TEA to TBOT were 0.5, 1.0, 2.0, and 3.0. The solution was stirred for 12 h at 30 °C. The precipitates were collected by centrifugation and thoroughly rinsed by DI water and ethanol. Upon vacuum drying for 10 h, the deep-yellow, nitrogen-doped titanium dioxide (N-TiO₂) nanoparticles were obtained.

2.3. Synthesis of F-SiO₂ Nanoparticles

Tetraethyl orthosilicate (TEOS, 1.0 g) was added dropwise to a solution of hydrochloric acid (HCl, 0.01 M) in DI water (100 g), followed by the addition of 1H,1H,2H,2H-perfluorodecyl trichlorosilane (1.0 g). The solution was stirred for 60 min at 60 °C, and the precipitates were collected by centrifugation. Following a thorough rinsing by DI water and ethanol, and after 10 h of vacuum drying, the perfluoro silane-grafted silica (F-SiO₂) nanoparticles were obtained.

2.4. Photocatalytic Membrane Fabrication

A commercial membrane surface was spin-coated with a Norland ultraviolet (UV) light-curable optical adhesive (NOA 61) (1.0 wt% in acetone). Please note that the commercial membrane (i.e., Sterlitech TRISEP ACM5) consisted of three layers of a thin polyamide layer with a molecular weight cut-off equal to 100 Da, a porous polysulfone layer, and a non-woven polyester as the support. The suspension of the N-TiO₂ and F-SiO₂ nanoparticles mixture (i.e., N-TiO₂/F-SiO₂) in DI water (10 wt%) was then sprayed (iWata spray gun, Anest iwata, Yokohama, Japan) onto the adhesive-coated membrane for one minute. The spraying distance and nitrogen gas pressure were maintained at 15 cm and 200 kPa, respectively. Please note that the concentrations of N-TiO₂ nanoparticles in the N-TiO₂/F-SiO₂ mixture were 0 wt%, 20 wt%, 40 wt%, 60 wt%, 80 wt%, and 100 wt%. Subsequently, the membrane surface was irradiated by a long-wavelength UV light (100 W, $\lambda = 365$ nm, Analytikjena, Upland, CA, USA) for 5 min to cure the adhesive. The membrane was thoroughly rinsed with DI water and ethanol.

2.5. Preparation of the Oil-in-Water Emulsion Dissolved with Salt

An oil-in-water emulsion containing salt was prepared by vigorous mixing of n-hexadecane and DI water (10:90 vol:vol n-hexadecane:water) dissolved with salt (NaCl, 1.0 wt% with respect to the water mass). Sodium dodecyl sulfate (SDS, 0.015 wt%) was added to stabilize the emulsion.

2.6. N-TiO₂ and F-SiO₂ Size Measurements

The average size of the N-TiO₂ and F-SiO₂ nanoparticles was measured by utilizing dynamic light scattering (DLS) (ZetaPALS zeta potential analyzer, Brookhaven Instruments, Holtsville, NY, USA) equipped with a BI-9000AT digital autocorrelator. Suspensions of N-TiO₂ (0.01 wt%) and F-SiO₂ (0.01 wt%) were prepared in DI water, followed by ultrasonication.

2.7. N-TiO₂ Crystal Structure Analyses

The crystal structure of N-TiO₂ was studied by powder X-ray diffraction (XRD) (PANalytical Model X'Pert PRO diffractometer, PANalytical, Almelo, The Netherlands) with Cu K α radiation ($\lambda = 1.54$ Å) by scanning at a rate of 2° (2 θ) min⁻¹. X-ray photoelectron spectroscopy (XPS) was utilized to study the nitrogen doping of N-TiO₂. XPS was conducted by a Phi Versaprobe II, Ulvac-PHI, Kanagawa, Japan utilizing monochromatic source Mg Ka.

2.8. N-TiO₂ and F-SiO₂ Absorbance Measurements

Ultraviolet–visible (UV-Vis) spectrophotometry was utilized to analyze the nanoparticles' absorbance spectrum. UV-Vis spectrophotometry was conducted by utilizing a Thermo Evolution 600, Waltham, MA, USA at a scan rate of 240 nm min⁻¹ and a data interval of 2 nm.

2.9. N-TiO₂ Photocatalytic Performance Measurements

The photocatalysis performance of N-TiO₂ nanoparticles was analyzed by conducting the dye degradation test. UV-Vis spectrophotometry was utilized to study the dye degradation performance. N-TiO₂ nanoparticles (0.5 wt%) were dispersed in DI water dissolved with Solvent Blue 38 dye (0.5 wt%). Of the dispersion, 20 mL was poured into a glass beaker equipped with a magnetic stirrer. The visible light (13.1 W, Sugarcube ultraLED, USHIO, Vergennes, VT, USA) guide was submerged into the beaker to irradiate the dispersion. A small quantity (2 mL) of the dispersion was taken every 1 h. It was centrifuged and filtered by filter paper, followed by UV-Vis spectrophotometry. UV-Vis spectrophotometry was conducted at a scan rate of 240 nm min⁻¹ and a data interval of 2 nm.

2.10. Membrane Surface Analysis

Scanning electron microscopy (SEM, FEI Versa 3D DualBeam, Hillsboro, OR, USA) was utilized to study the surface porosity and texture of the N-TiO₂/F-SiO₂ coated membrane. An accelerating voltage of 10 kV was utilized. All surfaces were sputter-coated with a gold layer (≈4–5 nm) to prevent the charging effect.

2.11. Visible Light Intensity Measurement

A photometer (Fisherbrand Traceable DualDisplay Lightmeter, Control company, Webster, TX, USA) was utilized to measure the intensity of the incident visible light on the membrane surface. The photometer was placed underneath the top cover of the cross-flow cell and irradiated by the visible light source from the same distance (≈5 cm) at which the membrane was irradiated during the separation and desalination.

2.12. Salt and Oil Concentration Measurements

We determined the salt concentration in the water-rich permeate by calculating the electrical conductivity of the permeate and comparing the value with the calibration curve. Two probes (1 cm² each) of a multimeter (GDT-3190, Gardner Bender, New Berlin, WI, USA) at a distance of 2 cm were submerged in the permeate (20 mL). The multimeter measured the electrical resistance (*R*), which was converted to electrical resistivity. Subsequently, the inverse of the electrical resistivity yielded the electrical conductivity (*s*). We determined the oil concentration by utilizing thermogravimetric analyses (TGA, PerkinElmer PYRIS 1, PerkinElmer, Waltham, MA, USA). Approximately 10 mg of the water-rich permeate was heated from room temperature (≈22 °C) to 110 °C at a rate of 5 °C min⁻¹, followed by maintaining the temperature at 110 °C for 50 min.

2.13. Engineering a Continuous Separation and Desalination Apparatus

We engineered a continuous separation and desalination apparatus consisting of a cross-flow cell (CF042A, Sterlitech, Kent, WA, USA), a feed storage tank, a pump (2SF22SEEL, WEG industries, Jaraguá do Sul, Brazil), a differential pressure gauge (DPG409-500DWU, OMEGA, Stamford, CT, USA), a visible light source, and a permeate tank. The membrane with an effective surface area of ≈42 cm² was sandwiched in between two transparent acrylic counterparts of the cross-flow cell. The membrane surface was irradiated by visible light of varying intensities.

3. Results and Discussion

3.1. Synthesis of N-TiO₂ and Characterization of Its Photocatalysis upon Visible Light Irradiation

To fabricate a visible-light-responsive photocatalytic coating with selective wettability (i.e., hydrophilic and oleophobic), we utilized a mixture of nitrogen-doped titanium dioxide (N-TiO₂) and perfluoro silane-grafted silica (F-SiO₂) nanoparticles. N-TiO₂ can degrade organic substances when it is exposed to visible light irradiation [39] and exhibit hydrophilic wettability [40], while F-SiO₂ can lower the overall surface free energy (γ_{sv}) [41]. We hypothesized that an optimal balance of N-TiO₂ and F-SiO₂ could result in hydrophilic and oleophobic wettability.

To verify this hypothesis, we first synthesized the N-TiO₂ nanoparticles by utilizing the sol-gel method [42] (further described in the Section 2). Triethylamine (TEA) and titanium butoxide (TBOT) were used as a nitrogen dopant and a TiO₂ precursor, respectively (Figure 1a). Hydrolysis of the TBOT (concentration = 0.5 wt%) in an acidic solution (pH \approx 2.0) that was dissolved with TEA (concentration = 0.3 wt%) resulted in N-TiO₂ nanoparticles with an average diameter of 50 nm \pm 1 nm (Supporting Information, Section S1). During this reaction, the TEA introduced nitrogen (e.g., elemental nitrogen or complex nitrogen species such as NO, NO₂, or NH) into the TiO₂ lattice [43]. X-ray photoelectron spectroscopy (XPS) spectra demonstrated a peak at a binding energy of \approx 399.2 eV, which indicated the presence of anionic nitrogen from the O-Ti-N bond [42], while the neat TiO₂ lacked such a peak (Figure 1b).

Doping with nitrogen can narrow the bandgap energy of the TiO₂, which may extend the absorption spectra further toward the visible light region (i.e., 390 nm $<$ λ $<$ 750 nm) [44]. The ultraviolet-visible (UV-Vis) spectrophotometry data verified that N-TiO₂ absorbed a broad range of the visible light spectrum, whereas the neat TiO₂ and SiO₂ showed negligible absorption (Figure 1c). Furthermore, the results showed that the N-TiO₂ fabricated with a higher molar ratio of TEA to TBOT (i.e., higher dopant concentration) tended to exhibit stronger absorbance in the range of wavelengths from 390 nm to 750 nm. However, once the molar ratio exceeded 2.0, this would have a negligible effect on the absorbance of the resulting N-TiO₂. Thus, we utilized a TEA-to-TBOT molar ratio of 2.0 (hereafter denoted as N-TiO₂) in this study.

Given that the resulting N-TiO₂ exhibited a photocatalytic anatase crystalline phase (Supporting Information, Section S2), we demonstrated that it could degrade organic substances upon visible light irradiation. Figure 1d presents the time-dependent degeneration of the absorbance for water dissolved with organic dye (Solvent Blue 38, concentration = 0.5 wt%) and N-TiO₂ (concentration = 0.5 wt%). The light intensity (I) was maintained at $I \approx 198$ mW cm⁻² (see Section 2). The water solution became nearly colorless after 10 h of irradiation, indicating that almost all of the dye molecules were degraded. Please note that the dye molecules degraded more rapidly when placed under a higher intensity of light (Supporting Information, Section S3).

The F-SiO₂ nanoparticles were synthesized through the hydrolysis of tetraethyl orthosilicate (TEOS), followed by grafting of 1H,1H,2H,2H-perfluorodecyl trichlorosilane [41,45] (see Section 2). The average diameter of the F-SiO₂ nanoparticles was 50 nm \pm 2 nm (Supporting Information, Section S4).

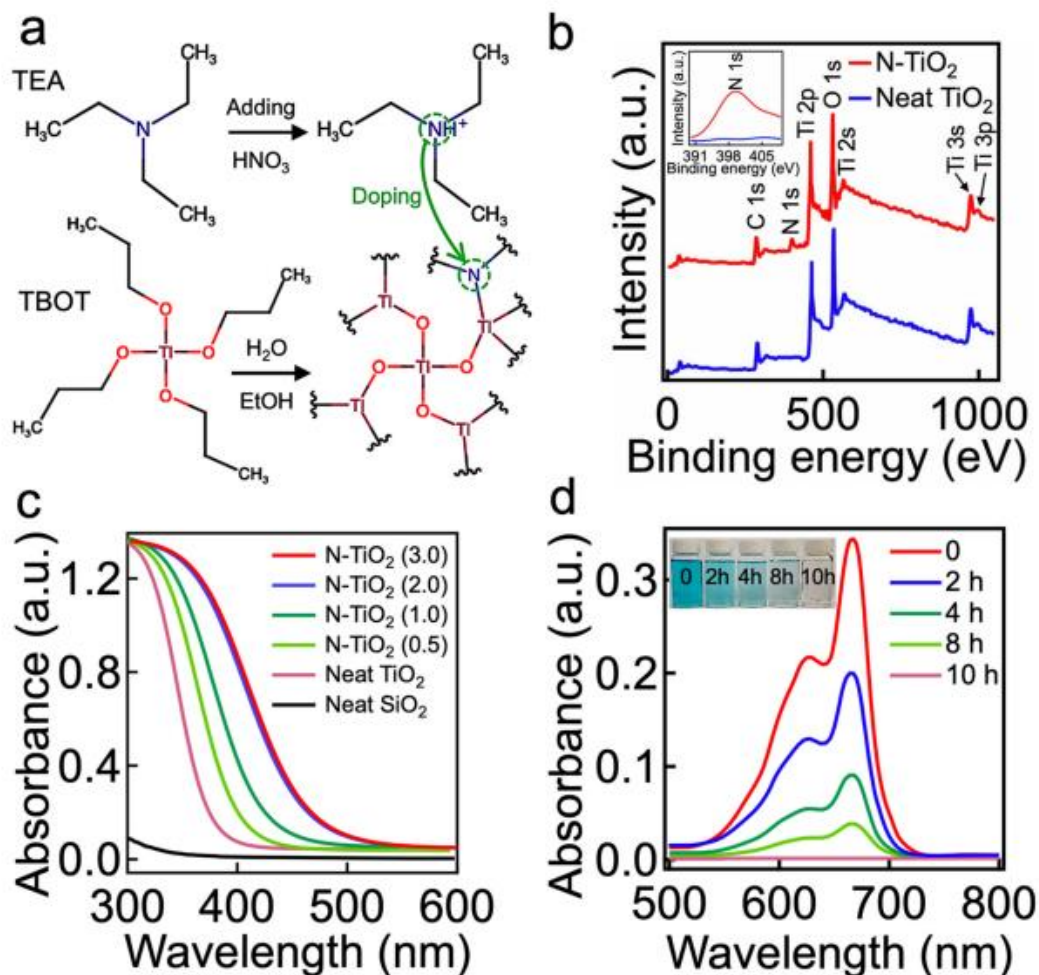


Figure 1. (a) Schematic illustrating the synthesis of N-TiO₂ nanoparticles by utilizing titanium butoxide (TBOT) and triethylamine (TEA) as a TiO₂ precursor and nitrogen dopant, respectively. (b) The XPS spectrum of N-TiO₂, exhibiting characteristic peaks of N 1s, Ti 2p, and O 1s. The spectrum of a neat TiO₂ is also shown for comparison. The inset shows the core level spectrum of characteristic N 1s. (c) Ultraviolet–visible (UV–Vis) absorption spectra of N-TiO₂ synthesized by varied molar ratios of TEA to TBOT (e.g., 0.5, 1.0, 2.0, and 3.0). Neat TiO₂ and SiO₂ absorption spectra are also shown for comparison. (d) UV–Vis absorption spectra of water dissolved with N-TiO₂ and Solvent Blue dye as a function of the visible light irradiation time. The inset is a photograph showing the water dissolved with Solvent Blue dye after visible light irradiation for 2 h, 4 h, 8 h, and 10 h. The as-prepared water dissolved with Solvent Blue dye (concentration = 0.5 wt%) is also shown.

3.2. Fabrication and Characterization of N-TiO₂/F-SiO₂ Coated Membrane

By utilizing N-TiO₂ and F-SiO₂ nanoparticles, we created a photocatalytic membrane with hydrophilic and oleophobic wettability both in air and saline water. A commercial filter (TRISEP ACM5) was utilized as a membrane, on which our visible light-responsive photocatalytic coating with selective wettability was applied. Please note that the TRISEP ACM5 was chosen because of its applicability to a wide range of separation processes [46]. First, we spin-coated the membrane surface with a thiol-ene-based UV-curable adhesive. Immediately following this step, a solution of N-TiO₂ and F-SiO₂ (i.e., N-TiO₂/F-SiO₂) (concentration = 10 wt%, Section 2) was sprayed for one minute. Then, the membrane was irradiated by UV light ($\lambda = 365$ nm, intensity ≈ 78 mW cm⁻²) for five minutes at room

temperature ($\approx 22^\circ\text{C}$) to cure the adhesive. Please note that we varied the concentrations of N-TiO₂/F-SiO₂ (e.g., 0, 20 wt%, 40 wt%, 60 wt%, 80 wt%, and 100 wt%). Figure 2 shows a schematic illustrating the overall process of membrane fabrication.

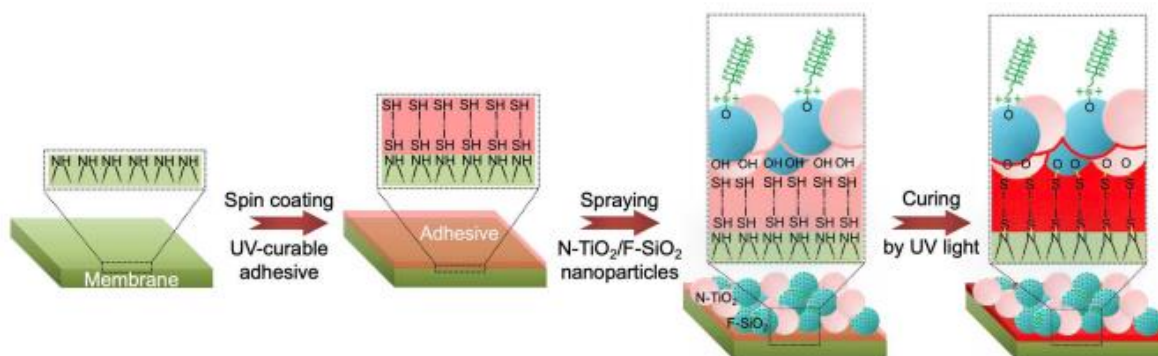


Figure 2. Schematic illustrating the fabrication of a photocatalytic membrane with hydrophilic and oleophobic wettability. A commercial filter is coated with an ultraviolet (UV) light-curable adhesive, followed by being sprayed with a mixture of N-TiO₂ and F-SiO₂ nanoparticles. The membrane was placed under UV light for curing.

The resulting membrane's surface was covered with a N-TiO₂/F-SiO₂ coating possessing a hierarchical roughness with a re-entrant texture (Figure 3a and the inset image). We measured the advancing (θ^*_{adv}) and receding (θ^*_{rec}) contact angles for the saline water (1.0 wt% NaCl in DI water, $\gamma_{lv} = 73.1 \text{ mN m}^{-1}$) and oil (n-hexadecane, $\gamma_{lv} = 27.5 \text{ mN m}^{-1}$) in air (Figure 3b). The results indicated that a membrane coated with N-TiO₂/F-SiO₂ with a lower N-TiO₂ concentration exhibited higher contact angles for both saline water and oil. We found that when the N-TiO₂ concentration reached 60 wt%, the contact angle for saline water became zero (i.e., $\theta^*_{saline\ water, adv (in-air)} = 0^\circ$ and $\theta^*_{saline\ water, rec (in-air)} = 0^\circ$), while that for oil remained constant ($\theta^*_{oil, adv (in-air)} = 95^\circ \pm 4^\circ$, $\theta^*_{oil, rec (in-air)} = 61^\circ \pm 3^\circ$). Further increases in the N-TiO₂ concentrations resulted in sharp decreases in contact angles for oil.

Given that membrane operations in real-world applications often result in continuous immersion in liquids (e.g., water), we also measured the contact angles for oil on the membrane surface submerged in saline water (Figure 3c). The results indicated that a membrane with a lower in-air water contact angle was likely to have a higher oil contact angle when submerged in saline water. For example, a membrane coated with N-TiO₂/F-SiO₂ of 60 wt% N-TiO₂ (i.e., N-TiO₂/F-SiO₂ (60 wt%)) exhibited contact angles of $\theta^*_{oil, adv (under\ saline\ water)} = 175^\circ \pm 3^\circ$ and $\theta^*_{oil, rec (under\ saline\ water)} = 171^\circ \pm 2^\circ$, while the one coated with N-TiO₂/F-SiO₂ (20 wt%) exhibited $\theta^*_{oil, adv (under\ saline\ water)} = 169^\circ \pm 2^\circ$ and $\theta^*_{oil, rec (under\ saline\ water)} = 161^\circ \pm 3^\circ$. The results could be further corroborated by analyzing the adhesion force of an oil droplet (n-hexadecane) placed on the membrane surface that was submerged in saline water [47] (Figure 3c). The adhesion force was $1.1 \pm 0.3 \text{ mN}$ on a membrane coated with N-TiO₂/F-SiO₂ (60 wt%) and $1.7 \pm 0.4 \text{ mN}$ on a membrane coated with N-TiO₂/F-SiO₂ (20 wt%).

The membrane's wettability for saline water can affect the flux because it determines the breakthrough pressure (i.e., the maximum pressure difference across the membrane that is required for a liquid to permeate through it) [48]. We measured the flux of saline water (1.0 wt% NaCl in DI water) through the membranes coated with various concentrations of N-TiO₂/F-SiO₂. A total of 100 L of saline water was continuously fed for 180 min through the membrane, which was attached to a cross-flow cell. We measured the volume of the permeate every 10 min. It must be noted that the transmembrane pressure (TMP) (i.e., the pressure exerted across the membrane) was maintained at $\Delta p \approx 760 \text{ kPa} \pm 9 \text{ kPa}$. Figure 3d shows the normalized flux (J_n) of the permeate, which is defined as J_t/J_0 , where $J_t = \Delta m / A \rho \Delta t \Delta p$. Here, Δm represents the change in the permeate mass during a particular time interval (i.e., $\Delta t = 10 \text{ min}$), A is the membrane's projected area ($A \approx 42 \text{ cm}^2$), ρ is

the density of the permeate ($\rho = 1000 \text{ kg m}^{-3}$), and J_0 symbolizes the flux over the TMP value obtained during the first three minutes of submersion. While J_n gradually decreased and reached a constant value ($J_n \approx 0.59 \pm 0.04$) after approximately $t = 150 \text{ min}$ for all membranes, one coated with N-TiO₂/F-SiO₂ with a higher concentration of N-TiO₂ showed less of a decrease in the J_n value at $t = 150 \text{ min}$. For example, a membrane coated with N-TiO₂/F-SiO₂ (60 wt%) yielded a J_n value of 0.61, whereas one coated with N-TiO₂/F-SiO₂ (20 wt%) showed a value of 0.56 at $t = 150 \text{ min}$. This finding can be attributed to the difference in the breakthrough pressure of saline water [48] (Supporting Information, Section S5). Please note that the as-purchased filter and the one coated only with the cured adhesive exhibited $J_n = 0.59$ and $J_n = 0.58$, respectively, at $t = 150 \text{ min}$ (Figure 3d). This clearly indicates that neither the cured adhesive nor the N-TiO₂/F-SiO₂ coating affected the membrane's flux. We then measured the salt rejection (ζ) of the membranes coated with various concentrations of N-TiO₂/F-SiO₂ (Supporting Information, Section S6). We also observed almost no change in the mass of the membranes after 180 min, implying that the N-TiO₂/F-SiO₂ nanoparticles were securely bound to the membrane surface (Supporting Information, Section S7).

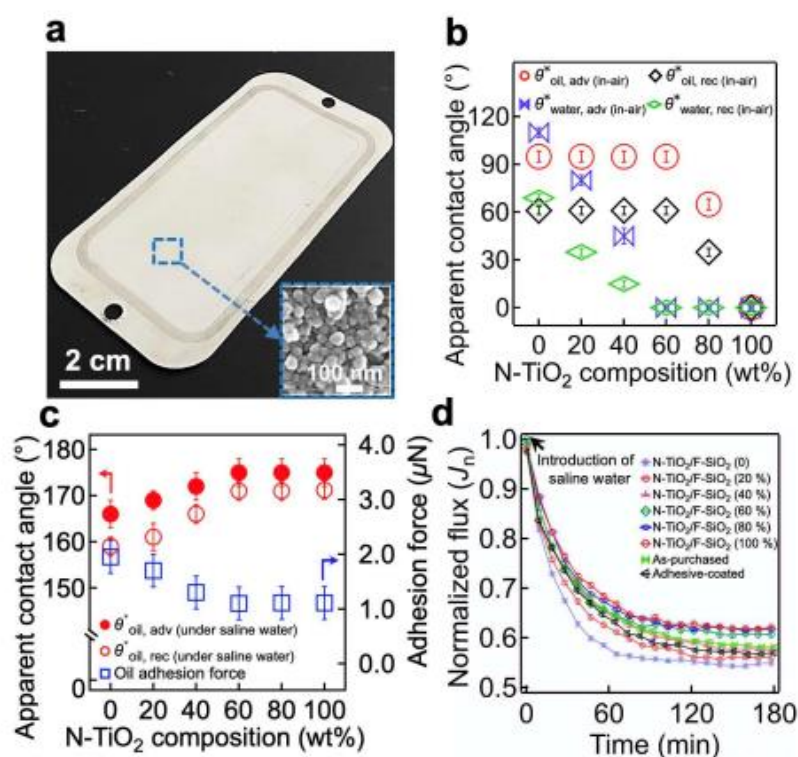


Figure 3. (a) A photograph showing a commercial filter coated with N-TiO₂/F-SiO₂ (60 wt%). The inset displays a scanning electron microscopy (SEM) image of the membrane surface, showing a hierarchical roughness with a re-entrant texture. (b) The measured in-air advancing and receding apparent contact angles for saline water (1.0 wt% NaCl in DI water) and oil (n-hexadecane) on the membrane surface, coated with N-TiO₂/F-SiO₂ with varied compositions. (c) The measured advancing and receding apparent contact angles, as well as the adhesion force for an oil droplet (n-hexadecane) on the membrane surface, coated with N-TiO₂/F-SiO₂ with various compositions submerged in saline water. (d) The normalized flux (J_n) of the permeate through the membranes coated with N-TiO₂/F-SiO₂ with varied compositions. The data for the as-purchased commercial filter and for the one coated only with cured adhesive were also provided for comparison.

3.3. Continuous Separation and Desalination of an Oil–Saline Water Mixture and Simultaneous Photocatalytic Degradation of Organic Fouling upon Visible Light Irradiation

The photocatalytic capability of our coating, in conjunction with its hydrophilic and oleophobic wettability both in air and under saline water, enables the membrane to separate and desalinate an oil–saline water mixture while simultaneously degrading the organic foulants adsorbed onto the membrane surface during exposure to visible light irradiation [49,50]. To demonstrate this, we mounted the membrane to an apparatus and irradiated it with visible light (Figure 4a). The feed oil–saline water mixture was continuously fed to the cell while the water-rich permeate continuously passed through the membrane and collected in a permeate tank. Here, we utilized an emulsion of n-hexadecane in water (10:90 vol:vol, n-hexadecane:water) dissolved with salt (1.0 wt% NaCl with respect to the water mass) that was stabilized by sodium dodecyl sulfate (SDS) (see Section 2). We tested membranes coated with various concentrations of N-TiO₂/SiO₂. Of note, all membranes were prewetted by soaking them in saline water (1.0 wt% NaCl) for 150 min to obtain a constant flux over the TMP (J_{prewet}) before being subjected to the feed emulsion.

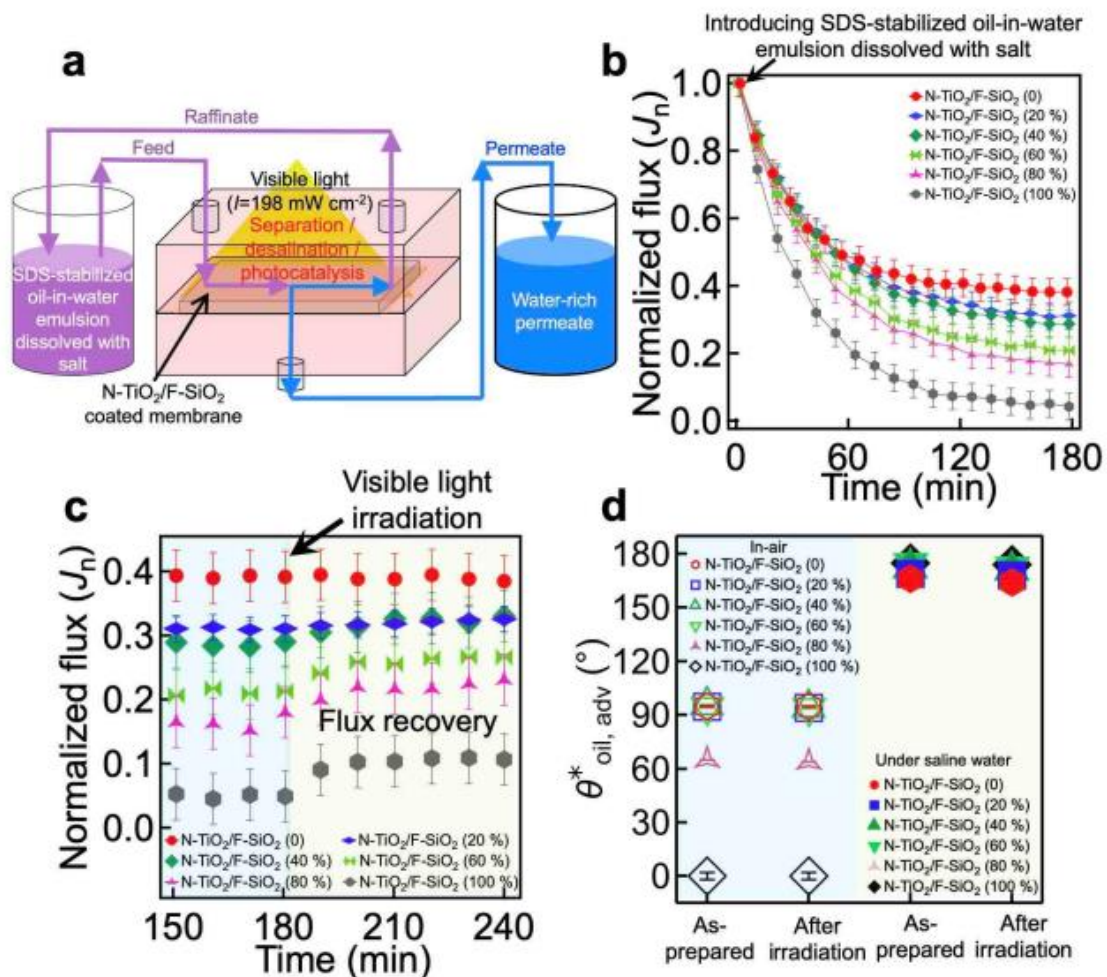


Figure 4. (a) Schematic illustrating the cross-flow apparatus that enables continuous separation and desalination of an oil–saline water mixture and simultaneous photocatalytic degradation of the organic foulants adsorbed onto the membrane’s

surface upon visible light irradiation. (b) The normalized flux (J_n) of the water-rich permeate through the membranes coated with N-TiO₂/F-SiO₂ with varied compositions that are subjected to sodium dodecyl sulfate (SDS)-stabilized n-hexadecane-in-water emulsion (10:90 vol:vol, n-hexadecane:water) dissolved with salt (1.0 wt% NaCl with respect to the water mass). (c) The normalized flux (J_n) of the water-rich permeate through the membranes being irradiated by visible light ($I \approx 198 \text{ mW cm}^{-2}$). (d) The apparent contact angles for oil (n-hexadecane) droplets on the membranes in air and under saline water before and after visible light irradiation for 120 min. The data of the as-prepared membranes are also shown for comparison.

When the feed emulsion was introduced, the flux of the water-rich permeate began to rapidly decrease due to membrane fouling by the oil (Figure 4b and Table 1). This is a consequence of the oil's adsorption to the membrane surface, which can hamper the permeation of water and cause a rapid decline in the flux. Note that J_n is defined as J_t/J_{prewet} . According to our findings, an N-TiO₂/F-SiO₂-coated membrane with a higher N-TiO₂ composition exhibited a steeper decrease in flux. For example, when a membrane was coated with N-TiO₂/F-SiO₂ (80 wt%), $J_n \approx 0.17$ ($J_t \approx 0.0135 \text{ Lm}^{-2}\text{h}^{-1}\text{kPa}^{-1}$). However, when it was coated with N-TiO₂/F-SiO₂ (20 wt%), $J_n \approx 0.30$ ($J_t \approx 0.0163 \text{ Lm}^{-2}\text{h}^{-1}\text{kPa}^{-1}$) at $t = 180 \text{ min}$. This can be primarily attributed to the fact that N-TiO₂ is more vulnerable to oil adsorption [51], while F-SiO₂ can repel it [52] (Supporting Movie S1). Note that such a rapid flux decline in the membranes after the introduction of an oil–water mixture has been reported previously [53,54]. Despite the membranes' decline in flux, the concentration of oil in the permeate remained very low (i.e., <0.1 wt%; see Supporting Information, Section S8).

Table 1. The values of the flux of the water-rich permeate through the membranes coated with N-TiO₂/F-SiO₂ with varied compositions that were subjected to sodium dodecyl sulfate (SDS)-stabilized n-hexadecane-in-water emulsion (10:90 vol:vol, n-hexadecane:water) dissolved with salt (1.0 wt% NaCl with respect to the water mass).

N-TiO ₂ /F-SiO ₂ Compositions	Flux at $t = 0$ (J_o) ($\text{Lm}^{-2}\text{h}^{-1}\text{kPa}^{-1}$)	Flux at $t = 180 \text{ min}$ (J_t) ($\text{Lm}^{-2}\text{h}^{-1}\text{kPa}^{-1}$)
N-TiO ₂ /F-SiO ₂ (0)	0.0467	0.0177
N-TiO ₂ /F-SiO ₂ (20 wt%)	0.0547	0.0163
N-TiO ₂ /F-SiO ₂ (40 wt%)	0.0627	0.0174
N-TiO ₂ /F-SiO ₂ (60 wt%)	0.0786	0.0157
N-TiO ₂ /F-SiO ₂ (80 wt%)	0.0826	0.0135
N-TiO ₂ /F-SiO ₂ (100 wt%)	0.0826	0.0033

When the water-rich permeate flux reached a constant value at $t = 180 \text{ min}$, we began to irradiate the membrane surface with visible light ($I \approx 198 \text{ mW cm}^{-2}$) to induce photocatalytic degradation of the surface's adsorbed oil. This was a result of electron–hole (e^- - h^+) pairs generated upon light irradiation with an energy greater than the bandgap energy of the photocatalyst (e.g., N-TiO₂) [55]. The electrons and holes can react with the ambient molecules (e.g., oxygen or water) and generate reactive radicals such as hydroxyl, which can remove organic contaminants such as oil by chemical oxidation (or reduction) [31]. The membrane was then continuously subjected to a fresh feed emulsion. We observed that a membrane coated with N-TiO₂/F-SiO₂ with a higher concentration of N-TiO₂ caused a more significant increase in the J_n value, which was a direct result of the photocatalysis-driven recovery of the clean membrane surface that exhibited a lower breakthrough pressure for saline water (Figure 4c and Table 2). For example, a membrane coated with N-TiO₂/F-SiO₂ (80 wt%) yielded $J_n \approx 0.24$ ($J_t \approx 0.0190 \text{ Lm}^{-2}\text{h}^{-1}\text{kPa}^{-1}$), while the one coated with N-TiO₂/F-SiO₂ (20 wt%) exhibited $J_n \approx 0.31$ ($J_t \approx 0.0174 \text{ Lm}^{-2}\text{h}^{-1}\text{kPa}^{-1}$) after 60 min of irradiation.

Table 2. The values of the flux of the water-rich permeate through the membranes coated with N-TiO₂/F-SiO₂ with varied compositions after 60 min of irradiation with visible light ($I \approx 198 \text{ mW cm}^{-2}$).

N-TiO ₂ /F-SiO ₂ Compositions	Flux at t = 180 min (before Irradiation) (Lm ⁻² h ⁻¹ kPa ⁻¹)	Flux at t = 240 min (after 60 min of Irradiation) (Lm ⁻² h ⁻¹ kPa ⁻¹)
N-TiO ₂ /F-SiO ₂ (0)	0.0177	0.0177
N-TiO ₂ /F-SiO ₂ (20 wt%)	0.0163	0.0174
N-TiO ₂ /F-SiO ₂ (40 wt%)	0.0174	0.0200
N-TiO ₂ /F-SiO ₂ (60 wt%)	0.0157	0.0212
N-TiO ₂ /F-SiO ₂ (80 wt%)	0.0135	0.0190
N-TiO ₂ /F-SiO ₂ (100 wt%)	0.0033	0.0090

While an in situ photocatalysis-driven recovery of the clean membrane surface is presented in this work, a majority of the previous studies have demonstrated this ex situ. For example, Zhang et al. [33] synthesized an electrospun membrane anchored with photocatalytic β -FeOOH nanorods. The membrane demonstrated that it could photocatalytically degrade the surface adsorbed organic matter and recover its flux upon visible light irradiation after 40 min. Peyravi et al. [56] incorporated photocatalytic TiO₂/zeolite into a composite membrane and demonstrated $\approx 83.6\%$ flux recovery under UV irradiation. Liu et al. [34] fabricated a membrane utilizing TiO₂/carbon nitride nanosheets and showed membrane surface cleaning with a flux recovery ratio of $>95\%$. In addition, Kovács et al. [57] demonstrated that a TiO₂-coated ultrafiltration membrane could almost completely recover its original flux after 1 h of UV irradiation. Furthermore, Xie et al. [58] fabricated a photocatalytic membrane using β -FeOOH, which demonstrated $>98\%$ flux recovery within 10 min under visible light.

We also measured the contact angles for oil and saline water after 60 min of visible light irradiation and found that they remained unchanged (Figure 4d). This indicates that the photocatalytic reaction taking place within the N-TiO₂ did not affect the perfluoro silane molecules grafted to the SiO₂ (Supporting Information, Section S9). Moreover, both the salt rejection (ζ) of the membranes and the cured adhesive layer remained nearly unchanged (Supporting Information, Section S10).

4. Conclusions

In summary, we have developed a photocatalytic coating with hydrophilic and oleophobic wettability by intercalating a mixture of visible light-responsive N-TiO₂ and low surface energy F-SiO₂ nanoparticles. We tested the feasibility of our membrane coating by spraying it on a commercial membrane surface with UV-curable adhesive. Subsequent irradiation with UV light resulted in a chemically heterogeneous surface with intercalating high surface energy (N-TiO₂) and low surface energy (F-SiO₂) regions that were securely bound to the surface. Our membrane could recover the flux upon visible light irradiation. We attributed this to the photocatalytic degradation of the surface adsorbed oil when placed under visible light irradiation. Such photocatalytic degradation did not compromise the wettability or integrity of the membrane due to the robust chemistry of the adhesive. We engineered an apparatus that enabled the continuous separation and desalination of a surfactant-stabilized oil-in-water emulsion that was dissolved with salt and the photocatalytic degradation of organic substances that were adsorbed on the coated membrane surface when it was exposed to visible light irradiation. It was found that the coated membrane was able to recover its permeate flux in situ when placed under visible light irradiation. We envision that our membrane will have a wide range of practical applications, including wastewater treatment, fuel purification, and desalinating brackish water.

Supplementary Materials: The following are available online at <https://www.mdpi.com/article/10.3390/nano11061397/s1>. Figure S1: (a) A number size distribution of N-TiO₂ nanoparticles obtained by utilizing the DLS method. (b,c) Transmission electron microscopy (TEM) image of N-TiO₂ nanoparticles (b) and high-resolution TEM image showing N-TiO₂ lattice structure with an average spacing of ≈ 0.35 nm (c). Figure S2: XRD pattern of N-TiO₂ nanoparticles synthesized by utilizing a molar ratio of TEA and TBOT of 2.0. For comparison, the XRD pattern of a neat TiO₂ is shown. Figure S3: UV-Vis absorption spectra of water solutions dissolved with Solvent Blue 38 dye (concentration = 0.5 wt%) and N-TiO₂ (concentration = 0.5 wt%) after 2 h of visible light irradiation with varied intensity. The UV-Vis absorption spectra of the water solution dissolved with Solvent Blue 38 dye (concentration = 0.5 wt%) and N-TiO₂ (concentration = 0.5 wt%) after 10 h in the dark is also provided. Figure S4: (a) Schematic illustrating the synthesis of F-SiO₂ nanoparticles by utilizing tetraethyl orthosilicate (TEOS) as a SiO₂ precursor and 1H,1H,2H,2H-perfluorodecyl trichlorosilane (i.e., perfluoro silane). (b) A number size distribution of F-SiO₂ nanoparticles, obtained by utilizing the DLS method. Figure S5: A plot of the measured breakthrough pressure for saline water (1.0 wt% NaCl in DI water) of the membranes coated with N-TiO₂/F-SiO₂ with varied compositions. Figure S6: (a) The calibration curve established by calculating the electrical conductivity of water as a function of salt (NaCl) concentrations. The inset shows zoomed-in electrical conductivity data in the NaCl concentration range of 0.00–0.20 wt%. (b) The salt rejection (ξ) data of the membranes coated with N-TiO₂/F-SiO₂ with varied compositions. The data of the as-purchased commercial filter and that coated only with cured adhesive are also provided for comparison. Figure S7: The mass loss of the membranes coated with N-TiO₂/F-SiO₂ with varied compositions after 180 min of desalination of saline water at a flow rate of 1.5 L min⁻¹. For comparison, the results obtained by utilizing the membranes without cured adhesive are also shown. Figure S8: The TGA data of the water-rich permeates after the separation of SDS-stabilized oil-in-water emulsion dissolved with NaCl (1.0 wt% with respect to the water mass) through the membranes coated N-TiO₂/F-SiO₂ with varied compositions. Figure S9: The FT-IR spectra of a membrane surface coated with N-TiO₂/F-SiO₂ (60 wt%) after 120 min of visible light irradiation with an intensity of ≈ 198 mW cm⁻². For comparison, the FT-IR spectra of the as-prepared membrane surface is shown. Figure S10: The FT-IR spectra of the cured adhesive after 180 min of visible light-driven photocatalysis by N-TiO₂ ($I \approx 198$ mW cm⁻²). For comparison, the FT-IR spectra of the as-prepared adhesive is also shown. Figure S11: The salt rejection (ξ) of the membranes coated with N-TiO₂/F-SiO₂ with varied compositions after exposure to 60 min of visible light irradiation.

Author Contributions: B.S. and M.E. performed the experiments, analyzed the data, and wrote the manuscript. G.K. conceived the project, designed the experiments, and wrote the manuscript. All authors have read and agreed to the published version of the manuscript.

Funding: This research was supported by the U.S. Department of Interior-Bureau of Reclamation [grant number: R17AC00132], National Science Foundation RET Site: Exploring Career Opportunities through Water-Themed Engineering Research (ECO-WaTER) [grant number: 1801710], and the National Science Foundation [grant number: CBET-1944314].

Data Availability Statement: The datasets generated during and/or analyzed during this study are not publicly available but are available from the corresponding author on reasonable request.

Conflicts of Interest: The authors declare that they have no known competing financial interests or personal relationships that could have appeared to influence the work reported in this paper.

References

1. Eseev, M.; Goshev, A.; Kapustin, S.; Tsykareva, Y. Creation of Superhydrophobic Coatings Based on MWCNTs Xerogel. *Nanomaterials* **2019**, *9*, 1584. [[CrossRef](#)]
2. Dong, S.; Wang, Z.; An, L.; Li, Y.; Wang, B.; Ji, H.; Wang, H. Facile Fabrication of a Superhydrophobic Surface with Robust Micro-/Nanoscale Hierarchical Structures on Titanium Substrate. *Nanomaterials* **2020**, *10*, 1509. [[CrossRef](#)] [[PubMed](#)]
3. Li, J.; Qin, Q.H.; Shah, A.; Ras, R.H.A.; Tian, X.; Jokinen, V. Oil droplet self-transportation on oleophobic surfaces. *Sci. Adv.* **2016**, *2*, e1600148. [[CrossRef](#)] [[PubMed](#)]
4. Geng, H.; Bai, H.; Fan, Y.; Wang, S.; Ba, T.; Yu, C.; Cao, M.; Jiang, L. Unidirectional water delivery on a superhydrophilic surface with two-dimensional asymmetrical wettability barriers. *Mater. Horiz.* **2018**, *5*, 303–308. [[CrossRef](#)]
5. Lv, J.; Gong, Z.; He, Z.; Yang, J.; Chen, Y.; Tang, C.; Liu, Y.; Fan, M.; Lau, W.-M. 3D printing of a mechanically durable superhydrophobic porous membrane for oil–water separation. *J. Mater. Chem. A* **2017**, *5*, 12435–12444. [[CrossRef](#)]

6. Sun, S.; Zhu, L.; Liu, X.; Wu, L.; Dai, K.; Liu, C.; Shen, C.; Guo, X.; Zheng, G.; Guo, Z. Superhydrophobic Shish-kebab Membrane with Self-Cleaning and Oil/Water Separation Properties. *ACS Sustain. Chem. Eng.* **2018**, *6*, 9866–9875. [[CrossRef](#)]
7. Kwon, G.; Post, E.; Tuteja, A. Membranes with selective wettability for the separation of oil-water mixtures. *MRS Commun.* **2015**, *5*, 475–494. [[CrossRef](#)]
8. Law, K.Y.; Zhao, H. *Surface Wetting: Characterization, Contact Angle, and Fundamentals*; Springer International Publishing: New York, NY, USA, 2015; pp. 95–150.
9. Ezazi, M.; Shrestha, B.; Klein, N.; Lee, D.H.; Seo, S.; Kwon, G. Self-Healable Superomniphobic Surfaces for Corrosion Protection. *ACS Appl. Mater. Interfaces* **2019**, *11*, 30240–30246. [[CrossRef](#)] [[PubMed](#)]
10. Kota, A.K.; Kwon, G.; Tuteja, A. The design and applications of superomniphobic surfaces. *NPG Asia Mater.* **2014**, *6*, e109. [[CrossRef](#)]
11. Vahabi, H.; Wang, W.; Popat, K.C.; Kwon, G.; Holland, T.B.; Kota, A.K. Metallic superhydrophobic surfaces via thermal sensitization. *Appl. Phys. Lett.* **2017**, *110*, 251602. [[CrossRef](#)]
12. Brown, P.S.; Bhushan, B. Mechanically durable, superomniphobic coatings prepared by layer-by-layer technique for self-cleaning and anti-smudge. *J. Colloid Interface Sci.* **2015**, *456*, 210–218. [[CrossRef](#)]
13. Moizy, A.; Padhye, R.; Wang, X. Durable Superomniphobic Surface on Cotton Fabrics via Coating of Silicone Rubber and Fluoropolymers. *Coatings* **2018**, *8*, 104. [[CrossRef](#)]
14. Zhang, H.; Ji, X.; Liu, L.; Ren, J.; Tao, F.; Qiao, C. Versatile, mechanochemically robust, sprayed superomniphobic coating enabling low surface tension and high viscous organic liquid bouncing. *Chem. Eng. J.* **2020**, *402*, 126160. [[CrossRef](#)]
15. Vilčnik, A.; Jerman, I.; Vuk, A.; Šurca Koželj, M.; Orel, B.; Tomšič, B.; Simončič, B.; Kovač, J. Structural Properties and Antibacterial Effects of Hydrophobic and Oleophobic Sol–Gel Coatings for Cotton Fabrics. *Langmuir* **2009**, *25*, 5869–5880. [[CrossRef](#)] [[PubMed](#)]
16. Hayn, R.A.; Owens, J.R.; Boyer, S.A.; McDonald, R.S.; Lee, H.J. Preparation of highly hydrophobic and oleophobic textile surfaces using microwave-promoted silane coupling. *J. Mater. Sci.* **2010**, *46*, 2503–2509. [[CrossRef](#)]
17. Wang, W.; Salazar, J.; Vahabi, H.; Joshi-Imre, A.; Voit, W.E.; Kota, A.K. Metamorphic Superomniphobic Surfaces. *Adv. Mater.* **2017**, *29*, 1700295. [[CrossRef](#)] [[PubMed](#)]
18. Yun, G.-T.; Jung, W.-B.; Oh, M.S.; Jang, G.M.; Baek, J.; Kim, N.I.; Im, S.G.; Jung, H.-T. Springtail-inspired superomniphobic surface with extreme pressure resistance. *Sci. Adv.* **2018**, *4*, eaat4978. [[CrossRef](#)]
19. Mertens, M.; Mohr, M.; Bruehne, K.; Fecht, H.-J.; Łojkowski, M.; Świąszkowski, W.; Łojkowski, W. Patterned hydrophobic and hydrophilic surfaces of ultra-smooth nanocrystalline diamond layers. *Appl. Surf. Sci.* **2016**, *390*, 526–530. [[CrossRef](#)]
20. Howarter, J.A.; Youngblood, J.P. Self-Cleaning and Next Generation Anti-Fog Surfaces and Coatings. *Macromol. Rapid Commun.* **2008**, *29*, 455–466. [[CrossRef](#)]
21. Jayaramulu, K.; Geyer, F.; Petr, M.; Zboril, R.; Vollmer, D.; Fischer, R.A. Shape Controlled Hierarchical Porous Hydrophobic/Oleophilic Metal-Organic Nanofibrous Gel Composites for Oil Adsorption. *Adv. Mater.* **2017**, *29*, 1605307. [[CrossRef](#)]
22. Brown, P.; Atkinson, O.D.L.A.; Badyal, J.P.S. Ultrafast Oleophobic-Hydrophilic Switching Surfaces for Antifogging, Self-Cleaning, and Oil–Water Separation. *ACS Appl. Mater. Interfaces* **2014**, *6*, 7504–7511. [[CrossRef](#)]
23. Qing, W.; Liu, F.; Yao, H.; Sun, S.; Chen, C.; Zhang, W. Functional catalytic membrane development: A review of catalyst coating techniques. *Adv. Colloid Interface Sci.* **2020**, *282*, 102207. [[CrossRef](#)]
24. Li, Q.; Zhao, T.; Li, M.; Li, W.; Yang, B.; Qin, D.; Lv, K.; Wang, X.; Wu, L.; Wu, X.; et al. One-step construction of Pickering emulsion via commercial TiO₂ nanoparticles for photocatalytic dye degradation. *Appl. Catal. B Environ.* **2019**, *249*, 1–8. [[CrossRef](#)]
25. Li, X.; Wu, X.; Liu, S.; Li, Y.; Fan, J.; Lv, K. Effects of fluorine on photocatalysis. *Chin. J. Catal.* **2020**, *41*, 1451–1467. [[CrossRef](#)]
26. Coelho, F.E.B.; Gionco, C.; Paganini, M.C.; Calza, P.; Magnacca, G. Control of Membrane Fouling in Organics Filtration Using Ce-Doped Zirconia and Visible Light. *Nanomaterials* **2019**, *9*, 534. [[CrossRef](#)]
27. Liu, T.; Wang, L.; Liu, X.; Sun, C.; Lv, Y.; Miao, R.; Wang, X. Dynamic photocatalytic membrane coated with ZnIn₂S₄ for enhanced photocatalytic performance and antifouling property. *Chem. Eng. J.* **2020**, *379*, 122379. [[CrossRef](#)]
28. Qahtan, T.F.; Gondal, M.A.; Dastageer, M.A.; Kwon, G.; Ezazi, M.; Al-Kuban, M.Z. Thermally Sensitized Membranes for Crude Oil–Water Remediation under Visible Light. *ACS Appl. Mater. Interfaces* **2020**, *12*, 48572–48579. [[CrossRef](#)]
29. Lv, Y.; Zhang, C.; He, A.; Yang, S.-J.; Wu, G.-P.; Darling, S.B.; Xu, Z.-K. Photocatalytic Nanofiltration Membranes with Self-Cleaning Property for Wastewater Treatment. *Adv. Funct. Mater.* **2017**, *27*, 1700251. [[CrossRef](#)]
30. Yu, J.C.; Ho, W.; Lin, J.; Yip, H.; Wong, P.K. Photocatalytic Activity, Antibacterial Effect, and Photoinduced Hydrophilicity of TiO₂ Films Coated on a Stainless Steel Substrate. *Environ. Sci. Technol.* **2003**, *37*, 2296–2301. [[CrossRef](#)]
31. Ezazi, M.; Shrestha, B.; Kim, S.; Jeong, B.; Gorney, J.; Hutchison, K.; Lee, D.H.; Kwon, G. Selective Wettability Membrane for Continuous Oil–Water Separation and In Situ Visible Light-Driven Photocatalytic Purification of Water. *Glob. Chall.* **2020**, *4*, 2000009. [[CrossRef](#)]
32. Song, S.; Yang, H.; Zhou, C.; Cheng, J.; Jiang, Z.; Lu, Z.; Miao, J. Underwater superoleophobic mesh based on BiVO₄ nanoparticles with sunlight-driven self-cleaning property for oil/water separation. *Chem. Eng. J.* **2017**, *320*, 342–351. [[CrossRef](#)]
33. Zhang, L.; He, Y.; Ma, L.; Chen, J.; Fan, Y.; Zhang, S.; Shi, H.; Li, Z.; Luo, P. Hierarchically Stabilized PAN/β-FeOOH Nanofibrous Membrane for Efficient Water Purification with Excellent Antifouling Performance and Robust Solvent Resistance. *ACS Appl. Mater. Interfaces* **2019**, *11*, 34487–34496. [[CrossRef](#)]
34. Liu, Y.; Su, Y.; Guan, J.; Cao, J.; Zhang, R.; He, M.; Gao, K.; Zhou, L.; Jiang, Z. 2D Heterostructure Membranes with Sunlight-Driven Self-Cleaning Ability for Highly Efficient Oil-Water Separation. *Adv. Funct. Mater.* **2018**, *28*, 1706545. [[CrossRef](#)]

35. Zhao, J.; Zhu, W.; Wang, X.; Liu, L.; Yu, J.; Ding, B. Environmentally benign modification of breathable nanofibrous membranes exhibiting superior waterproof and photocatalytic self-cleaning properties. *Nanoscale Horiz.* **2019**, *4*, 867–873. [[CrossRef](#)]
36. Luster, E.; Avisar, D.; Horovitz, I.; Lozzi, L.; Baker, M.A.; Grilli, R.; Mamane, H. N-Doped TiO₂-Coated Ceramic Membrane for Carbamazepine Degradation in Different Water Qualities. *Nanomaterials* **2017**, *7*, 206. [[CrossRef](#)]
37. Wang, D.; Liu, Y.; Liu, X.; Zhou, F.; Liu, W.; Xue, Q. Towards a tunable and switchable water adhesion on a TiO₂ nanotube film with patterned wettability. *Chem. Commun.* **2009**, *2009*, 7018–7020. [[CrossRef](#)]
38. Horovitz, I.; Gitis, V.; Avisar, D.; Mamane, H. Ceramic-based photocatalytic membrane reactors for water treatment—Where to next? *Rev. Chem. Eng.* **2020**, *36*, 593–622. [[CrossRef](#)]
39. Di Valentin, C.; Finazzi, E.; Pacchioni, G.; Selloni, A.; Livraghi, S.; Paganini, M.C.; Giamello, E. N-doped TiO₂: Theory and experiment. *Chem. Phys.* **2007**, *339*, 44–56. [[CrossRef](#)]
40. Premkumar, J. Development of Super-Hydrophilicity on Nitrogen-Doped TiO₂ Thin Film Surface by Photoelectrochemical Method under Visible Light. *Chem. Mater.* **2004**, *16*, 3980–3981. [[CrossRef](#)]
41. Brassard, J.-D.; Sarkar, D.K.; Perron, J. Synthesis of Monodisperse Fluorinated Silica Nanoparticles and Their Superhydrophobic Thin Films. *ACS Appl. Mater. Interfaces* **2011**, *3*, 3583–3588. [[CrossRef](#)]
42. Burda, C.; Lou, Y.; Chen, X.; Samia, A.C.S.; Stout, J.; Gole, J.L. Enhanced Nitrogen Doping in TiO₂ Nanoparticles. *Nano Lett.* **2003**, *3*, 1049–1051. [[CrossRef](#)]
43. Cong, Y.; Zhang, J.; Chen, F.; Anpo, M. Synthesis and Characterization of Nitrogen-Doped TiO₂ Nanophotocatalyst with High Visible Light Activity. *J. Phys. Chem. C* **2007**, *111*, 6976–6982. [[CrossRef](#)]
44. Yang, G.; Jiang, Z.; Shi, H.; Xiao, T.; Yan, Z. Preparation of highly visible-light active N-doped TiO₂ photocatalyst. *J. Mater. Chem.* **2010**, *20*, 5301–5309. [[CrossRef](#)]
45. Stöber, W.; Fink, A.; Bohn, E. Controlled growth of monodisperse silica spheres in the micron size range. *J. Colloid Interface Sci.* **1968**, *26*, 62–69. [[CrossRef](#)]
46. Zhang, Z.; Zhang, W.; Lichtfouse, E. *Membranes for Environmental Applications*; Springer International Publishing: New York, NY, USA, 2020; pp. 200–220.
47. Furmidge, C. Studies at phase interfaces. I. The sliding of liquid drops on solid surfaces and a theory for spray retention. *J. Colloid Sci.* **1962**, *17*, 309–324. [[CrossRef](#)]
48. Tuteja, A.; Choi, W.; Ma, M.; Mabry, J.M.; Mazzella, S.A.; Rutledge, G.C.; McKinley, G.H.; Cohen, R.E. Designing Superoleophobic Surfaces. *Science* **2007**, *318*, 1618–1622. [[CrossRef](#)] [[PubMed](#)]
49. Kwon, G.; Kota, A.K.; Li, Y.; Sohani, A.; Mabry, J.M.; Tuteja, A. On-Demand Separation of Oil-Water Mixtures. *Adv. Mater.* **2012**, *24*, 3666–3671. [[CrossRef](#)]
50. Kwon, G.; Panchanathan, D.; Mahmoudi, S.R.; Gondal, M.A.; McKinley, G.H.; Varanasi, K.K. Visible light guided manipulation of liquid wettability on photoresponsive surfaces. *Nat. Commun.* **2017**, *8*, 14968. [[CrossRef](#)] [[PubMed](#)]
51. Vaiano, V.; Sacco, O.; Sannino, D.; Navarra, W.; Daniel, C.; Venditto, V. Influence of aggregate size on photoactivity of N-doped TiO₂ particles in aqueous suspensions under visible light irradiation. *J. Photochem. Photobiol. A Chem.* **2017**, *336*, 191–197. [[CrossRef](#)]
52. Hsieh, C.-T.; Chang, B.-S.; Lin, J.-Y. Improvement of water and oil repellency on wood substrates by using fluorinated silica nanocoating. *Appl. Surf. Sci.* **2011**, *257*, 7997–8002. [[CrossRef](#)]
53. Mohammadi, T.; Kazemimoghadam, M.; Saadabadi, M. Modeling of membrane fouling and flux decline in reverse osmosis during separation of oil in water emulsions. *Desalination* **2003**, *157*, 369–375. [[CrossRef](#)]
54. Mondal, S.; Wickramasinghe, S.R. Produced water treatment by nanofiltration and reverse osmosis membranes. *J. Membr. Sci.* **2008**, *322*, 162–170. [[CrossRef](#)]
55. Hoffmann, M.R.; Martin, S.T.; Choi, W.; Bahnemann, D.W. Environmental Applications of Semiconductor Photocatalysis. *Chem. Rev.* **1995**, *95*, 69–96. [[CrossRef](#)]
56. Peyravi, M.; Jahanshahi, M.; Mirmousaei, S.M.; Lau, W.-J. Dynamically Coated Photocatalytic Zeolite–TiO₂ Membrane for Oil-in-Water Emulsion Separation. *Arab. J. Sci. Eng.* **2020**, *1–9*. [[CrossRef](#)]
57. Kovács, I.; Veréb, G.; Kertész, S.; Beszédes, S.; Hodúr, C.; László, Z. Investigation of surface and filtration properties of TiO₂ coated ultrafiltration polyacrylonitrile membranes. *Water Sci. Technol.* **2018**, *77*, 931–938. [[CrossRef](#)]
58. Xie, A.; Cui, J.; Yang, J.; Chen, Y.; Dai, J.; Lang, J.; Li, C.; Yan, Y. Photo-Fenton self-cleaning membranes with robust flux recovery for an efficient oil/water emulsion separation. *J. Mater. Chem. A* **2019**, *7*, 8491–8502. [[CrossRef](#)]

Paper P2

Predicting kinetics of water-rich permeate flux through photocatalytic mesh under visible light illumination

Reproduced with the permission from [**Shrestha, Bishwash**, Mohammadamin Ezazi, Seyed Vahid Rad, and Gibum Kwon. "Predicting kinetics of water-rich permeate flux through photocatalytic mesh under visible light illumination." *Scientific reports* 11, no. 1 (2021): 1-9] is licensed under CC BY-ND 2.0



OPEN Predicting kinetics of water-rich permeate flux through photocatalytic mesh under visible light illumination

Bishwash Shrestha^{1,2}, Mohammadamin Ezazi^{1,2}, Seyed Vahid Rad¹ & Gibum Kwon^{1✉}

Membrane-based separation technologies are attractive to remediating unconventional water sources, including brackish, industrial, and municipal wastewater, due to their versatility and relatively high energy efficiency. However, membrane fouling by dissolved or suspended organic substances remains a primary challenge which can result in an irreversible decline of the permeate flux. To overcome this, membranes have been incorporated with photocatalytic materials that can degrade these organic substances deposited on the surface upon light illumination. While such photocatalytic membranes have demonstrated that they can recover their inherent permeability, less information is known about the effect of photocatalysis on the kinetics of the permeate flux. In this work, a photocatalytic mesh that can selectively permeate water while repelling oil was fabricated by coating a mixture of nitrogen-doped TiO₂ (N-TiO₂) and perfluorosilane-grafted SiO₂ (F-SiO₂) nanoparticles on a stainless steel mesh. Utilizing the photocatalytic mesh, the time-dependent evolution of the water-rich permeate flux as a result of photocatalytic degradation of the oil was studied under the visible light illumination. A mathematical model was developed that can relate the photocatalytic degradation of the organic substances deposited on a mesh surface to the evolution of the permeate flux. This model was established by integrating the Langmuir–Hinshelwood kinetics for photocatalysis and the Cassie–Baxter wettability analysis on a chemically heterogeneous mesh surface into a permeate flux relation. Consequently, the time-dependent water-rich permeate flux values are compared with those predicted by using the model. It is found that the model can predict the evolution of the water-rich permeate flux with a goodness of fit of 0.92.

With growing environmental awareness and tighter regulations, there is an increase in investments for developing water remediation technologies^{1–8}. Membrane-based technologies are attractive because they are relatively energy-efficient and versatile to different effluents generated in industrial processes^{9–12}. One of the primary challenges of membranes is fouling by dissolved or suspended organic substances that can get adsorbed on the membrane surface or pore walls^{13,14}. This results in a decrease in the permeability and can eventually shorten the membrane's life cycle^{14–16}. Therefore, membrane-based remediation technologies often involve prefiltration to remove the suspended or dissolved substances¹⁷. Also, membranes are periodically subjected to cleaning processes such as backwashing, forward flushing, and chemical treatment to remove the surface-deposited contaminants^{18,19}. While these methodologies are effective and widely employed in real applications, they can irreversibly degrade membrane's performance over time^{20,21}.

Manipulating the membrane's wettability has been reported as an alternative to enhance its fouling resistance^{22–25}. For example, membranes with hydrophilic (i.e., water contact angle < 90°) or superhydrophilic (i.e., water contact angle ≈ 0°) wettability can prevent adsorption of the organic substances (e.g., oil) to the surface by allowing water to form a thin film^{26–28}. Also, these membranes can exhibit selective permeation for water while repelling oils, which enables separation of oil–water mixtures with a high separation efficiency²⁹. In comparison, membranes possessing lower solid surface energy (γ_{sv}) can repel the organic substances without needing for a water film^{30–32}. We⁶ and others^{26–28} have reported fouling-resistant membranes that can separate oil–water mixtures with an insignificant decline in the permeate flux by combining hydrophilic (or superhydrophilic) wettability along with lower solid surface energy.

¹Department of Mechanical Engineering, University of Kansas, Lawrence, KS 66045, USA. ²These authors contributed equally: Bishwash Shrestha and Mohammadamin Ezazi. ✉email: gbkwon@ku.edu

Membranes with selective wettability have been incorporated with photocatalytic materials (e.g., TiO_2 ^{6,33}, N-TiO_2 ³⁴, $\alpha\text{-Fe}_2\text{O}_3$ ^{16,35}, Fe_3O_4 ³⁶, WO_3 ³⁷, ZnO ³⁸, BiVO_4 ⁷, $\alpha\text{-FeOOH}$ ³⁹, MoO_3 ⁴⁰, Co_3O_4 ⁴¹, $\text{Gd}_2\text{ZnMnO}_6/\text{ZnO}$ ⁴²) that can degrade the organic substances deposited on the surface upon light illumination. These membranes have demonstrated that they can oxidize (or reduce) the organic substances either dissolved in a liquid (e.g., water) or adsorbed on the membrane surface when irradiated by light with an energy higher than their bandgap energy^{43,44}. This can clean the membrane's surface and purify the permeate. Moreover, these photocatalytic membranes can recover the water-rich permeate flux upon light illumination after being fouled by organic substances. For example., Zhang et al.⁴⁵ demonstrated in situ recovery of the water-rich permeate flux utilizing a nitrogen doped TiO_2 coated membrane under visible light illumination. Guo et al.⁴⁶ fabricated a photocatalytic membrane by utilizing BiOBr/Ag nanoparticles that can degrade organic dyes (e.g., methylene blue, crystal violet, acid red 18, and acid yellow 36) upon UV light illumination and recover the water-rich permeate flux. Liu et al.⁴⁷ fabricated a PVDF-Ni-ZnO composite membrane and demonstrated in situ photocatalysis-driven recovery of the water-rich permeate flux during the filtration of an aqueous solution dissolved with organic substances (e.g., humic acid, sodium alginate, bovine serum albumin). Recently, we^{3,6} developed photocatalytic membranes by coating a commercial filter with a mixture of visible light-active iron-doped TiO_2 or nitrogen-doped TiO_2 and perfluorosilane-grafted SiO_2 . These membranes have demonstrated in situ recovery of the water-rich permeate flux upon visible light illumination during oil–water separation.

An increase in the permeate flux upon light illumination has been attributed to the photocatalytic degradation of the organic substances deposited on the membrane surface^{27,48,49}. Also, such photocatalytic membranes have demonstrated that they exhibit a time-dependent evolution of the surface chemistry heterogeneity (e.g., clean and contaminated regions) upon light illumination which can be quantitatively described by the contact angle measurements^{6,22,50–52}. To our knowledge, quantitative relationships of the evolution of surface chemistry heterogeneity on a membrane surface and that of permeate flux upon visible light illumination are lacking. Establishing such a relation is critical to understand both membrane fouling and photocatalytic cleaning mechanisms, which enables one to design a separation membrane with tailored performance.

Based on these findings, herein, we conducted experimental analysis on the effect of wettability and photocatalysis on the permeate flux through a photocatalytic material-coated stainless steel mesh and developed a mathematical relation between them under visible light illumination. For this, we fabricated a photocatalytic mesh utilizing a stainless steel mesh coated with nitrogen-doped TiO_2 (N-TiO_2) and perfluorosilane-grafted SiO_2 (F-SiO_2) nanoparticles mixture. A mathematical model was derived by integrating the Langmuir–Hinshelwood kinetic model of photocatalysis^{22,30} and the Cassie–Baxter analysis of the contact angles for water on a photocatalytic surface⁵³ into a permeate flux relation⁵⁴. The mathematical model was then utilized to predict the water-rich permeate flux through the photocatalytic mesh during visible light illumination. The accuracy of the predicted flux values was then validated by comparing with the experimentally acquired results.

Results and discussion

Photocatalytic mesh fabrication and under-oil water wettability. A mixture of nitrogen-doped TiO_2 (N-TiO_2) and perfluorosilane-grafted SiO_2 (F-SiO_2) nanoparticles was utilized to fabricate a visible light-active photocatalytic mesh (see “Methods”). Please note that the synthesis of a mixture of N-TiO_2 and F-SiO_2 nanoparticles (i.e., $\text{N-TiO}_2/\text{F-SiO}_2$) was reported in previous work⁶ which demonstrated selective wettability for water over oil (i.e., hydrophilic and oleophobic wettability). Briefly, a dispersion of $\text{N-TiO}_2/\text{F-SiO}_2$ in deionized (DI) water (solute concentration = 10 wt%) was sprayed onto a stainless steel (SS) 316 Twill Dutch weave mesh (SS mesh) for one minute. Note that the SS mesh was pre-treated with an ultraviolet (UV)-curable adhesive. Here, we utilized dispersions with varied N-TiO_2 concentrations in the $\text{N-TiO}_2/\text{F-SiO}_2$ mixture (i.e., 0, 25 wt%, 50 wt%, 75 wt%, and 100 wt%). Subsequently, the SS mesh was illuminated by a long-wavelength UV light (100 W, $\lambda = 365$ nm) for 5 min to completely cure the adhesive. Finally, the resulting mesh was thoroughly rinsed with ethanol and DI water.

Figure 1a demonstrates a scanning electron microscopy (SEM) image of a SS mesh coated with $\text{N-TiO}_2/\text{F-SiO}_2$ mixture that includes 50 wt% N-TiO_2 (i.e., $\text{N-TiO}_2/\text{F-SiO}_2$ (50 wt%)). The mesh surface was evenly coated with $\text{N-TiO}_2/\text{F-SiO}_2$ nanoparticles showing a hierarchical structure (i.e., surface texture with two or more length scales⁵⁵) with a root mean square (RMS) surface roughness¹ of 0.75 ± 0.03 μm (see “Methods”). Further, the nominal pore size of the mesh was measured as 0.40 ± 0.03 μm after coating with $\text{N-TiO}_2/\text{F-SiO}_2$ mixture (see “Methods”). Please note that the mesh exhibited mechanical robustness against external stress because the cured adhesive can securely hold nanoparticles on the mesh surface (Supporting Information (SI) Sect. 1).

We⁶ have demonstrated that a commercial filter surface coated with $\text{N-TiO}_2/\text{F-SiO}_2$ mixture can exhibit varying wettability for water and oil depending on the composition of N-TiO_2 and F-SiO_2 (SI Sect. 2). Here, we choose SS meshes exhibiting selective wettability for water over oil in air (i.e., hydrophilic and oleophobic wettability); those coated with 50 wt% or 75 wt% N-TiO_2 (i.e., $\text{N-TiO}_2/\text{F-SiO}_2$ (50 wt%) and $\text{N-TiO}_2/\text{F-SiO}_2$ (75 wt%), respectively). Note that SS meshes coated with $\text{N-TiO}_2/\text{F-SiO}_2$ (25 wt%) or $\text{N-TiO}_2/\text{F-SiO}_2$ (0) are excluded in this study because they exhibit in air omniphobic wettability (i.e., hydrophobic and oleophobic wettability) making them less suitable for oil–water separation.

Time-dependent change of mesh surface wettability submerged in oil. When a hydrophilic (or superhydrophilic) surface is fouled by oil, it often exhibits an increase in the water contact angles²². To study the fouling behavior, we submerged our coated mesh in an oil (*n*-hexadecane) bath and measured the underoil apparent contact angles for water ($\theta_{\text{w,o}}^*$) as a function of submerging time. The results show that a mesh coated with a higher concentration of N-TiO_2 shows a steeper increase in the values of $\theta_{\text{w,o}}^*$ (Fig. 1b). For example, a mesh coated with $\text{N-TiO}_2/\text{F-SiO}_2$ (100 wt%) shows $\theta_{\text{w,o}}^* = 97^\circ \pm 3^\circ$ while those coated with $\text{N-TiO}_2/\text{F-SiO}_2$ (75

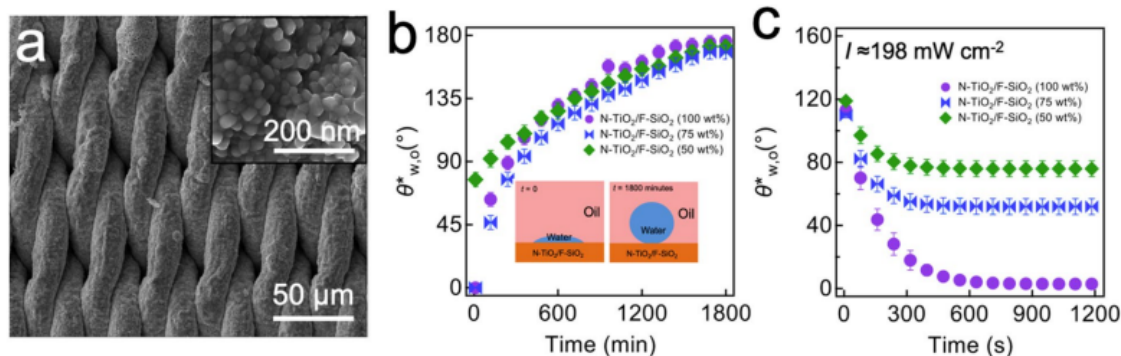


Figure 1. N-TiO₂/F-SiO₂ coated mesh surface morphology and evolution of water wettability under oil. **(a)** Scanning electron microscopy (SEM) image of stainless steel (SS) 316 Twill Dutch weave mesh coated with N-TiO₂/F-SiO₂ (50 wt%). The inset shows a higher magnification SEM image of the mesh surface. **(b)** The measured apparent contact angles for water on the mesh surfaces coated with N-TiO₂/F-SiO₂ mixture with various N-TiO₂ concentrations (50 wt%, 75 wt%, and 100 wt%) that are submerged in an oil (n-hexadecane) bath as a function of submerging time. The inset images illustrate schematics of the time-dependent evolution of the water contact angles on a mesh surface submerged in oil. **(c)** The measured apparent contact angles for water on the mesh surfaces coated with N-TiO₂/F-SiO₂ mixture with various N-TiO₂ concentrations (50 wt%, 75 wt%, and 100 wt%) while being illuminated by visible light (Intensity (I) = 198 mW cm⁻²). Note that all meshes were precontaminated by oil for 600 min.

wt%) and N-TiO₂/F-SiO₂ (50 wt%) exhibits $88^\circ \pm 3^\circ$ and $107^\circ \pm 3^\circ$, respectively, at $t = 300$ min. Please note that the values of $\theta^*_{w,o}$ on as-prepared meshes coated with N-TiO₂/F-SiO₂ (100 wt%) and N-TiO₂/F-SiO₂ (75 wt%) were zero while we measured $\theta^*_{w,o} = 79^\circ \pm 3^\circ$ on an as-prepared mesh coated with N-TiO₂/F-SiO₂ (50 wt%). Such a transition to underoil hydrophobicity (i.e., $\theta^*_{w,o} > 90^\circ$) can be attributed to an increase in the area fraction of the oil adsorbed region on the coated mesh surface which lowers the solid surface energy^{22,29}. Note that the $\theta^*_{w,o}$ values became constant at $176^\circ \pm 2^\circ$, $171^\circ \pm 4^\circ$, and $178^\circ \pm 2^\circ$ on a mesh coated with N-TiO₂/F-SiO₂ (50 wt%), N-TiO₂/F-SiO₂ (75 wt%), and N-TiO₂/F-SiO₂ (100 wt%), respectively, at $t = 1800$ min.

When an oil-contaminated photocatalytic mesh surface is illuminated by light, it can exhibit a conversion to underoil hydrophilic (or superhydrophilic) wettability due to photocatalytic degradation of the surface adsorbed oil molecules which can lead to an increase in the area fraction of clean (i.e., high solid surface energy) regions^{22,29}. We conducted in situ measurements for the $\theta^*_{w,o}$ values on our mesh under visible light illumination ($I \approx 198$ mW cm⁻²). All meshes were precontaminated with oil for 600 min. Upon the onset of visible light illumination, the $\theta^*_{w,o}$ values started to rapidly decrease and reached constant values after $t \approx 900$ s (i.e., ≈ 15 min, see Fig. 1c). Note that a mesh coated with a N-TiO₂/F-SiO₂ mixture with a higher concentration of N-TiO₂ exhibits a rapid decrease in the $\theta^*_{w,o}$ values. For example, a mesh coated with N-TiO₂/F-SiO₂ (75%) showed $\theta^*_{w,o} = 51^\circ \pm 3^\circ$ whereas that coated with N-TiO₂/F-SiO₂ (50%) exhibited $\theta^*_{w,o} = 75^\circ \pm 3^\circ$ at $t \approx 900$ s. Note that a mesh coated with N-TiO₂/F-SiO₂ (100%) can completely recover its inherent hydrophilic wettability. We also demonstrated that visible light illumination with a higher intensity can result in a rapid change in the $\theta^*_{w,o}$ values (SI Sect. 3).

Evolution of the water-rich permeate flux. The selective wettability for water over oil, along with its photocatalytic degradation capability enable our mesh to exhibit enhanced resistance to oil fouling and photocatalytic cleaning of the surface under light illumination when subjected to an oil–water mixture^{22,29}. A continuous cross-flow separation apparatus^{6,56} was utilized to conduct oil–water separation and in situ photocatalysis (Fig. 2a). Here, a feed oil–water mixture is continuously fed by a plunger pump and the water-rich permeate passes through the mesh and collected in a container. An n-hexadecane-in-water emulsion (1:9 volumetric ratio, n-hexadecane:water) stabilized by a surfactant (sodium dodecyl sulfate, SDS) was utilized (see “Methods”). Note that a mesh was prewetted by SDS-dissolved water (SDS concentration = 0.015 wt% with respect to water weight) for 30 min (flow rate = $2.0 \text{ L s}^{-1} \pm 0.2 \text{ L s}^{-1}$) to obtain a constant flux (J_0) for the water-rich permeate before introducing a feed emulsion. The transmembrane pressure (Δp , i.e., the difference in pressure at two opposite sides of the mesh) was maintained at $\Delta p = 13.0 \pm 0.5$ kPa for prewetting process.

When a feed oil-in-water emulsion was introduced ($\Delta p = 13.0 \pm 0.7$ kPa and flow rate = $2.0 \text{ L s}^{-1} \pm 0.1 \text{ L s}^{-1}$), the flux values (J) for the water-rich permeate rapidly decreased, which can be primarily attributed to fouling of the mesh surface by oil (Fig. 2b)^{3,6,15,39,57}. The results show that a mesh coated with N-TiO₂/F-SiO₂ with a higher concentration of N-TiO₂ exhibits a steeper decrease in the J values that eventually reaches lower values at $t = 90$ min. For example, a mesh coated with N-TiO₂/F-SiO₂ (50 wt%) exhibits $J \approx 261 \text{ L m}^{-2} \text{ h}^{-1}$ (LMH) while that coated with N-TiO₂/F-SiO₂ (75 wt%) shows $J \approx 253$ LMH at $t \approx 90$ min. Given that the J_0 values were ≈ 435 LMH and ≈ 441 LMH for a mesh coated with 50 wt% N-TiO₂ and 75 wt% N-TiO₂ respectively, they correspond to $\approx 60\%$ and $\approx 57\%$ of the respective J_0 values. Please note that the J values were measured by a relation⁵⁸, $J = \Delta m / (A \rho \Delta t)^{-1}$. Here, Δm represents the change in the water-rich permeate mass for a given time interval ($\Delta t = 5$ min), A is the projected area of the mesh ($A = 42 \text{ cm}^2$), and ρ is the density of the permeate ($\rho \approx 0.998 \text{ g cm}^{-3}$). Also note that

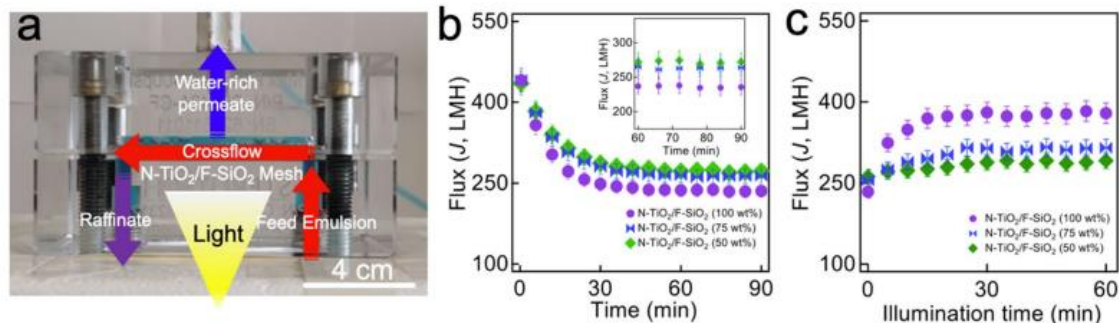


Figure 2. Evolution of water-rich permeate flux during continuous cross-flow separation of oil–water emulsion upon visible light illumination. **(a)** Photograph of the apparatus that enables continuous cross-flow separation of an oil–water mixture and in situ photocatalysis. (water is dyed blue and oil is dyed red). **(b)** The measured flux values (J) of the water-rich permeate through the mesh coated with various N-TiO₂/F-SiO₂ concentrations (50 wt%, 75 wt%, and 100 wt%) of N-TiO₂/F-SiO₂ mixture during separation of SDS-stabilized n-hexadecane-in-water emulsion (1:9 n-hexadecane:water volumetric ratio). The inset shows zoomed-in flux values in the time interval of 60–90 min. **(c)** The measured water-rich permeate flux values (J) while being illuminated by visible light ($I \approx 198 \text{ mW cm}^{-2}$).

the oil concentration in the water-rich permeate remains very low (i.e., <0.2 wt%) despite a decrease in water-rich permeate flux (SI Sect. 4).

When the water-rich permeate flux exhibited a constant value at $t = 90 \text{ min}$ (i.e., illumination time, $t_i = 0$), we started illuminating the mesh surface with visible light ($I \approx 198 \text{ mW cm}^{-2}$) while the mesh was continuously subjected to a fresh feed emulsion. Figure 2c shows that the J values start to increase upon visible light illumination. This indicates cleaning of the oil-contaminated mesh surface which consequently results in a lower breakthrough pressure (i.e., a minimum applied pressure at which the water permeates through the mesh) for the water-rich permeate^{3,6}. Also, a mesh coated with higher concentration of N-TiO₂ exhibited a higher recovery rate of the permeate flux values. For example, a mesh coated with N-TiO₂/F-SiO₂ (50 wt%) showed $J \approx 291 \text{ LMH}$ after 60 min of visible light illumination (i.e., $t_i = 60 \text{ min}$), whereas that coated with N-TiO₂/F-SiO₂ (75 wt%) showed $J \approx 315 \text{ LMH}$. This corresponds to 17% and 30% recovery.

Mathematical representation of the permeate flux kinetics. It is postulated that the extent of permeate flux recovery upon light illumination depends on various experimental parameters that include the incident light intensity (I), the active surface area (A) of the N-TiO₂/F-SiO₂ coating, and the photocatalytic degradation rate (k_p)⁵⁹. Here, we develop a mathematical model that can describe the time-dependent evolution of the water-rich permeate flux through a mesh coated with N-TiO₂/F-SiO₂ upon visible light illumination.

When a photocatalytic mesh surface is subjected to oil submerged in water while being illuminated by visible light, three chemical reactions can take place: adsorption, desorption, and photocatalytic degradation of oil molecules^{30,60–62}. We²² recently showed that these reactions obey the first-order kinetics. Assuming that N-TiO₂ is photocatalytic^{63–65} while F-SiO₂ is not⁶, the following differential equation can be obtained which describes a time-dependent photocatalysis-driven evolution of the area fraction of the mesh surface contaminated with oil ($f_c(t_i)$):

$$\frac{d}{dt}f_c(t_i) = f_T \times \frac{d}{dt}f_{c(T)}(t_i) + f_F \times \frac{d}{dt}f_{c(F)}(t_i) \quad (1)$$

where $f_{(T)}$ and $f_{(F)}$ are the area fraction of N-TiO₂ and F-SiO₂, respectively. The subscripts T and F symbolize N-TiO₂ and F-SiO₂, respectively. Solving Eq. (1) by substituting $\frac{d}{dt}f_{c(T)}(t_i) = k_{a(T)}f_{nc(T)} - k_{d(T)}f_{c(T)} - k_{p(T)}f_{c(T)}$ and $\frac{d}{dt}f_{c(F)}(t_i) = k_{a(F)}f_{nc(F)} - k_{d(F)}f_{c(F)}$, where k_a , k_d , and k_p are the rate constant values for adsorption, desorption, and photocatalytic degradation of oil, respectively, on a particular phase (e.g., N-TiO₂ or F-SiO₂), and $f_{nc(T)} = 1 - f_{c(T)}$ and $f_{nc(F)} = 1 - f_{c(F)}$ (i.e., non-contaminated area fraction of each phase, $f_{nc(T)}$ or $f_{nc(F)}$) results in:

$$f_c(t_i) = \left[\frac{k_{a(T)}}{K_{(T)}} - \left(\frac{k_{a(T)}}{K_{(T)}} - f_{c(T)}(t_i = 0) \right) e^{-(K_{(T)})t_i} \right] \times f_{(T)} + \left[\frac{k_{a(F)}}{K_{(F)}} - \left(\frac{k_{a(F)}}{K_{(F)}} - f_{c(F)}(t_i = 0) \right) e^{-(K_{(F)})t_i} \right] \times f_{(F)} \quad (2)$$

where $f_{c(T)}(t_i = 0)$ and $f_{c(F)}(t_i = 0)$ are the initial area fraction of the contaminated regions for N-TiO₂ and F-SiO₂ at the start of visible light illumination, respectively, which are assumed to be zero. Here $K_{(T)}$ and $K_{(F)}$ are defined as $K_{(T)} = k_{a(T)} + k_{d(T)} + k_{p(T)}$ and $K_{(F)} = k_{a(F)} + k_{d(F)}$, respectively.

The time-dependent flux of the water-rich permeate under visible light illumination ($J(t_i)$) can be written as⁵⁴:

$$J(t_i) = \Delta P / \left[(r_m + R_c / A(1 - f_c(t_i))) \mu \right] \quad (3)$$

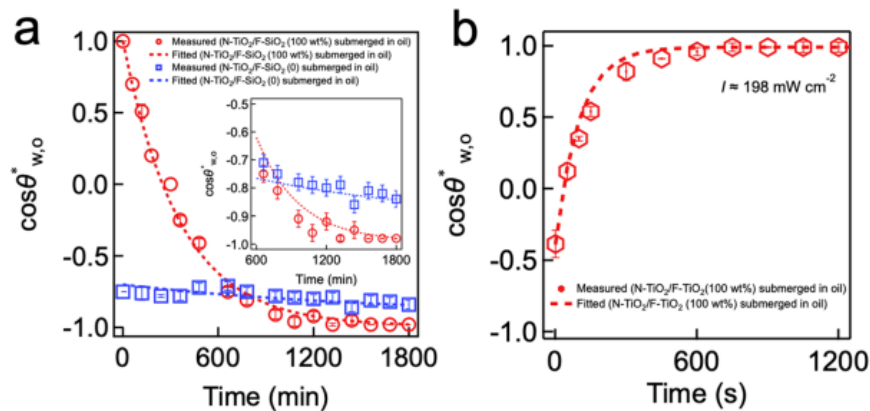


Figure 3. Extraction of adsorption, desorption, and photocatalytic rate constants. **(a)** Plots of the cosine values of the measured apparent water contact angle ($\theta^*_{w,o}$) on an N-TiO₂ surface and an F-SiO₂ surface submerged in oil (n-hexadecane) as a function of submerging time. The values of k_a and k_d for oil on N-TiO₂ and F-SiO₂ surfaces were determined by fitting Eq. (5). Inset: Zoomed-in plot of the $\cos\theta^*_{w,o}$ data. **(b)** A plot of the cosine values of the measured apparent water contact angle ($\theta^*_{w,o}$) on an N-TiO₂ surface submerged in oil as a function of visible light illumination ($I \approx 198 \text{ mW cm}^{-2}$) time. The k_p value for N-TiO₂ was determined by fitting Eq. (5).

where ΔP and A are the transmembrane pressure and the total surface area of the mesh, respectively. r_m and R_c are the resistance per unit area of the mesh to the permeation of the water-rich permeate originated from the mesh itself and oil contamination, respectively. μ is the dynamic viscosity of the water-rich permeate⁶⁶ ($\approx 0.953 \text{ mPa}\cdot\text{s}$). By substituting $f_c(t_i)$ in Eq. (3), we obtain the following equation:

$$J(t_i) = \Delta P / \left[r_m + \frac{R_c}{A} \times \left(1 - \left(\frac{k_a(T)}{K(T)} - \left(\frac{k_d(T)}{K(T)} - f_{c(T)}(t_i = 0) \right) e^{-(K(T)t_i)} \right) \times f_{(T)} + \left[\frac{k_a(F)}{K(F)} - \left(\frac{k_d(F)}{K(F)} - f_{c(F)}(t_i = 0) \right) e^{-(K(F)t_i)} \right] \times f_{(F)} \right) \right] \mu \quad (4)$$

This equation describes the time-dependent evolution of the water-rich permeate flux through the mesh subjected to oil upon illumination by visible light. Please note that the details of calculations for the variables (e.g., r_m , R_c , $f_{c(T)}$, and $f_{c(F)}$) in Eq. (4) are included in SI Sect. 5.

Extraction of rate constants and prediction of the flux. The values of k_a and k_d can be determined by analyzing the time-dependent evolution of the $\theta^*_{w,o}$ values in dark, whereas the k_p values can be determined under visible light illumination. In our recent work²², we demonstrated that these rate constants (k_a , k_d , and k_p) can be related to the measured $\theta^*_{w,o}$ values on a photocatalytic surface. Here, we develop a new relation by considering that our mesh surface is heterogenous consisting of photocatalytic N-TiO₂ and inert (i.e., non-catalytic) F-SiO₂. By integrating the Langmuir–Hinshelwood kinetics for photocatalysis^{22,30} and the Cassie–Baxter wettability analysis³³ on a chemically heterogeneous mesh surface, we can obtain a relation given as:

$$\cos\theta^*_{w,o} = 1 - 2 \left(\left[\frac{k_a(T)}{K(T)} - \left(\frac{k_d(T)}{K(T)} - f_{c(T)}(t_i = 0) \right) e^{-(K(T)t_i)} \right] \times f_{(T)} + \left[\frac{k_a(F)}{K(F)} - \left(\frac{k_d(F)}{K(F)} - f_{c(F)}(t_i = 0) \right) e^{-(K(F)t_i)} \right] \times f_{(F)} \right) \quad (5)$$

The values of k_a , k_d , and k_p for a given phase (e.g., N-TiO₂ or F-SiO₂) can be obtained by fitting Eq. (5) to the cosine values of the experimentally measured $\theta^*_{w,o}$ values. Figure 3a shows a plot of the cosine values of the experimentally measured $\theta^*_{w,o}$ on N-TiO₂ and F-SiO₂ surfaces submerged in oil as a function of submerging time. Note that we utilized the $\theta^*_{w,o}$ values of N-TiO₂/F-SiO₂ (100%) shown in Fig. 1b. We obtained the values of k_a and k_d for oil on an N-TiO₂ surface as $k_{a(T)} = 4.65 \times 10^{-5} \text{ s}^{-1}$ and $k_{d(T)} = 2.3 \times 10^{-7} \text{ s}^{-1}$, respectively, while those on an F-SiO₂ surface were $k_{a(F)} = 9.54 \times 10^{-6} \text{ s}^{-1}$ and $k_{d(F)} = 4.06 \times 10^{-7} \text{ s}^{-1}$, respectively. Please note that the k_a value for oil on an F-SiO₂ surface is an order of magnitude lower than that on an N-TiO₂ surface which clearly indicates that F-SiO₂ is more resistant to oil adsorption.

Similarly, the k_p value can be obtained by fitting Eq. (5) to the cosine values of the experimentally measured time-dependent $\theta^*_{w,o}$ on a surface that was submerged in oil and placed under visible light illumination (Fig. 3b). Note that the $\theta^*_{w,o}$ values of N-TiO₂/F-SiO₂ (100%) shown in Fig. 1c were utilized. The $k_{p(T)}$ value for N-TiO₂ is $9.8 \times 10^{-3} \text{ s}^{-1}$ which is two orders of magnitude higher than the $k_{a(T)}$ value ($k_{a(T)} = 4.65 \times 10^{-5} \text{ s}^{-1}$). Thus, it can be inferred that N-TiO₂ can rapidly clean itself upon visible light illumination despite being submerged in oil. Note that the k_p value for F-SiO₂ surface (i.e., $k_{p(F)}$) is zero. The k_p values for N-TiO₂ obtained by using different visible light intensities are also included in SI Sect. 6.

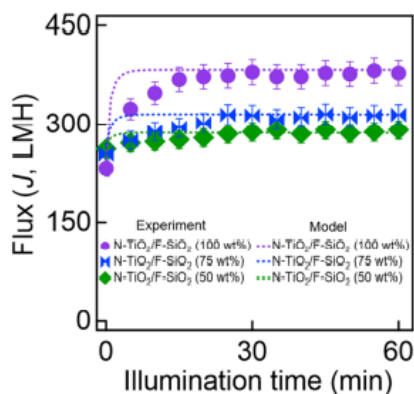


Figure 4. The measured and the predicted values of water-rich permeate flux (J) by using Eq. (4) through the meshes coated with varied compositions of N-TiO₂/F-SiO₂ under visible light illumination ($I = 198 \text{ mW cm}^{-2}$).

Finally, we calculated the $J(t_i)$ values for the mesh coated with varied compositions of N-TiO₂/F-SiO₂ by using the values of k_a , k_d , and k_p in Eq. (4) and compared them with the experimentally measured values. Figure 4 shows that they match reasonably well with a goodness of fit equal to 0.92.

Conclusions

In summary, a photocatalytic mesh with selective wettability for water over oil was developed by coating a mixture of N-TiO₂/F-SiO₂ onto a surface of a stainless steel mesh. The mesh was utilized to study the kinetics of the water-rich permeate flux as a result of the photocatalytic degradation of the surface-adsorbed oil under visible light illumination. A mathematical model was derived by integrating the Langmuir–Hinshelwood kinetics of photocatalysis and the Cassie–Baxter wettability analysis on a chemically heterogeneous surface into a permeate flux relation. Finally, this model demonstrated that it can predict the evolution of the water-rich permeate flux through the photocatalytic mesh with a goodness of fit of 0.92. We envision that the outcomes of this study can find applicability in designing and optimizing photocatalytic membranes for multiphase interfacial engineering applications such as oil–water separation.

Methods

Synthesis of N-TiO₂ and F-SiO₂ nanoparticles. N-TiO₂ and F-SiO₂ nanoparticles were synthesized by employing a modified sol–gel method according to the procedures in our previous work⁶. For N-TiO₂, titanium butoxide (TBOT, 5.0 g) was added dropwise to a mixture of isopropyl alcohol (IPA) and DI water (1:9 volumetric ratio, IPA:DI water). The pH of the solution was adjusted to 2.0 ± 0.1 by adding nitric acid (0.01 M). Subsequently, triethylamine with a molar ratio of 2.0 with respect to TBOT was added dropwise to the solution. After stirring the solution for 12 h at 30 °C, the precipitates were collected by centrifugation and thoroughly rinsed with ethanol and DI water. The product was vacuum dried to obtain N-TiO₂. For synthesizing F-SiO₂, tetraethyl orthosilicate (TEOS, 1.0 g) was mixed with a 0.01 M hydrochloric acid in DI water (100 g). 1H,1H,2H,2H-perfluorodecyl trichlorosilane (1.0 g) was then added to the mixture dropwise. The solution was magnetically stirred for 60 min at 60 °C, and the centrifugation was utilized to collect the resulting precipitates. The precipitates were then thoroughly rinsed with ethanol and DI water followed by vacuum drying to obtain F-SiO₂ nanoparticles.

Fabrication of photocatalytic mesh with selective wettability for water over oil. Stainless steel (SS) 316 Twill Dutch weave mesh (area = 42 cm²) was cleaned with ethanol in an ultrasonic bath for 10 min. The mesh was then dip-coated in a Norland ultraviolet (UV) light-curable optical adhesive (NOA 61) (1.0 wt% in acetone). Subsequently, a dispersion of N-TiO₂/F-SiO₂ mixture in DI water (solute concentration = 10 wt%) was sprayed (IWata Eclipse, Anest IWata) onto the adhesive-coated mesh for one minute. The spraying distance and nitrogen gas pressure were maintained at 15 cm and 200 kPa, respectively. The concentrations of N-TiO₂ nanoparticles in the N-TiO₂/F-SiO₂ mixture were 0, 25 wt%, 50 wt%, 75 wt%, and 100 wt%. The mesh was then illuminated by a long-wavelength UV light (100 W, $\lambda = 365 \text{ nm}$, UVA Blak-Ray B100A, Analytikjena) for 5 min to cure the adhesive. Finally, the fabricated photocatalytic mesh was thoroughly rinsed with ethanol and DI water.

Surfactant-stabilized oil-in-water emulsion. An oil-in-water emulsion was prepared by mixing n-hexadecane and DI water at 1:9 n-hexadecane:water volumetric ratio. Sodium dodecyl sulfate (SDS) surfactant (0.015 wt% with respect to water) was then added and mixed vigorously to stabilize the emulsion.

Scanning electron microscopy (SEM). The surface texture of a mesh coated with N-TiO₂/F-SiO₂ nanoparticles was characterized by field-emission scanning electron microscopy (FESEM, FEI Versa 3D). The characterizations were performed at an accelerating voltage of 10 kV.

Determining the nominal pore size of mesh. Filter retention analysis^{3,67} was utilized to determine the nominal pore size of the mesh. We sequentially fed monodisperse SiO₂ particles with various diameters to the mesh in the order of the lowest to the highest diameter. We calculated the proportion of the particles retained on the mesh for each diameter according to, $%R = M_R/M_T$, where M_R and M_T are the mass of SiO₂ retained on the mesh and the total mass of that introduced to the mesh, respectively. We assigned the diameter of SiO₂ as the nominal pore size of the mesh if %R exceeds 50% for that particular diameter. Note that we used SiO₂ particles with diameters of 120, 150, 200, 300, 400, 500, 600, and 750 nm and prepared suspensions in ethanol with a concentration of 50 mg mL⁻¹. We measured the %R as 66, 69, and 71% with the SiO₂ possessing a diameter of 400 nm for meshes coated with N-TiO₂/F-SiO₂ mixture with 50, 75 and 100 wt% of N-TiO₂, respectively. Therefore, 400 nm was assigned as the nominal pore size of meshes.

Contact angle measurement. All contact angle measurements were conducted by utilizing a Rame' hart 190-U1 goniometer. About 3 μ L of liquids were used during the measurements.

Visible light intensity measurement. To measure the intensity of the incident visible light on a mesh surface coated with N-TiO₂/F-SiO₂, a photometer (Fisherbrand Traceable DualDisplay Lightmeter) was employed. The photometer was placed underneath the top cover of the continuous cross-flow separation cell and illuminated by the visible light source. Please note that the visible light was illuminated onto the photometer from a distance of \approx 5 cm, which is the same as the distance between the light source and the mesh surface during the separation.

Root mean square (RMS) roughness measurements. Optical profiler (Veeco Wyko NT 1100) was utilized to measure the root mean square (RMS) surface roughness of coated meshes. The scan rate was set to 50 nm s⁻¹. The scanned area was 5 μ m \times 5 μ m.

Received: 19 August 2021; Accepted: 8 October 2021
Published online: 26 October 2021

References

1. Etchepare, R., Oliveira, H., Azevedo, A. & Rubio, J. Separation of emulsified crude oil in saline water by dissolved air flotation with micro and nanobubbles. *Sep. Purif. Technol.* **186**, 326–332 (2017).
2. Vocciant, M., Bagatin, R. & Ferro, S. Enhancements in electrokinetic remediation technology: Focus on water management and wastewater recovery. *Chem. Eng. J.* **309**, 708–716 (2017).
3. Ezazi, M. *et al.* Selective wettability membrane for continuous oil–water separation and in situ visible light-driven photocatalytic purification of water. *Global Chall.* **4**, 2000009 (2020).
4. Jiang, C. *et al.* Robust multifunctional superhydrophobic fabric with UV induced reversible wettability, photocatalytic self-cleaning property, and oil–water separation via thiol–ene click chemistry. *Appl. Surf. Sci.* **463**, 34–44 (2019).
5. Kota, A. K., Kwon, G., Choi, W., Mabry, J. M. & Tuteja, A. Hygro-responsive membranes for effective oil–water separation. *Nat. Commun.* **3**, 1–8 (2012).
6. Shrestha, B., Ezazi, M. & Kwon, G. Engineered nanoparticles with decoupled photocatalysis and wettability for membrane-based desalination and separation of oil–saline water mixtures. *Nanomaterials* **11**, 1397 (2021).
7. Song, S. *et al.* Underwater superoleophobic mesh based on BiVO₄ nanoparticles with sunlight-driven self-cleaning property for oil/water separation. *Chem. Eng. J.* **320**, 342–351 (2017).
8. Tetteh, E., Rathilal, S. & Naidoo, D. Photocatalytic degradation of oily waste and phenol from a local South Africa oil refinery wastewater using response methodology. *Sci. Rep.* **10**, 1–12 (2020).
9. Shenvi, S. S., Isloor, A. M. & Ismail, A. A review on RO membrane technology: Developments and challenges. *Desalination* **368**, 10–26 (2015).
10. Lutchmiah, K., Verliefe, A., Roest, K., Rietveld, L. C. & Cornelissen, E. Forward osmosis for application in wastewater treatment: A review. *Water Res.* **58**, 179–197 (2014).
11. Mohammad, A. W. *et al.* Nanofiltration membranes review: Recent advances and future prospects. *Desalination* **356**, 226–254 (2015).
12. Woo, S., Park, H. R., Park, J., Yi, J. & Hwang, W. Robust and continuous oil/water separation with superhydrophobic glass microfiber membrane by vertical polymerization under harsh conditions. *Sci. Rep.* **10**, 1–10 (2020).
13. Tummies, E. *et al.* Membrane fouling by emulsified oil: A review. *Sep. Purif. Technol.* **248**, 116919 (2020).
14. Guo, W., Ngo, H.-H. & Li, J. A mini-review on membrane fouling. *Biores. Technol.* **122**, 27–34 (2012).
15. Kovács, I., Veréb, G., Kertész, S., Hodúr, C. & László, Z. Fouling mitigation and cleanability of TiO₂ photocatalyst-modified PVDF membranes during ultrafiltration of model oily wastewater with different salt contents. *Environ. Sci. Pollut. Res.* **25**, 34912–34921 (2018).
16. Qahtan, T. F. *et al.* Thermally sensitized membranes for crude oil–water remediation under visible light. *ACS Appl. Mater. Interfaces.* **12**, 48572–48579 (2020).
17. Ali, I. & Gupta, V. Advances in water treatment by adsorption technology. *Nat. Protoc.* **1**, 2661–2667 (2006).
18. Zhang, W., Luo, J., Ding, L. & Jaffrin, M. Y. A review on flux decline control strategies in pressure-driven membrane processes. *Ind. Eng. Chem. Res.* **54**, 2843–2861 (2015).
19. Chen, J. P., Kim, S. & Ting, Y. Optimization of membrane physical and chemical cleaning by a statistically designed approach. *J. Membr. Sci.* **219**, 27–45 (2003).
20. Wang, Z. *et al.* Membrane cleaning in membrane bioreactors: A review. *J. Membr. Sci.* **468**, 276–307 (2014).

21. Zsirai, T., Buzatu, P., Aerts, P. & Judd, S. Efficacy of relaxation, backflushing, chemical cleaning and clogging removal for an immersed hollow fibre membrane bioreactor. *Water Res.* **46**, 4499–4507 (2012).
22. Panchanathan, D. *et al.* Kinetics of photoinduced wettability switching on nanoporous titania surfaces under oil. *Adv. Mater. Interfaces* **4**, 1700462 (2017).
23. Liu, Y., Su, Y., Li, Y., Zhao, X. & Jiang, Z. Improved antifouling property of PVDF membranes by incorporating an amphiphilic block-like copolymer for oil/water emulsion separation. *RSC Adv.* **5**, 21349–21359 (2015).
24. Zhang, L., Zhong, Y., Cha, D. & Wang, P. A self-cleaning underwater superoleophobic mesh for oil-water separation. *Sci. Rep.* **3**, 1–5 (2013).
25. Li, Y. *et al.* A robust salt-tolerant superoleophobic alginate/graphene oxide aerogel for efficient oil/water separation in marine environments. *Sci. Rep.* **7**, 1–7 (2017).
26. Kaner, P., Dudchenko, A. V., Mauter, M. S. & Asatekin, A. Zwitterionic copolymer additive architecture affects membrane performance: Fouling resistance and surface rearrangement in saline solutions. *J. Mater. Chem. A* **7**, 4829–4846 (2019).
27. Xie, A. *et al.* Photo-fenton self-cleaning membranes with robust flux recovery for an efficient oil/water emulsion separation. *J. Mater. Chem. A* **7**, 8491–8502 (2019).
28. Cheng, X. *et al.* Construction of superhydrophilic hierarchical polyacrylonitrile nanofiber membranes by in situ asymmetry engineering for unprecedentedly ultrafast oil–water emulsion separation. *J. Mater. Chem. A* (2020).
29. Nishimoto, S., Sawai, Y., Kameshima, Y. & Miyake, M. Underwater superoleophobicity of TiO₂ nanotube arrays. *Chem. Lett.* **43**, 518–520 (2014).
30. Foran, P. S., Boxall, C. & Denison, K. R. Photoinduced superhydrophilicity: A kinetic study of time dependent photoinduced contact angle changes on TiO₂ surfaces. *Langmuir* **28**, 17647–17655 (2012).
31. Yang, J. *et al.* Superhydrophilic–superoleophobic coatings. *J. Mater. Chem.* **22**, 2834–2837 (2012).
32. Zhu, X., Tu, W., Wee, K.-H. & Bai, R. Effective and low fouling oil/water separation by a novel hollow fiber membrane with both hydrophilic and oleophobic surface properties. *J. Membr. Sci.* **466**, 36–44 (2014).
33. Huo, J., Yuan, C. & Wang, Y. Nanocomposites of three-dimensionally ordered porous TiO₂ decorated with Pt and reduced graphene oxide for the visible-light photocatalytic degradation of waterborne pollutants. *ACS Appl. Nano Mater.* **2**, 2713–2724 (2019).
34. Lee, A. *et al.* Conformal nitrogen-doped TiO₂ photocatalytic coatings for sunlight-activated membranes. *Adv. Sustain. Syst.* **1**, 1600041 (2017).
35. Tan, B. Y. L., Juay, J., Liu, Z. & Sun, D. Flexible hierarchical TiO₂/Fe₂O₃ composite membrane with high separation efficiency for surfactant-stabilized oil-water emulsions. *Chem. Asian J.* **11**, 561–567 (2016).
36. Chalasani, R. & Vasudevan, S. Cyclodextrin-functionalized Fe₃O₄@TiO₂: Reusable, magnetic nanoparticles for photocatalytic degradation of endocrine-disrupting chemicals in water supplies. *ACS Nano* **7**, 4093–4104 (2013).
37. Gondal, M. A. *et al.* Fabrication and wettability study of WO₃ coated photocatalytic membrane for oil-water separation: A comparative study with ZnO coated membrane. *Sci. Rep.* **7**, 1–10 (2017).
38. Rajeswari, A., Vismaiya, S. & Pius, A. Preparation, characterization of nano ZnO-blended cellulose acetate-polyurethane membrane for photocatalytic degradation of dyes from water. *Chem. Eng. J.* **313**, 928–937 (2017).
39. Zhang, L. *et al.* Hierarchically stabilized PAN/β-FeOOH nanofibrous membrane for efficient water purification with excellent antifouling performance and robust solvent resistance. *ACS Appl. Mater. Interfaces.* **11**, 34487–34496 (2019).
40. Etman, A. S. *et al.* Facile water-based strategy for synthesizing MoO₃-x nanosheets: efficient visible light photocatalysts for dye degradation. *ACS Omega* **3**, 2193–2201 (2018).
41. Sonkusare, V. N. *et al.* Mesoporous octahedron-shaped tricobalt tetroxide nanoparticles for photocatalytic degradation of toxic dyes. *ACS Omega* **5**, 7823–7835 (2020).
42. Orooji, Y., Mohassel, R., Amiri, O., Sobhani, A. & Salavati-Niasari, M. Gd₂ZnMnO₇/ZnO nanocomposites: green sol-gel auto-combustion synthesis, characterization and photocatalytic degradation of different dye pollutants in water. *J. Alloys Compds.* **835**, 155240 (2020).
43. McCullagh, C., Skillen, N., Adams, M. & Robertson, P. K. Photocatalytic reactors for environmental remediation: A review. *J. Chem. Technol. Biotechnol.* **86**, 1002–1017 (2011).
44. Zhang, H., Wan, Y., Luo, J. & Darling, S. B. Drawing on membrane photocatalysis for fouling mitigation. *ACS Appl. Mater. Interfaces.* **13**, 14844–14865 (2021).
45. Zhang, H. *et al.* Visible-light-activated photocatalytic films toward self-cleaning membranes. *Adv. Funct. Mater.* **30**, 2002847 (2020).
46. Guo, J. *et al.* Self-cleaning BiOBr/Ag photocatalytic membrane for membrane regeneration under visible light in membrane distillation. *Chem. Eng. J.* **378**, 122137 (2019).
47. Liu, Y. *et al.* A novel strategy based on magnetic field assisted preparation of magnetic and photocatalytic membranes with improved performance. *J. Membr. Sci.* **612**, 118378 (2020).
48. Bortot Coelho, F. E., Gionco, C., Paganini, M. C., Calza, P. & Magnacca, G. Control of membrane fouling in organics filtration using Ce-doped zirconia and visible light. *Nanomaterials* **9**, 534 (2019).
49. Heu, R., Ateia, M. & Yoshimura, C. Photocatalytic nanofiltration membrane using Zr-MOF/GO nanocomposite with high-flux and anti-fouling properties. *Catalysts* **10**, 711 (2020).
50. Barmeh, A., Nilforoushan, M. R. & Otraj, S. Wetting and photocatalytic properties of Ni-doped TiO₂ coating on glazed ceramic tiles under visible light. *Thin Solid Films* **666**, 137–142 (2018).
51. Zhang, X. *et al.* Preparation and photocatalytic wettability conversion of TiO₂-based superhydrophobic surfaces. *Langmuir* **22**, 9477–9479 (2006).
52. Upadhaya, D., Kumar, P. & Purkayastha, D. D. Tuning the wettability and photocatalytic efficiency of heterostructure ZnO-SnO₂ composite films with annealing temperature. *Mater. Sci. Semicond. Process.* **95**, 28–34 (2019).
53. De Gennes, P.-G., Brochard-Wyart, F. & Quéré, D. *Capillarity and Wetting Phenomena: Drops, Bubbles, Pearls, Waves.* (Springer, 2013).
54. Coulson, J. M., Richardson, J. F., Backhurst, J. R. & Harker, J. H. *Chemical Engineering: Fluid Flow, Heat Transfer and Mass Transfer.* (Pergamon Press, 1954).
55. Tuteja, A., Choi, W., Mabry, J. M., McKinley, G. H. & Cohen, R. E. Robust omniphobic surfaces. *Proc. Natl. Acad. Sci.* **105**, 18200–18205 (2008).
56. Ezazi, M. *et al.* Selective Wettability membrane for continuous oil–water separation and in situ visible light-driven photocatalytic purification of water. *Glob. Challenges.* 2000009.
57. Li, Y. *et al.* Carboxylated Nanodiamond-enhanced photocatalytic membranes with improved antifouling and self-cleaning properties. *Ind. Eng. Chem. Res.* **59**, 3538–3549 (2020).
58. Darcy, H. *Les Fontaines Publiques de la Ville de Dijon: Exposition et Application.* (Victor Dalmont, 1856).
59. Mamane, H., Horovitz, I., Lozzi, L., Di Camillo, D. & Avisar, D. The role of physical and operational parameters in photocatalysis by N-doped TiO₂ sol–gel thin films. *Chem. Eng. J.* **257**, 159–169 (2014).
60. Mills, A., Wang, J. & Ollis, D. F. Dependence of the kinetics of liquid-phase photocatalyzed reactions on oxygen concentration and light intensity. *J. Catal.* **243**, 1–6 (2006).
61. Emeline, A. V., Ryabchuk, V. & Serpone, N. Factors affecting the efficiency of a photocatalyzed process in aqueous metal-oxide dispersions: Prospect of distinguishing between two kinetic models. *J. Photochem. Photobiol. A* **133**, 89–97 (2000).
62. Mills, A. & Le Hunte, S. An overview of semiconductor photocatalysis. *J. Photochem. Photobiol. A* **108**, 1–35 (1997).

63. Wetterer, S., Lavrich, D., Cummings, T., Bernasek, S. & Scoles, G. Energetics and kinetics of the physisorption of hydrocarbons on Au (111). *J. Phys. Chem. B* **102**, 9266–9275 (1998).
64. Pelizzetti, E. *et al.* Photocatalytic degradation of dodecane and of some dodecyl derivatives. *Anal. Chim.* **80**, 81–87 (1990).
65. Sturini, M., Soana, F. & Albini, A. Reaction paths in the titanium dioxide photocatalysed degradation of dodecane and some of its derivatives. *Tetrahedron* **58**, 2943–2950 (2002).
66. Cooper, J. & Dooley, R. *Release of the IAPWS Formulation 2008 for the Viscosity of Ordinary Water Substance*. (The International Association for the Properties of Water and Steam, 2008).
67. Bernhardt, I. C. *Particle Size Analysis: Classification and Sedimentation Methods*. Vol. 5. (Springer, 1994).

Acknowledgements

This research was supported by the National Science Foundation [award number: CBET-1944314], the U.S. Department of Interior-Bureau of Reclamation [award number: R17AC00132], and National Science Foundation RET Site: Exploring Career Opportunities through Water-Themed Engineering Research (ECO-WaTER) [award number: 1801710]. We also thank Dr. J. Kang at the University of Illinois and Dr. D. Ahn at the University of Texas for the use of facilities.

Author contributions

B.S. and M.E. performed the experiments, analyzed data, and wrote the manuscript. S.V.R. wrote the manuscript. G.K. conceived the project, designed the experiments, and wrote the manuscript.

Competing interests

The authors declare no competing interests.

Additional information

Supplementary Information The online version contains supplementary material available at <https://doi.org/10.1038/s41598-021-00607-w>.

Correspondence and requests for materials should be addressed to G.K.

Reprints and permissions information is available at www.nature.com/reprints.

Publisher's note Springer Nature remains neutral with regard to jurisdictional claims in published maps and institutional affiliations.



Open Access This article is licensed under a Creative Commons Attribution 4.0 International License, which permits use, sharing, adaptation, distribution and reproduction in any medium or format, as long as you give appropriate credit to the original author(s) and the source, provide a link to the Creative Commons licence, and indicate if changes were made. The images or other third party material in this article are included in the article's Creative Commons licence, unless indicated otherwise in a credit line to the material. If material is not included in the article's Creative Commons licence and your intended use is not permitted by statutory regulation or exceeds the permitted use, you will need to obtain permission directly from the copyright holder. To view a copy of this licence, visit <http://creativecommons.org/licenses/by/4.0/>.

© The Author(s) 2021

Paper P3




Delamination-Free In-Air and Underwater Oil-Repellent Filters for Oil-Water Separation:

Gravity-Driven and Cross-Flow Operations

Reproduced with permission from [**Shrestha, Bishwash**, Mohammadamin Ezazi, and Gibum Kwon], [Energies]; published by [Multidisciplinary Digital Publishing Institute], [2021].

Article

Delamination-Free In-Air and Underwater Oil-Repellent Filters for Oil-Water Separation: Gravity-Driven and Cross-Flow Operations

Bishwash Shrestha [†], Mohammadamin Ezazi [†] and Gibum Kwon ^{*}

Department of Mechanical Engineering, University of Kansas, Lawrence, KS 66045, USA;

bishwashes@ku.edu (B.S.); aminezazi@ku.edu (M.E.)

* Correspondence: gbkwon@ku.edu

† Indicating equal contributions.



Citation: Shrestha, B.; Ezazi, M.; Kwon, G. Delamination-Free In-Air and Underwater Oil-Repellent Filters for Oil-Water Separation: Gravity-Driven and Cross-Flow Operations. *Energies* **2021**, *14*, 7429. <https://doi.org/10.3390/en14217429>

Academic Editor: Gustavo Fimbres Weihs

Received: 22 September 2021

Accepted: 2 November 2021

Published: 8 November 2021

Publisher's Note: MDPI stays neutral with regard to jurisdictional claims in published maps and institutional affiliations.



Copyright: © 2021 by the authors. Licensee MDPI, Basel, Switzerland. This article is an open access article distributed under the terms and conditions of the Creative Commons Attribution (CC BY) license (<https://creativecommons.org/licenses/by/4.0/>).

Abstract: Separating oil-water mixtures is critical in a variety of practical applications, including the treatment of industrial wastewater, oil spill cleanups, as well as the purification of petroleum products. Among various methodologies that have been utilized, membranes are the most attractive technology for separating oil-water emulsions. In recent years, selective wettability membranes have attracted particular attention for oil-water separations. The membrane surfaces with hydrophilic and in-air oleophobic wettability have demonstrated enhanced effectiveness for oil-water separations in comparison with underwater oleophobic membranes. However, developing a hydrophilic and in-air oleophobic surface for a membrane is not a trivial task. The coating delamination process is a critical challenge when applying these membranes for separations. Inspired by the above, in this study we utilize poly(ethylene glycol)diacrylate (PEGDA) and 1H,1H,2H,2H-heptadecafluorodecyl acrylate (F-acrylate) to fabricate a hydrophilic and in-air oleophobic coating on a filter. We utilize methacryloxypropyl trimethoxysilane (MEMO) as an adhesion promoter to enhance the adhesion of the coating to the filter. The filter demonstrates robust oil repellency preventing oil adhesion and oil fouling. Utilizing the filter, gravity-driven and continuous separations of surfactant-stabilized oil-water emulsions are demonstrated. Finally, we demonstrate that the filter can be reused multiple times upon rinsing for further oil-water separations.

Keywords: surfactant-stabilized oil-water emulsions; in-air and underwater oleophobic filter; gravity-driven oil-water separation; coating robustness

1. Introduction

Oil-water separation is a crucial step in a wide variety of industries [1,2]. For example, 140,000 L of oil-contaminated water is produced during conventional mining operations on a daily basis [3]. Additionally, oil leakage and spillage during marine transportation not only pose a threat to the marine environment and ecosystem but is a waste of valuable natural resources [4,5]. Typically, an oil-water mixture can be classified into three categories based on the dispersed phase size (diameter, d)-as free oil-water, if $d > 150 \mu\text{m}$, as a dispersion if $20 \mu\text{m} < d < 150 \mu\text{m}$, or as an emulsion if $d < 20 \mu\text{m}$ [6]. Oil-water emulsions are stable in the presence of the adsorbed interface-active chemicals (e.g., surfactant) [7]. Spontaneous separation of stable oil-water emulsions can be impractically time-consuming. Further, the separation process becomes more challenging with the decrease in the size of the dispersed phase [8].

There have been extensive efforts devoted to developing effective separation technologies for oil-water emulsions [8]. Membrane-based technologies are the most attractive because they can separate oil and water without requiring chemical additives [9–14]; thus, they are relatively energy-saving and applicable to a broad range of industrial effluents [15–17]. The working principle and operation of these technologies are simple. A

membrane can regulate the transportation of two phases (e.g., oil and water) by allowing the selective passage of one phase while inhibiting the permeation of another phase [18,19]. Various methods have been employed to enable the permeation of one phase through a membrane while repelling another phase. For example, a careful modulation of the applied pressure can overcome the hydraulic resistance of one phase while being insufficient for another phase [11,14,20,21]. Additionally, we [20,21] and others [22–24] have demonstrated that a water-in-oil emulsion can be demulsified upon applying an electric field due to the coalescence of the dispersed water droplets. The resulting free oil and water can be readily separated under gravity.

While membranes have become an industry benchmark to compare the performance of conventional separation technologies, they are limited by fouling when continuously operated [13,14,25–27]. When a membrane is subjected to an oil-water mixture, oils and organic substances are deposited onto its surface. This membrane fouling can result in a decrease in permeability over time [28]. To compensate for this compromised performance, membrane operation often requires an increase in the applied trans-membrane pressure (i.e., TMP, the pressure gradient generated across the two opposite membrane sides [29]), which results in an increase in the energy consumption [30]. In some instances, the oil-water mixture treatment system becomes oversized to compensate for the permeate flux loss [30]. Further, due to fouling, membranes undergo periodic cleaning protocols that include backwashing, forward washing, and chemically enhanced cleaning to restore membrane permeability [31]. Although these cleaning protocols allow a membrane to restore its inherent permeability and selectivity, they may shorten the membrane's lifespan due to mechanical or chemical damage [32,33].

The development of fouling-resistant membranes has been an active research topic for decades [34,35]. A membrane with hydrophilic (i.e., water contact angle, $\theta_{\text{water}} < 90^\circ$) or superhydrophilic ($\theta_{\text{water}} = 0^\circ$) wettability can retain a hydration layer on its surface when subjected to water, which can reduce the adhesion of organic substances such as oil [20,36]. While these membranes show resistance to oil fouling, they become vulnerable when a hydration layer disappears [37]. For example, the hydration layer can be evaporated or compromised due to a large exerted drag force (e.g., applied pressure), which results in direct contact and deposition of an oily phase on the membrane surface [38,39].

Hydrophilic and in-air oleophobic (i.e., oil contact angle, $\theta_{\text{oil}} > 90^\circ$) membranes can overcome this limitation by providing oil repellency, not only underwater, but also in the air [20,40]. This enables them to exhibit unique features in oil-water separations. For example, there is no need to prewet the membrane to introduce a hydration layer. Additionally, water-in-oil emulsions can be separated without prewetting, as long as the breakthrough pressure for oil (P_b , i.e., the lowest applied pressure required to force a liquid permeation through a porous filter) is higher than the operating pressure.

Fabricating a hydrophilic and in-air oleophobic membrane requires one to reconcile two conflicting design criteria. It should possess low solid surface energy to repel oil, while water should wet the surface. Given that the water surface tension ($\gamma_{\text{lv}} = 72.1 \text{ mN m}^{-1}$, $T = 22^\circ\text{C}$) is higher than that of oils ($\gamma_{\text{lv}} = 20\text{--}30 \text{ mN m}^{-1}$, $T = 22^\circ\text{C}$), a large volume of reports [9,41–46] have utilized materials composed of a low surface energy component along with a hydrogen-bond-capable hydrophilic moiety as the membrane coating to achieve selective wettability for water over oil [20,47–51]. For example, Brown et al [52] utilized a fluorosurfactant as a low surface energy material and poly(diallyl dimethylammonium chloride) (PDDA) for hydrophilic moieties. Yang et al [49] fabricated a membrane coated with a mixture of PDDA, chitosan, and perfluorooctanoic acid (PFOA). These surfaces often exhibit selective reconfiguration of the coating components. Upon contact with water, a hydrophilic component will expand to the surface for enthalpic gain, while a low surface energy material (e.g., fluorinated moiety) minimizes its contact with water [20,47]. When oil comes into contact, the surface reverts back to its inherent configuration to lower the overall free energy.

Utilizing surface reconfiguration, herein we report on a superhydrophilic and in-air oleophobic filter by grafting a composite mixture of poly(ethylene glycol)diacrylate (PEGDA) and 1H,1H,2H,2H-heptadecafluorodecyl acrylate (F-acrylate) via silane chemistry. This enables the resulting coating (F-PEGDA) to firmly attach to the filter surface. The filter exhibits ultralow oil adhesion forces, both in air and underwater, which results in resistance to oil fouling during oil-water separation. Utilizing this filter, separation of surfactant-stabilized oil-in-water and water-in-oil emulsions is demonstrated. Finally, we demonstrate that the filter can be reused multiple times upon cleansing for further oil-water separations.

2. Result and Discussion

We fabricated a hydrophilic and in-air oleophobic filter by coating it with F-PEGDA, utilizing filters with nominal pore sizes of 6.0 μm and 2.0 μm (Experimental Section). Note that we utilized varying compositions of PEGDA and F-acrylate, while the photoinitiator concentration remained at 5.0 wt.% with respect to the mass of the PEGDA and F-acrylate mixture. The filters were irradiated by a long-wavelength ultraviolet (UV) light, which resulted in the grafting of F-PEGDA to the MEMO-treated filter surface (Figure 1a and Section S1). We analyzed the filter surface's morphology using scanning electron microscopy (SEM) (Figure 1b). It was clear that the surface morphology remained nearly unaffected after coating with F-PEGDA. Additionally, the uniform coating of F-PEGDA on the filter surface was verified by the energy-dispersive spectroscopy (EDS) analysis. The EDS elemental mapping demonstrated a uniform coverage of fluorine (F) across the filter surface (Figure 1b, insets).

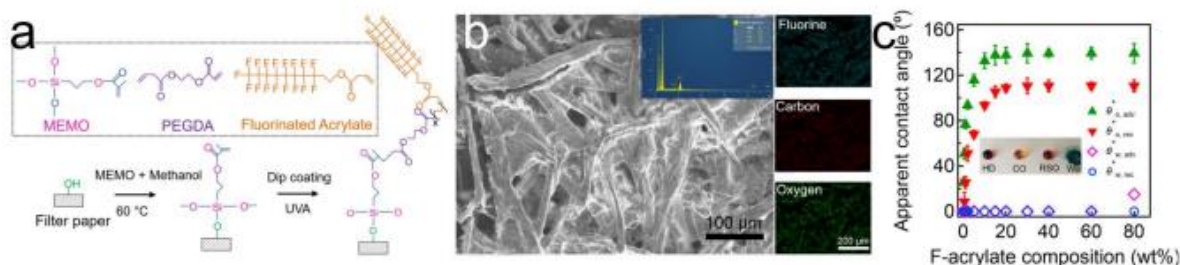


Figure 1. (a) Schematic demonstrating the grafting of the filter surface with MEMO and the subsequent coating with F-PEGDA. (b) SEM image showing the morphology of the filter after coating with F-PEGDA (20 wt.%). Inset shows the elemental EDS spectrum and the elemental mappings for fluorine. (c) The measured apparent advancing and receding contact angles of water and oil (n-hexadecane) on the F-PEGDA-coated filter surface with varied compositions of F-acrylate. A filter with a 6.0 μm inherent nominal pore size was used.

It is critical to ensure that the F-PEGDA coating has a negligible effect on the pore size of the filters. We measured the nominal pore size of the filters after coating with F-PEGDA (Table 1). The results indicated that filters coated with F-PEGDA with a higher PEGDA composition demonstrate more decreased pore sizes. For example, the filter coated with F-PEGDA with 20 wt.% F-acrylate (F-PEGDA (20 wt.%)) exhibited a pore size of $5.0 \mu\text{m} \pm 0.5 \mu\text{m}$, while the filter coated with F-PEGDA (80 wt.%) showed $5.5 \mu\text{m} \pm 0.5 \mu\text{m}$. We attributed this to an increase in the viscosity of the coating solution with an increase in the PEGDA composition (i.e., decrease in the F-acrylate composition), which resulted in an increase in the coating thickness (Section S2).

Table 1. Pore size of as-purchased filters and those coated with F-PEGDA with various F-acrylate compositions.

Filter	Pore Size	
	6.0 μm	2.0 μm
As-purchased	6.0 μm	2.0 μm
F-PEGDA (0)	4.8 \pm 0.5 μm	0.9 \pm 0.2 μm
F-PEGDA (5 wt.%)	4.8 \pm 0.3 μm	0.9 \pm 0.1 μm
F-PEGDA (10 wt.%)	4.9 \pm 0.3 μm	1.0 \pm 0.1 μm
F-PEGDA (15 wt.%)	5.0 \pm 0.4 μm	1.0 \pm 0.3 μm
F-PEGDA (20 wt.%)	5.0 \pm 0.3 μm	1.0 \pm 0.4 μm
F-PEGDA (40 wt.%)	5.2 \pm 0.5 μm	1.2 \pm 0.2 μm
F-PEGDA (60 wt.%)	5.3 \pm 0.5 μm	1.4 \pm 0.3 μm
F-PEGDA (80 wt.%)	5.5 \pm 0.4 μm	1.5 \pm 0.5 μm
F-PEGDA (100 wt.%)	5.6 \pm 0.1 μm	1.6 \pm 0.5 μm

The wettability of our F-PEGDA-coated filters was analyzed by measuring the apparent contact angles for water (deionized (DI) water, $\gamma_{lv} = 72.1 \text{ mN m}^{-1}$, $T = 22 \text{ }^\circ\text{C}$) and oil (n-hexadecane, $\gamma_{lv} = 27.5 \text{ mN m}^{-1}$, $T = 22 \text{ }^\circ\text{C}$) in the air (Figure 1c). The results showed that the filter (inherent nominal pore size = 6.0 μm) coated with F-PEGDA with a higher F-acrylate composition exhibited higher oil apparent contact angles. When the composition reached 20 wt.%, the advancing ($\theta_{oil,adv}^*$) and receding ($\theta_{oil,rec}^*$) apparent contact angles for oil were measured as $131^\circ \pm 3^\circ$ and $108^\circ \pm 3^\circ$, respectively, while those for water remained at zero ($\theta_{water,adv}^* = 0$ and $\theta_{water,rec}^* = 0$). Further increases in the F-acrylate composition in F-PEGDA had a negligible effect on the oil apparent contact angles, which can be attributed to the complete coverage of the filter surface by F-acrylate (see also Figure 1b inset). When the F-acrylate composition reached 80 wt.% in the F-PEGDA coating, the value for $\theta_{water,adv}^*$ reached $25^\circ \pm 3^\circ$. We attributed this to the reduced presence of -OH moieties, which are responsible for inducing hydrophilicity and creating more fluorine moieties, which are responsible for omniphobic wettability.

In previous reports, we [20] and others [47,53,54] have shown that a water droplet can gradually wet the surface with hydrophilic and in-air oleophobic wettability due to surface reconfiguration. The required time for a water droplet to completely spread on a given reconfigurable surface is defined as the time of wetting (ToW) [20]. The measured initial contact angles and the time of wetting for water on our F-PEGDA surfaces are included in Section S3. We also calculated the solid surface energy (γ_{sv}) values of the F-PEGDA surfaces (Section S4). Furthermore, the measured apparent contact angles for water and oil on the filters with an inherent nominal pore size of 2.0 μm are included in Section S5. Based on these results, a filter coated with 20 wt.% of F-acrylate (F-PEGDA (20 wt.%)) was utilized for the rest of the study.

We measured the adhesion force of a sessile oil droplet on the filters submerged in DI water using a high-precision microelectromechanical system (Figure 2a, see also Experimental Section). The results showed that the adhesion force values were nearly constant ($\approx 1.32 \mu\text{N} \pm 0.10 \mu\text{N}$) on filters with an inherent nominal pore size of 6.0 μm , which were coated with F-PEGDA, irrespective of the F-acrylate composition. Note that the adhesion force value measured on the neat PEGDA-coated filter was slightly lower ($1.27 \mu\text{N} \pm 0.10 \mu\text{N}$), while that measured on the neat F-acrylate-coated filter was slightly higher ($1.45 \mu\text{N} \pm 0.10 \mu\text{N}$). The measured adhesion forces of an oil droplet on a filter with an inherent nominal pore size of 2.0 μm are also demonstrated in Figure 2a. This ultralow oil adhesion was a direct consequence of the underwater superoleophobic wettability (i.e., apparent oil contact angle $> 150^\circ$ on a surface submerged in water) (Section S6). Additionally, the experimental results regarding water uptake by F-PEGDA-coated filters are provided in Section S7.

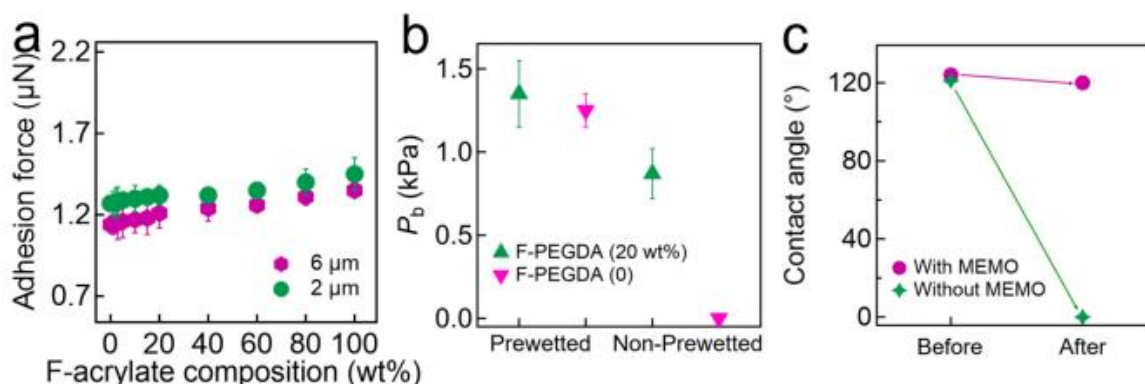


Figure 2. (a) The measured adhesion force of a sessile oil (n-hexadecane) droplet on the filter surfaces coated with F-PEGDA with various F-acrylate concentrations. (b) The breakthrough pressure of oil on prewetted and dry filters coated with F-PEGDA (20 wt.%). The data obtained from a filter coated with neat PEGDA are also provided for comparison. (c) The measured apparent contact angles of oil on the F-PEGDA (20 wt.%), which was prepared with MEMO before and after being submerged in water for 1 h. For comparison, the data for F-PEGDA (20 wt.%) prepared without MEMO are also shown.

Filters exhibiting hydrophilic and in-air oleophobic wettability do not need to undergo prewetting in order to introduce a hydration layer before conducting oil-water separation. This is because the in-air superoleophobic wettability plays a key role in resistance to oil adhesion on the surface by repelling it [38]. In contrast, an in-air superoleophilic surface such as a neat PEGDA-coated filter or an unmodified filter allows oil to wet and adhere to the surface.

We measured the breakthrough pressure (P_b) for oil of an F-PEGDA-coated filter. It was observed that filters coated with F-PEGDA (20 wt.%) and with neat PEGDA (i.e., F-PEGDA (0)) can both exhibit high P_b values for oil. For example, a filter coated with F-PEGDA (20 wt.%) exhibited $P_b = 1.35 \pm 0.2$ kPa while another filter coated with neat PEGDA showed $P_b = 1.25 \pm 0.1$ kPa when they were prewetted (Figure 2b). When the filters were dry, the neat PEGDA-coated filter immediately allowed oil to pass through ($P_b \approx 0$), whereas the filter coated with F-PEGDA (20 wt.%) maintained a breakthrough pressure of $P_b = 0.87 \pm 0.2$ kPa.

Filters grafted with MEMO can prevent delamination of the F-PEGDA coating from the surface after being submerged in water. To test this, we measured the apparent contact angles of in-air oil on a filter coated with F-PEGDA after being submerged in DI water for 1 h. For comparison, we conducted the same experiment using a filter without MEMO grafting. The results showed that the apparent contact angles of oil remained almost unchanged on the filters coated with MEMO and F-PEGDA, while those on the filter without MEMO grafting equaled zero (Figure 2c). This was the direct consequence of delamination of the F-PEGDA coating from the filter surface (Section S8). Consequently, the oil droplet contacts the underlying filter surface and completely wets it due to the absence of fluorine on the filter surface.

Using our hydrophilic and in-air oleophobic filter, we separated oil-water mixtures under gravity. Here, we utilized a surfactant-stabilized oil-in-water emulsion (10 vol% n-hexadecane in water) and a water-in-oil emulsion (90 vol% water in n-hexadecane) (see Experimental Section and Section S9). The separation apparatus consisted of two vertical tubes and a filter coated with F-PEGDA (20 wt.%), which was sandwiched between them. Here, we utilized a filter with an inherent nominal pore size of 6.0 μm . Upon introducing an emulsion (15 mL) into an upper tube, a filter allows the water-rich phase to permeate through, while the oil-rich phase is retained above it within 11.2 ± 2 min (Figure 3a). We also calculated the flux ($J = \Delta m(A\rho\Delta t)^{-1}$, where Δm is the mass change of the water-rich permeate in a given time interval (i.e., $\Delta t = 1$ min), A is the projected area of the filter surface, and ρ is the permeate density) values by periodically measuring the volume of

the water-rich permeate through filters pretwetted with water for 30 min. The results for the oil-in-water emulsion showed that the permeate flux gradually declined from $J(t = 0) = 261 \pm 10 \text{ L m}^{-2} \text{ h}^{-1}$ and reached $J(t = 10 \text{ min}) = 245 \pm 10 \text{ L m}^{-2} \text{ h}^{-1}$. This can be attributed to the decreased height of the emulsion column as the water-rich phase permeated through the filter, which resulted in a decrease in the exerted pressure. The filter also separated the water-in-oil emulsion in $13.1 \pm 2 \text{ min}$. Similarly, the permeate flux values were determined as $J(t = 0) = 242 \pm 10 \text{ L m}^{-2} \text{ h}^{-1}$ and $J(t = 10 \text{ min}) = 225 \pm 10 \text{ L m}^{-2} \text{ h}^{-1}$. Note that almost all water droplets dispersed in an emulsion can come into contact with the filter surface under gravity. For comparison, we conducted the same experiments using a filter coated with F-PEGDA (0) after pretwetting with water for 30 min. The results showed that the filter can separate both oil-in-water and water-in-oil emulsions in $11.9 \pm 2 \text{ min}$ and $13.5 \pm 2 \text{ min}$, respectively (Figure 3a). The permeate flux values were measured as $J(t = 10 \text{ min}) = 239 \pm 10 \text{ L m}^{-2} \text{ h}^{-1}$ and $J(t = 10 \text{ min}) = 219 \pm 10 \text{ L m}^{-2} \text{ h}^{-1}$ for the separation of the oil-in-water and water-in-oil emulsions, respectively.

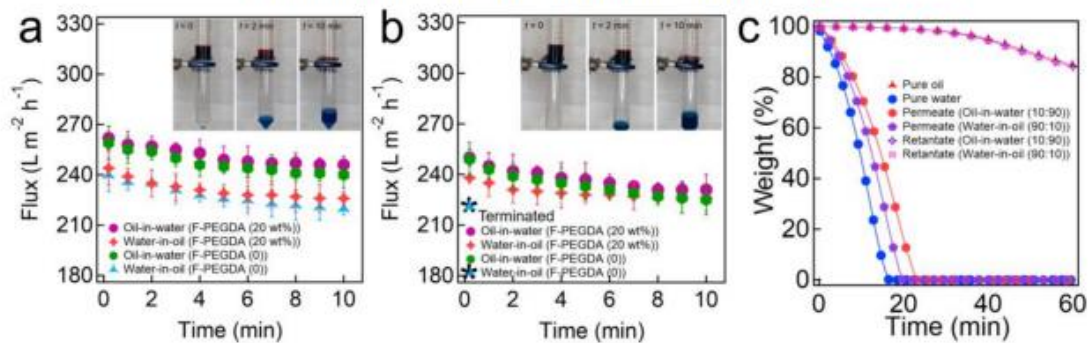


Figure 3. (a–c) Time-dependent flux measurements during the separation of oil-water mixtures under gravity by (a) pretwetted and (b) dry filters coated with F-PEGDA (20 wt.%) and neat PEGDA. The inset shows images of the oil-water separation experiments with oil-in-water emulsions by utilizing a filter coated with F-PEGDA (20 wt.%). (c) The TGA plots of the permeate and retentates after the separation of both oil-in-water and water-in-oil emulsions using a filter coated with F-PEGDA (20 wt.%). The TGA data for pure water and oil are also shown for comparison.

When a filter coated with F-PEGDA (0) is subjected to a water-in-oil emulsion without pretwetting, both oil and water immediately pass through. Note that the filter exhibited similar separation performance for the oil-in-water emulsion (Figure 3b). This is attributed to the water as a continuous medium in the emulsion, which provides a hydration layer on the filter surface and prevents oil droplets from permeating. The filter coated with F-PEGDA (20 wt.%) exhibited similar water-rich permeate flux values for both oil-in-water and water-in-oil emulsions ($J(t = 10 \text{ min}) = 231 \pm 10 \text{ L m}^{-2} \text{ h}^{-1}$ and $J(t = 10 \text{ min}) = 222 \pm 20 \text{ L m}^{-2} \text{ h}^{-1}$). Figure 3c shows the TGA plots of the permeates and retentates after the separation experiments for oil-in-water and water-in-oil emulsions using a filter coated with F-PEGDA (20 wt.%). The results showed that our filter can separate both oil-in-water and water-in-oil emulsions with very high efficiency (>98%). Please note that our F-PEGDA filter surfaces after the separation remained clean (i.e., no fouling). We attributed this to a combinatorial effect of fouling resistance due to hydrophilic wettability and a relatively lower surfactant concentration (0.03 wt.%, see Experimental Section). It is anticipated that our F-PEGDA-coated filter surface may suffer from a cake layer when it is subjected to emulsions stabilized by high-concentration surfactants [55–57]. Additionally, it should be noted that the surfactants used in this study were either anionic (sodium dodecyl sulfate for the oil-in-water emulsion) or nonionic (Tween 80 for the water-in-oil emulsion). Given that the zeta potential (ζ) value of our F-PEGDA (20 wt.%) coated filter surface was measured as $-0.83 \text{ mV} \pm 0.19 \text{ mV}$, it is anticipated that our filter may be fouled by emulsions stabilized with cationic or amphoteric surfactants [55,58,59].

Finally, we continuously separated an oil-in-water emulsion utilizing a cross-flow apparatus (Experimental Section). An emulsion (total volume = 20 L) was gradually introduced into a cell in which a filter (inherent nominal pore size = 6.0 μm , coated with F-PEGDA (20 wt.%) was mounted. We measured the volume of the water-rich permeates every 5 min for the entire 60 min of operation. The TMP value was maintained at $0.90 \text{ kPa} \pm 0.20 \text{ kPa}$. The results showed that $J(t = 0) = 285 \pm 10 \text{ L m}^{-2} \text{ h}^{-1}$, after which it declined and reached $J(t = 60 \text{ min}) = 210 \pm 10 \text{ L m}^{-2} \text{ h}^{-1}$ (Figure 4a). We conducted the same experiments using a filter with an inherent nominal pore size of 2.0 μm . The results showed that $J(t = 0) = 245 \pm 10 \text{ L m}^{-2} \text{ h}^{-1}$, after which it declined over time and reached $J(t = 60 \text{ min}) = 176 \pm 10 \text{ L m}^{-2} \text{ h}^{-1}$. Unlike the flux decline during batch separation, which was primarily caused by a decrease in the exerted pressure (see Figure 3a,b), the continuous separation was conducted at a constant TMP. Therefore, we attributed the flux decline to the oil droplet accumulation above the membrane surface [4]. Although our filter exhibits very low oil adhesion forces (see Figure 2a), oil can still accumulate on the surfaces and pore walls due to transmembrane pressure. The accumulation of oil can cause pore blockages. As a consequence, the volume of water passing through the filter in a given period of time (i.e., permeate flux) decreases. This results in a decline of the flux. We cleaned the filter by first rinsing it with ethanol for 10 s followed by washing it with DI water for 30 s (flow rate $\approx 20.0 \text{ L min}^{-1}$). The cleansed filter was subjected to the same separation experiments. The results showed that the filter nearly recovered its inherent flux values (Figure 4b). An analysis of the separation efficiency is included in Section S10. The flux values for the continuous separation experiment over 50 h are presented in Section S11.

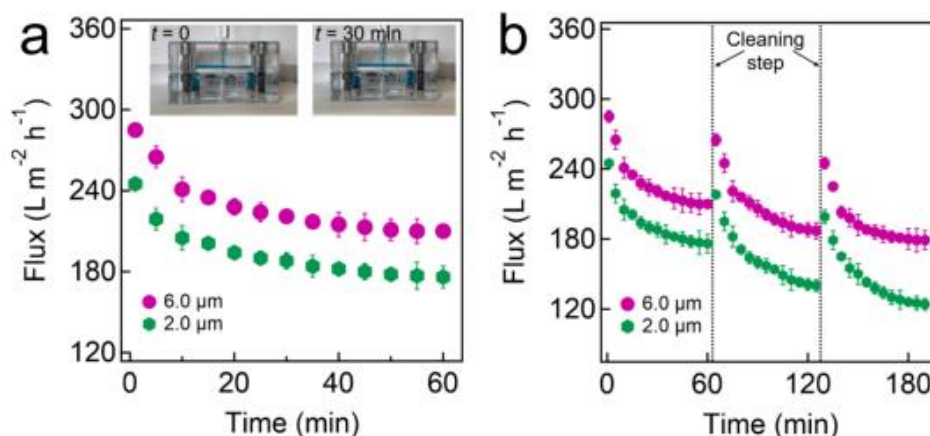


Figure 4. (a) Time-dependent flux measurements during the continuous separation of oil-water mixtures using pretreated filters with various inherent nominal pore sizes, which were coated with F-PEGDA (20 wt.%). The inset demonstrates the separation experiment using a cross-flow apparatus. (b) Time-dependent flux measurements during the continuous separation of oil-in-water emulsion with cleaning steps in between.

3. Conclusions

In this work, we prepared robust hydrophilic and in-air oleophobic F-PEGDA-coated filters to separate oil-water mixtures. We utilized MEMO as an adhesion promoter to enhance coating adhesion to the filter. The prepared surfaces were then subjected to fouling conditions representative of conventional oil-water separation applications. The results of the study demonstrated that the F-PEGDA-coated filter showed low oil adhesion forces and was able to withstand fouling conditions without delamination. Subsequently, gravity-driven oil-water separations were conducted by utilizing oil-in-water and water-in-oil emulsions. The F-PEGDA-coated filter was able to separate both emulsions and maintained high flux values, while the filter with underwater oleophobicity failed to separate the water-

in-oil emulsion, highlighting the advantages of in-air oleophobicity. Further, the F-PEGDA surface demonstrated good reusability upon cleansing.

4. Experimental Section

Grafting MEMO on filter surface: The filters (6 μm (Whatman Grade 3, Whatman, Marlborough, MA, USA) and 2 μm (Whatman Grade 602 h)) were rinsed with DI water followed by drying at room temperature. They were dip-coated in a 10 wt.% methacryloxypropyl trimethoxysilane (MEMO) solution in methanol for 30 min. Subsequently, the dip-coated filters were heated using a hot plate at 60° C for 1 h. Finally, the filters were thoroughly rinsed using DI water and ethanol to remove any unreacted MEMO molecules.

Coating F-PEGDA on filter: A solution of F-PEGDA was prepared by adding PEGDA, F-acrylate, and Darokur 1173 (Photo-initiator) to water with an overall concentration of 30 mg ml⁻¹. The MEMO-grafted filters were then dip-coated in F-PEGDA solution for 30 min. Varying compositions of PEGDA and F-acrylate (i.e., 0, 20, 40, 60, 80, and 100 wt.% of F-acrylate) were utilized. Note that the concentration of Darocur 1173 was maintained at 5.0 wt.% with respect to the PEGDA and F-acrylate mixture. Consequently, the filters were removed and exposed to UV light (100 W, $\lambda = 365$ nm, Analytikjena, Upland, CA, USA) for 5 min.

Measuring pore size of filters: A capillary flow porometer (Particle Technology Labs, Downers Grove, IL, USA) was utilized to measure the nominal size and the distribution of the filter pores, as described elsewhere [60]. A commercial wetting liquid (Porefil) was utilized to wet the filter. The nitrogen gas pressure and flow were controlled and recorded using a pressure transducer and a flow meter, respectively.

Contact angle measurements: A Ramé-Hart 200-F1 goniometer (Ramé-Hart, Succasunna, NJ, USA) was employed to measure the advancing and receding contact angles of liquid droplets (≈ 5 μL) on the filter surfaces. The initial advancing contact angle for water was measured based on the instantaneous value observed when a water droplet first contacted a filter surface, while the initial receding water contact angle was measured by gradually withdrawing a small volume of water from the same droplet. The time-dependent advancing and receding water contact angle measurements were conducted in a controlled environment ($T = 22^\circ \pm 1^\circ$, relative humidity = 79% \pm 4%) to minimize the evaporation effect. A sessile water droplet was placed on a filter surface followed by periodic measurements of contact angles. The measurements were conducted three times to ensure the accuracy of the values. A typical error in the goniometry was $\pm 2^\circ$.

Zeta potential measurements: Zeta potential measurements were conducted using a Brookhaven ZetaPALS instrument, Holtsville, NY, USA [61]. The electrophoretic velocity was calculated using a laser light-scattering phase analyzer. Then, the Smoluchowski model was utilized to calculate the zeta potential values.

Fabrication of oil-water emulsions: An oil-in-water emulsion was fabricated via vigorously stirring of n-hexadecane and DI water (10:90 vol%:vol% n-hexadecane:water). Sodium dodecyl sulfate (SDS, 0.03 wt.%) was introduced as a surfactant. Similarly, a water-in-oil emulsion (10:90 vol%:vol% n-hexadecane/water) was fabricated using Tween 80 (0.03 wt.%) as the surfactant. Please note that slight demulsification was observed over time in these emulsions. A multimeter was utilized to verify the type of emulsion. Note that the surfactant concentration (0.03 wt.%) employed in this work was similar or even higher than those reported in the literature [62,63].

Dispersed phase size measurements: The average size of the dispersed phase in an emulsion was characterized using dynamic light scattering (DLS) (ZetaPALS, Brookhaven Instruments, Holtsville, NY, USA).

Filter surface topology characterization: The PEGDA-coated filter surface's morphology was characterized using an SEM (FEI Versa 3D DualBeam, Hillsboro, OR, USA). A thin layer of gold (≈ 7 nm) was applied to the filter surface.

Underwater adhesion force measurements: A small piece of a filter (4 cm²) was attached to the bottom of the container. The container was filled with DI water. Subsequently,

a needle tip holding a droplet of n-hexadecane ($\approx 5 \mu\text{L}$) was immersed in the water (3 cm below the water surface). Then, the entire container was gradually elevated at a constant speed (6.0 mm min^{-1}) until the filter contacted the oil droplet. Subsequently, the container was gradually descended to detach the oil droplet from the filter. The force between the oil and filter surface was recorded using Data-Physics DCAT 11 (Data Physics, Filderstadt, Germany). The adhesion force was determined by the force at the detachment point.

Thermogravimetric analyses (TGA): PerkinElmer PYRIS 1 (PerkinElmer, Waltham, MA, USA) was utilized for TGA measurements. A sample ($\approx 50 \text{ mg}$) was heated to $110 \text{ }^\circ\text{C}$ at a rate of $5 \text{ }^\circ\text{C per minute}$, then the temperature was maintained for 60 min. The TGA data were compared with the data for DI water and as-obtained n-hexadecane to measure the purity of the permeate or retentate after the separation.

Continuous separation apparatus: We utilized a custom-made apparatus [9,10] for the continuous separation experiments. The apparatus consisted of a cross-flow cell CF042A, Sterlitech, Kent, WA, USA) connected to a container that stored the feed emulsion, a peristaltic pump (Model 2002, Vector, Minneapolis, MN, USA), a differential pressure gauge (DPG409-500DWU, OMEGA, Stamford, CT, USA), and a permeate tank. A filter (surface area $\approx 42 \text{ cm}^2$) was mounted to the cell. The feed oil-water emulsion was supplied from one side (feed in) of the apparatus while the permeate was collected at the opposite side of the apparatus. Note that the raffinate was readded to the feed emulsion storage container.

Supplementary Materials: The following are available online at <https://www.mdpi.com/article/10.3390/en14217429/s1>: Section S1: Fourier-transform infrared (FT-IR) spectroscopy analysis of F-PEGDA; Section S2: Effect of F-PEGDA solution viscosity on the pore size of a filter; Section S3: Initial contact angles and Time of Wetting values for water on F-PEGDA surfaces; Section S4: Calculation of the solid surface energy of F-PEGDA surfaces; Section S5: Apparent contact angles for water and oil on F-PEGDA coated filter with $2.0 \mu\text{m}$ of inherent pore size; Section S6: Apparent contact angles for oil on a filter submerged in water; Section S7: Measurements of water uptake by F-PEGDA coated filters; Section S8: Delamination of F-PEGDA coating from a filter without MEMO grafting; Section S9: Size distribution of the dispersed phases in oil-water emulsions; Section S10: TGA data for permeates from continuous separation of oil-water emulsion by cross-flow apparatus; Section S11: The measured flux values of continuous separation of oil-in-water emulsion.

Author Contributions: B.S. and M.E. conducted the experiments and collected and analyzed the data. G.K. conceived the project. B.S., M.E. and G.K. wrote the manuscript. All authors have read and agreed to the published version of the manuscript.

Funding: We thank the financial support from National Science Foundation (grant number: CBET-1944314), NASA Kansas EPSCoR (grant number: R52123-20-02314), and US Poultry and Egg Association (grant number: F091).

Institutional Review Board Statement: Not applicable.

Informed Consent Statement: Not applicable.

Data Availability Statement: The datasets generated during and/or analyzed during this study are not publicly available but are available from the corresponding author on reasonable request.

Conflicts of Interest: The authors declare that they have no known competing financial interests or personal relationships that could have appeared to influence the work reported in this paper.

References

1. Cheryan, M.; Rajagopalan, N. Membrane processing of oily streams. Wastewater treatment and waste reduction. *J. Membr. Sci.* **1998**, *151*, 13–28. [[CrossRef](#)]
2. Yuan, J.; Liu, X.; Akbulut, O.; Hu, J.; Suib, S.L.; Kong, J.; Stellacci, F. Superwetting nanowire membranes for selective absorption. *Nat. Nanotechnol.* **2008**, *3*, 332–336. [[CrossRef](#)]
3. Guerin, T.F. Heavy equipment maintenance wastes and environmental management in the mining industry. *J. Environ. Manag.* **2002**, *66*, 185–199. [[CrossRef](#)]
4. Chen, P.-C.; Xu, Z.-K. Mineral-coated polymer membranes with superhydrophilicity and underwater superoleophobicity for effective oil/water separation. *Sci. Rep.* **2013**, *3*, 1–6. [[CrossRef](#)]

5. Lian, Z.; Xu, J.; Wang, Z.; Yu, Z.; Weng, Z.; Yu, H. Nanosecond laser-induced underwater superoleophobic and underoil superhydrophobic mesh for oil/water separation. *Langmuir* **2018**, *34*, 2981–2988. [CrossRef]
6. Ali, N.; Bilal, M.; Khan, A.; Ali, F.; Iqbal, H.M. Design, engineering and analytical perspectives of membrane materials with smart surfaces for efficient oil/water separation. *TrAC Trends Anal. Chem.* **2020**, *127*, 115902. [CrossRef]
7. Chen, C.; Weng, D.; Mahmood, A.; Chen, S.; Wang, J. Separation mechanism and construction of surfaces with special wettability for oil/water separation. *ACS Appl. Mater. Interfaces* **2019**, *11*, 11006–11027. [CrossRef]
8. Fakhru'l-Razi, A.; Pendashteh, A.; Abdullah, L.C.; Biak, D.R.A.; Madaeni, S.S.; Abidin, Z.Z. Review of technologies for oil and gas produced water treatment. *J. Hazard. Mater.* **2009**, *170*, 530–551. [CrossRef]
9. Ezazi, M.; Shrestha, B.; Kim, S.I.; Jeong, B.; Gorney, J.; Hutchison, K.; Lee, D.H.; Kwon, G. Selective Wettability Membrane for Continuous Oil–Water Separation and In Situ Visible Light-Driven Photocatalytic Purification of Water. *Glob. Chall.* **2020**, *4*, 2000009.
10. Shrestha, B.; Ezazi, M.; Kwon, G. Engineered Nanoparticles with Decoupled Photocatalysis and Wettability for Membrane-Based Desalination and Separation of Oil-Saline Water Mixtures. *Nanomaterials* **2021**, *11*, 1397. [CrossRef]
11. Baig, U.; Matin, A.; Gondal, M.; Zubair, S. Facile fabrication of superhydrophobic, superoleophilic photocatalytic membrane for efficient oil-water separation and removal of hazardous organic pollutants. *J. Clean. Prod.* **2019**, *208*, 904–915. [CrossRef]
12. Gondal, M.A.; Sadullah, M.S.; Qahtan, T.F.; Dastageer, M.A.; Baig, U.; McKinley, G.H. Fabrication and wettability study of WO₃ coated photocatalytic membrane for oil-water separation: A comparative study with ZnO coated membrane. *Sci. Rep.* **2017**, *7*, 1–10. [CrossRef]
13. Jiang, C.; Liu, W.; Yang, M.; Liu, C.; He, S.; Xie, Y.; Wang, Z. Robust multifunctional superhydrophobic fabric with UV induced reversible wettability, photocatalytic self-cleaning property, and oil-water separation via thiol-ene click chemistry. *Appl. Surf. Sci.* **2019**, *463*, 34–44. [CrossRef]
14. Zhang, L.; Zhong, Y.; Cha, D.; Wang, P. A self-cleaning underwater superoleophobic mesh for oil-water separation. *Sci. Rep.* **2013**, *3*, 1–5. [CrossRef]
15. Henthorne, L. *Evaluation of Membrane Pretreatment for Seawater Reverse Osmosis Desalination*; US Department of the Interior, Bureau of Reclamation, Technical Service: Washington, DC, USA, 2007.
16. Duraisamy, R.T.; Beni, A.H.; Henni, A. *State of the Art Treatment of Produced Water. Water Treatment*; Intech: London, UK, 2013; pp. 199–222.
17. Mohammad, A.W.; Teow, Y.; Ang, W.; Chung, Y.; Oatley-Radcliffe, D.; Hilal, N. Nanofiltration membranes review: Recent advances and future prospects. *Desalination* **2015**, *356*, 226–254. [CrossRef]
18. Yuan, X.; Li, W.; Liu, H.; Han, N.; Zhang, X. A novel PVDF/graphene composite membrane based on electrospun nanofibrous film for oil/water emulsion separation. *Compos. Commun.* **2016**, *2*, 5–8. [CrossRef]
19. Padaki, M.; Murali, R.S.; Abdullah, M.S.; Misdan, N.; Moslehyani, A.; Kassim, M.; Hilal, N.; Ismail, A. Membrane technology enhancement in oil–water separation. A review. *Desalination* **2015**, *357*, 197–207. [CrossRef]
20. Kota, A.K.; Kwon, G.; Choi, W.; Mabry, J.M.; Tuteja, A. Hygro-responsive membranes for effective oil–water separation. *Nat. Commun.* **2012**, *3*, 1–8. [CrossRef] [PubMed]
21. Kwon, G.; Post, E.; Tuteja, A. Membranes with selective wettability for the separation of oil–water mixtures. *MRS Commun.* **2015**, *5*, 475–494. [CrossRef]
22. Ichikawa, T.; Nakajima, Y. Rapid demulsification of dense oil-in-water emulsion by low external electric field.: II. Theory. *Colloids Surf. A Physicochem. Eng. Asp.* **2004**, *242*, 27–37. [CrossRef]
23. Ren, B.; Kang, Y. Demulsification of oil-in-water (O/W) emulsion in bidirectional pulsed electric field. *Langmuir* **2018**, *34*, 8923–8931. [CrossRef] [PubMed]
24. Hano, T.; Ohtake, T.; Takagi, K. Demulsification kinetics of W/O emulsion in an AC electric field. *J. Chem. Eng. Jpn.* **1988**, *21*, 345–351. [CrossRef]
25. Guo, J.; Yan, D.Y.; Lam, F.L.-Y.; Deka, B.J.; Lv, X.; Ng, Y.H.; An, A.K. Self-cleaning BiOBr/Ag photocatalytic membrane for membrane regeneration under visible light in membrane distillation. *Chem. Eng. J.* **2019**, *378*, 122137. [CrossRef]
26. Nishimoto, S.; Tomoishi, S.; Kameshima, Y.; Fujii, E.; Miyake, M. Self-cleaning efficiency of titanium dioxide surface under simultaneous UV irradiation of various intensities and water flow. *J. Ceram. Soc. Jpn.* **2014**, *122*, 513–516. [CrossRef]
27. Zhang, H.; Mane, A.U.; Yang, X.; Xia, Z.; Barry, E.F.; Luo, J.; Wan, Y.; Elam, J.W.; Darling, S.B. Visible-light-activated photocatalytic films toward self-cleaning membranes. *Adv. Funct. Mater.* **2020**, *30*, 2002847. [CrossRef]
28. Qahtan, T.F.; Gondal, M.A.; Dastageer, M.A.; Kwon, G.; Ezazi, M.; Al-Kuban, M.Z. Thermally Sensitized Membranes for Crude Oil–Water Remediation under Visible Light. *ACS Appl. Mater. Interfaces* **2020**, *12*, 48572–48579. [CrossRef] [PubMed]
29. Defrance, L.; Jaffrin, M. Comparison between filtrations at fixed transmembrane pressure and fixed permeate flux: Application to a membrane bioreactor used for wastewater treatment. *J. Membr. Sci.* **1999**, *152*, 203–210. [CrossRef]
30. Cheryan, M. *Ultrafiltration Handbook*; Technomic Publishing, Co. Inc.: Lancaster, PA, USA, 1986.
31. Zhang, W.; Luo, J.; Ding, L.; Jaffrin, M.Y. A review on flux decline control strategies in pressure-driven membrane processes. *Ind. Eng. Chem. Res.* **2015**, *54*, 2843–2861. [CrossRef]
32. Wang, Z.; Ma, J.; Tang, C.Y.; Kimura, K.; Wang, Q.; Han, X. Membrane cleaning in membrane bioreactors: A review. *J. Membr. Sci.* **2014**, *468*, 276–307. [CrossRef]

33. Zsirai, T.; Buzatu, P.; Aerts, P.; Judd, S. Efficacy of relaxation, backflushing, chemical cleaning and clogging removal for an immersed hollow fibre membrane bioreactor. *Water Res.* **2012**, *46*, 4499–4507. [[CrossRef](#)]
34. Panchanathan, D.; Kwon, G.; Qahtan, T.F.; Gondal, M.A.; Varanasi, K.K.; McKinley, G.H. Kinetics of photoinduced wettability switching on nanoporous titania surfaces under oil. *Adv. Mater. Interfaces* **2017**, *4*, 1700462. [[CrossRef](#)]
35. Liu, Y.; Su, Y.; Li, Y.; Zhao, X.; Jiang, Z. Improved antifouling property of PVDF membranes by incorporating an amphiphilic block-like copolymer for oil/water emulsion separation. *RSC Adv.* **2015**, *5*, 21349–21359. [[CrossRef](#)]
36. Kwon, G.; Kota, A.K.; Li, Y.; Sohani, A.; Mabry, J.M.; Tuteja, A. On-demand separation of oil-water mixtures. *Adv. Mater.* **2012**, *24*, 3666–3671. [[CrossRef](#)] [[PubMed](#)]
37. Yong, J.; Chen, F.; Yang, Q.; Huo, J.; Hou, X. Superoleophobic surfaces. *Chem. Soc. Rev.* **2017**, *46*, 4168–4217. [[CrossRef](#)]
38. Tuteja, A.; Choi, W.; Ma, M.; Mabry, J.M.; Mazzella, S.A.; Rutledge, G.C.; McKinley, G.H.; Cohen, R.E. Designing superoleophobic surfaces. *Science* **2007**, *318*, 1618–1622. [[CrossRef](#)]
39. Zhu, X.; Tu, W.; Wee, K.-H.; Bai, R. Effective and low fouling oil/water separation by a novel hollow fiber membrane with both hydrophilic and oleophobic surface properties. *J. Membr. Sci.* **2014**, *466*, 36–44. [[CrossRef](#)]
40. Li, C.; Boban, M.; Snyder, S.A.; Kobaku, S.P.; Kwon, G.; Mehta, G.; Tuteja, A. Paper-based surfaces with extreme wettabilities for novel, open-channel microfluidic devices. *Adv. Funct. Mater.* **2016**, *26*, 6121–6131. [[CrossRef](#)]
41. Jiang, L.; Tang, Z.; Park-Lee, K.J.; Hess, D.W.; Breedveld, V. Fabrication of non-fluorinated hydrophilic-oleophobic stainless steel mesh for oil-water separation. *Sep. Purif. Technol.* **2017**, *184*, 394–403. [[CrossRef](#)]
42. Rohrbach, K.; Li, Y.; Zhu, H.; Liu, Z.; Dai, J.; Andreasen, J.; Hu, L. A cellulose based hydrophilic, oleophobic hydrated filter for water/oil separation. *Chem. Commun.* **2014**, *50*, 13296–13299. [[CrossRef](#)]
43. Wang, Y.; You, C.; Kowall, C.; Li, L. A Nanometer-Thick, Mechanically Robust, and Easy-to-Fabricate Simultaneously Oleophobic/Hydrophilic Polymer Coating for Oil-Water Separation. *Ind. Eng. Chem. Res.* **2018**, *57*, 15395–15399. [[CrossRef](#)]
44. Kordjazi, S.; Kamyab, K.; Hemmatinejad, N. Super-hydrophilic/oleophobic chitosan/acrylamide hydrogel: An efficient water/oil separation filter. *Adv. Compos. Hybrid Mater.* **2020**, *3*, 167–176. [[CrossRef](#)]
45. Guo, W.; Zhang, Q.; Xiao, H.; Xu, J.; Li, Q.; Pan, X.; Huang, Z. Cu mesh's super-hydrophobic and oleophobic properties with variations in gravitational pressure and surface components for oil/water separation applications. *Appl. Surf. Sci.* **2014**, *314*, 408–414. [[CrossRef](#)]
46. Wu, Z.; Zhang, T.; Zhang, H.; Liu, R.; Chi, H.; Li, X.; Wang, S.; Zhao, Y. One-pot fabrication of hydrophilic-oleophobic cellulose nanofiber-silane composite aerogels for selectively absorbing water from oil-water mixtures. *Cellulose* **2021**, *28*, 1443–1453. [[CrossRef](#)]
47. Brown, P.; Atkinson, O.; Badyal, J. Ultrafast oleophobic-hydrophilic switching surfaces for antifogging, self-cleaning, and oil-water separation. *ACS Appl. Mater. Interfaces* **2014**, *6*, 7504–7511. [[CrossRef](#)]
48. Pan, S.; Guo, R.; Xu, W. Durable superoleophobic fabric surfaces with counterintuitive superwettability for polar solvents. *AIChE J.* **2014**, *60*, 2752–2756. [[CrossRef](#)]
49. Yang, J.; Zhang, Z.; Xu, X.; Zhu, X.; Men, X.; Zhou, X. Superhydrophilic-superoleophobic coatings. *J. Mater. Chem.* **2012**, *22*, 2834–2837. [[CrossRef](#)]
50. Sawada, H.; Ikematsu, Y.; Kawase, T.; Hayakawa, Y. Synthesis and surface properties of novel fluoroalkylated flip-flop-type silane coupling agents. *Langmuir* **1996**, *12*, 3529–3530. [[CrossRef](#)]
51. Rambabu, G.; Bhat, S.D. Simultaneous tuning of methanol crossover and ionic conductivity of sPEEK membrane electrolyte by incorporation of PSSA functionalized MWCNTs: A comparative study in DMFCs. *Chem. Eng. J.* **2014**, *243*, 517–525. [[CrossRef](#)]
52. Brown, P.S.; Bhushan, B. Mechanically durable, superoleophobic coatings prepared by layer-by-layer technique for anti-smudge and oil-water separation. *Sci. Rep.* **2015**, *5*, 1–9. [[CrossRef](#)]
53. Lee, H.; Alcaraz, M.L.; Rubner, M.F.; Cohen, R.E. Zwitter-wettability and antifogging coatings with frost-resisting capabilities. *ACS nano* **2013**, *7*, 2172–2185. [[CrossRef](#)]
54. Pan, Y.; Huang, S.; Li, F.; Zhao, X.; Wang, W. Coexistence of superhydrophilicity and superoleophobicity: Theory, experiments and applications in oil/water separation. *J. Mater. Chem. A* **2018**, *6*, 15057–15063. [[CrossRef](#)]
55. Banchik, L.D. *Advances in Membrane-Based Oil/Water Separation*; Massachusetts Institute of Technology: Boston, MA, USA, 2017.
56. Chang, I.-S.; Chung, C.-M.; Han, S.-H. Treatment of oily wastewater by ultrafiltration and ozone. *Desalination* **2001**, *133*, 225–232. [[CrossRef](#)]
57. Tummons, E.N.; Chew, J.W.; Fane, A.G.; Tarabara, V.V. Ultrafiltration of saline oil-in-water emulsions stabilized by an anionic surfactant: Effect of surfactant concentration and divalent counterions. *J. Membr. Sci.* **2017**, *537*, 384–395. [[CrossRef](#)]
58. Wu, J.; Wei, W.; Li, S.; Zhong, Q.; Liu, F.; Zheng, J.; Wang, J. The effect of membrane surface charges on demulsification and fouling resistance during emulsion separation. *J. Membr. Sci.* **2018**, *563*, 126–133. [[CrossRef](#)]
59. Yang, Z.; Tarabara, V.V.; Bruening, M.L. Adsorption of anionic or cationic surfactants in polyanionic brushes and its effect on brush swelling and fouling resistance during emulsion filtration. *Langmuir* **2015**, *31*, 11790–11799. [[CrossRef](#)]
60. Shaulsky, E.; Nejati, S.; Boo, C.; Perreault, F.; Osuji, C.O.; Elimelech, M. Post-fabrication modification of electrospun nanofiber mats with polymer coating for membrane distillation applications. *J. Membr. Sci.* **2017**, *530*, 158–165. [[CrossRef](#)]
61. Barati, R.; Johnson, S.J.; McCool, S.; Green, D.W.; Willhite, G.P.; Liang, J.T. Polyelectrolyte complex nanoparticles for protection and delayed release of enzymes in alkaline pH and at elevated temperature during hydraulic fracturing of oil wells. *J. Appl. Polym. Sci.* **2012**, *126*, 587–592. [[CrossRef](#)]

-
62. Weiss, J.; Herrmann, N.; McClements, D. Ostwald ripening of hydrocarbon emulsion droplets in surfactant solutions. *Langmuir* **1999**, *15*, 6652–6657. [[CrossRef](#)]
 63. Krebs, T.; Schroën, C.; Boom, R. Separation kinetics of an oil-in-water emulsion under enhanced gravity. *Chem. Eng. Sci.* **2012**, *71*, 118–125. [[CrossRef](#)]

Paper P4

Reversible adsorption and desorption of PFAS on inexpensive graphite adsorbents via alternating electric field

Reproduced from [**Shrestha, Bishwash**, Mohammadamin Ezazi, Sanjay Ajayan, and Gibum Kwon. "Reversible adsorption and desorption of PFAS on inexpensive graphite adsorbents via alternating electric field." RSC Advances 11, no. 55 (2021): 34652-34659.] with permission from the Royal Society of Chemistry.

Cite this: *RSC Adv.*, 2021, 11, 34652

Reversible adsorption and desorption of PFAS on inexpensive graphite adsorbents *via* alternating electric field†

Bishwash Shrestha,[‡] Mohammadamin Ezazi,[‡] Sanjay Ajayan and Gibum Kwon^{‡*}

Per- and polyfluoroalkyl substances (PFAS) have been extensively utilized in practical applications that include surfactants, lubricants, and firefighting foams due to their thermal stability and chemical inertness. Recent studies have revealed that PFAS were detected in groundwater and even drinking water systems which can cause severe environmental and health issues. While adsorbents with a large specific surface area have demonstrated effective removal of PFAS from water, their capability in desorbing the retained PFAS has been often neglected despite its critical role in regeneration for reuse. Further, they have demonstrated a relatively lower adsorption capacity for PFAS with a short fluoroalkyl chain length. To overcome these limitations, electric field-aided adsorption has been explored. In this work, reversible adsorption and desorption of PFAS dissolved in water upon alternating voltage is reported. An inexpensive graphite adsorbent is fabricated by using a simple press resulting in a mesoporous structure with a BET surface area of $132.9 \pm 10.0 \text{ m}^2 \text{ g}^{-1}$. Electric field-aided adsorption and desorption experiments are conducted by using a custom-made cell consisting of two graphite electrodes placed in parallel in a polydimethylsiloxane container. Unlike the conventional sorption process, a graphite electrode exhibits a higher adsorption capacity for PFAS with a short fluoroalkyl chain (perfluoropentanoic acid, PFPA) in comparison to that with a long fluoroalkyl chain (perfluorooctanoic acid, PFOA). Upon alternating the voltage to a negative value, the retained PFPA or PFOA is released into the surrounding water. Finally, we engineered a device module mounted on a gravity-assisted apparatus to demonstrate electrosorption of PFAS and collection of high purity water.

Received 22nd June 2021
Accepted 18th October 2021

DOI: 10.1039/d1ra04821j

rsc.li/rsc-advances

1. Introduction

Per- and polyfluoroalkyl substances (PFAS)^{1–6} are a group of organofluorine compounds that possess functional groups such as carboxylic acid and sulfonic acid attached at one end while a fluoroalkyl chain is attached to the other end. Due to fluoroalkyl chain's excellent thermal stability^{7,8} and chemical durability,⁹ PFAS have been used in a wide range of practical applications including surfactants,^{10,11} lubricants,^{12,13} firefighting foams,^{14,15} and insulation.^{16,17} Extensive usage of PFAS over the past decades has resulted in unexpected environmental contamination.^{5,18,19} A recent study²⁰ has revealed that groundwater near a PFAS manufacturing facility was contaminated by more than 20 different types of PFAS. Further, PFAS have been detected in drinking water systems^{21–23} which has raised health concerns because they can accumulate in the human body.^{24,25} Thus, environment agencies have made regulatory actions to hamper the

production of PFAS,²⁶ and major manufacturing companies have voluntarily agreed to phase out the use of PFAS.²⁷ While these actions have resulted in a decrease in the total amount of PFAS manufacturing in past years,²⁸ there has been a drastic increase in the production of PFAS with a short fluoroalkyl chain (*e.g.*, (CF₂)₅ or shorter).²⁹ This is because most regulations have targeted PFAS with a long fluoroalkyl chain³⁰ such as perfluorooctanoic acid (PFOA) and perfluorooctanesulfonic acid (PFOS).³¹

Remediation of PFAS contaminated water has been tested by various technologies.^{32–34} Conventional coagulation or flocculation have demonstrated a limited performance due to the chemical inertness of PFAS which makes the adsorption to the coagulant ineffective.³² While physico-chemical processes such as plasma-based oxidation³⁵ and chemical oxidation³⁴ can decompose PFAS, they often result in secondary pollution by fragmented parts after the process.³³ Membrane-based technologies⁶ (*e.g.*, reverse osmosis and nanofiltration) are relatively effective to remove PFAS from water by size exclusion. However, they often require high operating pressure to collect water-rich permeate.⁶

Sorption is perhaps the most promising technology to remove PFAS from water. Various adsorbents including metal-organic frameworks (MOF),^{35,36} zeolites,^{37,38} activated carbons,^{39,40} and anion exchange resins^{41–43} have been utilized.

Department of Mechanical Engineering, University of Kansas, Lawrence, Kansas 66045, USA. E-mail: gkwon@ku.edu

† Electronic supplementary information (ESI) available. See DOI: 10.1039/d1ra04821j

‡ These authors contributed equally.



Carbonaceous adsorbents^{39,40,44–46} (e.g., activated carbon, graphene, carbon nanotubes) are attractive due to their chemical durability and thermal stability,⁴⁷ and a large specific surface area that can accelerate the adsorption kinetics.⁴⁸ However, most carbonaceous adsorbents exhibit a relatively low adsorption capacity (i.e., the amount of contaminant taken up by the unit mass of adsorbent)⁴⁹ for PFAS with a short fluoroalkyl chain length.^{50–54} Further, these adsorbents often suffer from a decrease in the adsorption capacity over time because the residual PFAS remains even after the regeneration process.⁵⁵

Electric-field aided sorption (i.e., electrosorption) is an emerging technology to remove ionized contaminants from water. When an external electric field is applied across the electrodes submerged in water, the ionized contaminants are attracted and adsorb to an electrode surface with an opposite charge.^{44,45,56,57} Thus, PFAS dissolved in water can adsorb to an anode upon application of an electric field. For example, Li *et al.*⁴⁴ demonstrated that PFOA adsorbed to a multiwalled carbon nanotube electrode upon application of voltage ($V = 0.6$ V) resulting in a 150-fold increase in adsorption capacity compared to that without an electric field. Niu *et al.*⁴⁵ reported that the adsorption rate and capacity for PFOA to a carbon nanotube/graphene anode became 12 times and 3 times higher than the results of adsorption without an electric field. Recently, Saeidi *et al.*⁴⁶ demonstrated reversible adsorption and desorption for PFOA and perfluorobutanoic acid upon reversing the voltage across the activated carbon electrode.

Herein, we demonstrate an inexpensive graphite adsorbent that enables reversible adsorption and desorption of PFAS with both short and long fluoroalkyl chain lengths (perfluoropentanoic acid (PFPA) and PFOA) in water upon alternating the voltage. The PFAS readily adsorbs to the graphite adsorbent upon application of a positive voltage within ≈ 10 s. We demonstrate that the adsorbed PFAS can be released into water with a high desorption efficiency of $\approx 96\%$ and $\approx 94\%$ for PFPA and PFOA, respectively, upon alternating voltage to a negative value. We also establish a quantitative relation to describe the kinetics of electrosorption for PFAS on a graphite adsorbent surface by utilizing a pseudo second-order kinetic model. Finally, we engineer a device module that can be mounted to a gravity-assisted apparatus and demonstrate electrosorption of PFAS and collection of high purity water.

2. Experimental section

2.1 Materials

Graphite powder (particle size <20 μm), PFPA, perfluorohexanoic acid (PFHxA), perfluoroheptanoic acid (PFHtA), PFOA, perfluorononanoic acid (PFNA), and perfluorodecanoic acid (PFDA) were purchased from Sigma Aldrich. Teflonized acetylene black was purchased from Denka Co. Ltd polydimethylsiloxane (PDMS) Sylgard 184 was purchased from Dow Corning.

2.2 Fabrication of graphite adsorbents

We fabricated graphite adsorbents by mixing the graphite powder and teflonized acetylene black (conductive binder) at

a ratio of 4 : 1 by weight. The mixture was pressed utilizing a vice to a final thickness of 0.2 cm. The resulting graphite film was then cut into the squares (2.5×2.5 cm^2) utilizing a blade followed by drying in an oven at 100 $^\circ\text{C}$ for 24 hours.

2.3 Characterization of graphite adsorbents

Surface morphology, surface area, and pore size distribution. The surface morphology of a graphite adsorbent was analyzed by scanning electron microscopy (SEM, FEI Versa 3D DualBeam). A graphite adsorbent was cut into a small piece of size ≈ 1.0 $\text{cm} \times 1.0$ cm . Then it was attached to a mount with an aid of carbon tape. SEM images were obtained at an accelerating voltage of 10 kV. Please note that metal sputtering was not involved. The Brunauer, Emmett and Teller (BET) surface area and pore size distribution (PSD) were analyzed by measuring the isotherms of nitrogen (N_2) adsorption–desorption utilizing a BET analyzer (TriStar II 3020 surface analyzer) at -196.15 $^\circ\text{C}$. The pore size distribution was measured by using the BJH methodology to the desorption section of the isotherms of nitrogen at -196.15 $^\circ\text{C}$, assuming the pores to be cylindrical in shape.⁵⁸

Electrochemical analyses. The electrochemical analyses were performed by utilizing a three-electrode cell setup (Model 760E Series Bipotentiostat workstation). The setup included a square-shaped graphite adsorbent (2.5×2.5 cm^2 , thickness = 0.2 cm), platinum (Pt), and an Ag/AgCl as a working electrode, a counter electrode, and a reference electrode, respectively. Utilizing this setup, we performed cyclic voltammetry to measure the capacitance of our graphite adsorbent. The cyclic voltammetry was performed at 10 mV s^{-1} scan rates with the cyclic voltage of -0.6 V and $+0.6$ V. Please note that electrodes were conditioned by running 100 cyclic voltammetry with a scan rate of 20 mV s^{-1} and cyclic voltage of -0.6 V and $+0.6$ V. Also, we carried out the electrochemical impedance spectroscopy (EIS) to measure the conductivity dynamics of PFAS dissolved in water by applying 10 mV amplitude sinusoidal potential perturbation scanned over a frequency range from 200 kHz to 10 MHz at open circuit potential. Please note that all measurements were conducted at a constant temperature ($T = 25.0 \pm 1.4$ $^\circ\text{C}$).

2.4 Reversible adsorption and desorption of PFAS

The adsorption experiments for PFAS on a graphite adsorbent was conducted by utilizing a custom-made cell consisting of two graphite adsorbents ($2.5 \times 2.5 \times 0.2$ cm^3) placed in parallel at a distance = 0.5 cm in a PDMS container. Please note that we fabricated two PDMS containers with dimensions of $2.5 \times 2.5 \times 1.2$ cm^3 and $3.0 \times 3.0 \times 3.0$ cm^3 . A power supply (TP3016M, Tekpower) was connected to the electrodes. A 20 mL of deionized (DI) water dissolved with PFAS (e.g., PFPA, PFHxA, PFHtA, PFOA, PFNA, and PFDA) was injected at the inlet of the cell with a flow rate of ≈ 3 mL min^{-1} by a syringe pump (KDS-230, KD Scientific). While injecting PFAS solution, a positive voltage (V) was applied across the electrodes. The solution was collected at the outlet of the cell. The temperature was maintained at $T = 22.0 \pm 1.4$ $^\circ\text{C}$. The desorption experiments were conducted by utilizing the same custom-made cell. A 20 mL of DI water was

injected at the inlet of the cell with a flow rate of $\approx 3 \text{ mL min}^{-1}$ while applying a negative voltage across the graphite electrodes that were adsorbed with PFAS. The DI water containing desorbed PFAS was collected at the outlet of the cell at $T = 22.0 \pm 1.4 \text{ }^\circ\text{C}$.

2.5 Fabrication of a device module for electrosorption of PFAS and gravity-assisted collection of high purity water

The device module was fabricated by alternatively stacking two pairs of graphite electrodes (two anodes and two cathodes) with a circular shape (diameter = 2.0 cm and thickness = 0.3 cm). Please note that nylon mesh was utilized as the spacer between the electrodes. The stacked electrodes were sandwiched between two cylindrical tubes (diameter = 2.0 cm and length = 15 cm) to form a gravity-assisted separation apparatus. Of note, the device module and tubes were sealed by a silicone sealant to prevent leakage.

2.6 PFAS concentration measurements

The concentration of PFAS was assessed by measuring the electrical conductivity of the solution. We measured the electrical conductivity by submerging two probes of a multimeter (Gardner Bender GDT-3190) with an offset distance of 2.0 cm in a PFAS solution. The multimeter measured the values of electrical resistance (R). The electrical resistivity (r) was then calculated by using the equation, $R = rL/A$. Here, L and A are the offset distance between two probes (*i.e.*, 2.0 cm), and the surface area of probe (*i.e.*, 1.5 cm²), respectively. The electrical conductivity (s) of the PFAS solution was obtained by the equation, $s = 1/r$. The electrical conductivity values were compared with a calibration curve of the electrical conductivity as a function of PFAS concentration (Fig. S1†).

3. Results and discussion

3.1 Characterization of surface morphology, surface area, and pore size distribution of graphite adsorbents

We characterized the surface morphology of a graphite adsorbent by SEM (Fig. 1a). It shows that graphite adsorbent possesses interconnected and overlapped planar sheets. Please note that such stacked sheets enable a large surface area for transport and diffusion of ionized species. The BET surface area was measured as approximately $132.9 \pm 10.0 \text{ m}^2 \text{ g}^{-1}$ which is comparable to those reported in the literature.^{45,59,60} The BET measurements also show that our graphite adsorbent exhibits a type IV isotherm with a hysteresis loop in the relative pressure (*i.e.*, P/P_0 , P_0 is the saturation pressure of N_2 at $-195.15 \text{ }^\circ\text{C}$) range of 0.4–0.9 indicating that it possesses mesopores⁶¹ (*i.e.*, pores size = 2.0–50.0 nm) (Fig. 1b). This was further corroborated by the pore size distribution (PSD) (Fig. 1c). The average pore size was measured as 18 nm and a total pore volume was measured as $0.1645 \text{ cm}^3 \text{ g}^{-1}$. A large surface area along with a wide range of pore size (*e.g.*, 3.0–130.0 nm) makes our graphite adsorbent suitable for an electrode in the electrosorption for PFAS as it helps relieve steric hindrance for adsorption of PFAS molecules. This has been verified in previous reports. For

example, Cao *et al.*⁶² have demonstrated that a silica gel with a widened pore size (*i.e.*, 6 nm) can facilitate the PFAS diffusion. Similarly, Sasi *et al.*⁶³ have shown that an adsorbent with a wide range of pore size (*e.g.*, mesopore, 2–50 nm) with an average pore size of 9 nm can overcome the steric hindrance. An adsorbent with a wide range of pore size can take advantage of both large and small pores. Pores with large size can facilitate the diffusion of PFAS molecules while small pores can contribute to a larger surface area that can provide adsorption sites. In contrast, an adsorbent with a narrow pore size distribution may compromise either its diffusion kinetics or the surface area. For example, when an adsorbent possesses a small pore size with narrow distribution, it may suffer from steric hindrance and exhibit slow diffusion kinetics. If an adsorbent possesses large pores with narrow distribution, its surface area is low which can limit its adsorption capacity.

3.2 Electrochemical analyses

Electrosorption for PFAS can be facilitated when an electrode (*i.e.*, anode) exhibits a high specific capacitance (*i.e.*, capacitance per unit mass).⁶⁴ We measured a specific capacitance (C) of our graphite adsorbent (electrode) by conducting cyclic voltammetry (CV) measurements at a scan rate of 10 mV s^{-1} (see Experimental). Fig. 2a and b show the measured CV curves for PFPA and PFOA, respectively, by applying a cyclic voltage between -0.6 V and $+0.6 \text{ V}$. Here we utilized PFPA and PFOA as representative PFAS with a short and a long fluoroalkyl chain length, respectively. The specific capacitance values were determined by calculating the enclosed area of a CV curve (eqn (S1)†). Table 1 lists the specific capacitance values for PFPA and PFOA with varied concentrations. The results show that the C values for PFPA are higher than those of PFOA at a given concentration. This can be attributed to a higher resistivity and lower polarization of PFOA in comparison to PFPA.⁶⁵ Also, it was observed that the C values are higher for solutions with higher concentrations. This was attributed to the fact that a larger number of PFAS can participate in the electrical double layer on a graphite electrode surface.⁶⁶

3.3 Reversible adsorption and desorption of PFAS upon alternating electric field

We utilized a custom-made cell (Fig. 3a, see also Experimental) to conduct adsorption and desorption experiments. The adsorption capacity (α , *i.e.*, mass of the adsorbed PFAS on one gram of anode, eqn (S2)†) was measured at varied voltage. The results show that a higher value of α was obtained upon applying a higher voltage. For example, the α value for PFPA at $V = +0.8 \text{ V}$ is 3.6 mg g^{-1} while $\alpha = 13.1 \text{ mg g}^{-1}$ at $V = +1.4 \text{ V}$ (Fig. 3b). This can be attributed to an increase in the charge density on the electrode surface. Also, the α value for PFPA is higher than that for PFOA at a given applied voltage. For example, the α value for PFPA is 10.2 mg g^{-1} while $\alpha = 2.15 \text{ mg g}^{-1}$ for PFOA at $V = +1.2 \text{ V}$ which can be attributed to higher mobility and a higher diffusion coefficient for PFPA due to its higher polarity along with its lower molecular weight.⁶⁷ Please note that the α values for PFHxA, PFHtA, PFNA, and PFDA are

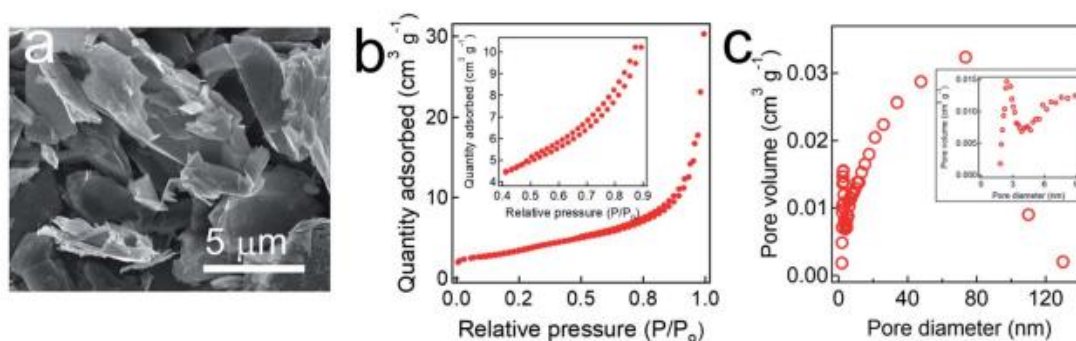


Fig. 1 (a) Scanning electron microscopy (SEM) image of a graphite adsorbent. (b) Brunauer, Emmett and Teller (BET) plot obtained by utilizing N_2 adsorption–desorption isotherms at $-196.15\text{ }^\circ\text{C}$. Inset shows isotherms in the relative pressure (P/P_0) range of 0.55–0.85. (c) Pore size distribution (PSD) data of a graphite adsorbent. Inset shows the PSD data of the pore diameter range of 2.0–10.0 nm.

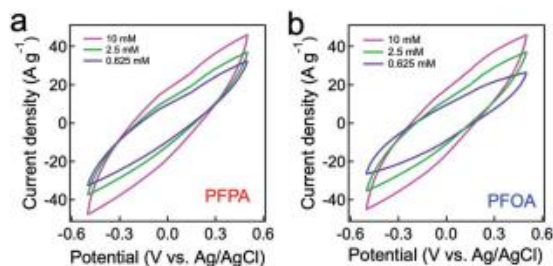


Fig. 2 (a) and (b) Cyclic voltammety measurements of graphite adsorbent (electrode) for PFPA (a) and PFOA (b) solutions with varying concentrations at a scan rate of 10 mV s^{-1} . The temperature was maintained at $25.0 \pm 1.4\text{ }^\circ\text{C}$ during the measurements.

Table 1 Specific capacitance values calculated for PFPA and PFOA at varied concentrations

Concentration (mM)	PFPA ($F\text{ g}^{-1}$)	PFOA ($F\text{ g}^{-1}$)
10	45.44	43.37
2.5	30.25	29.06
0.625	24.08	23.91

provided in ESI (Fig. S2†). It should be noted that the α values for PFPA or PFOA without applying voltage were almost 50-fold higher compared to those without applying voltage (Table S1†).

The concentration of PFAS in water can affect the adsorption capacity at a given applied voltage. The results show that the α values decrease with a decrease in the concentration (Fig. 3c). For example, the α value for PFPA solution with a concentration of $C_0 = 4000\text{ ppm}$ was measured as 17.08 mg g^{-1} while that for a solution with $C_0 = 2000\text{ ppm}$ is 9.80 mg g^{-1} at $V = +1.2\text{ V}$. This is a consequence of a decrease in the capacitance which can result in a lower mass transfer rate for PFAS (see also Fig. 2a).⁶⁵ We have also conducted Langmuir isotherm studies (Fig. 3c and Table 2). The results show that Langmuir isotherm for PFOA reasonably match well with the experimental data while that for PFPA deviates at a higher concentration. Such a discrepancy of

PFPA isotherm can be attributed to its lower molecular weight which in turn results in a higher ionic strength. Consequently, it is possible that PFPA exhibits multilayer deposition at a higher concentration.

Our electrosorption technique enables reversible adsorption and desorption of PFAS by alternating the applied voltage. A 20 mL of PFPA (or PFOA) solution with an initial concentration (C_0) of 30 ppm was poured into a custom-made cell. We continuously measured the electrical conductivity values of the solution by recording them. The measured values were compared to those in a calibration curve (see Fig. S1†) to determine the concentrations. Please note that the voltage was alternated between $+1.2\text{ V}$ and -1.2 V every 10 s. The results show that PFOA concentration becomes $17.6 \pm 2.4\text{ ppm}$ and $28.1 \pm 2.1\text{ ppm}$ at $V = +1.2\text{ V}$ (adsorption) and $V = -1.2\text{ V}$ (desorption), respectively (Fig. 3d). Similarly, PFPA concentration was measured as $9.8 \pm 2.5\text{ ppm}$ and $29.3 \pm 1.7\text{ ppm}$ at $V = +1.2\text{ V}$ and $V = -1.2\text{ V}$, respectively. These results indicate that our graphite electrode can adsorb and desorb PFAS upon alternating the voltage. The adsorption and desorption efficiency per each cycle is provided in ESI (Fig. S3†). Please note that such on-demand reversibility is critical for regenerating the electrode.

3.4 Kinetics of the reversible electrosorption for PFAS

We investigated the kinetics of electrosorption for PFAS. Fig. 4a shows the time-dependent change in the concentration of PFOA and PFPA solutions at $V = +1.2\text{ V}$. Note that we utilized the same concentration values (different molar concentration) that are shown in Fig. 3d. The results show that the concentration of PFOA and PFPA solutions rapidly decreased and reached constant values of $0.0426 \pm 0.004\text{ mM}$ and $0.03714 \pm 0.006\text{ mM}$, respectively, after $\approx 5\text{ s}$ of voltage application indicating that the equilibrium condition was attained. The electrosorption is a kinetic process that can be described by pseudo-second order kinetic model which is given as:

$$C(t) = C_0 - \frac{k_1 q_e^2 t}{1 + k_1 q_e t} \quad (1)$$

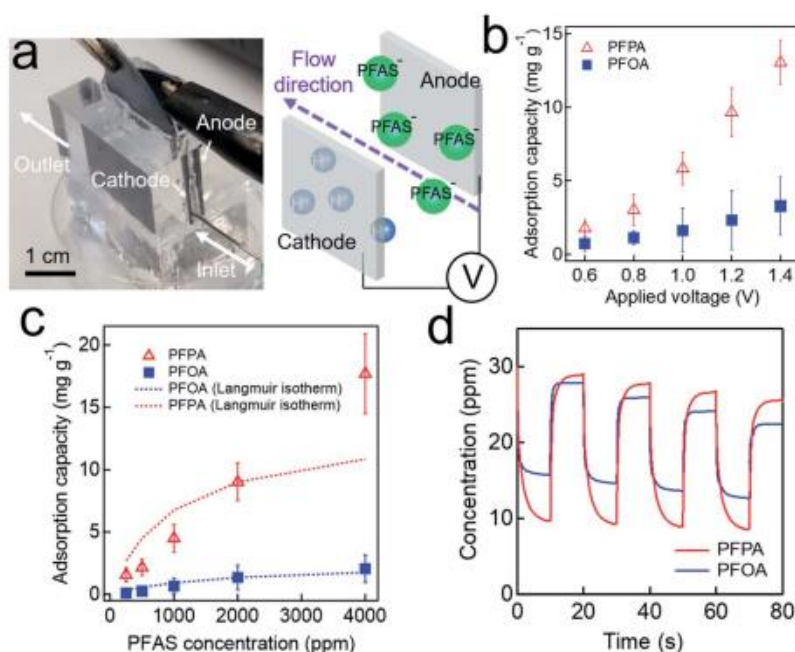


Fig. 3 (a) Photographs of the custom-made cell for electroadsorption of PFAS. (b) and (c) The measured adsorption capacity for PFPA and PFOA aqueous solutions ($C_0 = 0.01$ M for both solutions) at varied applied voltages ($V = \pm 1.2$ V) (c). (d) The measured concentration of PFPA and PFOA aqueous solutions upon reversible adsorption and desorption ($C_0 = 30$ ppm for both solutions) on graphite electrode by alternating the applied voltage between $+1.2$ V and -1.2 V. Note that the voltage alternated every 10 s.

Table 2 Langmuir isotherm parameters for PFPA and PFOA adsorption

PFAS	q_m (mg g^{-1})	b (mL mg^{-1})	R^2
PFPA	13.58	0.99	0.85
PFOA	2.52	0.57	0.99

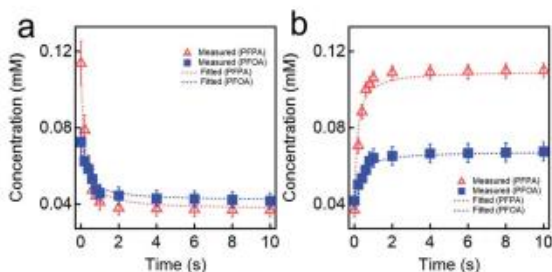


Fig. 4 (a) and (b) The measured concentrations for PFPA and PFOA aqueous solutions upon applying voltage of $V = +1.2$ V (a) or $V = -1.2$ V (b). The fitted values of concentration utilizing pseudo-second order kinetic model for adsorption (eqn (1)) and desorption (eqn (2)) are also provided.

where $C(t)$ and C_0 are the concentration of PFAS in a solution at time t and $t = 0$ (i.e., the initial concentration). q_e is the amount of PFAS adsorbed on the electrode at equilibrium and k_1 is the

adsorption rate constant. By fitting eqn (1) to the experimentally measured values, we obtained the k_1 values for PFPA and PFOA as 84.44 s^{-1} and 101.30 s^{-1} , respectively. This indicates that the adsorption rate for PFPA is higher than that of PFOA which can be attributed to higher mobility of the PFPA in comparison to PFOA due to its lower molecular weight.⁶⁷

Upon alternating the voltage ($V = -1.2$ V), the concentration of PFPA and PFOA started to increase and reached constant values of 0.111 ± 0.004 mM and 0.106 ± 0.004 mM, respectively, after ≈ 10 s of voltage application (Fig. 4b). This can also be described by pseudo-second order kinetic model which is given as:

$$C(t) = C_i + \frac{k_2 q_e^2 t}{1 + k_2 q_e t} \quad (2)$$

where C_i is the concentration of PFAS in a solution after the adsorption experiment, q_e is the amount of PFAS desorbed from the electrode at equilibrium, and k_2 is a desorption rate constant. We determined the k_2 values as 90.68 s^{-1} and 118.6 s^{-1} for PFPA and PFOA, respectively, by fitting eqn (2) to the experimentally measured values (Fig. 4b). The time-dependent adsorption and desorption of PFPA and PFOA at varied voltages are provided in Fig. S4 and S5,[†] respectively.

3.5 Electroadsorption of PFAS and gravity-assisted collection of high purity water

The module for electroadsorption for PFAS and gravity-assisted collection of clean water consists of two pairs of alternatively

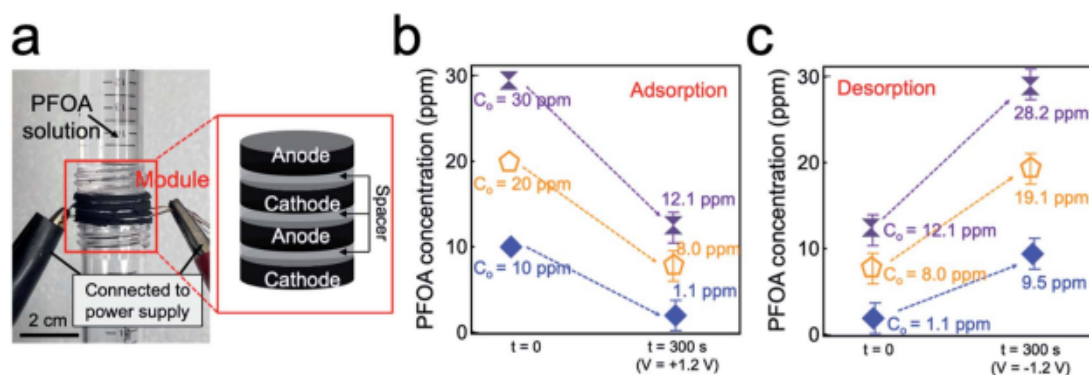


Fig. 5 (a) Photographs showing a device module utilized for gravity-assisted electrosorption for PFOA from water. (b) The measured concentrations of PFOA in the permeate after introducing 10 mL of feed PFOA solutions with varying concentrations ($C_0 = 30$ ppm, 20 ppm, and 10 ppm) to the device module. (c) The measured concentrations of PFOA after desorption for solutions with varying initial concentrations ($C_0 = 30$ ppm, 20 ppm, and 10 ppm) utilizing the device module.

stacked graphite electrodes (two anodes and two cathodes) with a circular shape that are separated by nylon mesh as a spacer. We found that a spacer with a width of 0.2 cm can result in the highest adsorption rate for both PFPA and PFOA (Fig. S6 and eqn (S3)†). The module was sandwiched between two cylindrical tubes to form a gravity-assisted apparatus (Fig. 5a). Upon pouring PFOA solution ($C_0 = 10$ ppm, 10 mL) into the upper tube, it started to permeate through the module under gravity and the permeate was collected in the bottom tube. A voltage of $V = +1.2$ V was continuously applied across a cathode and an anode during permeation. Please note that the entire solution passes through the module in approximately 300 ± 12 s. The concentration of PFOA in the permeate was measured as 1.1 ± 0.1 ppm. We conducted the same experiments using PFOA solution with varying concentrations (e.g., $C_0 = 20$ ppm and $C_0 = 30$ ppm). The results show that the permeate contains 8.0 ± 1.0 ppm ($C_0 = 20$ ppm) and 12.1 ± 2.2 ppm ($C_0 = 30$ ppm), respectively (Fig. 5b).

We conducted desorption experiments by submerging the module in DI water and applying a voltage of $V = -1.2$ V for 300 s. The results show that the water contained 9.45 ppm of PFOA ($C_0 = 10$ ppm) indicating that nearly all PFOA was released from graphite anodes. Please note that the water contained 19.1 ppm ($C_0 = 20$ ppm) and 28.2 ppm ($C_0 = 30$ ppm) of PFOA after desorption experiments (Fig. 5c). The experimental data of adsorption and desorption for PFPA solutions by using the device module are provided in Fig. S7 and S8,† respectively. We believe that our module has the potential for portable water purification device that can remove the dissolved contaminants and generate clean water at a low voltage (e.g., 1.2 V).

4. Conclusion

We demonstrated reversible adsorption and desorption of PFAS in water by an electric-field aided process utilizing an inexpensive graphite adsorbent as the electrode. A large BET surface area along with mesopores of graphite enabled a large

adsorption capacity for PFAS with both short and long fluoroalkyl chain lengths (e.g., PFPA and PFOA, respectively) upon application of the voltage. We demonstrated that an adsorption capacity value increases with an increase in the applied voltage as well as with the increase in the PFAS concentration. We also showed multiple adsorption–desorption cycles by alternating the voltage that can result in highly efficient adsorption and desorption of PFAS from the graphite electrode surface. The kinetics of electric-field aided adsorption and desorption of PFAS in water were investigated by utilizing a pseudo-second-order model. Finally, a device module was engineered that can be mounted to a gravity-assisted apparatus for electrosorption of PFAS and obtaining water with high purity.

Author contributions

BS, MAE, and SA performed the experiments. BS and MAE analyzed data and wrote the manuscript. GK conceived the project, designed the experiments and wrote the manuscript.

Conflicts of interest

There are no conflicts to declare.

Acknowledgements

This research was supported by National Science Foundation [award number: CBET-1944314], NASA Kansas EPSCoR [award number: R52123-20-02314], and National Science Foundation RET Site: Exploring Career Opportunities through Water-Themed Engineering Research (ECO-WaTER) [award number: 1801710].

References

- 1 R. C. Buck, J. Franklin, U. Berger, J. M. Conder, I. T. Cousins, P. De Voigt, A. A. Jensen, K. Kannan, S. A. Mabury and

- S. P. van Leeuwen, *Integr. Environ. Assess. Manage.*, 2011, **7**, 513–541.
- 2 E. M. Sunderland, X. C. Hu, C. Dassuncao, A. K. Tokranov, C. C. Wagner and J. G. Allen, *J. Exposure Sci. Environ. Epidemiol.*, 2019, **29**, 131–147.
- 3 M. F. Rahman, S. Peldszus and W. B. Anderson, *Water Res.*, 2014, **50**, 318–340.
- 4 G. B. Post, P. D. Cohn and K. R. Cooper, *Environ. Res.*, 2012, **116**, 93–117.
- 5 L. Ahrens and M. Bundschuh, *Environ. Toxicol. Chem.*, 2014, **33**, 1921–1929.
- 6 K. H. Kucharzyk, R. Darlington, M. Benotti, R. Deeb and E. Hawley, *J. Environ. Manage.*, 2017, **204**, 757–764.
- 7 M. P. Krafft and J. G. Riess, *Chemosphere*, 2015, **129**, 4–19.
- 8 N. Merino, Y. Qu, R. A. Deeb, E. L. Hawley, M. R. Hoffmann and S. Mahendra, *Environ. Eng. Sci.*, 2016, **33**, 615–649.
- 9 M. Haukäs, U. Berger, H. Hop, B. Gulliksen and G. W. Gabrielsen, *Environ. Pollut.*, 2007, **148**, 360–371.
- 10 C. A. Moody and J. A. Field, *Environ. Sci. Technol.*, 2000, **34**, 3864–3870.
- 11 M. M. Schultz, D. F. Barofsky and J. A. Field, *Environ. Eng. Sci.*, 2003, **20**, 487–501.
- 12 J. Glüge, M. Scheringer, I. T. Cousins, J. C. DeWitt, G. Goldenman, D. Herzke, R. Lohmann, C. A. Ng, X. Trier and Z. Wang, *Environ. Sci.: Processes Impacts*, 2020, **22**, 2345–2373.
- 13 H. Zhu and K. Kannan, *Environ. Technol. Innovation*, 2020, **19**, 100943.
- 14 W. J. Backe, T. C. Day and J. A. Field, *Environ. Sci. Technol.*, 2013, **47**, 5226–5234.
- 15 C. Baduel, C. J. Paxman and J. F. Mueller, *J. Hazard. Mater.*, 2015, **296**, 46–53.
- 16 E. Kissa, *Fluorinated surfactants and repellents*, CRC Press, 2001.
- 17 S. Rayne and K. Forest, *J. Environ. Sci. Health, Part A: Toxic/Hazard. Subst. Environ. Eng.*, 2009, **44**, 1145–1199.
- 18 F. Xiao, *Water Res.*, 2017, **124**, 482–495.
- 19 K. Kannan, *Environ. Chem.*, 2011, **8**, 333–338.
- 20 M.-A. Pétré, D. P. Genereux, L. Koropeckyj-Cox, D. R. Knappe, S. Duboscq, T. E. Gilmore and Z. R. Hopkins, *Environ. Sci. Technol.*, 2021, **55**(9), 5848–5856.
- 21 V. Gellrich, H. Brunn and T. Stahl, *J. Environ. Sci. Health, Part A: Toxic/Hazard. Subst. Environ. Eng.*, 2013, **48**, 129–135.
- 22 X. C. Hu, D. Q. Andrews, A. B. Lindstrom, T. A. Bruton, L. A. Schaidler, P. Grandjean, R. Lohmann, C. C. Carignan, A. Blum and S. A. Balan, *Environ. Sci. Technol. Lett.*, 2016, **3**, 344–350.
- 23 P. C. Rumsby, C. L. McLaughlin and T. Hall, *Philos. Trans. R. Soc., A*, 2009, **367**, 4119–4136.
- 24 G. W. Olsen, J. L. Butenhoff and L. R. Zobel, *Reprod. Toxicol.*, 2009, **27**, 212–230.
- 25 E. P. o. c. i. t. F. Chain, H. K. Knutsen, J. Alexander, L. Barregård, M. Bignami, B. Brüschweiler, S. Ceccatelli, B. Cottrill, M. Dinovi and L. Edler, *EFSA J.*, 2018, **16**, e05194.
- 26 The Interstate Technology & Regulatory Council (ITRC) Per and Polyfluoroalkyl Substances (PFAS) Team, *PFAS Technical and Regulatory Guidance Document and Fact Sheets PFAS-1*, p. 2020.
- 27 Environmental Protection Agency, Perfluoroalkyl Sulfonates; Significant New Use Rule, *Fed. Regist.*, 2002, **67**, 72854–72867.
- 28 C. f. D. Control and Prevention, US Department of Health and Human Services, Centers for Disease Control and Prevention, Atlanta, GA, 2019.
- 29 P. Zhao, X. Xia, J. Dong, N. Xia, X. Jiang, Y. Li and Y. Zhu, *Sci. Total Environ.*, 2016, **568**, 57–65.
- 30 S. Brendel, É. Fetter, C. Staude, L. Vierke and A. Biegel-Engler, *Environ. Sci. Eur.*, 2018, **30**, 1–11.
- 31 OECD/UNEP Global PFC Group, *Synthesis paper on per- and polyfluorinated chemicals (PFCs)*, Environment, health and safety, environment directorate, 2013, p. 60.
- 32 O. Quiñones and S. A. Snyder, *Environ. Sci. Technol.*, 2009, **43**, 9089–9095.
- 33 B. N. Nzeribe, M. Crimi, S. Mededovic Thagard and T. M. Holsen, *Crit. Rev. Environ. Sci. Technol.*, 2019, **49**, 866–915.
- 34 T. A. Bruton and D. L. Sedlak, *Environ. Sci. Technol.*, 2017, **51**, 13878–13885.
- 35 D. Barpaga, J. Zheng, K. S. Han, J. A. Soltis, V. Shutthanandan, S. Basuray, B. P. McGrail, S. Chatterjee and R. K. Motkuri, *Inorg. Chem.*, 2019, **58**, 8339–8346.
- 36 Y. Yang, Z. Zheng, W. Ji, J. Xu and X. Zhang, *J. Hazard. Mater.*, 2020, **395**, 122686.
- 37 V. Ochoa-Herrera and R. Sierra-Alvarez, *Chemosphere*, 2008, **72**, 1588–1593.
- 38 M. Van den Bergh, A. Krajnc, S. Voorspoels, S. R. Tavares, S. Mullens, I. Beurroies, G. Maurin, G. Mali and D. E. De Vos, *Angew. Chem.*, 2020, **132**, 14190–14194.
- 39 P. McCleaf, S. Englund, A. Östlund, K. Lindegren, K. Wiberg and L. Ahrens, *Water Res.*, 2017, **120**, 77–87.
- 40 C. Zeng, A. Atkinson, N. Sharma, H. Ashani, A. Hjelmstad, K. Venkatesh and P. Westerhoff, *AWWA Water Sci.*, 2020, **2**, e1172.
- 41 M. Haddad, C. Oie, S. V. Duy, S. Sauvé and B. Barbeau, *Sci. Total Environ.*, 2019, **660**, 1449–1458.
- 42 F. Taleb, M. Ben Mosbah, E. Elaloui and Y. Moussaoui, *Korean J. Chem. Eng.*, 2017, **34**, 1141–1148.
- 43 Q. Yu, S. Deng and G. Yu, *Water Res.*, 2008, **42**, 3089–3097.
- 44 X. Li, S. Chen, X. Quan and Y. Zhang, *Environ. Sci. Technol.*, 2011, **45**, 8498–8505.
- 45 Z. Niu, Y. Wang, H. Lin, F. Jin, Y. Li and J. Niu, *Chem. Eng. J.*, 2017, **328**, 228–235.
- 46 N. Saeidi, F.-D. Kopinke and A. Georgi, *Chem. Eng. J.*, 2021, **416**, 129070.
- 47 L. Liu, Y. Liu, B. Gao, R. Ji, C. Li and S. Wang, *Crit. Rev. Environ. Sci. Technol.*, 2020, **50**, 2379–2414.
- 48 H. Marsh and F. R. Reinoso, *Activated carbon*, Elsevier, 2006.
- 49 J. Han, T. Yan, J. Shen, L. Shi, J. Zhang and D. Zhang, *Environ. Sci. Technol.*, 2019, **53**, 12668–12676.
- 50 Z. Du, S. Deng, Y. Bei, Q. Huang, B. Wang, J. Huang and G. Yu, *J. Hazard. Mater.*, 2014, **274**, 443–454.
- 51 P. Chularueangakorn, S. Tanaka, S. Fujii and C. Kunacheva, *Desalin. Water Treat.*, 2014, **52**, 6542–6548.

- 52 T. D. Appleman, C. P. Higgins, O. Quiñones, B. J. Vanderford, C. Kolstad, J. C. Zeigler-Holady and E. R. Dickenson, *Water Res.*, 2014, **51**, 246–255.
- 53 E. Gagliano, M. Sgroi, P. P. Falciglia, F. G. Vagliasindi and P. Roccaro, *Water Res.*, 2020, **171**, 115381.
- 54 F. Li, J. Duan, S. Tian, H. Ji, Y. Zhu, Z. Wei and D. Zhao, *Chem. Eng. J.*, 2020, **380**, 122506.
- 55 I. M. Militao, F. A. Roddick, R. N. Bergamasco and L. Fan, *J. Environ. Chem. Eng.*, 2021, 105271.
- 56 S. Wang, X. Li, Y. Zhang, X. Quan, S. Chen, H. Yu and H. Zhao, *Chin. Sci. Bull.*, 2014, **59**, 2890–2897.
- 57 K. Kim, P. Baldaguez Medina, J. Elbert, E. Kayiwa, R. D. Cusick, Y. Men and X. Su, *Adv. Funct. Mater.*, 2020, 2004635.
- 58 E. P. Barrett, L. G. Joyner and P. P. Halenda, *J. Am. Chem. Soc.*, 1951, **73**, 373–380.
- 59 A. E. D. Mahmoud, A. Stolle and M. Stelter, *ACS Sustainable Chem. Eng.*, 2018, **6**, 6358–6369.
- 60 H.-Q. Li, Y.-G. Wang, C.-X. Wang and Y.-Y. Xia, *J. Power Sources*, 2008, **185**, 1557–1562.
- 61 K. Sing, *Pure Appl. Chem.*, 1982, **54**, 2201–2218.
- 62 D. Cao, M. Hu, C. Han, J. Yu, L. Cui, Y. Liu, H. Wang, Y. Cai, Y. Kang and Y. Zhou, *Analyst*, 2012, **137**, 2218–2225.
- 63 P. C. Sasi, A. Alinezhad, B. Yao, A. Kubátová, S. A. Golovko, M. Y. Golovko and F. Xiao, *Water Res.*, 2021, **200**, 117271.
- 64 M. Suss, S. Porada, X. Sun, P. Biesheuvel, J. Yoon and V. Presser, *Energy Environ. Sci.*, 2015, **8**, 2296–2319.
- 65 R. Rica, R. Ziano, D. Salerno, F. Mantegazza and D. Brogioli, *Phys. Rev. Lett.*, 2012, **109**, 156103.
- 66 D. Zhang, X. Wen, L. Shi, T. Yan and J. Zhang, *Nanoscale*, 2012, **4**, 5440–5446.
- 67 B. Dyatkin, N. C. Osti, A. Gallegos, Y. Zhang, E. Mamontov, P. T. Cummings, J. Wu and Y. Gogotsi, *Electrochim. Acta*, 2018, **283**, 882–893.

Paper P1 Copyright Permission



MDPI Support Team <support@mdpi.com>

Thu 3/31/2022 1:48 AM

To: Shrestha, Bishwash



Dear Bishwash,

Thank you for your email.

No special permission is required to reuse all or part of an article published by MDPI, including figures and tables. For articles published under an open access Creative Common CC BY license, any part of the article may be reused without permission, provided that the original article is clearly cited. Reuse of an article does not imply endorsement by the authors or MDPI.

Please Note: Some articles (especially Reviews) may contain figures, tables or text taken from other publications, for which MDPI does not hold the copyright or the right to re-license the published material. Please note that you should speak with the original copyright holder (usually the original publisher or authors), to enquire about whether or not this material can be re-used.

Please let us know if you have any further questions!

Kind regards,

Donna Toma | MDPI Support Team

Email: support@mdpi.com

Visit us: <https://www.mdpi.com/>

MDPI Headquarters

St. Alban-Anlage 66, 4052 Basel


Office Tel. +41 (0) 61 683 77 34

Response time: Mon-Fri (9am-5pm CET)

Paper P2 Copyright Permission



?
Help ▾


Live Chat

Predicting kinetics of water-rich permeate flux through photocatalytic mesh under visible light illumination

SPRINGER NATURE

Author: Bishwash Shrestha et al

Publication: Scientific Reports

Publisher: Springer Nature

Date: Oct 26, 2021

Copyright © 2021, The Author(s)

Creative Commons

This is an open access article distributed under the terms of the [Creative Commons CC BY](#) license, which permits unrestricted use, distribution, and reproduction in any medium, provided the original work is properly cited.

You are not required to obtain permission to reuse this article.

To request permission for a type of use not listed, please contact [Springer Nature](#)

© 2022 Copyright - All Rights Reserved | [Copyright Clearance Center, Inc.](#) | [Privacy statement](#) | [Terms and Conditions](#)
Comments? We would like to hear from you. E-mail us at customer@copyright.com

Paper P3 Copyright Permission



MDPI Support Team <support@mdpi.com>

Thu 3/31/2022 1:48 AM

To: Shrestha, Bishwash



Dear Bishwash,

Thank you for your email.

No special permission is required to reuse all or part of an article published by MDPI, including figures and tables. For articles published under an open access Creative Common CC BY license, any part of the article may be reused without permission, provided that the original article is clearly cited. Reuse of an article does not imply endorsement by the authors or MDPI.

Please Note: Some articles (especially Reviews) may contain figures, tables or text taken from other publications, for which MDPI does not hold the copyright or the right to re-license the published material. Please note that you should speak with the original copyright holder (usually the original publisher or authors), to enquire about whether or not this material can be re-used.

Please let us know if you have any further questions!

Kind regards,

Donna Toma | MDPI Support Team

Email: support@mdpi.com

Visit us: <https://www.mdpi.com/>

MDPI Headquarters

St. Alban-Anlage 66, 4052 Basel

Office Tel. +41 (0) 61 683 77 34

Response time: Mon-Fri (9am-5pm CET)

Paper P4 Copyright Permission



CONTRACTS-COPYRIGHT (shared) <Contracts-Copyright@rsc.org>

Fri 4/1/2022 5:13 AM

To: Shrestha, Bishwash



Dear Bishwash

The Royal Society of Chemistry (RSC) hereby grants permission for the use of your paper(s) specified below in the printed and microfilm version of your thesis. You may also make available the PDF version of your paper(s) that the RSC sent to the corresponding author(s) of your paper(s) upon publication of the paper(s) in the following ways: in your thesis via any website that your university may have for the deposition of theses, via your university's Intranet or via your own personal website. We are however unable to grant you permission to include the PDF version of the paper(s) on its own in your institutional repository. The Royal Society of Chemistry is a signatory to the STM Guidelines on Permissions (available on request).

Please note that if the material specified below or any part of it appears with credit or acknowledgement to a third party then you must also secure permission from that third party before reproducing that material.

Please ensure that the thesis includes the correct acknowledgement (see <http://rsc.li/permissions> for details) and a link is included to the paper on the Royal Society of Chemistry's website.

Please also ensure that your co-authors are aware that you are including the paper in your thesis.

Regards

Gill Cockhead

Contracts & Copyright Executive, Sales Operations
Royal Society of Chemistry

T: +44 (0) 1223 432134 | www.rsc.org

